TECHNISCHE UNIVERSITÄT MÜNCHEN

Fakultät für Physik

Neutron scattering studies of thermally and periodically driven spin correlations

Franz Xaver Haslbeck, M. Sc.

Vollständiger Abdruck der von der
Fakultät für Physik der Technischen Universität München
zur Erlangung des akademischen Grades eines

Doktors der Naturwissenschaften (Dr. rer. nat.)

genehmigten Dissertation.

Vorsitzende:		Prof. Dr. Simone Warzel
Prüfer der Dissertation:	1.	Prof. Dr. Christian Pfleiderer
	2.	Prof. Dr. Stefan Filipp
	3.	Prof. Dr. Marc Janoschek

Die Dissertation wurde am 07.10.2021 bei der Technischen Universität München eingereicht und durch die Fakultät für Physik am 03.12.2021 angenommen.

Abstract

In this thesis experimental studies investigating thermally and periodically driven magnetic correlations by means of neutron scattering and all-electrical microwave spectroscopy are presented. Specifically, we report results on the critical spin excitations in the prototypical ferromagnetic superconductor UGe_2, the weak crystallisation process of the magnetic skyrmion lattice (SkX) out of the paramagnetic state in the helimagnet MnSi, and fluctuation-induced instabilities in the magnetic SkX phase of the helimagnet Cu_2OSeO_3. The spin dynamics were investigated using the novel neutron resonance spin-echo spectroscopy (NRSE) technique longitudinal MIEZE (modulation of intensity with zero effort), small angle neutron scattering (SANS), and 2-tone all-electrical microwave spectroscopy.

In the course of this work, the longitudinal MIEZE option at the instrument RESEDA at the Heinz Maier-Leibnitz Zentrum in Garching was upgraded in terms of reduced instrumental background, small momentum transfer towards the SANS regime, and phase-lock of the MIEZE signal. New data analysis software as well as instrumental control software were developed and implemented.

In UGe_2 we demonstrated the potential of MIEZE with sub-μeV energy resolution for the study of quantum matter. We revealed purely longitudinal spin fluctuations at the paramagnetic-to-ferromagnetic phase transition at ambient pressure with a dual nature arising from $5f$ electrons that are hybridised with the conduction electrons. Whereas localised spin fluctuations are perfectly described by the critical exponents of a three-dimensional Ising ferromagnet, itinerant spin fluctuations occur over length scales comparable to the superconducting coherence length. Our results are consistent with the scenario of p-wave superconductivity in UGe_2 and show that MIEZE is able to spectroscopically disentangle the complex low-energy behaviour characteristic of quantum materials.

In MnSi the emergence of the SkX order out of the paramagnetic state was investigated experimentally. The comprehensive study comprised magnetic susceptibility, small-angle neutron scattering, neutron resonance spin-echo spectroscopy, and all-electrical microwave spectroscopy measurements. We revealed skyrmion patches exceeding sizes of 10^3 Å and lifetimes of above several nanoseconds that form already in the paramagnetic phase. The transition is well described by the Landau soft-mode mechanism of weak crystallisation. As part of this thesis, SANS measurements were analysed and neutron resonance spin-echo spectroscopy measurements were performed.

Finally, microwave-induced instabilities in the SkX phase of Cu_2OSeO_3 were investigated based on numerical simulations that reveal a melting of the long-range order under intense microwave magnetic fields. The 2-tone all-electrical microwave spectroscopy, which was developed as part of this thesis, allows to drive the collective magnetic excitations and to simultaneously observe the excitation spectra. In combination with SANS, microwave-

induced effects on the magnetic long-range order may be observed on a microscopic scale. We observed coupling between the sample and the intense microwave radiation already some Kelvin above the ordering temperature T_C for frequencies about the resonant modes of the SkX. Furthermore, parts of the SkX phase were not accessible. Signatures of the emergence of long-range magnetic order were not observed at T_C for intense excitation fields and frequencies below the counterclockwise (CCW) mode, suggesting a redshift of the modes. Furthermore, the neutron scattering pattern of the SkX phase broadened azimuthally under intense microwave radiation for frequencies about the resonant modes which indicates the loss of long-range hexagonal order and may be attributed empirically to the melting of the skyrmion lattice into a skyrmion liquid state. Our observations revealed a coupling of the excitation field to the magnetic order above T_C, indicate a redshift of the modes and the loss of long-range order and show that further theoretical investigations are necessary to understand the complex behaviour.

Kurzdarstellung

Diese Arbeit behandelt die experimentelle Untersuchung thermisch und periodisch getriebener magnetischer Korrelationen mit Hilfe von Neutronenstreuung und Mikrowellenspektroskopie. Die Ergebnisse umfassen die Charakterisierung kritischer magnetischer Anregungen im ferromagnetischen Supraleiter UGe_2, die Untersuchung des schwachen Kristallisationsprozesses des magnetischen Skyrmionengitters (SkX) aus dem paramagnetischen Zustand im Helimagneten MnSi und die Charakterisierung fluktuationsgetriebener Instabilitäten im magnetischen SkX des Helimagneten Cu_2OSeO_3. Hierfür wurden longitudinales MIEZE (modulation of intensity with zero effort), eine Neutronen-Resonanz-Spin-Echo Methode, Kleinwinkelneutronenstreuung und elektrische Mikrowellenspektroskopie eingesetzt.

Als Teil dieser Arbeit wurde die longitudinale MIEZE Option am Instrument RESEDA am Heinz Maier-Leibnitz Zentrum in Garching durch die Reduzierung der instrumentellen Untergrundstreuung, die Erweiterung des beobachtbaren Impulsübertrags zu kleineren Winkeln und die Phasenfixierung des MIEZE Signals verbessert. Neue Datenanalyse- und Instrumentensteuerungssoftware wurde entwickelt und implementiert.

In unserer Studie an UGe_2 wurde unter anderem gezeigt, welches Potenzial zur Untersuchung von Quantenmaterialien in MIEZE und ihrer Energieauflösung besser als $1\,\mu$eV steckt. Wir identifizierten rein longitudinale Spinanregungen am Übergang der para- zur ferromagnetischen Phase bei Umgebungsdruck, die einen dualen Charakter aufgrund der Hybridisierung der $5f$ Elektronen mit Leitungselektronen zeigen. Lokalisierte Spinfluktuationen sind perfekt durch die kritischen Exponenten eines dreidimensionalen

Ising Ferromagnets beschrieben. Hingegen treten auf Längenskalen der supraleitenden Kohärenzlänge itinerante Spinfluktuationen auf. Unsere Ergebnisse sind konsistent mit einer möglichen p-Wellensupraleitung in UGe_2 und zeigen, dass MIEZE ideal geeignet ist das komplexe niedrigenergetische Verhalten von Quantenmaterialien spektroskopisch zu analysieren.

Des Weiteren wurde die Formierung des magnetischen SkX aus dem paramagnetischen Zustand in MnSi experimentell untersucht. Die umfangreiche Studie wurde mit Hilfe von magnetischen Suszeptibilitätsmessungen, Kleinwinkelneutronenstreuung, Neutronen-Resonanz-Spin-Echo und elektrischer Mikrowellenspektroskopie durchgeführt. Wir zeigten, dass sich bereits in der paramagnetischen Phase Skyrmionengitterbereiche mit einer Größe von mehr als 10^3 Å und einer Lebensdauer von mehr als einer Nanosekunde bilden. Der Übergang kann gänzlich durch die schwache Kristallisierung des Landau Mechanismus der niederenergetischen Moden beschrieben werden. Als Teil dieser Arbeit wurden Daten der Kleinwinkelneutronenstreuung analysiert und Neutronen-Resonanz-Spin-Echo-Messungen durchgeführt.

Das Schmelzen der langreichweitigen Ordnung des SkX durch starke magnetische Wechselfelder konnte in numerischen Simulationen beobachtet werden, weshalb in dieser Arbeit durch Mikrowellenfelder induzierte Instabilitäten der Skyrmionenphase in Cu_2OSeO_3 untersucht wurden. Die elektrische 2-Ton-Mikrowellenspektroskopie wurde als Teil dieser Arbeit entwickelt und erlaubt eine intensive Anregung der kollektiven magnetischen Moden und die gleichzeitige Beobachtung des Anregungsspektrums. Mittels der Kleinwinkelneutronenstreuung konnten mikrowelleninduzierte Änderungen der langreichweitigen magnetischen Ordnung auf mikroskopischer Skala untersucht werden. Eine Kopplung zwischen dem intensiven Treibfeld und der Probe konnte bereits einige Kelvin oberhalb der Ordnungstemperatur T_C für Frequenzen um die resonanten Moden des SkX beobachtet werden. Des Weiteren waren Teile des Skyrmionenphase nicht zugänglich. Unter dem Einfluss eines starken Treibfeldes mit einer Frequenz unterhalb der resonanten CCW (counterclockwise) Mode beobachteten wir keine langreichweitige Ordnung an T_C. Dies ist ein Hinweis auf eine mögliche Rotverschiebung der Resonanzfrequenz. Die azimuthale Verbreiterung der Maxima der Bragg-Streuung unter Einfluss des starken Treibfeldes mit Frequenzen um die resonanten Moden deutet des Weiteren auf eine Abnahme der langreichweitigen hexagonalen Ordnung hin. Dies kann empirisch durch das Schmelzen des Skyrmionengitters und das Entstehen einer Skyrmionenflüssigkeit erklärt werden. Zusammenfassend zeigten die Beobachtungen eine Kopplung des Treibfeldes an die magnetische Ordnung oberhalb T_C und weisen auf eine Rotverschiebung der Moden und eine Abnahme der langreichweitigen Ordnung hin. Weitere theoretische Untersuchungen sind nötig um dieses komplexe Verhalten zu erklären.

Contents

1. Introduction

Nature yields a plethora of electronic and magnetic ordering phenomena such as ferro-, antiferro-, or ferrimagnetism, charge density and spin density waves, or superconductivity, some of which are already utilised for everyday applications. Especially ferromagnetism, as one of the simplest forms of magnetic order, is utilised in various applications ranging from large scale generators and electric motors to headphones to hard disk drives where terabytes of data are stored employing nanometre-sized, uniformly magnetised regions, so-called domains. Although the interactions underlying all these ordering phenomena are microscopic in origin, they generally lead to the formation of mesoscopic structures. Despite acute differences between the interactions, remarkable similarities in the formation of domains exist among these ordering phenomena, for example between magnetic order and superconductivity.

The formation of domains in finite ferromagnets is due to surface demagnetisation effects. Thereby, the system's energy is lowered by the transition from a saturated configuration to a domain configuration [1, 2]. Parameters such as magneto-crystalline anisotropies, shape anisotropies, or external magnetic fields further introduce preferred domain orientations. Fig. 1.1 (a) exemplarily displays the domain structure of a single crystalline, ferromagnetic garnet film with out-of-plane anisotropy where black and white regions denote the magnetisation orientation. Interestingly, similar patterns form in type-I superconductors in the Meissner phase as shown in Fig. 1.1 (b) [1, 3]. Here, the superconductor partitions into normal and superconducting domains under the influence of an external magnetic field.

Notably, both effects can be explained within the same framework [4–6]. Although the partition into domains lowers the overall energy, the transition regions where the magnetisation varies from one domain to another or the state changes from normal to superconducting, respectively, are usually associated with a positive energy. Hence, a balance establishes between maximising the number of domains and minimising the domain wall proportion. However, the Ginzburg-Landau theory of superconductors shows that magnetic field penetrating the interface lowers its energy, thus, suggesting the existence of another group of superconductors for which the surface energy is negative [1]. Abrikosov showed that in such a case the domain walls are unstable and instead of the interme-

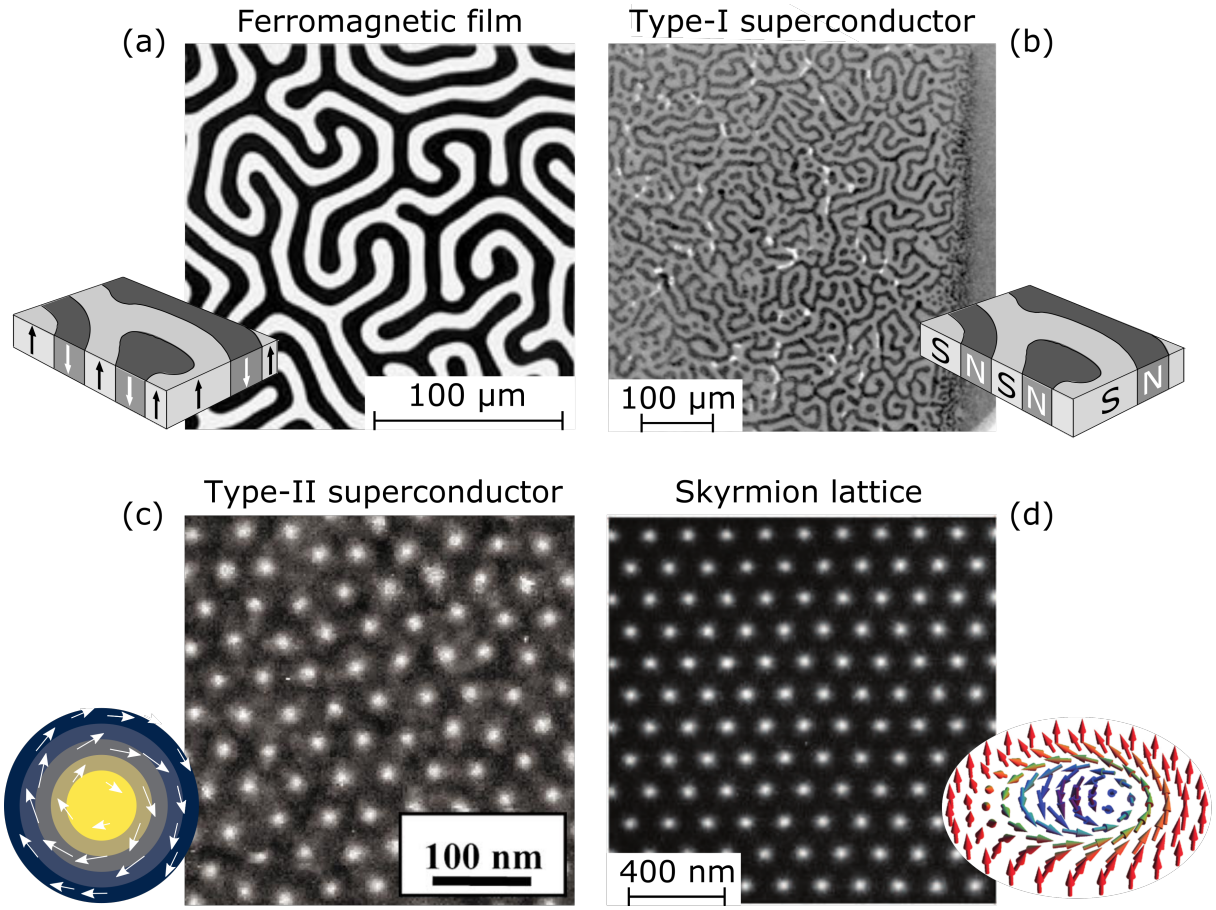

Figure 1.1.: Domain wall formation in superconductors and magnetic materials. (a) Ferromagnetic domains in a single crystal garnet film with out-of-plane anisotropy. (b) Intermediate state of indium, a type-I superconductor, with normal and superconducting regions at $T = 1.9\,\mathrm{K}$. (c) Hexagonal vortex lattice in V_3Si, a type-II superconductor, observed by means of scanning tunneling microscopy. (d) Bloch-type hexagonal skyrmion lattice in a thin-film FeGe sample observed with Lorentz transmission electron microscopy. The magnetic field is applied out-of-plane and $T = 200\,\mathrm{K}$. Figures taken from Refs. [8–12].

diate state a mixed state forms [7]. It consists of quantised, superconducting vortices, so-called flux lines, penetrating the superconductor which may order in lattices as shown in Fig. 1.1 (c).

Bogdanov utilised the analogy of superconductivity and magnetism and suggested a negative domain wall energy in magnetic materials with a so-called Dzyaloshinskii-Moriya interaction which should lead to the stabilisation of vortices in a similar mixed state [6, 13]. Eventually, Mühlbauer *et al.* discovered these magnetic vortices in form of topologically non-trivial skyrmion lines ordering in a hexagonal lattice in the chiral magnet MnSi [14]. Since then, magnetic skyrmions have attracted great scientific and technological interest and have been found in a variety of bulk materials, thin films, nanoscaled systems, and

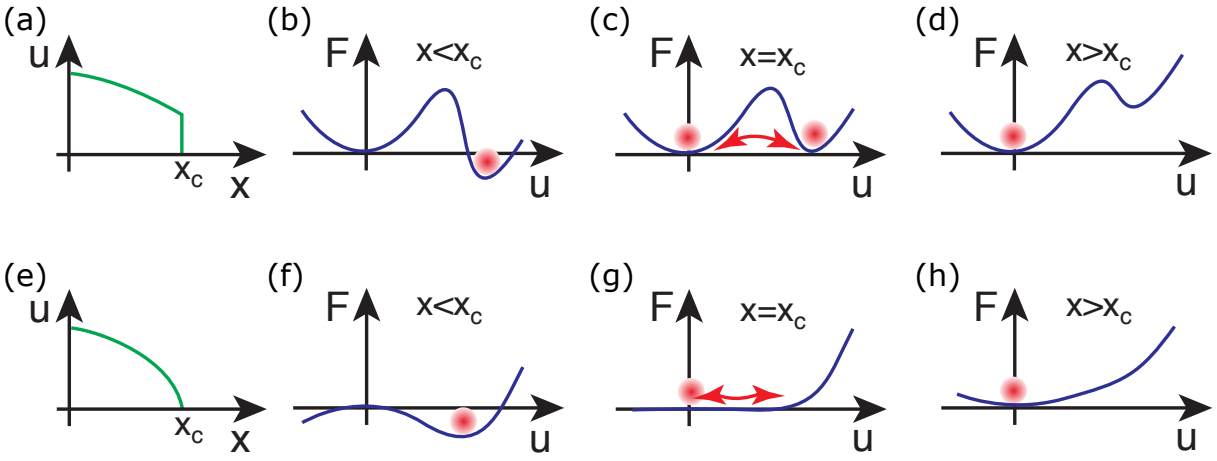

Figure 1.2.: First- and second-order phase transitions. Behaviour of the order parameter u as a function of control parameter x in the case of a (a) first- and (e) second-order phase transition. Free energy landscape around the critical value x_c for (b-d) a first- and (f-h) a second-order phase transition. Figure taken form Ref. [29].

heterostructures [12, 15–28]. Such a skyrmion lattice as observed in FeGe is shown in Fig. 1.1 (d) exhibiting remarkable similarity with the vortex lattice in type-II superconductors.

The endeavour to understand these ordering phenomena leads inevitably to the examination of the system's dynamics which reflect the underlying interactions and symmetries. In the ordered state, dynamics occur in the form of, for example, phonons that encode the atomic-scale bonding forces between the atoms in a solid. Similarly, magnons reflect the magnetic exchange interactions between neighboring magnetic moments. At phase transitions, fluctuations can play a decisive role in the loss of order. The transition between phases can be described by an order parameter which is zero in the disordered phase and finite in the ordered phase. An example for such a parameter is the spontaneous magnetisation in a ferromagnet [30].

Following the Ehrenfest classification, a distinction is made between phase transitions of first- and second-order as depicted in Fig. 1.2 [30]. In the former case, the order parameter vanishes discontinuously as a function of control parameter x at the critical value x_c displayed in Fig. 1.2 (a). The control parameter can be for example temperature, pressure, magnetic field, or chemical doping. The transition is associated with latent heat as the system changes from one local minimum in the free energy landscape to another as shown in Figs. 1.2 (b) to (d) and fluctuations are usually irrelevant. In the latter case, the order parameter appears continuously out of a global minimum as shown in Fig. 1.2 (e). The flat energy landscape allows for strong fluctuations of the order parameter in space and time as shown in Figs. 1.2 (f) to (h). They increase towards the transition and eventually

diverge at the critical value x_c according to universal scaling laws which are independent of the microscopic interactions and depend only on the symmetry of the order parameter and the spatial dimension d [31].

1.1. Fluctuations at magnetic quantum phase transitions

Over the past decades phase transitions in electronic systems at zero temperature attracted great scientific interest [32–35]. They are driven by a non-thermal control parameter such as pressure, chemical doping, or magnetic field. Here, the macroscopic behaviour is governed by quantum fluctuations instead of thermal fluctuations as $\hbar\omega > k_B T$. These so-called quantum phase transitions (QPTs) are frequently observed by the suppression of a continuous thermal phase transition to zero temperature by a non-thermal control parameter and behave distinctly different compared to well-understood thermal phase transitions.

The point where the continuous transition is suppressed to zero temperature is called quantum critical point (QCP). It is believed that the emergence of novel states of matter in its vicinity including prominent examples such as unconventional superconductivity or breakdown of the Fermi liquid theory is driven by the associated strong quantum fluctuations [32, 36–39]. Even at finite temperature the emerging quantum matter has profoundly different physical properties in a characteristically V-shaped region, referred to as quantum critical region, sometimes ranging up to room temperature, despite QPTs being a zero temperature instability [32, 37, 40]. Hence, the investigation of quantum phase transitions and the precise examination of the associated quantum fluctuations remains a vibrant field in solid state physics.

Magnetic quantum phase transitions are a fruitful starting basis, both experimentally and theoretically, for the discovery of new quantum matter states, understanding the underlying ordering mechanism and QPTs in general [35, 41]. The variety of magnetically ordered systems exhibiting QPTs include famous examples such as cuprates, which under the suppression of antiferromagnetic order through doping can become high temperature superconductors [35, 42, 43]. Furthermore, simple model systems such as the insulating Ising ferromagnets $CoHb_2O_6$ [44] and $LiHoF_4$ [45] where the application of a transverse field with respect to the Ising axis drives the system into a paramagnetic phase at zero temperature help to probe and advance the theoretical framework. In the case of itinerant ferromagnets, the continuous suppression of the second-order phase transition to zero temperature is typically not observed due to stray coupling of the ferromagnetic order parameter to electronic soft modes [34]. The system omits the resulting, strong quantum fluctuations by undergoing a first-order phase transition or masking the QCP via

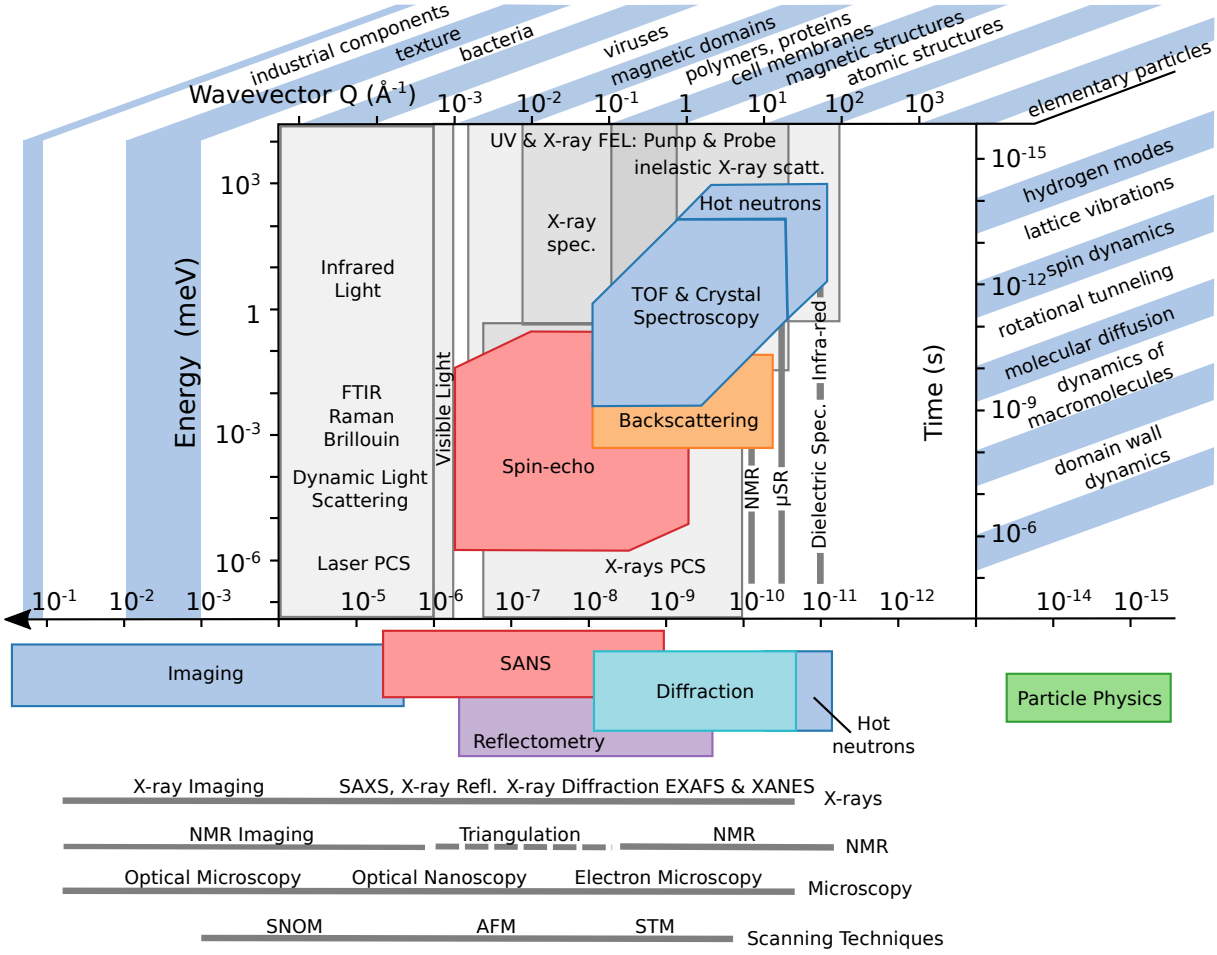

Figure 1.3.: Energy and momentum Resolution of state-of-the-art spectroscopy, diffraction, and imaging techniques. Spin-Echo techniques advance neutron spectroscopy (colored areas) towards higher energy and momentum resolution. Figure adapted from Ref. [49].

the formation of a spin-density wave or the emergence of unconventional superconductivity. Similarly, in heavy fermion systems the suppression of magnetic order can lead to the formation of unconventional superconductivity, 'hidden order', or electronic nematic states [46–48].

One of the experimental challenges is the investigation of the relevant energy scales that drive the emergence of these complex properties. This is complicated in various ways. At first, multiple energy scales might play a role as, for example, suggested by materials in which unconventional superconductivity is not only observed in the vicinity of the magnetic instability but even far away. Second, due to critical slowing down of the fluctuation frequency approaching the critical point the behaviour of the phase transition is dominated by soft modes [32]. As the relevant fluctuation energy scales with temperature, highest energy resolution is necessary as e.g. 100 mK corresponds to just $\sim 10\,\mu$eV.

Finally, the electronic ground state is very sensitive to effects of disorder which can be caused by chemical doping as tuning parameter [50, 51]. Since magnetic fields furthermore break rotational symmetry, external pressure is a privileged tuning parameter to study QPTs. Nevertheless, this restricts the range of accessible spectroscopic techniques as e.g. angle-resolved photoemission spectroscopy (ARPES) is not feasible with pressure cells. Neutron scattering is possible at high pressures but mostly limited to static properties. Hence, the relevant energy scales are typically measured indirectly through thermal, magnetic, or transport bulk properties.

As part of this thesis project, we showcase that the newly developed longitudinal modulation of intensity with zero effort (MIEZE) – a neutron spin-echo spectroscopy technique – can overcome these challenges. Fig. 1.3 shows the energy and momentum resolution of state-of-the-art spectroscopy techniques. While techniques such as NMR and μSR are not limited in terms of energy resolution, they are local probes and cannot measure collective excitations. Conventional neutron spectroscopy such as time-of-flight (TOF) neutron scattering and triple axis spectroscopy (TAS) are the standard techniques to study collective magnetic excitations, but typically highest energy resolutions "only" range from 500 μeV to 50 μeV. Instead, spin-echo techniques achieve an energy resolution down to several neV and momentum resolution down to the range of small angle neutron scattering. Furthermore, MIEZE overcomes inherent difficulties of spin-echo measurements on depolarising samples and sample environments such as magnetic fields or ferromagnetic systems.

We investigated the ferromagnet UGe_2 which is one of the few known systems where ferromagnetism and superconductivity microscopically coexist [37, 52]. Previous neutron spectroscopy measurements investigating the magnetic fluctuations at the continuous phase transition by means of triple axis spectroscopy showed ambiguous results even at ambient pressure [53]. MIEZE exceeds these studies in terms of energy resolution by at least one order of magnitude and by a factor of two in momentum transfer resolution. We determined the critical exponents at the paramagnetic to ferromagnetic phase transition which perfectly match a three-dimensional (3d) Ising ferromagnet. In addition, we observe a change from localised to itinerant character of the magnetic fluctuations on a length scale comparable to the superconducting coherence length. Notably, our measurements, though not performed at the QPT, might be able to capture and resolve signatures of the relevant fluctuations of the QPT as the ultrahigh energy resolution of at least 1 μeV corresponds to $T \to 0$.

1.2. Skyrmion lattices

Beside the investigation of spin fluctuations associated with the formation of ferromagnetism in UGe_2, the spin dynamics of skyrmion lattices have been studied via two different approaches. In this section, the main properties of magnetic skyrmion lattices are explained and an introduction into the stabilisation mechanism, emergent electrodynamics, and spin dynamics is given. Finally, the two scientific challenges addressed as part of this PhD project are presented.

A skyrmion is a topologically non-trivial stable field configuration. T. Skyrme proposed the concept in the early 1960s in the field of particle physics where he described nucleons as topologically non-trivial solitons of a pion field now referred to as skyrmions [54–56]. Since then, the concept has been employed in various forms in different fields of physics such as particle physics [57–61], quantum Hall states [62–64], Bose-Einstein condensates [65–67], and liquid crystals [68]. In the field of solid state magnetism, skyrmions are topologically non-trivial spin vortices, i.e. they cannot be continuously transformed into a topologically trivial spin order such as para- or ferromagnetism [69].

The existence of magnetic skyrmions was already theoretically predicted in 1989 for non-centrosymmetric magnetic materials with uniaxial anisotropy [6, 13]. But it took another 20 years until skyrmions were eventually observed by means of small angle neutron scattering (SANS) in the $B20$ transition metal MnSi in a small phase pocket where they form a two-dimensional trigonal lattice [14]. Magnetic skyrmion lattices were afterwards also observed in complementary real space measurements such as Lorentz force transmission electron microscopy (LTEM) [18, 20] and magnetic force microscopy (MFM) [70]. Since then, a variety of bulk compounds, thin films, heterostructures, and nanoscaled systems were discovered which host topologically non-trivial spin structures [6, 12–25, 27, 28, 69, 71–75]. The wide interest in skyrmions range from fundamental physics of the potential breakdown of the Fermi liquid theory [76–78] to new applications in spintronics [79]. Skyrmions are especially promising as future information carriers due to their efficient coupling to spin currents originating from their emergent electrodynamics [21, 26, 80] as well as in high-frequency devices exploiting the well-understood spin excitations [12, 20, 81–83].

Following the observation of skyrmions in the cubic chiral magnet MnSi, several bulk materials in the same non-centrosymmetric crystallographic space group $P2_13$ were discovered to also host skyrmion lattices. Interestingly, these materials exhibit various electronic structures ranging from metals like $Mn_{1-x}Fe_xSi$, $Mn_{1-x}Co_xSi$, FeGe, MnGe over the semiconductor $Fe_{1-x}Co_xSi$ to the Mott insulator Cu_2OSeO_3. Despite the difference in the underlying electronic structure, field, temperature, and length scales, their phase diagrams are conspicuously similar [69]. Furthermore, topologically non-trivial states also

exist in compounds such as the alloy $Co_{10-x}Zn_{10-y}Mn_{x+y}$ which belongs to a different space group [21]. These findings suggest that these complex magnetic structures might be rather common [69].

The skyrmion density is given by [14, 84]

$$\phi = \frac{1}{4\pi}\hat{n} \cdot \frac{\partial \hat{n}}{\partial x} \times \frac{\partial \hat{n}}{\partial y} \tag{1.1}$$

with the coordinates x and y perpendicular to the magnetic field H and the orientation of the magnetic field $\hat{n} = \boldsymbol{M}(\boldsymbol{r})/\left|\boldsymbol{M}(\boldsymbol{r})\right|$. The non-trivial topology of the skyrmion lattice is reflected by its finite topological invariant, the so-called winding number, which is the value of the integrated skyrmion density

$$\Phi = \int \phi \, dx \, dy. \tag{1.2}$$

The winding number Φ is quantised, for example, if the unit vector $\hat{n}$ points along a common direction on the integration boundaries [85]. Hence, spin configurations with a non-trivial topology can be counted. In contrast, the topologically trivial structures such as para-, ferro-, or helimagnetism have a winding number of zero.

As mentioned above, skyrmion lattices have been observed in reciprocal and real space by means of various measurement techniques. Typical data from SANS, MFM, and LTEM measurements on different materials are shown in Fig. 1.4 where the topologically trivial helical state is observed in the upper row and the non-trivial skyrmion lattice phase in the lower. In SANS measurements at zero magnetic field, magnetic Bragg peaks are observed with a momentum transfer $\boldsymbol{Q}$ corresponding to the helical propagation vector pointing along the magnetic easy axis, typically either $\langle 100 \rangle$ or $\langle 111 \rangle$, as shown in Fig. 1.4 (a) [87, 88]. In MFM, which can detect the stray field at the surface of a bulk sample, a stripy pattern is observed where the magnetisation direction varies periodically from positive to negative. The same pattern is observed in LTEM, which is sensitive to the in-plane component of the magnetisation, and allows the investigation of thinned bulk samples [69].

In the case of a skyrmion lattice at finite magnetic field, as shown in Fig. 1.4 (d), a sixfold scattering pattern is observed in a scattering plane perpendicular to the applied magnetic field. Here, two opposing Bragg peaks correspond to one of the three helices displayed in Fig. 1.5 (iv) and their orientation in-plane depends on magnetocrystalline anisotropies [14, 89, 90]. In real space, a hexagonal lattice of circular objects is observed where the magnetisation in their centres opposes the externally applied magnetic field H as in cubic chiral magnets skyrmion lattices consist of anti-skyrmions with a winding number of -1 [14].

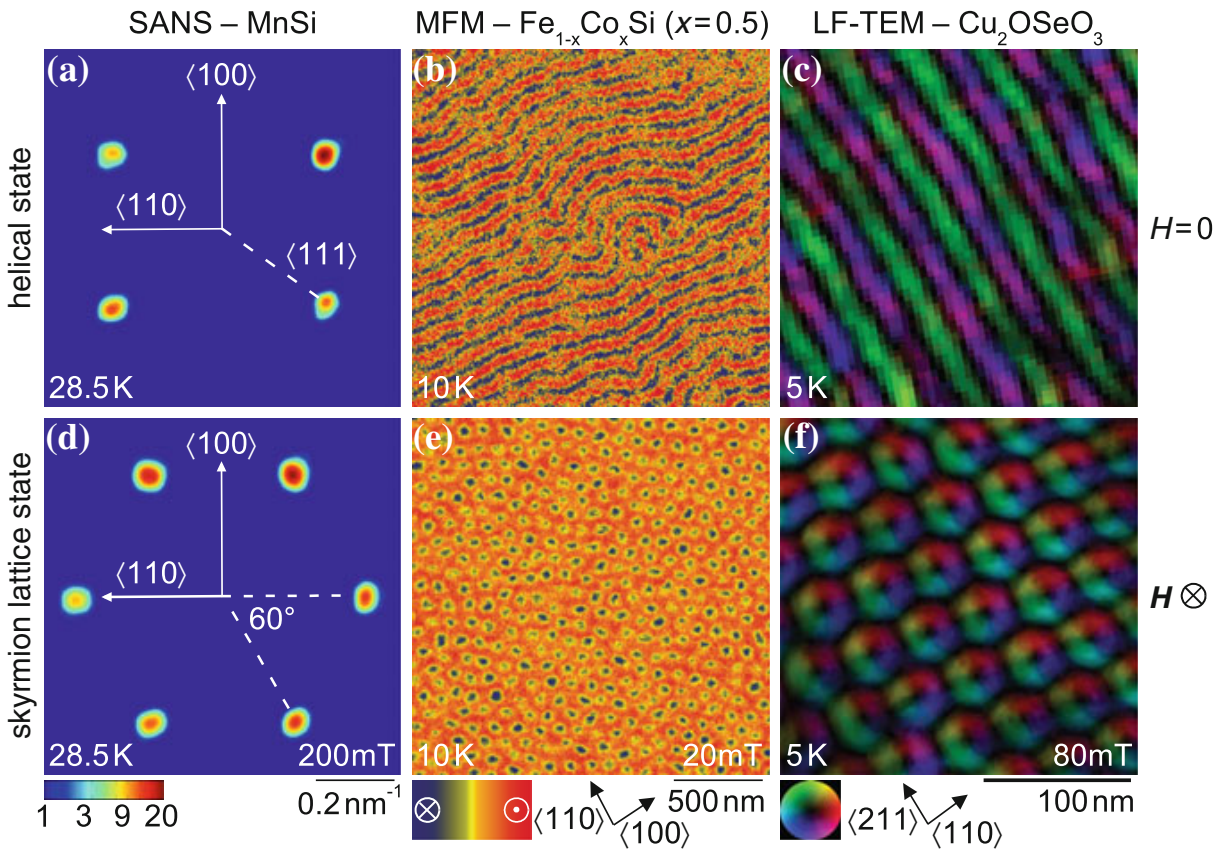

Figure 1.4.: Observation of helical and skyrmion lattice states in reciprocal and real space. (a-c) Zero-field helical state. (d-f) Skyrmion lattice at finite magnetic field. (a, d) Neutron scattering intensity of MnSi on a two-dimensional detector [14, 86]. Real space observation of the magnetic structure by means of (b, e) magnetic force microscopy (MFM) [70] and (c, f) Lorentz Force Transmission Electron Microscopy (LF-TEM or LTEM) [18, 20]. Figure taken from Ref. [69].

1.2.1. Magnetic phase diagram of cubic chiral magnets

Several mechanisms have been identified that stabilise single skyrmions or skyrmion lattices in magnetic materials. In cubic chiral magnets, such as MnSi, the skyrmion phase is stabilised in a small phase pocket by thermal fluctuations and, therefore, exists only at relatively high temperatures close to the transition temperature T_c [14]. Notably, recent studies revealed a second skyrmion phase in the cubic chiral magnet Cu_2OSeO_3 thermodynamically disconnected from the high temperature skyrmion phase and stabilised by cubic anisotropies [91]. Furthermore, the formation of topologically non-trivial phases can also be caused by magnetocrystalline anisotropies in systems with strong spin-orbit coupling or lower crystal symmetries, or by surface energies in thin films and heterostructures [12, 22, 91–94]. However, this thesis only focusses on skyrmion lattices in cubic chiral

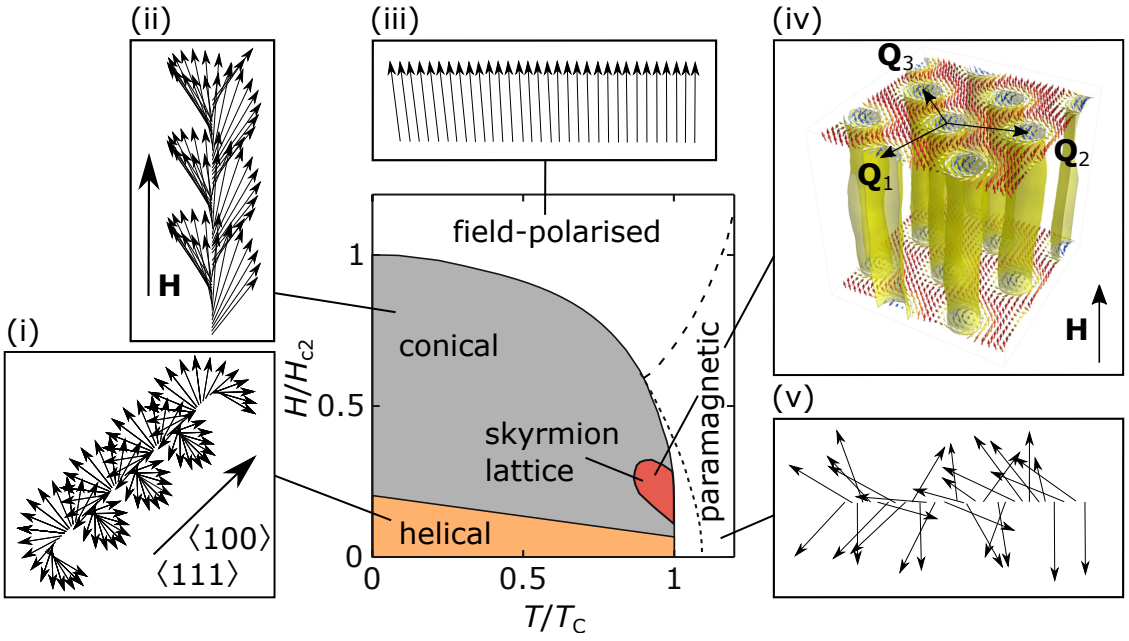

Figure 1.5.: Typical magnetic phase diagram and magnetic structures of cubic chiral magnets. The systems exhibit paramagnetic, helical, conical and field-polarised order. In a small phase pocket just below the transition temperature T_c in a finite field range, the two-dimensional triangular skyrmion lattice consisting of topologically non-trivial spin vortices is observed. Depictions taken from Refs. [70, 95].

magnets with Dzyaloshinskii-Moriya interaction (DMI) which are stabilised by thermal fluctuations. Their properties are described in the following.

The common magnetic phase diagram of cubic chiral magnets displayed in Fig. 1.5 is governed by a hierarchy of energy scales as already shown 40 years ago for MnSi in Ref. [96]. First and strongest is the exchange interaction favouring a parallel spin alignment. On the second strongest scale the DMI arising from the lack of inversion symmetry of the underlying crystal structure favours a perpendicular spin alignment [97–99]. The combination stabilises a helical spin modulation as ground state as shown in Fig. 1.5 (i) [87, 100]. The enantiomer of the crystal structure determines the chirality of the DMI and, hence, of the helix [101, 102]. On the weakest scale, cubic anisotropies comprising higher order spin-orbit coupling terms dictate the propagation direction of the helical modulation along certain crystallographic directions [88].

Well above the transition temperature T_c the system is paramagnetic with a large fluctuating moment [103]. Decreasing the temperature in zero field, the system transitions into a multi-domain helical phase below T_c. The domains are equally populated and the helical propagation is determined by weak cubic magnetic anisotropies [69]. Applying small magnetic fields, the domain population changes until the system transitions into

the conical phase through either a spin-flop transition or a second-order transition at the transition field H_{c1} depending on the angle between the applied magnetic field and the helical propagation vector [104]. The conical phase is a single-domain state where the helical modulation persists and its propagation vector points along the magnetic field, but in addition, the spins are canted towards the propagation vector as shown in Fig. 1.5 (ii). Increasing the magnetic field further, the spins tilt towards the magnetic field direction until a transition into the field-polarised phase takes place above H_{c2} [105].

Just above the ordering temperature T_c, a fluctuation-disordered regime is observed as indicated by a dashed line in Fig. 1.5 [89, 106, 107]. A small finite uniform magnetisation can be induced by a magnetic field. However, the region can be denoted as paramagnetic as it exhibits an abundance of fluctuations and Fourier components of the magnetisation at and around the ordering vector $\boldsymbol{Q}$ that are purely dynamic [108]. Three components can be differentiated. First, fluctuations akin to helical order are dominated by the magnetocrystalline anisotropies. Second, fluctuations governed by the Zeeman energy are reminiscent of the conical order parallel to an applied magnetic field and, third, fluctuations perpendicular to the applied magnetic field with a multi-$\boldsymbol{Q}$ character resemble the skyrmion lattice order.

In zero field strong interactions between isotropic chiral fluctuations are observed above the paramagnetic-to-helimagnetic transition. The nature of this regime and the associated transition have been the subject of heated discussions in the case of MnSi concerning speculations about a putative zero field skyrmion liquid phase [109–111]. Eventually, Janoschek *et al.* could conclusively show for MnSi that the strong interactions suppress the mean-field second-order phase transition resulting in a Brazovskii scenario of a fluctuation-induced first-order transition [112, 113]. In general for chiral magnets, the phase transition might also be described by the Wilson-Fisher-scenario or the Bak-Jensen-scenario depending on the so-called Ginzburg length [31, 88, 114–117].

Finally, just below T_c at finite field the skyrmion lattice stabilises in a small phase pocket which was historically referred to as A-phase [14, 118, 119]. The lattice consists of a regular hexagonal arrangement of spin whirls in two dimensions as shown in Fig. 1.5 (iv). The structure can be described as the superposition of three helices in a plane perpendicular to the applied magnetic field and having relative angles of 120° to one another as depicted by three vectors. Along the magnetic field the two-dimensional spin structure is repeated forming skyrmion tubes and an overall ferromagnetic component.

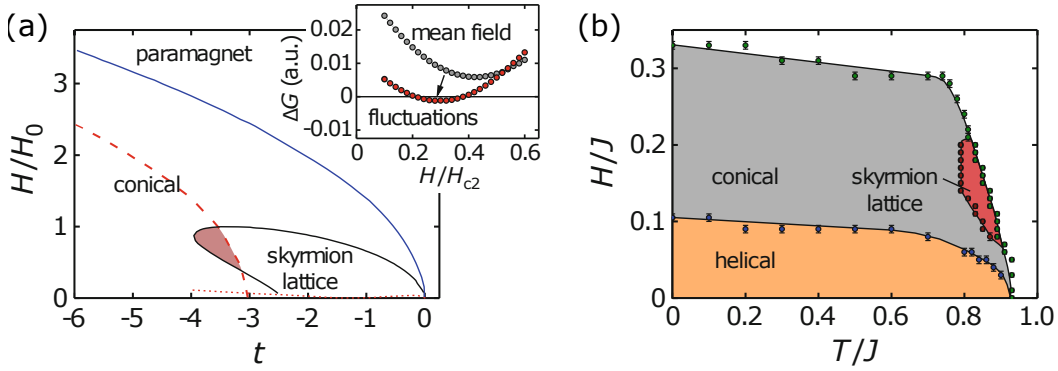

Figure 1.6.: Fluctuation-stabilised skyrmion lattice. (a) Theoretical phase diagram in a Ginzburg-Landau model depending on the magnetic field H/H_0 and t which is approximately proportional to $T - T_c$. (b) Magnetic phase diagram obtained by means of Monte Carlo simulations. Figures taken from Refs. [14, 120].

1.2.2. Stabilisation and emergent electrodynamics

The standard Ginzburg-Landau model of the free energy density describes the thermodynamic properties of the cubic chiral magnets well [14, 69]. The helical, conical, and field-polarised states are accounted for by a competition of ferromagnetic exchange, the DMI, the Zeeman interaction as well as spin-orbit coupling terms of second or higher order. Within this mean-field theory, the conical order is the ground state for a small applied field, but the energy difference to the skyrmion lattice order is small close to the ordering temperature T_c and at intermediate fields as shown in the inset of Fig. 1.6 (a) [14]. For the stabilisation of the skyrmion lattice phase, the model is extended by Gaussian fluctuations about the mean-field solution as leading correction. The resulting phase diagram is depicted in Fig. 1.6 (a). Although fluctuations on short length scales contribute predominantly, both short-range and long-range fluctuations favor a skyrmion lattice for intermediate magnetic fields [14]. The skyrmion lattice phase is stable at intermediate fields and below the ordering temperature. The model is only valid for small fluctuations and cannot be applied too close to T_c. Hence, the skyrmion lattice is stable in the red shaded area. The fact that the six-fold symmetry axis of the skyrmion lattice is unrelated to the symmetry of the cubic lattice (apart from higher-order anisotropies) supports this fluctuation-driven stabilisation mechanism. Cubic anisotropies only introduce slight temperature and field dependencies of the phase pocket size and define the orientation of the skyrmion lattice in-plane. The stabilisation mechanism by thermal fluctuations is demonstrated furthermore in Monte Carlo simulations where the experimental phase diagram is reproduced as shown in Fig. 1.6 (b).

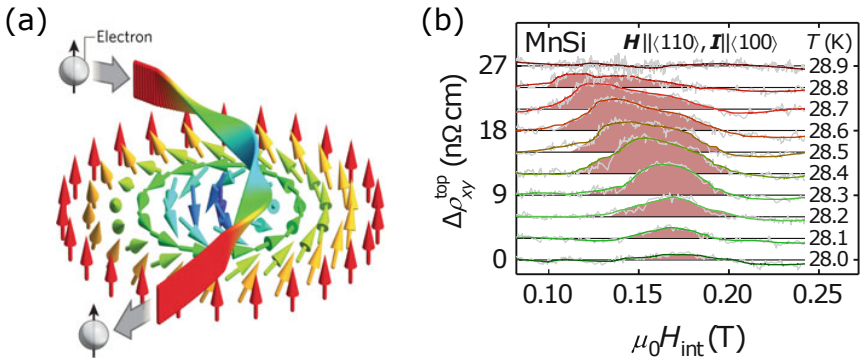

Figure 1.7.: Berry phase and topological Hall effect. (a) The spin of a traversing electron follows adiabatically the local magnetic spin structure of the skyrmion and picks up a Berry phase. (b) An emergent magnetic field originating in the real-space Berry phase leads to a topological Hall signal as observed in e.g. MnSi. Figures taken from Refs. [122, 123].

However, magnetocrystalline anisotropies can stabilise a skyrmion lattice for a magnetic field along specific directions. In recent studies on Cu_2OSeO_3 such a second skyrmion lattice phase thermodynamically disconnected from the well-known high-temperature skyrmion phase was identified for a magnetic field along $\langle 100 \rangle$ [91, 121].

An exciting topic covered in multiple scientific studies over recent years concern the efficient coupling of skyrmions to spin currents and the emerging electrodynamics [69, 80, 124]. In metallic systems hosting a topologically non-trival magnetic structure such as skyrmions, the spin of a conduction electron follows adiabatically the local magnetic spin structure and gains a real-space Berry phase as depicted in Fig. 1.7 (a). The emerging magnetic and electric fields due to the deflection of the electron can be expressed as [69]

$$\boldsymbol{B}_z^e = -\frac{\hbar}{2e}\hat{n}(\partial_x\hat{n} \times \partial_y\hat{n}) \tag{1.3}$$

$$\boldsymbol{E}_\alpha^e = -\frac{\hbar}{2e}\hat{n}(\partial_\alpha\hat{n} \times \partial_t\hat{n}) \tag{1.4}$$

with the reduced Planck constant $\hbar$, the elementary charge e, the local orientation of the magnetisation $\hat{n}(\boldsymbol{r}, t) = \boldsymbol{M}/|\boldsymbol{M}|$ and $\partial_i = \partial/\partial r_i$, $\partial_t = \partial/\partial t$. As a consequence an additional topological Hall signal is observed as shown in the case of MnSi in Fig. 1.7 (b). The emergent magnetic field is quantised as it is the product of the flux quantum of a single skyrmion $\phi_0 = h/e$ and the skyrmion density ϕ as given in Eq. 1.1.

Furthermore, the deflected conduction electrons transfer a momentum to the magnetic spin structure as they pass through the material, which leads to spin transfer torque effects, as first observed via SANS experiments in MnSi [80, 125]. Fig. 1.8 (a) depicts the Magnus force perpendicular to the current direction and the parallel drag force both caused by the electrical current which lead to a net motion of the skyrmion lattice if

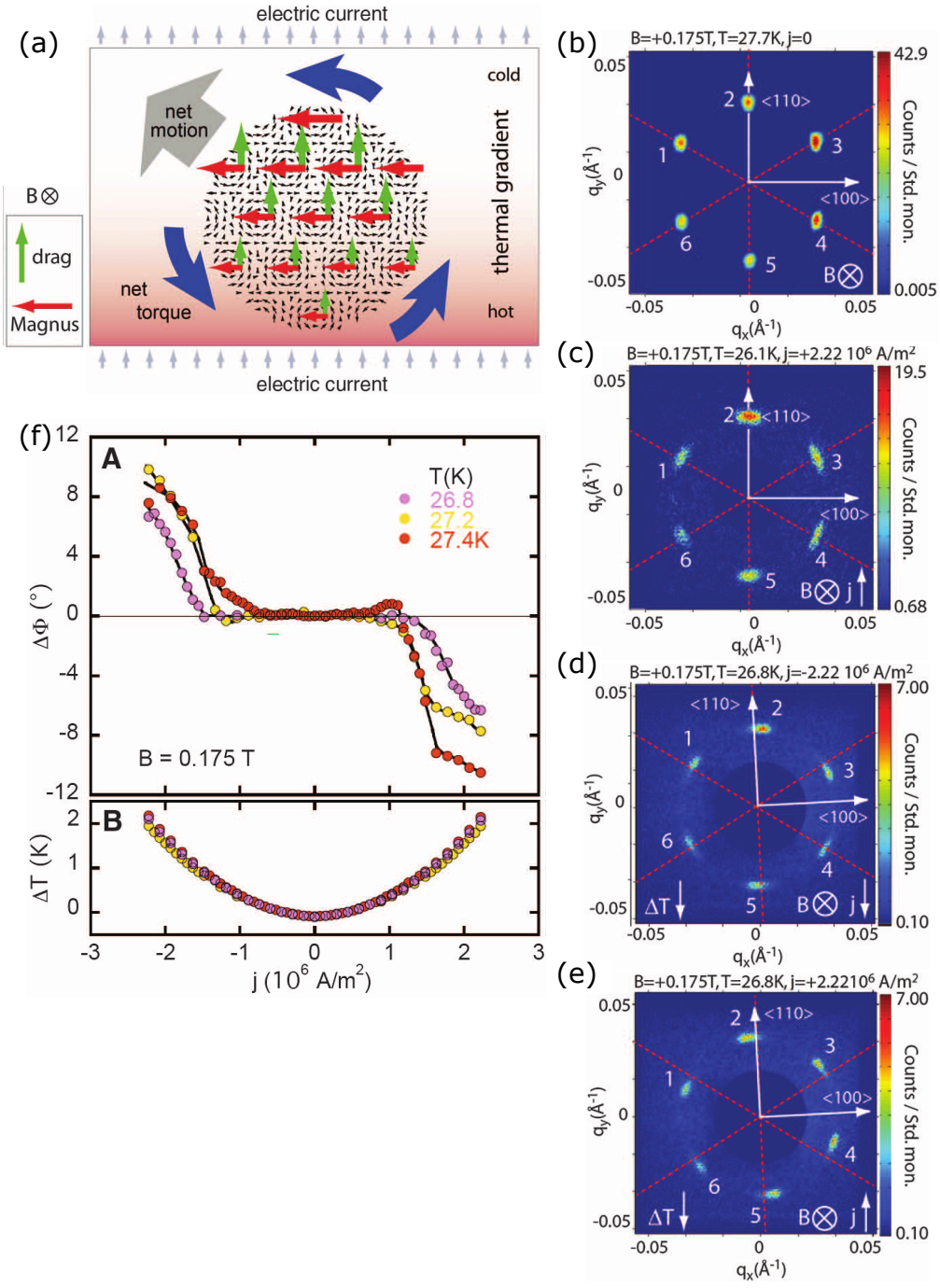

Figure 1.8.: Moving skyrmions with ultralow current densities. (a) The spin transfer torque effect leads to drag and Magnus forces which in combination with a thermal gradient are inhomogeneous over the sample and lead to a rotational torque. SANS signal of the skyrmion lattice (b) without and (c) with an applied electric current. (d) The combination of electric current and thermal gradient lead to the rotation of the scattering pattern and (e) reversing the electric current leads to the rotation in the opposite direction due to spin transfer torque. (f) Current dependence of the rotation angle $\Delta\Phi$, and the temperature gradient ΔT between sample surface and holder. Figures taken from Ref. [80].

they overcome the counteracting pinning forces. As a transverse motion is not observable in SANS measurements, Jonietz *et al.* created a temperature gradient along the current direction, which leads to a varying strength of the Magnus and drag force and a rotation of the skyrmion lattice. This rotation is observed as a gyration of the sixfold Bragg pattern [80]. Fig 1.8 (b) shows the sixfold Bragg pattern without an applied current and in Fig. 1.8 (c) a current is applied leading to a broadening of the Bragg peaks in azimuthal direction. An additional thermal gradient applied (d) parallel and (e) anti-parallel to the direction of the electric current results in a rotation of the skyrmion lattice in opposing directions above a threshold current density (see below). The red dashed line marks the equilibrium position of the magnetic Bragg peaks without an applied current. The thermal gradient for a rotating signal is on the order of $0.5 - 2\,\mathrm{K}$ between the sample surface and the sample holder as displayed in Fig. 1.8 (f).

The skyrmion lattice unpins and begins to move at a threshold current density of the order of $j_c \sim 1 \cdot 10^6\,\mathrm{A/m^2}$ as shown in Fig. 1.8 (f). The ultralow threshold current density originates from the efficient coupling to spin currents and the weak collective pinning to defects which is a consequence of the well-defined long-range order of the skyrmion lattice. As each skyrmion carries one emergent magnetic flux quantum, its movement induces an emergent electric field $\boldsymbol{E}^e$ following Faraday's law which could be observed directly by Schulz *et al.* [124]. Drift velocities of the skyrmion lattice of the order of 0.1 mm/s are comparable to drift velocities of conduction electrons.

Skyrmion lattices cannot only be manipulated by electrical currents, but also magnon currents as shown e.g. in $\sim 50\,\mathrm{nm}$-thick films of MnSi and Cu_2OSeO_3 by means of real-space measurements [126–131]. Irradiating a micrometre-sized sample using an electron beam in LTEM creates a local heat source and an inhomogeneous temperature distribution. The magnon current originating from the temperature gradient interacts with the skyrmion lattice and gets deflected which causes a unidirectional rotation of the skyrmion lattice.

The exceptionally efficient coupling of skyrmions to spin currents, their stability due to the non-trivial topology and the small size motivated multiple theoretical and experimental studies investigating the potential application of skyrmions in data storage and logic technologies. For example, experimental and theoretical studies showed that single skyrmions in thin films, stabilised by interfacial DMI, can be created, annihilated, stored and moved [26]. One of the most prominent example where skyrmions could be employed for data storage is the proposal of a race-track memory [26, 132, 133]. Moreover, the magnetic excitation of skyrmions promise high-frequency devices easily tunable by the emergent electrodynamics [81, 83, 134]. Hence, important studies on the excitations in cubic chiral magnets are discussed in the following.

1.2.3. Spin excitations in cubic chiral magnets

Early studies on the spin dynamics of chiral magnets have been performed by Ishikawa *et al.* [103, 135] in pioneering inelastic neutron scattering measurements on MnSi in the 1970s and 1980s. Around the same time the helical spin structure of MnSi with a period of 180 Å was revealed, well before the discovery of the skyrmion lattice. Notably, the helical periodicity is much larger than the atomic distance and MnSi can be considered ferromagnetic on short length scales. The inelastic neutron scattering measurements exhibit the first example of paramagnon fluctuations in a weak itinerant ferromagnet over large portions of the Brillouin zone. More recently, polarised neutron scattering studies determined a chiral character of the spin fluctuations above T_c and found spin-flip excitations in the field polarised phase [136–138]. Eventually, the interest in the spin dynamics of the cubic chiral magnets increased significantly with the discovery of the skyrmion lattice in MnSi.

Particular interest was attracted by the uniform spin dynamics at low magnetic fields that occur in the low GHz-regime and show potential for magnonics and high frequency applications [139]. Starting at high fields in the field polarised phase where the magnetic moments are co-aligned, only a single Kittel mode exists. In contrast, two excitation modes occur in the helical and conical phase. Fig. 1.9 (a) shows static helical order where the spin density is constant along the helix. In an excited state, the magnetic moments precess locally with the rotation direction fixed by the Landé factor. As shown in Fig. 1.9 (b), the relative rotational phase relation between the spins leads to periodic compression within the helix which propagates parallel or anti-parallel along the helical ordering vector $\boldsymbol{Q}$ resulting in the $+Q$ and $-Q$ modes, respectively [140]. Their degeneracy is in general lifted by dipolar interactions which in addition set their spectral weight [83]. The two modes could already be observed in a seminal work by means of electron spin resonance on MnSi in the 1970s [141].

In the topologically non-trivial skyrmion lattice phase, three magnetic resonance modes at zero momentum were predicted by Mochizuki [81]. They occur as two gyrating modes where the skyrmion core precesses clockwise (CW) or counter-clockwise (CCW) about the equilibrium position and as a breathing mode (BM) where the core inflates and contracts periodically as depicted in Figs. 1.9 (c) to (f). An oscillating magnetic field within the skyrmion lattice plane couples to the gyrating modes whereas an ac magnetic field out-of-plane excites the BM. The excitations were first observed in Cu_2OSeO_3 employing broadband ferromagnetic resonance spectroscopy by means of a coplanar waveguide [134]. The results are shown in Figs. 1.9 (g) and (h) where the microwave absorption as a function of frequency for increasing magnetic fields is displayed for the two configurations. Only a

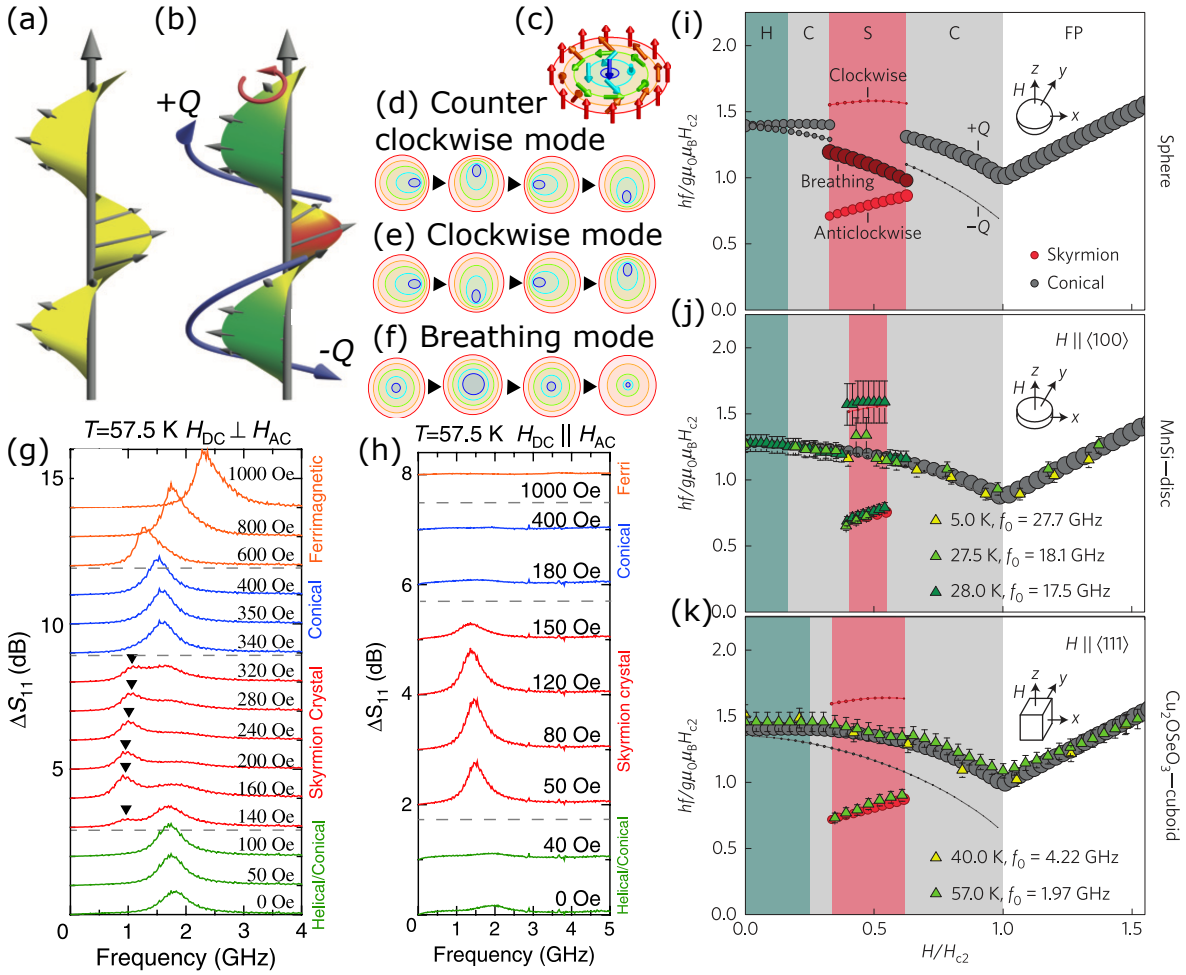

Figure 1.9.: Collective magnetic excitations of spin textures in cubic chiral magnets. (a) Schematic depiction of a magnetic helix. (b) The two finite-frequency excitations of the helix propagating with a finite phase velocity either parallel (+Q) or anti-parallel (-Q) to the pitch vector $\boldsymbol{Q}$. The rotational direction of the local spins is determined by the gyromagnetic ratio. (c) Schematic illustration of a single skyrmion. (d-f) Snapshots of the real-space spin alignment of the three excitations of the skyrmion crystal during one period. The colors correspond to the spin alignment in (c). Microwave absorption spectra ΔS_{11} as a function of frequency for various dc magnetic field values H_{dc} for an ac magnetic field H_{ac} (g) perpendicular and (h) parallel. (i) Theoretical excitation spectra in the helical (H), conical (C), skyrmion lattice (S) and field polarised (FP) phase of a sphere. The size of the dots represent the spectral weight. Theoretical spectra and observed resonance frequencies for (j) a MnSi-disc and (k) a Cu_2OSeO_3-cuboid. Figures taken from Refs. [83, 134].

single excitation is observed in the perpendicular field configuration as the spectral weight of the CW mode is too low to be seen with this setup.

Finally, Schwarze *et al.* [83] performed a quantitative experimental and theoretical study on the resonant magnetic spin excitations in the insulating Cu_2OSeO_3, the semiconducting $Fe_{1-x}Co_xSi$, and the transition metal MnSi. Although the systems have similar phase diagrams, they differ substantially on a microscopic scale giving rise to the difference in ordering temperature T_c, pitch length $2\pi/Q$, and critical field H_{c2}. However, the two magnetic excitation modes in the helical and conical phase $\pm Q$ as well as the three modes in the skyrmion lattice phase can quantitatively be described in a universal theoretical framework solely including the material specific chiral Dzyaloshinskii-Moriya energy $E_{\mathrm{DM}} \propto JQ^2$ and the temperature-dependent critical internal field energy $E_{\mathrm{CF}}(T) = g\mu_0\mu_{\mathrm{B}}H_{c2}^{\mathrm{int}}$ with the magnetic constant μ_0 and the Bohr magneton μ_{B}. Furthermore, demagnetisation effects described by the dimensionless demagnetisation factors $N_i\,(i = x, y, z)$ and depending on the sample shape influence the spectral weight and the frequency of the excitations.

The main results are shown in Figs. 1.9 (i) to (k) where the resonance frequencies as a function of field for a sphere, a MnSi-disc and a Cu_2OSeO_3-cuboid are displayed. The $\pm Q$ modes are degenerate for the sphere at zero field and split with increasing magnetic field. The ratio of spectral weights between $\pm Q$ shifts with increasing field. The frequency of the CCW (anticlockwise) mode within the skyrmion lattice phase increases with field whereas the resonance frequency of the BM behaves similar to the $-Q$ mode and decreases with field. The CW mode exhibits no distinct field dependence and its spectral weight is low. The experimental results are in excellent agreement with theory as shown in Figs. 1.9 (j) and (k). As predicted by theory, the spectral weight of certain excitations is low and they could not be observed. The theory also predicts the resonance modes of $Fe_{1-x}Co_xSi$ which is not shown here.

In a more general picture to describe the spin excitations for the entire Brillouin zone instead of being limited to the zone centre, the helical and conical states represent a one-dimensional magnetic crystal with a periodicity much larger than and incommensurate with the atomic lattice. Following Bloch's theorem, the spin wave excitations — the so-called helimagnons — form a band structure $\omega_{n,\boldsymbol{q}}$ with band index n reflecting the helical periodicity [142–144]. The periodicity suppresses the propagation along the helix due to Umklapp scattering at the zone boundary leading to gaps in the spectrum. As the pitch length of the helix is much larger than the atomic lattice spacing, the resulting Brillouin zone is small. It allows to describe the magnetisation dynamics in an effective continuum theory depending only on a few parameters rendering the dispersion $\omega_{n,\boldsymbol{q}}$ of the helimagnons universal [143].

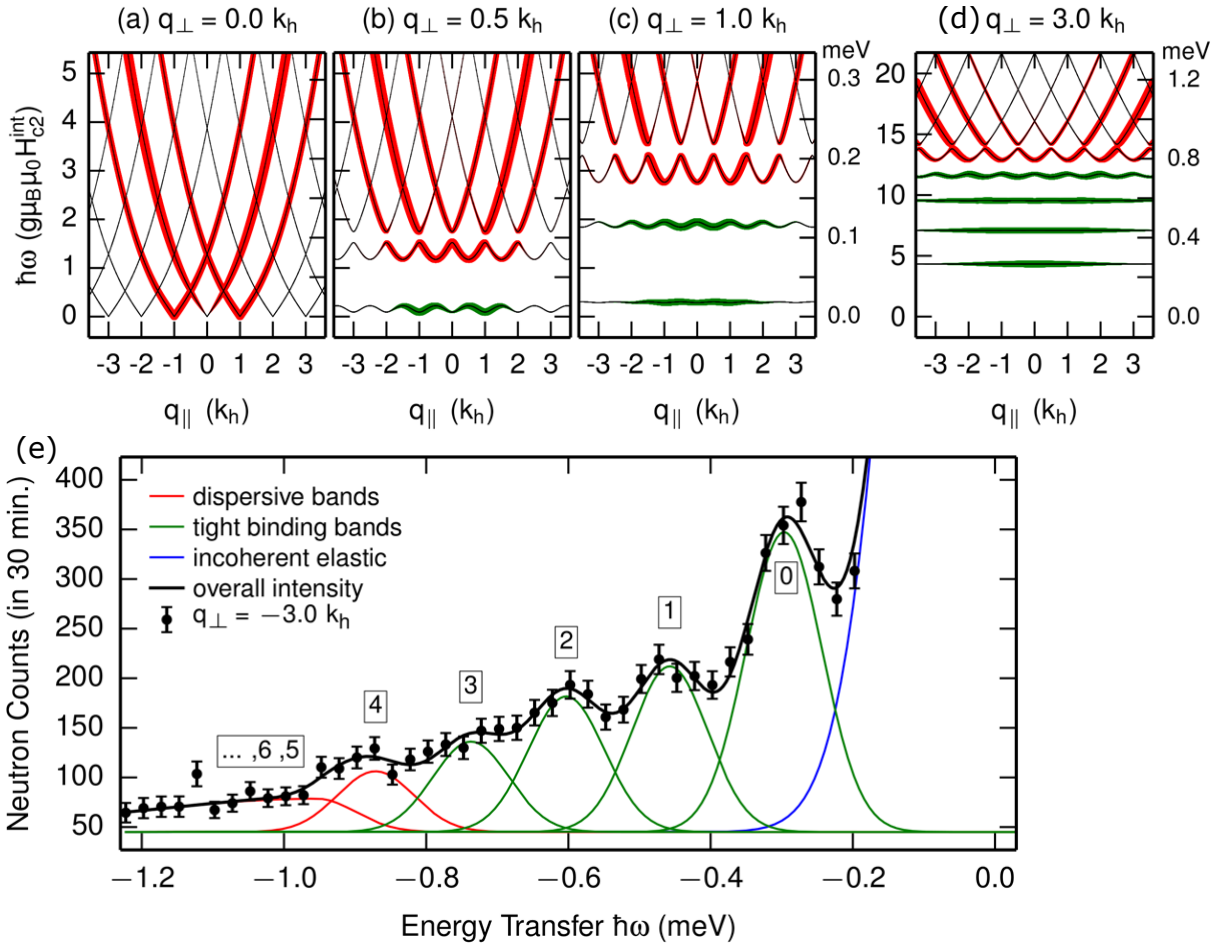

Figure 1.10.: Universal helimagnon spectrum at zero field in MnSi. (a-d) Collective spin wave excitation energy as a function of momentum $q_{\parallel}$ along the helical propagation vector $\boldsymbol{k}_{\mathrm{h}}$ in the repeated zone scheme for various values of perpendicular momentum $q_{\perp}$ for a temperature $T = 20\,\mathrm{K}$. The green and red color denote flat and dispersive bands, respectively, and their width the expected spectral weight in neutron scattering experiments. (e) Constant-Q scan with $q_{\parallel} = 0$ corresponding to (d). The data is fitted by multiple Gaussian functions. Figures taken from Ref. [143].

Helimagnons were investigated in extensive studies by inelastic neutron scattering by means of high-resolution triple axis spectroscopy in the archetypical chiral magnet MnSi [142–144]. MnSi is ideally suited for these studies with its characteristic energy scale defined by the critical field energy $\mathcal{D}Q^2 \sim 0.1\,\mathrm{meV}$ with the spin stiffness $\mathcal{D}$ as it can be resolved by state-of-the-art neutron spectrometers. On the contrary, inelastic neutron scattering studies on e.g. Cu_2OSeO_3 are limited to the higher energy magnon spectrum as typical helimagnon bandwidths are about one order of magnitude smaller [139, 144, 145]. First measurements were performed by Janoschek *et al.* [142] in the helical state where the helimagnon bands were identified and accounted for by a theoretical model based on only

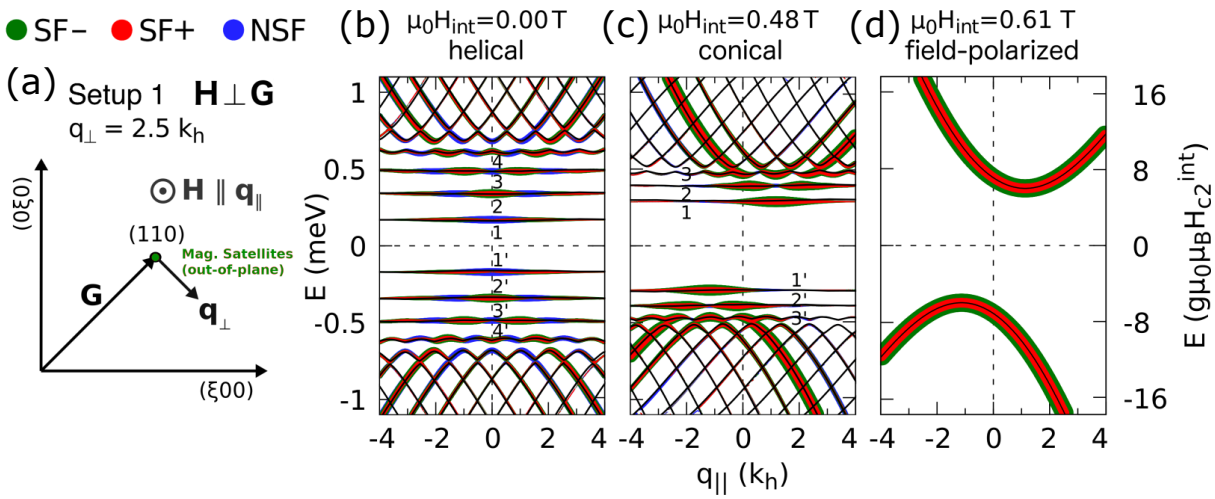

Figure 1.11.: Non-reciprocity and field dependence of helimagnon bands. (a) Orientation of the magnetic field and the wave vectors in reciprocal space. Helimagnon bands in the (b) helical and (c) conical state. (d) The spin excitation bands in the field-polarised phase. The thickness of the colored lines correspond to the spectral weight in neutron scattering experiments and the color indicates spin-flip (SF±) and non-spin-flip (NSF) scattering. Figure taken from Ref. [144].

three parameters. But measurements were complicated as helimagnon branches from four equally populated magnetic domains along the equivalent ⟨111⟩ directions contributed to the neutron scattering signal. Kugler *et al.* overcame this obstacle by applying a small magnetic field along one ⟨111⟩ direction to form a single domain state [143].

Their main results are shown in Fig. 1.10 observing helimagnon bands in a single domain helical state by means of inelastic neutron scattering. In Figs. 1.10 (a) to (d), the calculated collective excitation energies are shown as a function of momentum parallel to the helix pitch for various momentum values perpendicular to it. If the magnon momentum is only along the direction of the helix, i.e. $q_\perp = 0$, Bragg scattering is absent as the Fourier transform of the periodic potential vanishes due to the continuous screw symmetry of the helix and no band gaps are observed [139, 146]. For the other extreme of large perpendicular moment $q_\perp \gg Q$ and $q_\parallel = 0$, the wave equation is described by a particle with quadratic dispersion in a periodic cosine potential, i.e. by the *Mathieu equation*. Changing the perpendicular moment $q_\perp$ between these two limits, the strength of the periodic potential varies and the band structure can be tuned. For large $q_\perp \gg (n+1)^2 k_\mathrm{h}/\sin\theta$, the lowest bands become flat and non-dispersive, i.e. the helimagnons are localised along the helix direction. Eventually, five helimagnons – four flat, one dispersive – could be resolved in inelastic neutron scattering experiments shown in Fig. 1.10 (e).

The lack of inversion symmetry also leads to asymmetry in the spin wave dispersion $\epsilon(\boldsymbol{q}) \neq \epsilon(-\boldsymbol{q})$ [140, 147], observed in a multitude of experimental studies as e.g. sum-

marised in Ref. [144]. The non-reciprocal magnon propagation has experimentally been observed by means of spin wave spectroscopy in $LiFe_5O_8$ [148], Cu_2OSeO_3 [149], FeGe, as well as Co-Zn-Mn alloys [144, 150]. Furthermore, a magnon with momentum $\boldsymbol{q}$ and energy $\epsilon(\boldsymbol{q})$ can be absorbed, but it cannot be emitted at the same energy since $\epsilon(\boldsymbol{q}) \neq \epsilon(-\boldsymbol{q})$ [139] as observed in MnSi [101, 151, 152] and the chiral antiferromagnet $\alpha-Cu_2V_2O_7$ [153]. In the case of the multiferroic Cu_2OSeO_3, the coupling of the magnetic excitations to the collective oscillation of the electric polarisation leads to directional dichroism in the GHz-frequency regime [82, 154–157].

Weber *et al.* investigated the complete field-dependence of the reciprocity of the collective spin wave excitations from the helical to the conical and up to the field-polarised phase in MnSi [144]. A magnon spectrum of the three phases is shown exemplary in Figs. 1.11 (b) to (d) for an unpolarised neutron scattering setup depicted in Fig. 1.11 (a). Changing the direction of the magnetic field or the perpendicular momentum transfer $\boldsymbol{q}_\perp$ alters the spin excitation bands and the ratio between spin-flip (SF) and non-spin-flip (NSF) scattering significantly. In zero field, the helix is invariant under a π-rotation of spin and real space about the x-axis where the helical vector is along the z-axis which leads to the reciprocal helimagnon bands $\epsilon(\boldsymbol{q}) = \epsilon(-\boldsymbol{q})$. Increasing the magnetic field, the NSF scattering decreases and the spectral weight of the helimagnon bands becomes non-reciprocal. Above the critical field H_{c2}, only a single, parabolic magnon branch is left which is non-reciprocal with respect to flipping the magnetic field H_0, the reduced momentum transfer $\boldsymbol{q}$ or the energy transfer E. Recent polarised inelastic neutron scattering studies confirmed the non-reciprocity of the SF and NSF scattering in the conical phase [158].

Similar to the one-dimensional helical order, the hexagonal skyrmion lattice has a periodicity in the plane perpendicular to the applied magnetic field which according to Bloch's theorem leads to a magnon band structure $\omega_{n,\boldsymbol{q}}$ in a two-dimensional hexagonal Brillouin zone [85, 139]. Since the translational invariance is broken, the spectrum has a Goldstone mode which vanishes at the Γ-point. Similar to spin waves in ferromagnets, the mode has a quadratic dispersion $\omega \sim q^2$ for low excitation energies which has been explained by the topological nature of the skyrmions [159, 160]. Again, the spectrum exhibits non-reciprocity in momentum $\boldsymbol{q}$, energy E, and magnetic field H [161]. Besides, a variety of non-vanishing excitation modes exist at zero momentum with a finite energy $\omega_{n,0} > 0$. However, only three of them can be excited by a homogeneous ac magnetic field. As discussed beforehand, these are the CCW, CW, and BM as theoretically predicted by Mochizuki [81].

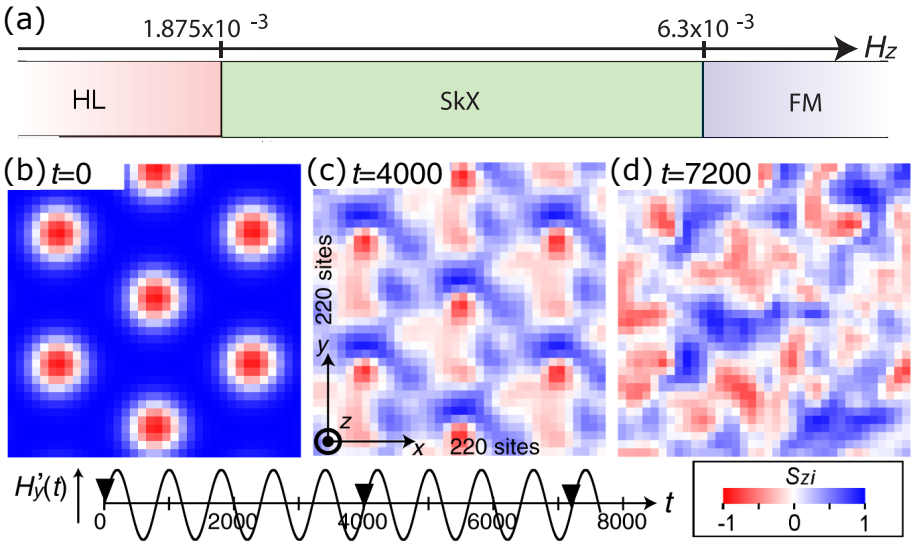

Figure 1.12.: Melting of the skyrmion lattice under intense magnetic microwave radiation. (a) Phase diagram of the simulated system at $T = 0$. (b) Real space equilibrium configuration of the skyrmion lattice. The color indicates the out-of-plane magnetisation component. Skyrmion lattice under intense left-handed circularly polarised microwave radiation after approximately (c) 40 ns and (d) 70 ns. Figure taken from Ref. [81].

1.2.4. Intense spin wave excitations

Mochizuki *et al.* showed in the same study numerical simulations of a 2d system where an intense external microwave field drives the CCW spin wave excitations periodically and melts the skyrmion lattice [81]. Figs. 1.12 (b) to (d) show real space snapshots of the melting process where the colour indicates the magnitude of the out-of-plane spin component. At the beginning of the simulation, the skyrmion phase is stabilised at zero temperature at the border to the ferromagnetic phase as shown in the phase diagram in Fig. 1.12 (a). The skyrmion lattice driven by an in-plane left-handed circularly polarised (LHP) microwave melts within $t \sim 5000-6000$ which corresponds to $\sim 50-60$ ns displayed in Figs. 1.12 (c) and (d). Notably, the skyrmion cores in dark red colour in Figs. 1.12 (c) do not move compared to their original position. Instead, the surrounding moves in a CCW rotation about the cores. The same observation of the surrounding rotating around the cores can be made for the CW mode as well as for lower excitation fields. Hence, for the CW and CCW modes the excitation field drives the ferromagnetic surrounding of the skyrmion cores in a rotary motion rather than the cores themselves.

Furthermore, the spin structure is altered by the intense microwave radiation which results in a redshift of the CCW resonant frequency. Consequently, the excitation frequency is chosen slightly below the resonant frequency of the undisturbed system. Coupling by a linearly polarised microwave is slightly weaker. Melting by a right-handed circularly po-

larised (RHP) microwave is difficult to achieve as well as if the frequency is off-resonance in the LHP case. Finally as shown in Fig. 1.12 (d), the skyrmion lattice periodicity is completely lost indicating chaotic melting dynamics.

1.3. Thermally and periodically driven spin dynamics of skyrmion lattices

In the course of the present work, spin dynamics of the magnetic skyrmion lattice are investigated in two different approaches. At first, the emergence of the skyrmion order at the paramagnetic-to-skyrmion lattice transition is investigated experimentally in the transition metal MnSi. The comprehensive study comprises magnetic susceptibility, small-angle neutron scattering, neutron resonance spin-echo spectroscopy, and all-electrical microwave spectroscopy measurements. Skyrmion patches exceeding sizes of 10^3 Å and lifetimes of 1 ns form already in the paramagnetic phase and the transition is well described by the Landau soft-mode mechanism of weak crystallisation. As part of this thesis, the SANS measurements were analysed and neutron resonance spin-echo measurements were performed.

Second, we investigate experimentally the influence of intense microwave radiation on the skyrmion lattice in the insulating helimagnet Cu_2OSeO_3. We search for microwave-induced instabilities as observed in numerical simulations by Mochizuki *et al.* where the long-range order of the skyrmion lattice melts [81]. A ferromagnetic resonance spectroscopy setup by means of a coplanar waveguide is employed for the generation of intense microwave fields and, simultaneously, as probe of the collective spin dynamics. The influence on the long-range order of the skyrmion lattice may be observed on a microscopic scale by small angle neutron scattering. As our main results, we observed coupling between the sample and the intense microwave radiation already some Kelvin above the ordering temperature T_c for frequencies about the resonant modes of the SkX. Furthermore, parts of the skyrmion lattice phase are not accessible under intense microwave radiation. In particular for excitation frequencies below the CCW mode, the sample temperature remains at or just above the ordering temperature T_c for sufficiently high excitation fields. This redshift of the resonant mode might originate from a pronounced ferromagnetic character of the CCW resonant mode induced by the intense microwave radiation that couples to the ferromagnetic background. For intermediate excitation fields the coupling to the CCW mode is observed in all-electrical microwave spectroscopy spectra, but no long-range skyrmion lattice order emerges. Furthermore, azimuthal broadening of the hexagonal SANS pattern of the skyrmion lattice is observed for highest excitation fields

and all excitation frequencies around the resonant modes. In a power series a threshold for the onset of azimuthal broadening is observed.

1.4. Outline of this thesis

The following chapter is an introduction into neutron scattering and neutron scattering techniques employed in this work. The concepts of nuclear and magnetic neutron scattering in the elastic and inelastic case are summarised. Furthermore, the behaviour of neutron spins in magnetic fields is explained. Subsequently, the neutron scattering techniques mainly used in the course of this work – small angle neutron scattering (SANS) and modulation of intensity with zero effort (MIEZE) – are introduced.

Chapter 3 presents the employed and developed experimental methods. In the course of this work, several improvements and developments have been conducted at the instrument RESEDA at the Heinz Maier-Leibnitz Zentrum in Garching, Germany. Beside technical progress such as a phase locking of the spin-echo signal, software was developed for data analysis and simulation of MIEZE measurements. At the end of the chapter, broadband ferromagnetic resonance spectroscopy is explained, the reduction of typical data shown and discussed.

In Chapter 4, results on the critical dynamics of the prototypical ferromagnetic superconductor UGe_2 at ambient pressure are presented employing the newly developed longitudinal MIEZE technique. The spin fluctuations about the Curie temperature T_C are purely longitudinal with a dual nature arising from the hybridisation of $5f$ electrons with the conduction electrons. The Ising universality class in three dimensions perfectly matches the local spin fluctuations whereas itinerant spin fluctuations are observed on length scales similar to the superconducting coherence length. The disentanglement of the complex low-energy excitations demonstrates the great potential of MIEZE to study quantum matter.

Chapter 5 presents results of the comprehensive study on the Landau soft-mode mechanism of weak crystallisation of the skyrmion lattice phase in MnSi. As part of this thesis, SANS measurements were analysed and neutron resonance spin-echo measurements performed. After a brief motivation, the neutron scattering setups are described and experimental results presented. SANS measurements show magnetic correlations above T_c that are reminiscent of the magnetic order in the skyrmion lattice phase. Evaluating the magnetic Bragg peak widths, the inferred correlation lengths are at least several thousand Ångström. Neutron resonance spin-echo measurements employing the MIEZE option show that the magnetic correlations above T_c are fully dynamic with lifetimes of several nanosec-

onds. Finally, the results are combined with ac susceptibility and all-electrical microwave spectroscopy data and discussed with respect to the mechanism of weak crystallisation.

In chapter 6, the response of the magnetic skyrmion lattice in Cu_2OSeO_3 driven by intense microwave radiation is investigated by means of all-electrical microwave spectroscopy and small angle neutron scattering. At first, the current state of research on Cu_2OSeO_3 beyond the generic properties of helimagnets discussed in Sec. 1.2 is introduced. After a detailed description of the employed setups, data of the sample temperature during field and temperature sweeps are presented, which are necessary for an accurate correction for resonant and ohmic heating effects. Subsequently, the excitation spectra of Cu_2OSeO_3 under intense microwave radiation close to or matching the resonant modes of the skyrmion lattice phase are displayed and discussed. Finally, the small angle neutron scattering data yielding information on the magnetic correlations and the correlation lengths on a microscopic scale are discussed. The results are summarised, linked, and discussed at the end of the chapter.

2. Neutron scattering and neutron scattering techniques

Understanding materials on an atomic scale is the basis for research ranging from biology and chemistry to materials science to physics. Over the last decades neutron scattering has proven to be a powerful technique for the investigation of the static and dynamic properties of matter, especially in solid state physics. The following chapter introduces main concepts behind neutron scattering following standard textbooks [162–165] and the neutron scattering techniques mainly employed in this thesis.

As a particle without electrical charge, the neutron interacts with the nucleus via nuclear forces. The probability for neutron-nuclear interaction varies strongly between isotopes and has no simple correlation with the atomic number Z and mass number N. This results in substantial scattering contrast for different elements with similar atomic numbers but also different isotopes of a single element. An important example is the large difference in total scattering between hydrogen and deuterium of more than one order of magnitude. Mainly because of its charge neutrality, the neutron has a large penetration depth and therefore probes bulk properties. This also allows using extreme sample environments e.g. large magnetic fields, low and high temperatures or high pressures because the sample environment can be made "transparent" for neutrons through the choice of suitable materials such as aluminium and sapphire.

The de Broglie wavelength of cold and thermal neutrons is of the order of interatomic distances in condensed matter. Hence, the diffraction of neutrons from solids and liquids can display interference effects yielding information on the structure of the scattering system. In addition, the energy of cold and thermal neutrons is in the range of elementary excitations in matter, e.g. lattice vibrations, allowing the investigation of dynamic properties. Furthermore, the neutron is a fermion with spin 1/2. The associated magnetic moment interacts with magnetic fields arising from unpaired electrons in magnetic samples. It makes neutrons an ideal tool for probing the correlation of electron spins and the distribution of unpaired electrons as well as dynamical magnetic properties like magnetic excitations and spin fluctuations.

The chapter is organised as follows. First, we give a short introduction to neutron scattering and, in particular, magnetic neutron scattering. Subsequently, the behaviour of the neutron spin in magnetic fields is described. The chapter concludes with the introduction of the small angle neutron scattering (SANS) technique and modulation of intensity with zero effort (MIEZE), an option of the neutron resonance spin-echo technique.

2.1. Neutron scattering cross-section

The neutron scattering cross-section describes the probability that a neutron with wavevector $\boldsymbol{k_i}$ and spin state $\boldsymbol{\sigma_i}$ is scattered by the sample into a final state with wavevector $\boldsymbol{k_f}$ and spin state $\boldsymbol{\sigma_f}$. In this process the neutron acts only as a weak perturbation. Hence, during the scattering process the scatterer undergoes a transition from its initial quantum state $|\lambda_i\rangle$ to its final state $|\lambda_f\rangle$, but the nature of the states remains unmodified. Thus, applying Fermi's Golden Rule, we obtain the double-differential cross-section

$$\frac{\mathrm{d}^2\sigma}{\mathrm{d}\Omega\mathrm{d}\omega} = \left(\frac{m}{2\pi\hbar^2}\right)^2 \frac{k_f}{k_i} \sum_{\lambda_f,\sigma_f} \sum_{\lambda_i,\sigma_i} p_{\lambda_i} p_{\sigma_i} \left|\langle \boldsymbol{k_f}, \boldsymbol{\sigma_f}, \lambda_f | \hat{V} | \boldsymbol{k_i}, \boldsymbol{\sigma_i}, \lambda_i \rangle\right|^2 \delta(\hbar\omega + E_{\lambda_i} - E_{\lambda_f}) \quad (2.1)$$

that describes the number of neutrons scattered per time into the solid angle $\mathrm{d}\Omega$ with a final energy within $\hbar\omega$ and $\hbar(\omega + \mathrm{d}\omega)$ divided by the incident neutron flux Φ. Here, m is the neutron mass, $\hbar$ the Planck constant divided by 2π, p_{λ_i} and p_{σ_i} are the probabilities to find the sample in state λ_i and the neutron in the spin state σ_i, respectively. $\hat{V}$ is the interaction potential between the neutron and the sample. In the scattering process both the momentum and energy are conserved, the latter described by the δ-function. The momentum transfer to the sample is given by

$$\hbar\boldsymbol{Q} = \hbar(\boldsymbol{k_i} - \boldsymbol{k_f}) \quad (2.2)$$

and the corresponding energy transfer by

$$\hbar\omega = \frac{\hbar^2}{2m}(\boldsymbol{k_i}^2 - \boldsymbol{k_f}^2). \quad (2.3)$$

Measuring the double differential cross-section as a function of $\boldsymbol{Q}$ and ω, we can extract information about the interaction potential $\hat{V}$ and as a result about the scattering system itself.

2.2. Nuclear scattering

2.2.1. The Fermi pseudo-potential

The neutron interacts with matter, e.g. nuclei, via the nuclear force which is very short-range around 10^{-15} m. Since in addition the radius of the nucleus is of the same order, much less than the wavelength of cold to thermal neutrons of $\lambda \approx 1 - 10$ Å, the neutron-nucleus scattering only contains s-wave components. It is isotropic and can be characterized by a single parameter b, called the scattering length which is of the order of 10^{-12} cm. Using the Born approximation, the neutron-nucleus interaction is described by the Fermi pseudo-potential

$$\hat{V} = \frac{2\pi\hbar^2}{m} \sum_j b_j \delta(\boldsymbol{r} - \boldsymbol{R}_j) \tag{2.4}$$

for nuclei positioned at fixed positions $\boldsymbol{R}_j$ with their individual scattering lengths b_j and a neutron at position $\boldsymbol{r}$. The incoming and outgoing neutrons may be described by plane waves

$$|\boldsymbol{k}_i\rangle = e^{i\boldsymbol{k}_i \cdot \boldsymbol{r}} \tag{2.5}$$

and

$$|\boldsymbol{k}_f\rangle = e^{i\boldsymbol{k}_f \cdot \boldsymbol{r}}. \tag{2.6}$$

Considering an unpolarised neutron beam neglecting the spin states $\boldsymbol{\sigma}_i$ and $\boldsymbol{\sigma}_f$, the matrix element can be written as

$$\langle \boldsymbol{k_f}, \lambda_f | \hat{V} | \boldsymbol{k_i}, \lambda_i \rangle = \left(\frac{2\pi\hbar^2}{m} \right) \langle \lambda_f | \sum_j b_j e^{i\boldsymbol{Q} \cdot \boldsymbol{R}_j} | \lambda_i \rangle \tag{2.7}$$

where we used the transformation $\boldsymbol{R} = \boldsymbol{r} - \boldsymbol{R}_j$ and applied Eq. 2.2. The δ-function in Eq. 2.1 can be written in integral form

$$\delta(\hbar\omega + E_{\lambda_i} - E_{\lambda_f}) = \frac{1}{2\pi\hbar} \int_{-\infty}^{\infty} e^{i(E_{\lambda_i} - E_{\lambda_f})t/\hbar} e^{-i\omega t} \mathrm{d}t. \tag{2.8}$$

Furthermore, if $\hat{H}$ is the Hamiltonian of the scattering system, the states λ_i and λ_f are eigenfunctions of $\hat{H}$ with eigenvalues E_{λ_i} and E_{λ_f} and we can rewrite the position operator $\boldsymbol{R}_j$ in terms of the time-dependent Heisenberg operator $\boldsymbol{R}_j(t) = \exp(i\hat{H}t/\hbar)\boldsymbol{R}\exp(-i\hat{H}t/\hbar)$. Using the expectation value of an operator $\hat{A}$

$$\langle A \rangle = \sum_\lambda p_\lambda \langle \lambda | \hat{A} | \lambda \rangle \tag{2.9}$$

the final cross-section formula reads

$$\frac{\mathrm{d}^2\sigma}{\mathrm{d}\Omega \mathrm{d}\omega} = \frac{k_f}{k_i} \frac{1}{2\pi\hbar} \sum_{j,j'} b_j b_{j'} \int_{-\infty}^{\infty} \langle e^{-i\boldsymbol{Q} \cdot \hat{\boldsymbol{R}}_{j'}(0)} e^{i\boldsymbol{Q} \cdot \hat{\boldsymbol{R}}_{j'}(t)} \rangle e^{-i\omega t} \mathrm{d}t. \tag{2.10}$$

2.2.2. Pair correlation function

The operator part in Eq. 2.10 can be identified as the intermediate pair correlation function or intermediate scattering function

$$I(\boldsymbol{Q},t) = \frac{1}{N}\sum_{j,j'}\langle e^{-i\boldsymbol{Q}\cdot\hat{\boldsymbol{R}}_{j'}(0)} e^{i\boldsymbol{Q}\cdot\hat{\boldsymbol{R}}_{j'}(t)}\rangle \tag{2.11}$$

where N denotes the number of atoms in the system. In 1954 van Hove introduced the space-time pair correlation function $G(\boldsymbol{r},t)$ as the Fourier transform with respect to $\boldsymbol{Q}$ and time t of Eq. 2.11 as

$$G(\boldsymbol{r},t) = \frac{1}{(2\pi)^3}\int I(\boldsymbol{Q},t)e^{-\boldsymbol{Q}\cdot\boldsymbol{r}}\mathrm{d}\boldsymbol{Q} \tag{2.12}$$

and the dynamical structure factor

$$S(\boldsymbol{Q},\omega) = \frac{1}{2\pi\hbar}\int I(\boldsymbol{Q},t)e^{-i\omega t}\mathrm{d}t. \tag{2.13}$$

Combining Eqs. 2.11 and 2.12 yields

$$G(\boldsymbol{r},t) = \frac{1}{(2\pi)^3}\frac{1}{N}\int\sum_{j,j'}\langle e^{-i\boldsymbol{Q}\cdot\hat{\boldsymbol{R}}_{j'}(0)} e^{i\boldsymbol{Q}\cdot\hat{\boldsymbol{R}}_{j}(t)}\rangle e^{-i\boldsymbol{Q}\cdot\boldsymbol{r}}\mathrm{d}t. \tag{2.14}$$

We can rewrite Eq. 2.14 in terms of δ-functions as

$$G(\boldsymbol{r},t) = \frac{1}{N}\sum_{j,j'}\int\langle\delta\left(\boldsymbol{r'}-\hat{\boldsymbol{R}}_{j'}(0)\right)\delta\left(\boldsymbol{r'}+\boldsymbol{r}-\hat{\boldsymbol{R}}_{j}(t)\right)\rangle\mathrm{d}\boldsymbol{r'}. \tag{2.15}$$

For a detailed derivation of Eq. 2.15 we refer to Ref. [165]. $G(\boldsymbol{r},t)$ describes the density-density correlation in the system, i.e. the probability to have the atom j' at the time $t=0$ at the position $\boldsymbol{r'}$ and find the atom j at a later time t at another position $\boldsymbol{r'}+\boldsymbol{r}$.

2.2.3. Coherent and incoherent scattering

To include the correlation function Eq. 2.14 into the scattering cross-section Eq. 2.10, we need to evaluate the sum over different scattering lengths b_j. The scattering length b_j of each nucleus in a scattering system depends on the isotope as well as the nuclear spin quantum number I. Since the neutron carries a spin, there are two distinct scattering lengths for each isotope with non-zero nuclear spin I, i.e. b^+ for parallel alignment of the neutron spin with the nuclear spin and b^- for antiparallel alignment, respectively. If we assume that the distribution of nuclear spins and the distribution of isotopes in our scattering system are each uncorrelated – a condition commonly fulfilled – the sum in Eq. 2.10 has to be averaged over the sample volume

$$\frac{\mathrm{d}^2\sigma}{\mathrm{d}\Omega\mathrm{d}\omega} = \frac{k_f}{k_i}\frac{1}{2\pi\hbar}\sum_{j,j'}\langle b_j b_{j'}\rangle\int_{-\infty}^{\infty}\langle e^{-i\boldsymbol{Q}\cdot\hat{\boldsymbol{R}}_{j'}(0)} e^{i\boldsymbol{Q}\cdot\hat{\boldsymbol{R}}_{j'}(t)}\rangle e^{-i\omega t}\mathrm{d}t. \tag{2.16}$$

Using

$$\langle b_j b_{j'} \rangle = \langle b_j \rangle \langle b_{j'} \rangle = \langle b \rangle^2 \qquad \text{for } j \neq j' \tag{2.17}$$

$$\langle b_j b_{j'} \rangle = \langle b_j^2 \rangle = \langle b^2 \rangle \qquad \text{for } j = j' \tag{2.18}$$

we can separate the cross-section into two parts, the coherent cross-section

$$\left(\frac{\mathrm{d}^2\sigma}{\mathrm{d}\Omega \mathrm{d}E}\right)_{\mathrm{coh}} = \frac{\sigma_{coh}}{4\pi}\frac{k_f}{k_i}\frac{1}{2\pi\hbar}\sum_{j,j'}\int_{-\infty}^{\infty}\langle e^{-i\boldsymbol{Q}\cdot\hat{\boldsymbol{R}}_{j'}(0)} e^{i\boldsymbol{Q}\cdot\hat{\boldsymbol{R}}_j(t)}\rangle e^{-i\omega t}\mathrm{d}t \tag{2.19}$$

and the incoherent cross-section

$$\left(\frac{\mathrm{d}^2\sigma}{\mathrm{d}\Omega \mathrm{d}E}\right)_{\mathrm{incoh}} = \frac{\sigma_{inc}}{4\pi}\frac{k_f}{k_i}\frac{1}{2\pi\hbar}\sum_{j}\int_{-\infty}^{\infty}\langle e^{-i\boldsymbol{Q}\cdot\hat{\boldsymbol{R}}_{j}(0)} e^{i\boldsymbol{Q}\cdot\hat{\boldsymbol{R}}_j(t)}\rangle e^{-i\omega t}\mathrm{d}t \tag{2.20}$$

where we have defined $\sigma_{\mathrm{coh}} = 4\pi\langle b\rangle^2$ and $\sigma_{\mathrm{inc}} = 4\pi(\langle b^2\rangle - \langle b\rangle^2)$. The coherent part accounts for interference effects since it describes correlations between the positions of the same nucleus at different times and the positions of different nuclei at different times. The incoherent part does not lead to interference effects since it only depends on the correlation between the positions of the same nucleus at different times.

2.3. Magnetic scattering

2.3.1. Magnetic scattering cross-section

Magnetic scattering of neutrons occurs due to the dipole-dipole interaction between the neutron spin and the magnetic field arising from unpaired electrons in the scattering system. The operator corresponding to the magnetic dipole moment of the neutron can be described by

$$\hat{\boldsymbol{\mu}}_{\mathrm{n}} = -\gamma\mu_{\mathrm{N}}\hat{\boldsymbol{\sigma}} \tag{2.21}$$

with the nuclear magneton

$$\mu_{\mathrm{N}} = \frac{e\hbar}{2m_{\mathrm{p}}}. \tag{2.22}$$

e denotes the proton charge and m_{p} its mass. $\gamma = 1.913$ is the gyromagnetic ratio of the neutron and $\hat{\boldsymbol{\sigma}}$ the Pauli spin operator with

$$\hat{\sigma}_x = \begin{pmatrix} 0 & 1 \\ 1 & 0 \end{pmatrix} \qquad \hat{\sigma}_y = \begin{pmatrix} 0 & -i \\ i & 0 \end{pmatrix} \qquad \hat{\sigma}_z = \begin{pmatrix} 1 & 0 \\ 0 & -1 \end{pmatrix}. \tag{2.23}$$

The interaction of the dipole moment of the neutron with a magnetic field $\boldsymbol{H}$ is

$$\hat{U} = \hat{\boldsymbol{\mu}}_{\mathrm{n}} \cdot \boldsymbol{H} = -\gamma\mu_{\mathrm{N}}\hat{\boldsymbol{\sigma}} \cdot \boldsymbol{H}. \tag{2.24}$$

In a sample the magnetic field $\boldsymbol{H}$ originates from unpaired electrons. A single electron moving with velocity $\boldsymbol{v}_e$ generates a magnetic field

$$\boldsymbol{H} = \nabla \times \left(\frac{\boldsymbol{\mu}_\mathrm{e} \times \boldsymbol{R}}{|\boldsymbol{R}|^3} \right) - \frac{e}{c} \frac{\boldsymbol{v}_\mathrm{e} \times \boldsymbol{R}}{|\boldsymbol{R}|^3} \tag{2.25}$$

where the first term describes magnetic fields from the spin of the electron and the second from its orbital motion. $\boldsymbol{R}$ is the distance from the electron to the point at which the field is measured, e the elementary charge and c the velocity of light. The magnetic moment operator of an electron is given by $\hat{\boldsymbol{\mu}}_\mathrm{e} = -2\mu_\mathrm{B}\hat{\boldsymbol{s}}$ where μ_B is the Bohr magneton and $\hat{\boldsymbol{s}}$ the spin operator of the electron.

To derive the magnetic scattering cross-section the transition matrix element in Eq. 2.1 has to be evaluated. The evaluation is rather involved and we only state the final result. For more details we refer to Ref. [162, 165]. For the scattering system we make the following assumptions. First, the Heitler-London model is valid, i.e. the scattering system is a crystal where the unpaired electrons are localised close to the equilibrium positions of the ions in the lattice. Secondly, the total angular momentum L and total spin S are good quantum numbers and therefore LS-coupling is assumed. For spin-only scattering, i.e. $L = 0$, the magnetic scattering cross-section reads

$$\begin{aligned} \frac{\mathrm{d}^2\sigma}{\mathrm{d}\Omega \mathrm{d}\omega} = (\gamma r_0)^2 \frac{k'}{k} \sum_{\alpha,\beta} \left(\delta_{\alpha,\beta} - \frac{Q_\alpha Q_\beta}{Q^2} \right) \sum_{l'd'} \sum_{ld} F^*_{d'}(\boldsymbol{Q}) F_d(\boldsymbol{Q}) \\ \times \sum_{\lambda,\lambda'} p_\lambda \langle\lambda| e^{-i\boldsymbol{Q}\cdot\hat{\boldsymbol{R}}_{l'd'}} \hat{S}^\alpha_{l'd'} |\lambda'\rangle \langle\lambda'| e^{i\boldsymbol{Q}\cdot\hat{\boldsymbol{R}}_{ld}} \hat{S}^\beta_{ld} |\lambda\rangle \delta(\hbar\omega + E_\lambda - E_{\lambda'}). \end{aligned} \tag{2.26}$$

$F^*_{d'}(\boldsymbol{Q})F_d(\boldsymbol{Q})$ is the dimensionless magnetic structure factor defined as the Fourier transformation of the normalised spin density associated with the magnetic ion. It usually decreases with increasing modulus of the wave vector transfer $\boldsymbol{Q}$. l denotes the unit cell where the ion is located and d specifies the location within the unit cell. $\hat{S}^\alpha_{ld}$ ($\alpha = x, y, z$) is the spin operator of the ldth ion at site $\boldsymbol{R}_{ld}$. The magnetic neutron cross-section is similar to the size of the nuclear cross-section since the coupling $(\gamma r_0)^2 \approx 10^{-24}\,\mathrm{cm}^2$ is of the same order. Neutrons can only couple to magnetic moments or spin fluctuations perpendicular to the wavevector transfer $\boldsymbol{Q}$ which is implied in the polarisation factor $(\delta_{\alpha,\beta} - Q_\alpha Q_\beta/Q^2)$. It allows to determine moment directions or distinguish between different polarisations of spin fluctuations.

In a more general instance, the orbital angular momentum of magnetic ions is not zero or quenched by crystal fields, respectively. A theoretical treatment of such ions based on the dipole approximation is given by Johnston [166], but since the calculation is rather complicated we simply quote the result for $Q \to 0$. Here, the neutron measures the combination of spin and orbital momentum $\boldsymbol{\mu} = -\mu_\mathrm{B}(\boldsymbol{L} + 2\boldsymbol{S})$. The previously derived

cross-section Eq. 2.30 is still valid with the modification that the magnetic form factor $F(\boldsymbol{Q})$ is replaced by

$$\frac{1}{2}gF(\boldsymbol{Q}) = \frac{1}{2}g_S\mathcal{J}_0 + \frac{1}{2}g_L(\mathcal{J}_0 + \mathcal{J}_2) \tag{2.27}$$

where

$$g = 1 + \frac{J(J+1) - L(L+1) + S(S+1)}{2J(J+1)} \tag{2.28}$$

$$\mathcal{J}_n = 4\pi \int_0^\infty j_n(Qr)s(r)r^2dr. \tag{2.29}$$

g is the Landé splitting factor, $j_n(Qr)$ a spherical Bessel function of order n and $s(r)$ the normalised density of the unpaired electrons averaged over all directions in space. In addition, the spin operator $\hat{S}$ has to be replaced by the total angular momentum operator $\hat{J}$.

2.3.2. Magnetic correlation function

We can describe the magnetic cross-section by means of time-dependent Heisenberg operators in a similar manner as in the nuclear case in Sec. 2.2.1 using the integral form of the δ-function. Hence, the magnetic cross-section from Eq. 2.30 is given by

$$\begin{aligned}\frac{\mathrm{d}^2\sigma}{\mathrm{d}\Omega\mathrm{d}\omega} = \frac{(\gamma r_0)^2}{2\pi\hbar}\frac{k'}{k}\sum_{\alpha,\beta}\left(\delta_{\alpha,\beta} - \frac{Q_\alpha Q_\beta}{Q^2}\right)\sum_{l'd'}\sum_{ld}\frac{1}{4}g_{d'}g_d F^*_{d'}(\boldsymbol{Q})F_d(\boldsymbol{Q}) \\ \times \int_{-\infty}^{\infty}\langle e^{-i\boldsymbol{Q}\cdot\hat{\boldsymbol{R}}_{l'd'}(0)}e^{i\boldsymbol{Q}\cdot\hat{\boldsymbol{R}}_{ld}(t)}\rangle\langle\hat{S}^\alpha_{l'd'}(0)\hat{S}^\beta_{ld}(t)\rangle e^{-i\omega t}\end{aligned} \tag{2.30}$$

where we used the time dependent operator

$$\hat{S}^\beta_{ld}(t) = e^{iHt/\hbar}S^\beta_{ld}e^{-iHt/\hbar} \tag{2.31}$$

as well as the form factor derived in the previous section. The electron spin has only little effect on the interatomic forces and therefore on the motion of the nuclei. Here, we assume that the effect is zero and hence we can factorise the thermal average $\langle\rangle$.

We can split the cross-section into its elastic and inelastic components and further into a time-dependent part and time-independent part at $t = \infty$

$$I_{jj'}(\boldsymbol{Q},t) = \langle e^{-i\boldsymbol{Q}\cdot\hat{\boldsymbol{R}}_{l'd'}(0)}e^{i\boldsymbol{Q}\cdot\hat{\boldsymbol{R}}_{ld}(t)}\rangle = I_{jj'}(\boldsymbol{Q},\infty) + I'_{jj'}(\boldsymbol{Q},t) \tag{2.32}$$

$$J^{\alpha\beta}_{jj'}(t) = \langle\hat{S}^\alpha_{l'd'}(0)\hat{S}^\beta_{ld}(t)\rangle = J^{\alpha\beta}_{jj'}(\infty) + J'^{\alpha\beta}_{jj'}(t) \tag{2.33}$$

where j is the combination of l, d. Hence, the cross-section is divided into four components:

- $I_{jj'}(\boldsymbol{Q},\infty)J^{\alpha\beta}_{jj'}(\infty)$ describes elastic magnetic scattering that is used to determine magnetic structures. This part is evaluated in more detail in the next section.

- The term $I_{jj'}(\boldsymbol{Q},t)J^{\alpha\beta}_{jj'}(\infty)$ gives magnetovibrational scattering which is inelastic in the nuclear system but elastic in the spin system, i.e. the neutron excites or de-excites phonons through the magnetic interaction. It will not be considered in this work.
- $I'_{jj'}(\boldsymbol{Q},t)J'^{\alpha\beta}_{jj'}(t)$ describes inelastic scattering in both the spin and phonon system. It will also not be considered in this work.
- Inelastic magnetic scattering with no change in the phonon system, e.g. magnetic fluctuations or spin waves, is given by $I'_{jj'}(\boldsymbol{Q},\infty)J'^{\alpha\beta}_{jj'}(t)$. We will evaluate this term in more detail below.

2.3.3. Magnetic Bragg scattering

Scattering from magnetic crystals where spins can be arranged e.g. in a ferromagnetic, antiferromagnetic, or helical order, is described by the term $I_{jj'}(\boldsymbol{Q},\infty)J^{\alpha\beta}_{jj'}(\infty)$. In a Bravais lattice with localised electrons, we obtain the elastic cross-section through the limit $t\to\infty$. As $t\to\infty$ the matrix component in Eq. 2.30

$$\lim_{t\to\infty}\langle S^{\alpha}_0(0)S^{\beta}_l(t)\rangle = \langle S^{\alpha}_0\rangle\langle S^{\beta}_l\rangle \tag{2.34}$$

becomes independent of time. For a helical structure we define the vector $\boldsymbol{k}$ pointing in the direction of the incommensurate helix with magnitude $\frac{2\pi}{\lambda}$ where λ is the pitch length. Hence, the spin components read

$$\langle S^x_l\rangle = \langle S\rangle\cos(\boldsymbol{k}\cdot\boldsymbol{l}),\quad \langle S^y_l\rangle = \langle S\rangle\sin(\boldsymbol{k}\cdot\boldsymbol{l}),\quad \langle S^z_l\rangle = 0. \tag{2.35}$$

Inserting this spin structure into Eq. 2.30, taking the limit from Eq. 2.34 and integrate with respect to energy, the elastic magnetic cross-section yields

$$\left(\frac{\mathrm{d}\sigma}{\mathrm{d}\Omega}\right)_{el} = (\gamma r_0)^2\left\{\frac{1}{2}gF(\boldsymbol{Q})\right\}^2 e^{-2W(\boldsymbol{Q})}\frac{N}{4}\frac{(2\pi)^3}{v_0}\langle S\rangle^2(1+\hat{k}_z^2)\sum_{\tau}\{\delta(\boldsymbol{Q}+\boldsymbol{k}-\boldsymbol{\tau})+\delta(\boldsymbol{Q}-\boldsymbol{k}-\boldsymbol{\tau})\} \tag{2.36}$$

where N is the total number of magnetic ions and $e^{-2W(\boldsymbol{Q})}$ the Debye Waller factor. Assuming identical magnetic ions, the magnetic form factor is reduced to $\{\frac{1}{2}gF(\boldsymbol{Q})\}^2$. The δ-function shows that magnetic Bragg scattering occurs at

$$\boldsymbol{Q} = \boldsymbol{\tau}\pm\boldsymbol{k}. \tag{2.37}$$

Hence, nuclear Bragg peaks $\boldsymbol{Q}=\boldsymbol{\tau}$ are surrounded by magnetic satellites. For a magnetic structure commensurate with the underlying crystal lattice $\boldsymbol{k}=0$, e.g. for a ferromagnet, the magnetic scattering intensity appears at $\boldsymbol{Q}=\boldsymbol{\tau}$.

2.3.4. Inelastic magnetic scattering

In the following, we will connect the inelastic term $I'_{jj'}(\boldsymbol{Q},\infty)J'^{\alpha\beta}_{jj'}(t)$ and the dynamic magnetic susceptibility $\chi^{\alpha\beta}(\boldsymbol{Q},\omega)$. The inelastic magnetic cross-section for identical magnetic ions in the sample reads

$$\frac{\mathrm{d}^2\sigma}{\mathrm{d}\Omega\mathrm{d}\omega} = (\gamma r_0)^2\frac{k'}{k}\{\frac{1}{2}gF(\boldsymbol{Q})\}^2 e^{-2W(\boldsymbol{Q})}\sum_{\alpha,\beta}\left(\delta_{\alpha,\beta}-\frac{Q_\alpha Q_\beta}{Q^2}\right)S^{\alpha\beta}(\boldsymbol{Q},\omega) \tag{2.38}$$

with the magnetic scattering function

$$S^{\alpha\beta}(\boldsymbol{Q},\omega) = \frac{1}{2\pi\hbar}\sum_{l'd'}\sum_{ld}\int_{-\infty}^{\infty}\langle e^{-i\boldsymbol{Q}\cdot\hat{\boldsymbol{R}}_{l'd'}(0)}e^{i\boldsymbol{Q}\cdot\hat{\boldsymbol{R}}_{ld}(\infty)}\rangle\langle\hat{S}^{\alpha}_{l'd'}(0)\hat{S}^{\beta}_{ld}(t)\rangle e^{-i\omega t}. \tag{2.39}$$

$\langle\hat{S}^{\alpha}_{l'd'}(0)\hat{S}^{\beta}_{ld}(t)\rangle$ is the thermal average of the time-dependent spin operators. It describes the correlation between the magnetic moment $l'd'$ at position $\boldsymbol{R'}$ at time $t=0$ with the magnetic moment ld at position $\boldsymbol{R}$ at time t and reflects the van Hove pair correlation function. Hence, using neutron scattering techniques, we typically measure the Fourier transform of the pair correlation function in space and time.

The scattering cross-section is related to the fluctuation-dissipation theorem through

$$S^{\alpha\beta}(\boldsymbol{Q},\omega) = \frac{N\hbar}{\pi}\left(1-e^{-\frac{\hbar\omega}{k_BT}}\right)^{-1}\mathrm{Im}\chi^{\alpha\beta}(\boldsymbol{Q},\omega) \tag{2.40}$$

where k_B is the Boltzmann constant and T the temperature of the system. The neutron detects the response, $M(\boldsymbol{Q},\omega)$, of the frequency- and wavevector-dependent magnetic field, $H^{\beta}(\boldsymbol{Q},\omega)$, it produces itself within the sample

$$M^{\alpha}(\boldsymbol{Q},\omega) = \chi^{\alpha\beta}(\boldsymbol{Q},\omega)H^{\beta}(\boldsymbol{Q},\omega). \tag{2.41}$$

$\chi^{\alpha\beta}(\boldsymbol{Q},\omega)$ is the generalised magnetic susceptibility tensor.

2.4. Neutron spin and neutron beam polarisation

2.4.1. Neutron beam polarisation

The neutron spin quantum number is 1/2 and hence its spin operator $\hat{\boldsymbol{S}} = (S_x, S_y, S_z)$ is described by the 2×2 Pauli matrices Eq. 2.23 through

$$\hat{\boldsymbol{S}} = \frac{\hbar}{2}\hat{\boldsymbol{\sigma}} \tag{2.42}$$

with two eigenvalues $\pm\hbar/2$ with respect to an arbitrary quantisation axis. Using the corresponding eigenstates $\boldsymbol{\chi}_\uparrow$ and $\boldsymbol{\chi}_\downarrow$ in the two-dimensional Hilbert space $\mathscr{H}_2$, i.e. the spin is parallel or antiparallel to the quantisation axis, any state is described as a superposition

$$\boldsymbol{\chi} = a\boldsymbol{\chi}_\uparrow + b\boldsymbol{\chi}_\downarrow = a\begin{pmatrix}1\\0\end{pmatrix} + b\begin{pmatrix}0\\1\end{pmatrix}. \tag{2.43}$$

The two eigenvectors are in the following referred to as spin up and spin down. To satisfy the normalisation condition for $\boldsymbol{\chi}$, the complex coefficients a and b must fulfil

$$\boldsymbol{\chi}^\dagger\boldsymbol{\chi} = |a|^2 + |b|^2 = 1. \tag{2.44}$$

We define the polarisation as the expectation value of the Pauli matrices

$$\boldsymbol{P} \equiv \frac{2}{\hbar}\langle\hat{\boldsymbol{S}}\rangle = \langle\hat{\boldsymbol{\sigma}}\rangle = \chi^\dagger\hat{\boldsymbol{\sigma}}\chi = \mathrm{Tr}\hat{\rho}\hat{\boldsymbol{\sigma}} \tag{2.45}$$

where

$$\hat{\rho} = \chi\chi^\dagger = \begin{pmatrix}|a|^2 & ab^*\\ ba^* & |b|^2\end{pmatrix} \tag{2.46}$$

is the density matrix operator defining the probability of a certain spin state. For a single neutron the polarisation is always $|\boldsymbol{P}| = 1$. We can expand $\hat{\rho}$ in terms of the unit matrix $\mathbf{1}$ and the Pauli matrices $\hat{\boldsymbol{\sigma}}$

$$\hat{\rho} = \frac{1}{2}(\mathbf{1} + \boldsymbol{P}\cdot\hat{\boldsymbol{\sigma}}). \tag{2.47}$$

The polarisation can be expressed as the unit vector $\hat{\boldsymbol{n}}$ in spherical coordinates (θ, ϕ)

$$\boldsymbol{P} = \begin{pmatrix}2\mathrm{Re}(a^*b)\\ 2\mathrm{Im}(a^*b)\\ |a|^2 - |b|^2\end{pmatrix} = \begin{pmatrix}\sin\theta\cos\phi\\ \sin\theta\sin\phi\\ \cos\theta\end{pmatrix} = \hat{\boldsymbol{n}} \tag{2.48}$$

using

$$a = \cos\frac{\theta}{2}e^{i\frac{\phi}{2}} \qquad b = \sin\frac{\theta}{2}e^{-i\frac{\phi}{2}}. \tag{2.49}$$

This geometrical representation is called the Bloch sphere. Considering a neutron beam with N neutrons, the polarisation is defined as the average over the polarisations of each single neutron $\boldsymbol{P}_j$

$$\boldsymbol{P} = \frac{1}{N}\sum_j \boldsymbol{P}_j. \tag{2.50}$$

For an unpolarised beam $\boldsymbol{P} = 0$, for a fully polarised beam $|\boldsymbol{P}| = 1$ and for a partially polarised beam $0 < |\boldsymbol{P}| < 1$.

2.4.2. Spins in magnetic fields

An external magnetic field exerts a torque on the neutron magnetic moment resulting in Larmor precession of the neutron spin about the magnetic field $\boldsymbol{H}$. The Hamiltonian for a spin in a magnetic field is

$$\hat{H} = \gamma \boldsymbol{H} \cdot \hat{\boldsymbol{S}} \tag{2.51}$$

where γ is the gyromagnetic ratio of the neutron and $\hat{\boldsymbol{S}}$ the spin operator associated with the Pauli matrices described in detail in Sec. 2.4.1. With an external magnetic field along the z-direction, i.e. $\boldsymbol{H} = H\hat{z}$, the Schrödinger equation for the spin component χ reads

$$-i\hbar\frac{\partial}{\partial t}\chi = \hat{H}\chi. \tag{2.52}$$

With the ansatz

$$a = \cos\frac{\theta}{2}e^{i\omega_a t} \qquad b = \sin\frac{\theta}{2}e^{i\omega_b t}, \tag{2.53}$$

the equation is solved for

$$\omega_a = \frac{\gamma H}{2} \qquad \omega_b = \frac{-\gamma H}{2}. \tag{2.54}$$

Using the wave function Eq. 2.43, the expectation value of the spin operator is given by

$$\langle \hat{\boldsymbol{S}} \rangle = \langle \chi^* | \hat{\boldsymbol{S}} | \chi \rangle = \frac{\hbar}{2}\left\langle \begin{pmatrix} a \\ b \end{pmatrix} \middle| \hat{\boldsymbol{\sigma}} \middle| \begin{pmatrix} a \\ b \end{pmatrix} \right\rangle \tag{2.55}$$

$$= \frac{\hbar}{2}\begin{pmatrix} \frac{1}{2}\sin(\theta)(e^{i(-\omega_a+\omega_b)t} + e^{i(\omega_a-\omega_b)t}) \\ \frac{1}{2}i\sin(\theta)(e^{i(-\omega_a+\omega_b)t} - e^{i(\omega_a-\omega_b)t}) \\ \cos(\theta) \end{pmatrix} \tag{2.56}$$

$$= \frac{\hbar}{2}\begin{pmatrix} \sin(\theta)\cos(\omega_L t) \\ \sin(\theta)\sin(\omega_L t) \\ \cos(\theta) \end{pmatrix} \tag{2.57}$$

where we define the Larmor frequency

$$\omega_{\mathrm{L}} = \omega_a - \omega_b = \gamma H. \tag{2.58}$$

Hence, $\langle \hat{\boldsymbol{S}} \rangle$ is a vector inclined by the angle θ with respect to the z-axis whose parallel component remains constant over time whereas the perpendicular component precesses with frequency $\gamma H = \gamma_{\mathrm{L}} B$ about the z-axis, where $\gamma_{\mathrm{L}} = 29.16\,\mathrm{MHz}\cdot\mathrm{T}^{-1}$ and B the magnetic field.

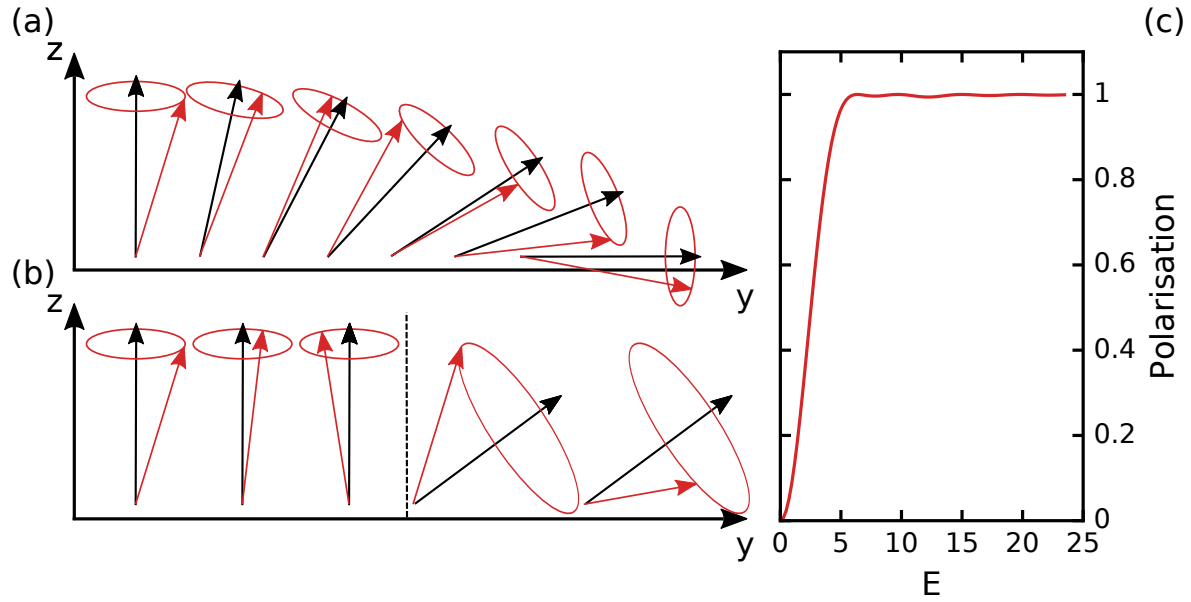

Figure 2.1.: Comparison between adiabatic and non-adiabatic transition. (a) The neutron spin $\boldsymbol{S}$ (red) moves in y-direction, precesses about the magnetic field $\boldsymbol{B}$ (black) and follows adiabatically the rotation of the magnetic field. (b) The magnetic field $\boldsymbol{B}$ rotates much faster than the Larmor frequency and the neutron spin $\boldsymbol{S}$ performs a non-adiabatic transition. (c) The polarisation as a function of the adiabaticity parameter E (see text for more details).

A neutron beam is easily depolarised by magnetic fields as small as the earth magnetic field of $B \approx 25 - 65\,\mu$T. However, from inspecting Eqs. 2.55 - 2.58, it is clear that a magnetic field applied parallel to the neutron polarisation can be used to conserve it. Such a field is typically referred to as 'guide field'. There are two types of transition when the direction of the guide field rotates along the flight path of the neutron with ω_B (see Fig. 2.1). If the direction changes slowly with respect to the Larmor frequency $\omega_\mathrm{B} \ll \omega_\mathrm{L}$, the parallel component will follow the change of the magnetic field and the polarisation is conserved. This process is illustrated in Fig. 2.1(a) where a neutron moves along the y-axis and called *adiabatic transition*. If the magnetic field direction rotates much faster than the Larmor frequency $\omega_\mathrm{B} \gg \omega_\mathrm{L}$, the polarisation will start to rotate about the new field direction as shown in Fig. 2.1(b). This transition is called *non-adiabatic*. We can introduce an adiabaticity parameter

$$E = \frac{\omega_\mathrm{L}}{\omega_\mathrm{B}} = \frac{\gamma_\mathrm{L} B}{\frac{d\theta_\mathrm{B}}{dt}} = \frac{\gamma_\mathrm{L} B}{\frac{d\theta_\mathrm{B}}{dy} v} \tag{2.59}$$

where θ_B is the angle between the magnetic field $\boldsymbol{B}$ and the y-axis and v the neutron velocity. To conserve the polarisation in an adiabatic transition, $E \gtrapprox 7$ as shown in Fig. 2.1(c) where the polarisation with respect to the magnetic field as a function of the adiabaticity parameter E is shown.

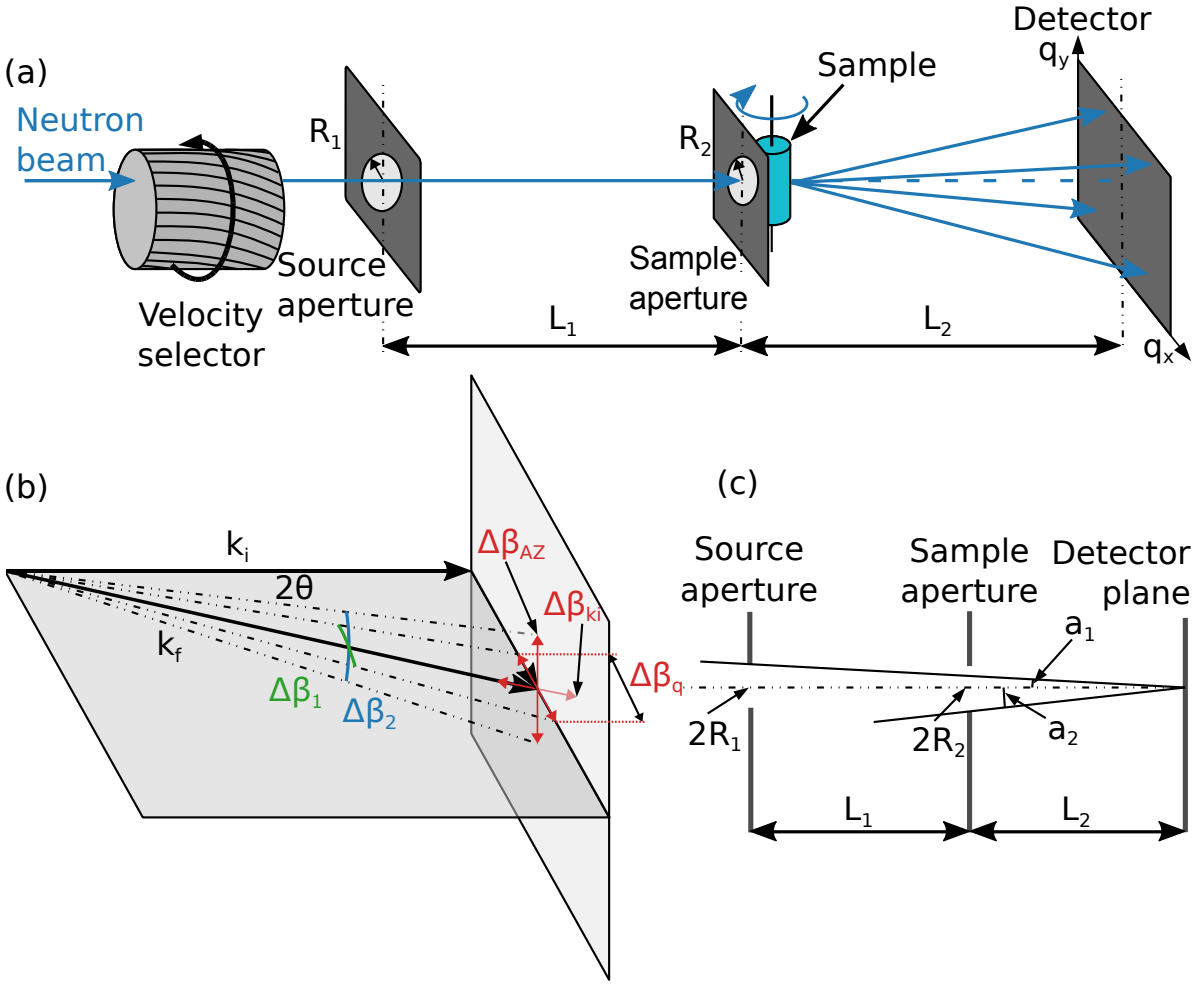

Figure 2.2.: Instrumental setup of SANS. (a) A "white" neutron beam enters the instrument from the left side. A velocity selector defines the wavelength λ and wavelength bandwidth $\Delta\lambda$. A pair of apertures collimate the beam before it hits the sample. The scattered neutrons are detected on a position sensitive detector. (b) The scattering triangle with the different uncertainties (see text). (c) Top view onto the SANS setup described in (a). Figure taken from Ref. [167].

2.5. Small angle neutron scattering

Small angle neutron scattering (SANS) techniques take advantage of cold neutrons and long collimation lengths to resolve wave vector transfers down to $10^{-4}\,\text{Å}^{-1}$ and hence, investigate structures with sizes ranging from 10 to 50.000 Å, length scales much larger than interatomic distances. A typical SANS setup is shown in Fig. 2.2 (a). A "white" neutron beam enters from the left into a velocity selector which selects a wavelength band with typical width between $\frac{\Delta\lambda}{\lambda} = 0.05-0.2$. After the collimation through several pinholes over a length L_1 typically between $2-20\,\text{m}$, neutrons are scattered from the sample. At a

distance L_2 between $2-20\,\mathrm{m}$ behind the sample, the neutrons are detected by a position-sensitive detector. Except for short paths at the sample, neutrons fly through vacuum to avoid air scattering which would result in experimental background.

In the following, we will summarise the analytical approach for the resolution function of SANS by Pedersen [168]. The three main contributions defining the SANS resolution are (1) the width of the wavelength band, (2) collimation effects, and (3) the spatial resolution of the detector which we assume are all independent. The resolution effects can be described by the resolution function $R(\boldsymbol{Q}, \bar{\boldsymbol{Q}})$, where $\bar{\boldsymbol{Q}}$ is the average scattering vector. The measured intensity at $\bar{\boldsymbol{Q}}$ is proportional to

$$I(\bar{\boldsymbol{Q}}) = \int R(\boldsymbol{Q}, \bar{\boldsymbol{Q}}) \frac{\mathrm{d}\sigma(\boldsymbol{Q})}{\mathrm{d}\Omega} d\boldsymbol{Q} \tag{2.60}$$

where $\mathrm{d}\sigma(\boldsymbol{Q})/\mathrm{d}\Omega$ is the scattering cross-section.

The wavelength distribution defined by the velocity selector has a triangular shape which we approximate, for simplicity, with a Gaussian distribution centred around the mean value $\bar{\lambda}$ with a full-width-at-half-maximum value (FWHM) $\Delta\lambda$. The standard deviation σ_λ and the FWHM $\Delta\lambda$ are related through

$$\sigma_\lambda = \frac{\Delta\lambda}{2(2\ln 2)^{1/2}}. \tag{2.61}$$

The standard deviation σ_W of the signal due to the wavelength spread is

$$\sigma_W = \sigma_\lambda \frac{\bar{\boldsymbol{Q}}}{\bar{\lambda}} = \bar{\boldsymbol{Q}} \frac{\Delta\lambda}{\bar{\lambda}} \frac{1}{2(2\ln 2)^{1/2}}. \tag{2.62}$$

For the influence of the finite collimation on the resolution, we consider the neutron beam divergence in the scattering plane defined by the FWHM $\Delta\beta_1$ and the divergence perpendicular to the scattering plane with FWHM $\Delta\beta_2$, respectively, as shown in Fig. 2.2 (b). The collimation system is depicted in Fig. 2.2 (a) consisting of the source aperture with R_1 and the sample aperture with radius R_2 separated by the distance L_1. The sample-detector distance is defined by L_2. We assume that the radii of the apertures R_1 and R_2 are small compared to the separation L_1 and and the sample-detector distance L_2. From a point on the detector the angles $a_1 = R_1/(L_1+L_2)$ and $a_2 = R_2/L_2$ are defined as half the angular extent of the source aperture and the sample aperture, respectively.

One can distinguish two cases for $\bar{\boldsymbol{Q}} \approx 0$ and for an arbitrary value of $\bar{\boldsymbol{Q}} \neq 0$. For the first case, the unscattered beam can be described by the delta function $\mathrm{d}\sigma(\boldsymbol{Q})/\mathrm{d}\Omega = \delta(\boldsymbol{Q})$ and hence, the resolution function $R(\boldsymbol{Q}, \bar{\boldsymbol{Q}})$ is given by the direct beam profile. For the

second case, the FWHM within the scattering plane is given by

$$\Delta\beta_1 = \frac{2R_1}{L_1} - \frac{1}{2}\frac{R_2^2}{R_1}\frac{\cos^4(2\theta)}{L_2^2 L_1}\left(L_1 + \frac{L_2}{\cos^2(2\theta)}\right)^2 \quad \text{for } a_1 \geq a_2 \tag{2.63}$$

$$\Delta\beta_1 = 2R_2\left(\frac{1}{L_1} + \frac{\cos^2(2\theta)}{L_2}\right) - \frac{1}{2}\frac{R_1^2}{R_2^2}\frac{L_2}{L_1}\frac{1}{\cos^2(2\theta)(L_1 + L_2/\cos^2(2\theta))} \quad \text{for } a_1 < a_2 \tag{2.64}$$

and perpendicular to the scattering plane by

$$\Delta\beta_2 = \frac{2R_1}{L_1} - \frac{1}{2}\frac{R_2^2}{R_1}\frac{\cos^2(2\theta)}{L_2^2 L_1}\left(L_1 + \frac{L_2}{\cos(2\theta)}\right)^2 \quad \text{for } a_1 \geq a_2 \tag{2.65}$$

$$\Delta\beta_2 = 2R_2\left(\frac{1}{L_1} + \frac{\cos(2\theta)}{L_2}\right) - \frac{1}{2}\frac{R_1^2}{R_2^2}\frac{L_2}{L_1}\frac{1}{\cos(2\theta)(L_1 + L_2/\cos(2\theta))} \quad \text{for } a_1 < a_2. \tag{2.66}$$

The standard deviation in the scattering plane σ_{C1} and perpendicular σ_{C2} are given by

$$\sigma_{\mathrm{C1}} = \bar{k}\cos(\bar{\theta})\frac{\Delta\beta_1}{2(2\ln 2)^{1/2}} \tag{2.67}$$

$$\sigma_{\mathrm{C2}} = \bar{k}\frac{\Delta\beta_2}{2(2\ln 2)^{1/2}} \tag{2.68}$$

where $\bar{k} = 2\pi/\bar{\lambda}$.

For the detector resolution the method of detection, the method of position determination and the segmentation into pixels define the spatial resolution which we describe by a Gaussian distribution of width Δ. The standard deviation within the scattering plane is given by

$$\sigma_{\mathrm{D1}} = \bar{k}\cos(\bar{\theta})\cos^2(2\bar{\theta})\frac{\Delta}{L_2 2(2\ln 2)^{1/2}} \tag{2.69}$$

and perpendicular to the scattering plane by

$$\sigma_{\mathrm{D2}} = \bar{k}\cos(2\bar{\theta})\frac{\Delta}{L_2(2\ln 2)^{1/2}}. \tag{2.70}$$

Eventually, the resolution is given as

$$R(\boldsymbol{Q}, \bar{\boldsymbol{Q}}) = \frac{1}{2\pi\sigma_1\sigma_2}\exp\left[-\frac{1}{2}\left(\frac{(Q_1 - \bar{Q})^2}{\sigma_1^2} + \frac{Q_2^2}{\sigma_2^2}\right)\right] \tag{2.71}$$

with the total standard deviations within the scattering plane σ_1 and perpendicular to it σ_2

$$\sigma_1^2 = \sigma_{\mathrm{W}}^2 + \sigma_{\mathrm{C1}}^2 + \sigma_{\mathrm{D1}}^2 \tag{2.72}$$

$$\sigma_2^2 = \sigma_{\mathrm{C2}}^2 + \sigma_{\mathrm{D2}}^2. \tag{2.73}$$

$Q_1 - \bar{Q}$ denotes the in-plane component and Q_2 the out-of-plane component. It is important to note that the latter does not depend on the wavelength.

2.6. Modulation of intensity with zero effort

Modulation of intensity with zero effort (MIEZE) is a neutron spin echo (NSE) method which achieves a sub-μeV energy resolution and reaches a large q-range from the SANS regime up to several inverse Angström [169–172]. Contrary to triple axis or time-of-flight spectroscopy where the absolute velocity before and after the scattering event is measured, NSE techniques measure smallest changes of the velocity of scattered neutrons by encoding the time of flight in the Larmor precession phase of the neutron. Classical NSE as proposed by Mezei in 1972 [173, 174] uses static magnetic fields for the spin precession. In 1987, Golub and Gähler introduced neutron resonance spin echo (NRSE) where the static magnetic fields are replaced by resonant spin flippers consisting of a static field and an oscillating field [175]. The static magnetic field can be oriented perpendicular to the neutron beam, referred to as transverse NRSE (TNRSE), or parallel, referred to as longitudinal NRSE (LNRSE). Since in NSE and NRSE the time of flight is encoded in the Larmor precession phase, they are sensitive to depolarisation effects at the sample position that can be caused by the sample itself (e.g. ferromagnetism) or the sample environment (e.g. magnetic fields). MIEZE as a modification of NRSE overcomes this limitation since the spin manipulation is performed only in front of the sample and the energy resolution is encoded in a modulation of the intensity rather than the Larmor precession phase [169]. Longitudinal or transverse configurations are also possible for MIEZE.

In principle, classical NSE consists of very homogeneous magnetic fields in front of and behind the sample position with the same magnitude but opposite field directions. In reality, both fields have the same orientation, but a spin flipper after the sample inverts the neutron polarisation instead of the second field to avoid a vanishing field at the sample position. A neutron precesses in the first magnetic field before it is scattered. If the scattering event is elastic, neutrons spend the same period of time in the second magnetic field, the precession is reversed and the polarisation restored. This condition is also what provides the name for the technique as the spin configuration at the end of the instrument “echoes” the configuration at the instrument entrance. If the neutron loses or gains energy through the scattering event, the neutron velocity changes and it traverses the second magnetic field faster or slower and the polarisation is not fully restored. As neutrons precess up to several 10^4 times in one magnetic field, a change of velocity in the order of 10^{-4} can be detected, hence, the outstanding energy resolution. In addition, the energy resolution is decoupled from the wavelength band width and typical widths of $\frac{\Delta\lambda}{\lambda} = 10 - 20\%$ can be employed. This is one of the great advantages of NSE techniques as very high resolutions are achieved while a high neutron flux is maintained.

MIEZE as a modification of NRSE is a resonant spin echo technique where the complete spin manipulation takes place in front of the sample. In the following we will focus on longitudinal MIEZE as it is the configuration used throughout this work. A schematic depiction of a longitudinal MIEZE is shown in Fig. 2.3 (a). A white neutron beam enters the instrument from the left where a velocity selector defines the incoming wavelength and a polariser generates a beam of neutrons polarised along the beam direction. The neutrons are rotated into the plane perpendicular to the guide field by a $\pi/2$-flipper and start to precess. The main components for the MIEZE technique are two resonant spin flippers referred to as rf-flippers. At each of the rf-flippers, which are separated by a distance L_1, the neutron performs a resonant π-flip as will be explained in more detail below. A solenoid between the rf-flippers, a so-called field-subtraction coil, can be used to reduce the accumulated neutron spin phase. It allows to precisely tune the accumulated phase and, as we will explain in more detail below, allows to extend the dynamic range towards very fast processes. After another $\pi/2$-flip the beam is again polarised by the analyser, scattered by the sample and finally detected at a distance L_{SD} behind the sample on a time resolved, position-sensitive detector.

In the following, we will derive the relationship between the MIEZE signal and the scattering function $S(q,\omega)$. Here, we will employ a classical description of the neutron spin and its interactions with the magnetic fields along the beam path. For longitudinal MIEZE setup the static fields between the $\pi/2$-flippers point along the flight path. In the following we define a coordinate frame (see Fig. 2.3) for which the flight path is along the y-direction, whereas x and z describe the plane perpendicular to the flight path in which the neutron starts to precess after passing the first static $\pi/2$-flipper. The rf-flipper produces a static magnetic field B_0 perpendicular to the precession plane and a rotating magnetic field B_{rf} rotating with frequency ω within the precession plane. The magnetic field of a rf-flipper is given by

$$\boldsymbol{B} = \begin{pmatrix} B_{\mathrm{rf}}\cos(\omega t) \\ B_0 \\ B_{\mathrm{rf}}\sin(\omega t) \end{pmatrix}. \tag{2.74}$$

Neutrons precess about the static field with Larmor frequency ω_L and the resonant flipper frequency ω is matched, i.e. $\omega_L = \gamma B_0 = \omega$. Hence, neutrons precess with the same frequency as the rotating magnetic field and in the rotating reference frame neutrons experience a field

$$\boldsymbol{B} = \begin{pmatrix} B_{\mathrm{rf}}\cos(\phi_1) \\ 0 \\ B_{\mathrm{rf}}\sin(\phi_1) \end{pmatrix}. \tag{2.75}$$

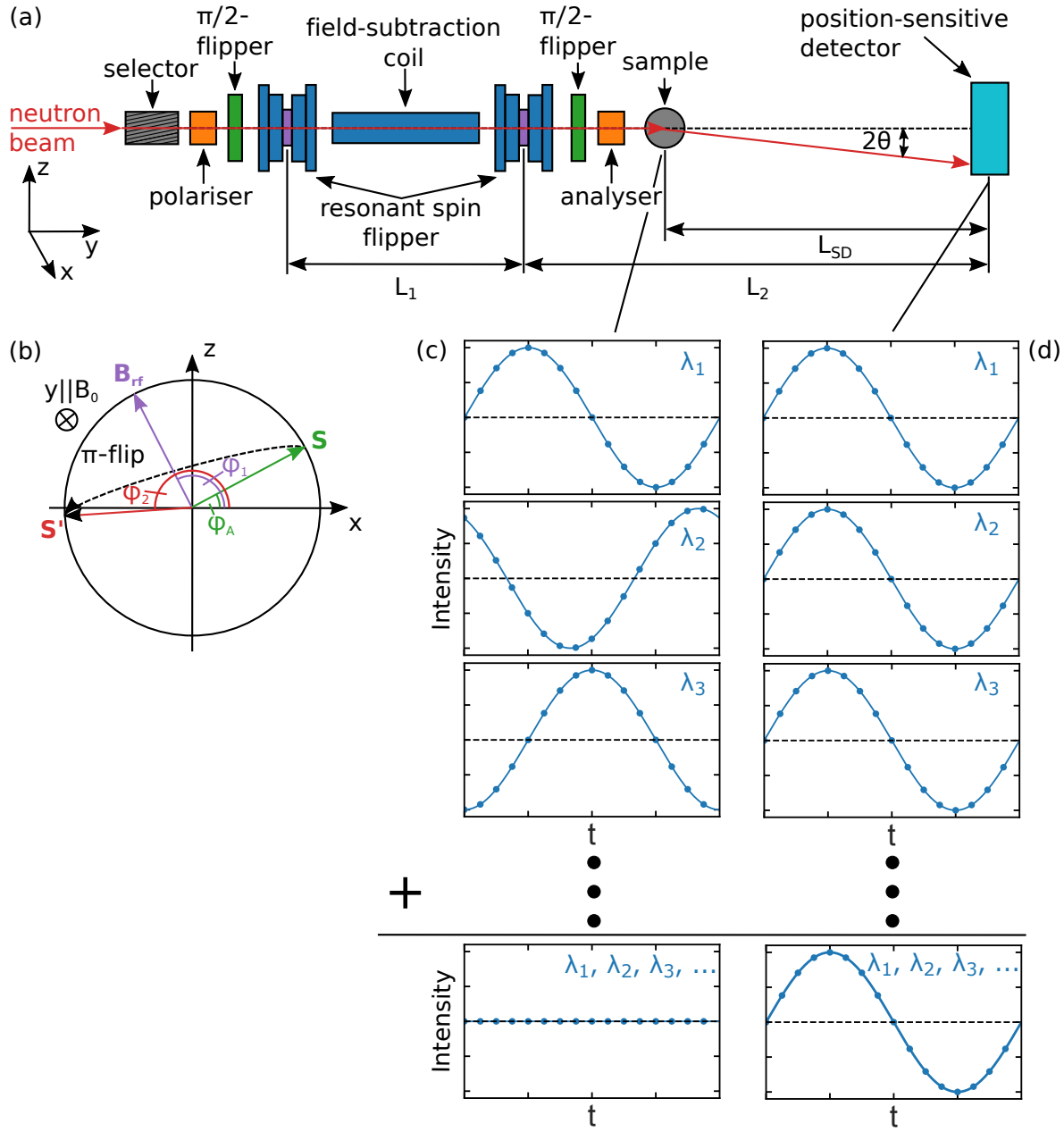

Figure 2.3.: Schematic of a MIEZE spectrometer. (a) Neutrons enter the instrument from left through a selector. Before the spin manipulation by resonant and static magnetic fields between the $\pi/2$-flippers, the beam is polarised by a polariser. An analyser in front of the sample leads to the modulation of intensity before the neutrons are scattered by the sample and detected. (b) π-flip of a neutron spin as seen in the rotating reference frame of a resonant spin flipper. (c, d) Modulation of intensity as a function of time t at the sample and the detector, respectively, for several wavelengths. Using a broad wavelength bandwidth $\Delta\lambda/\lambda$, the modulation is only in phase at the detector where the signal is sinusoidal with frequency $2(\omega_\mathrm{B} - \omega_\mathrm{A})$.

where ϕ_1 denotes the angle between $\boldsymbol{B}$ and the x-axis. A neutron spin enters the rf-flipper with an initial spin pointing along $\boldsymbol{S}$ at an angle ϕ_A with respect to the x-axis as depicted in Fig. 2.3 (b) where the static magnetic field B_0 points into the plane. The rotation angle about the rotating magnetic field B_rf at an angle ϕ_1 depends on the time spent in the flipper as well as its magnitude. It is chosen so that a neutron performs a π-flip and points along $\boldsymbol{S'}$ at an angle $\phi_2 = \phi_\mathrm{A} + 2(\phi_1 - \phi_\mathrm{A})$. In summary, the accumulated phase after the first rf-flipper running with the frequency ω_A is

$$\phi_{\mathrm{A}'} = \phi_\mathrm{A} + 2(\phi_1 - \phi_\mathrm{A}) + \omega_\mathrm{A} t \tag{2.76}$$
$$= \phi_\mathrm{A} + 2(\omega_\mathrm{A} t_\mathrm{A} - \phi_\mathrm{A}) + \omega_\mathrm{A} t \tag{2.77}$$
$$= 2\omega_\mathrm{A} t_\mathrm{A} + \omega_\mathrm{A} t - \phi_\mathrm{A} \tag{2.78}$$

where t denotes the time spent in the rotating field and t_A the time of arrival at the rf-flipper. Within the field subtraction coil the neutron accumulates a phase

$$\phi_\mathrm{sub} = \frac{\gamma}{v} \int B_\mathrm{sub} \mathrm{dy} \tag{2.79}$$

depending on the neutron velocity v and the field integral along the flight path. The spin phase after the second rf-flipper is

$$\phi_{B'} = 2\omega_B t_B + \omega_B t - \phi_{A'} - \phi_\mathrm{sub}(B_\mathrm{sub}, v) \tag{2.80}$$
$$= 2\omega_B t_B + \omega_B t - 2\omega_A t_A - \omega_A t + \phi_A - \phi_\mathrm{sub}(B_\mathrm{sub}, v) \tag{2.81}$$

where t_B denotes the time of arrival at the second rf-flipper. Since the time spent in the rf-flipper $t = \frac{l}{v}$ is equal for both flippers where l denotes their length and we can use $t_\mathrm{B} = t_\mathrm{A} + L_1/v$, the total accumulated spin phase after the second flipper is

$$\phi_{\mathrm{B}'} = 2\omega_\mathrm{B}(t_A + L_1/v) + \omega_\mathrm{B}\frac{l}{v} - 2\omega_\mathrm{A} t_\mathrm{A} - \omega_\mathrm{A}\frac{l}{v} + \phi_\mathrm{A} - \phi_\mathrm{sub}(B_\mathrm{sub}, v) \tag{2.82}$$
$$= 2t_\mathrm{A}(\omega_\mathrm{B} - \omega_\mathrm{A}) - \frac{l}{v}(\omega_\mathrm{B} - \omega_\mathrm{A}) + 2\omega_\mathrm{B}\frac{L_1}{v} + \phi_\mathrm{A} - \phi_\mathrm{sub}(B_\mathrm{sub}, v). \tag{2.83}$$

The time of arrival at the detector t_D is given by

$$t_\mathrm{D} = t_\mathrm{A} + \frac{L_1}{v} + \frac{L_2}{v} \tag{2.84}$$

where L_2 is the distance between the second rf-flipper and the detector. Hence, the spin phase at the detector is

$$\phi_\mathrm{D} = 2t_\mathrm{D}(\omega_\mathrm{B} - \omega_\mathrm{A}) + 2\omega_\mathrm{A}(\frac{L_1}{v} + \frac{L_2}{v}) - 2\omega_\mathrm{B}\frac{L_2}{v} + \frac{l}{v}(\omega_\mathrm{B} - \omega_\mathrm{A}) + \phi_0 - \phi_\mathrm{sub}(B_\mathrm{sub}, v). \tag{2.85}$$

If we choose

$$2\omega_\mathrm{A}(\frac{L_1}{v} + \frac{L_2}{v}) - 2\omega_\mathrm{B}\frac{L_2}{v} + \frac{l}{v}(\omega_\mathrm{B} - \omega_\mathrm{A}) - \phi_\mathrm{sub}(B_\mathrm{sub}, v) \stackrel{!}{=} 0 \tag{2.86}$$

for the instrument parameters, all velocity dependent factors cancel and the phases of all neutrons are in-phase at the echo point where the detector is placed. This is the so-called MIEZE condition which reads using Eq. 2.79

$$2\omega_{\mathrm{A}}(L_1+L_2)-2\omega_{\mathrm{B}}L_2+l(\omega_{\mathrm{B}}-\omega_{\mathrm{A}})=\gamma\int B_{\mathrm{sub}}\mathrm{d}y. \tag{2.87}$$

W.l.o.g. we can set $\phi_{\mathrm{A}}=0$ and receive a rotating polarisation at the detector which depends on the difference between the two rf-flipper frequencies $\omega_{\mathrm{A,B}}$ and the flight time to the detector t_{D}

$$\phi_{\mathrm{D}}=2t_{\mathrm{D}}(\omega_{\mathrm{B}}-\omega_{\mathrm{A}}). \tag{2.88}$$

A spin analyser anywhere between the second rf-flipper and the detector converts the phase modulation into an intensity modulation in time

$$I(t_{\mathrm{D}})=\frac{I_0}{2}(\underbrace{\cos 2(\omega_{\mathrm{B}}-\omega_{\mathrm{A}})t_{\mathrm{D}}}_{\text{time dependent}}+1) \tag{2.89}$$

since the probability for a neutron to pass the analyser is given by

$$T=\frac{1}{2}(\cos(\phi)+1) \tag{2.90}$$

where ϕ is the angle between the spin and the quantisation axis of the analyser. As shown in Fig. 2.3 (c, d), the signal is sinusoidal for all wavelengths with the same frequency $2(\omega_{\mathrm{B}}-\omega_{\mathrm{A}})$ but different phases except at the echo point.

The intensity is a sinusoidal signal as a function of time for a fixed distance behind the analyser. In addition, it is sinusoidal as a function of distance for a fixed time. Considering that any detector has a finite neutron conversion layer, it must be much thinner than the spatial width of one oscillation in space

$$d_{2\pi}=\frac{2\pi}{2(\omega_{\mathrm{B}}-\omega_{\mathrm{A}})}v. \tag{2.91}$$

Otherwise, a destructive superposition of the sinusoidal signal of neutrons with different velocities occurs and reduces the amplitude of the signal.

Considering a monochromatic beam, the intensity modulation in Eq. 2.89 can be observed anywhere behind the analyser whereas for a finite wavelength distribution $f(v)$ with mean width Δv the signal is suppressed by an envelope. At a distance Δl away from the focus point, the intensity can be expressed by

$$I=\frac{I_0}{2}\int \mathrm{d}v f(v)\left(\cos(2(\omega_{\mathrm{B}}-\omega_{\mathrm{A}})(t_{\mathrm{D}}+\Delta l/v))+1\right). \tag{2.92}$$

To estimate the mean width of this envelope, we assume $2(\omega_{\mathrm{B}}-\omega_{\mathrm{A}})\Delta l/v\approx\pi$. Hence, the mean width in first order is given by

$$\bar{\Delta l}=\frac{\pi v}{\frac{\Delta v}{v}2(\omega_{\mathrm{B}}-\omega_{\mathrm{A}}))}. \tag{2.93}$$

Considering an energy transfer $\hbar\omega$ through a scattering event between the neutron of velocity v and a sample placed L_{SD} in front of the detector as shown in Fig. 2.3 (a), the change in time of arrival is

$$\Delta t = L_{\mathrm{SD}} \left(\frac{1}{v} - \frac{1}{\sqrt{v^2 + 2\frac{\hbar\omega}{m_{\mathrm{n}}}}} \right). \tag{2.94}$$

Using the spin echo approximation, i.e. $\hbar\omega \ll \frac{m_{\mathrm{n}}}{2} v^2$, the equation can be simplified through a Taylor expansion to

$$\Delta t_{\mathrm{D}} \approx \frac{L_{\mathrm{SD}} \hbar\omega}{m_{\mathrm{n}} v^3}. \tag{2.95}$$

The probability for a scattering event with energy transfer $\hbar\omega$ is given by the scattering function $S(\omega)$ (see Eq. 2.39 for inelastic magnetic scattering). Using Eq. 2.89 and integrating over the whole energy spectrum measured at the detector yields

$$I = \frac{I_0}{2} \int (\cos(2(\omega_{\mathrm{B}} - \omega_{\mathrm{A}})(t_{\mathrm{D}} + \Delta t_{\mathrm{D}})) + 1) S(\omega) \mathrm{d}\omega. \tag{2.96}$$

If we assume a symmetric scattering function $S(\omega)$ around $\omega = 0$, i.e. $\hbar\omega \ll k_B T$, Eq. 2.96 reads

$$I = \frac{I_0}{2} \int (\cos 2(\omega_{\mathrm{B}} - \omega_{\mathrm{A}}) t_{\mathrm{D}} \cdot \cos(\omega_{\mathrm{B}} - \omega_{\mathrm{A}}) \Delta t_{\mathrm{D}} + 1) S(\omega) \mathrm{d}\omega \tag{2.97}$$

$$= \frac{I_0}{2} \left(\int \underbrace{\cos 2(\omega_{\mathrm{B}} - \omega_{\mathrm{A}}) t_{\mathrm{D}}}_{\text{time dependent}} \cdot \underbrace{\cos(\omega_{\mathrm{B}} - \omega_{\mathrm{A}}) \Delta t_{\mathrm{D}} \cdot S(\omega) \mathrm{d}\omega}_{\text{amplitude}} + 1 \right) \tag{2.98}$$

where we used $\int S(\omega)\mathrm{d}\omega = 1$. The scattering function $S(\omega)$ causes a change of the signal amplitude and its relation to the MIEZE contrast is

$$C := \int \cos(\omega \tau_{\mathrm{MIEZE}}) S(\omega) \mathrm{d}\omega \tag{2.99}$$

with the MIEZE time

$$\tau_{\mathrm{MIEZE}} = \frac{2\hbar}{m_{\mathrm{n}} v^3} L_{SD} (\omega_{\mathrm{B}} - \omega_{\mathrm{A}}) = \frac{m_{\mathrm{n}}^2}{\pi h^2} \lambda^3 L_{\mathrm{SD}} (\omega_{\mathrm{B}} - \omega_{\mathrm{A}}) \tag{2.100}$$

defining the resolution of the MIEZE spectrometer. Hence, the contrast C is the cosine Fourier transform in time of the scattering function $S(\omega)$.

3. Experimental methods

In the course of this thesis measurements were mainly conducted at two instruments at the Heinz Maier-Leibnitz Zentrum in Garching, Germany. Modulation of intensity with zero effort (MIEZE) measurements were performed at the instrument RESEDA to investigate the critical spin fluctuations of UGe_2 in the vicinity of the Curie temperature T_C and the weak crystallisation of the skyrmion lattice in MnSi. Both materials were furthermore investigated by small angle neutron scattering (SANS) at SANS-1. SANS was also employed for the investigation of spin wave excitations driven by intense microwave radiation in the skyrmion phase of Cu_2OSeO_3. RESEDA was upgraded to improve the capability for small angle neutron scattering and a phase locking was implemented allowing to control the MIEZE phase with high accuracy. Additionally, software was developed for data analysis at RESEDA and for simulations of MIEZE measurements. Finally, ferromagnetic resonance spectroscopy (FMR) was used at the Walther-Meißner-Institut, Garching, Germany, to investigate the uniform magnetic excitations in Cu_2OSeO_3.

The chapter begins with a description of the MIEZE setup at RESEDA and the recent developments at the instrument followed by an overview of the data reduction techniques employed for MIEZE measurements. After a brief description of the instrument SANS-1, the chapter concludes with remarks on the employed FMR setup.

3.1. Modulation of intensity with zero effort at RESEDA

High-resolution MIEZE measurements were performed at the instrument RESEDA (Resonance Spin Echo for Diverse Applications) at the Heinz Maier-Leibnitz Zentrum (MLZ) in Garching, Germany [176–178]. It is located at the cold neutron guide NL5-S in the Neutron Guide Hall West and provides a longitudinal MIEZE option alongside a longitudinal NRSE option. The beamline allows to access a large range in of momentum transfers from $q \approx 0.005\,\text{Å}^{-1}$ at $\lambda = 6\,\text{Å}$ to $q = 2\,\text{Å}^{-1}$ at $\lambda = 4.5\,\text{Å}$ as well as a large range of time scales $\tau = 0.001 - 20\,\text{ns}$ at $\lambda = 10\,\text{Å}$.

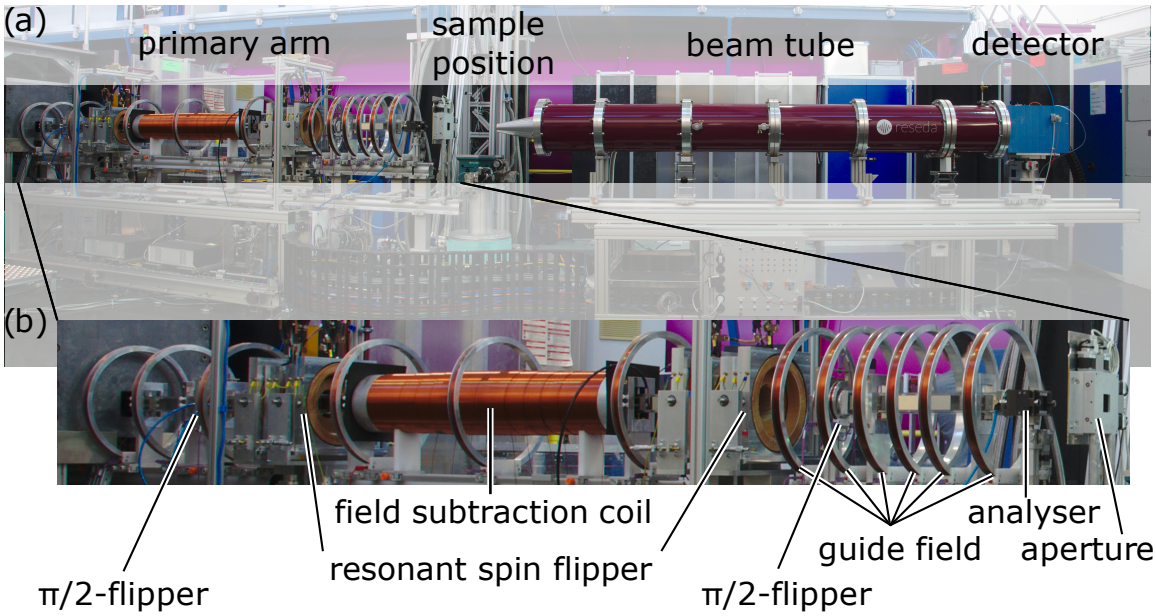

Figure 3.1.: MIEZE setup at RESEDA. (a) Neutrons enter the instrument from the left and the neutron spins are manipulated entirely in front of the sample. Upstream of the sample position an evacuated beam tube minimises background scattering before neutrons are detected on the position-sensitive detector. (b) Detailed image of the primary arm. The neutron wavelength and polarisation are defined by a selector and a polariser, respectively, upstream of the first $\pi/2$-flipper within the lead shielding. Within the precession region defined by the $\pi/2$-flippers, the neutron spin is manipulated by the rf-flippers and the field subtraction coil. The analyser in front of the sample transforms the time-dependent polarisation modulation into an intensity modulation (see text for details). Guide fields along the primary arm preserve the beam polarisation. Photographs taken in January 2019.

In 2013/14 the instrument was reconstructed from a transverse resonant spin echo beamline to a longitudinal setup introducing some major advantages. (1) In contrast to Neutron Spin Echo (NSE), the system does not need correction elements for non-divergent neutron beams to compensate depolarising effects arising from field inhomogeneity and the necessary corrections for divergent beams are smaller. (2) In a longitudinal setup guide fields can be used throughout the instrument to maintain the polarisation instead of field-free regions used in a transverse setup that are challenging to realise and (3) less material is directly in the beam minimising background scattering. (4) With a longitudinal setup field integral subtraction allows access to very small spin echo times [179].

3.1.1. MIEZE setup

A photograph of the MIEZE setup is shown in Fig. 3.1. In front of the first spectrometer arm, there is a velocity selector providing a wavelength range $\lambda = 3.5 - 15\,\text{Å}$ and a wavelength bandwidth $\Delta\lambda/\lambda = 0.09 - 0.17$ as well as a 2 m long double V-cavity as polariser, all covered by lead shielding. Within the precession region defined by the two static $\pi/2$-flippers (Mezei flippers) the two rf-flippers produce the time-dependent sinusoidal polarisation which is transformed into an intensity modulation by a bender analyser with subsequent collimator. Evacuated neutron guides ($m = 1.2$ and width $\times$ height $= 32\,\text{mm} \times 32\,\text{mm}$) on the primary spectrometer arm increase the neutron flux at the sample position. However, collimation can be employed for small angle scattering studies. Because the spin manipulation takes place in the primary spectrometer arm, there is only an evacuated beam tube and the detector downstream from the sample.

3.1.2. Improvements at RESEDA

Since the change in 2013/14 from a transverse to a longitudinal setup, RESEDA has been improved substantially via the upgrade of several instrument components, implementation of a new instrument control software, improved data reduction and analysis as well as lowering of spurious scattering and background. Contributing in these projects improving the instrument was a main part of this thesis project.

(i) Upgrade of instrumental components

The MIEZE option and its position sensitive 2D CASCADE detector, in principle, allow measurements in the SANS regime $q < 0.02\,\text{Å}^{-1}$. However, due to insufficient beam quality and too large background signals for these smallest accessible momentum transfers, this region could previously not be exploited. We therefore improved the setup in terms of beam quality and reduction of background for smallest scattering angles.

A new 2 m long double V-cavity polariser providing an increased polarisation, a cleaner beam profile, a lower background, and access to wavelengths up to 15 Å was installed. The former 5-V-cavity analyser produced a stripe like beam profile and a spurious second beam of opposite polarisation. It was replaced by a new transmission bender with subsequent collimator that improved the polarisation and the beam profile. Evacuated neutron guides of $m = 1.2$ with sapphire windows were installed in the first spectrometer arm to increase the flux at the sample position and reduce background from air scattering. Because they increase the beam divergence, motorised apertures at the entrance of the instrument and in front of the sample position were implemented to collimate the beam if necessary.

Additionally, boron carbide apertures can be installed manually at several positions in the beam path. The evacuated flight tube from sample to detector was extended with a nose suitable for the MLZ magnets to minimize the flight path through air, and thus a much lower low-q background. Over the short distance between flight tube and detector of $\approx$ 10 cm, the direct beam was previously scattered by air producing substantial background. A new segment placed in between the flight tube and the detector that is filled with Helium at atmospheric pressure eliminates this effect. Extending the evacuated flight tube further to the detector is currently not possible as the CASCADE detector window is not suitable for vacuum conditions.

Controlling the absolute phase of the MIEZE signal at the detector with high accuracy allows to (1) detect changes of the phase due to scattering processes in the sample and (2) obtain reliable fits of data even in case that either the count rate or the MIEZE contrast are low. Typical data is fitted by a cosine where the phase, amplitude and mean value are unknown. The frequency is defined by the frequencies of the resonant flippers. The data analysis will be discussed in more detail in Sec. 3.1.3. The phase of the MIEZE signal is defined by the phase between the two resonant flippers and the detector as well as the field integral produced by the guide fields and the field subtraction coil (see Eq. 2.85). To realise a high accuracy, a phase lock between the resonant spin flippers and the detector was implemented. All frequency generators use the same clock generator and run in "burst mode", i.e. a start signal defines the start of the oscillation.

A set of measurements taken with the same instrumental parameters is shown in Fig. 3.2. The MIEZE signal of UGe_2 at a momentum transfer of $q = 0.017\,\text{Å}^{-1}$ is shown for different sample temperatures as well as the resolution measurement with active coal. The detector frequency is $f = 47\,\text{kHz}$. The fitted phase is shown as a function of temperature in Fig. 3.2 (b) with the mean value of all phases as blue line and one standard deviation as blue shading. All measurements of UGe_2 have the same phase within one standard deviation whereas the resolution measurement is slightly off. The small deviation is most likely caused by the different shapes of the sample and the cuvette with the active coal. Whereas the sample is a cylinder with a length of approx. 16 mm and a diameter of 7 mm, the active coal is within a cuboid-shaped cuvette. An offset of the resolution phase has no influence on the data treatment of a quasielastic measurement if the offset is the same for all foils. Evaluation of all measured spin echo times for all momentum transfers are shown in App. A. All measurements show that reproducing the phase with high accuracy is well feasible. For higher spin echo times, i.e. detector frequencies, the signal amplitude is smaller and for larger scattering vectors the mean value is lower, hence, fits of the UGe_2 data are less reliable. A new high precision power supply for the field subtraction

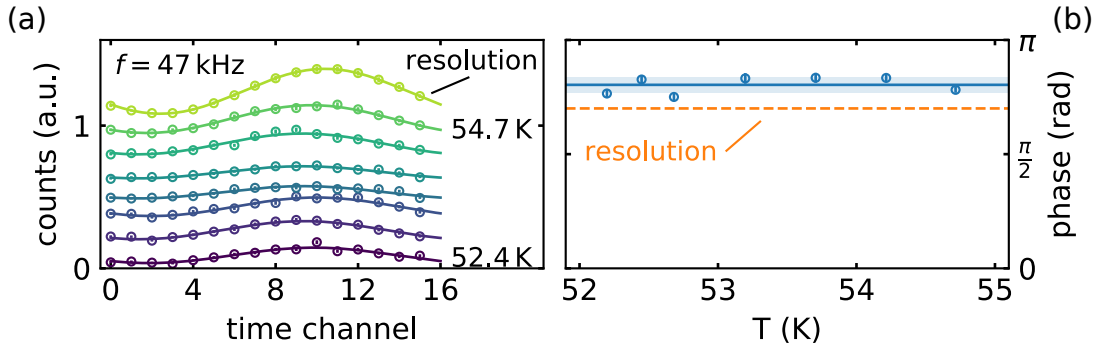

Figure 3.2.: Phase lock at RESEDA. (a) Neutron intensity as a function of time as measured in UGe_2 for several temperatures with a detector frequency of $f = 47\,\mathrm{kHz}$. The resolution was measured using active coal. The intensities are shifted for better readability. The solid line is a cosine fit with a fixed frequency. (b) The phase as a function of temperature extracted from the fits in (a). The solid line is the mean value and the shaded area denotes the error as 1σ standard deviation.

coil with one order of magnitude higher accuracy will improve the control of the MIEZE signal phase further.

(ii) Software development

The IGOR Pro instrument control software was replaced by Python based NICOS that is developed and maintained at the MLZ Garching [180][1]. With the new software the instrument is more reliable, devices are monitored permanently and data from the detector can be pulled continuously. In addition, it allows for easier control of the sample environment.

For data reduction and analysis Igor Pro was replaced by a "MIEZE analysis" package written in Python 2.7 as part of this thesis. It is open source and available on the git repository of the MLZ Garching[2]. It allows fast data reduction and signal integration over arbitrary regions of interest and all detector foils through phase correction which will be explained in more detail in Sec. 3.1.3. Every step of the data analysis can be visualised. It provides the basis for a newly developed, open source data analysis software based on Python 3 which is written and maintained by the MLZ software development group [181][3].

[1] available at https://nicos-controls.org/
[2] available at https://forge.frm2.tum.de/cgit/cgit.cgi/frm2/reseda/dataeval.git
[3] available at https://scgmlz.github.io/MIEZEPY_website/

3.1.3. Data reduction and treatment

Recording

The intensity of the neutron beam at the spin echo point is modulated in time and given by Eq. 2.97

$$I = \frac{I_0}{2}(1 + C \cdot \cos 2(\omega_\mathrm{B} - \omega_\mathrm{A})t_\mathrm{D}). \tag{3.1}$$

A time resolved detector measures the signal by binning every period of the sinusoidal intensity modulation into 16 time channels. As shown in Fig. 3.3 the contrast is extracted as

$$C = \frac{A}{M} \tag{3.2}$$

through a cosine fit where the frequency is given as $2(\omega_\mathrm{B} - \omega_\mathrm{A})$. A is the amplitude and M the mean value. The contrast is measured for several spin echo times τ. It is directly proportional to the intermediate scattering function $S(\mathrm{q}, \tau)$ through Eq. 2.99.

Normalisation and background subtraction

The measured contrast is a product of the sample contribution and the instrumental resolution

$$C_\mathrm{sample} = C_\mathrm{reso}(\boldsymbol{q}, \tau) S(\boldsymbol{q}, \tau) \tag{3.3}$$

where the instrumental resolution $C_\mathrm{reso}(\boldsymbol{q}, \tau)$ can be obtained by measuring a scatterer under the same conditions as the sample that is static on the investigated time scales. For a static scatterer the intermediate scattering function is $S(\boldsymbol{q}, \tau) = 1$ and, hence, the measured contrast reduces to

$$C = C_\mathrm{reso}(\boldsymbol{q}, \tau) \tag{3.4}$$

yielding directly the instrumental resolution. To account for the instrumental resolution, the signal is normalised with regard to $S(q, 0)$ and the normalised intermediate scattering function reads

$$\frac{S(\boldsymbol{q}, \tau)}{S(\boldsymbol{q}, 0)} = \frac{C_\mathrm{sample}}{C_\mathrm{reso}}. \tag{3.5}$$

The instrumental resolution of RESEDA is shown in Fig. 3.4 (a). It can cover six orders of magnitude in Fourier time. Depolarising effects such as beam divergence and field inhomogeneities or neutron beam polarisation smaller than 1 arising from the polarisation efficiency of the polariser and analyser lead to a reduction of the contrast. At small spin echo times τ the contrast is further reduced because the rotating wave approximation fails at small frequencies [182].

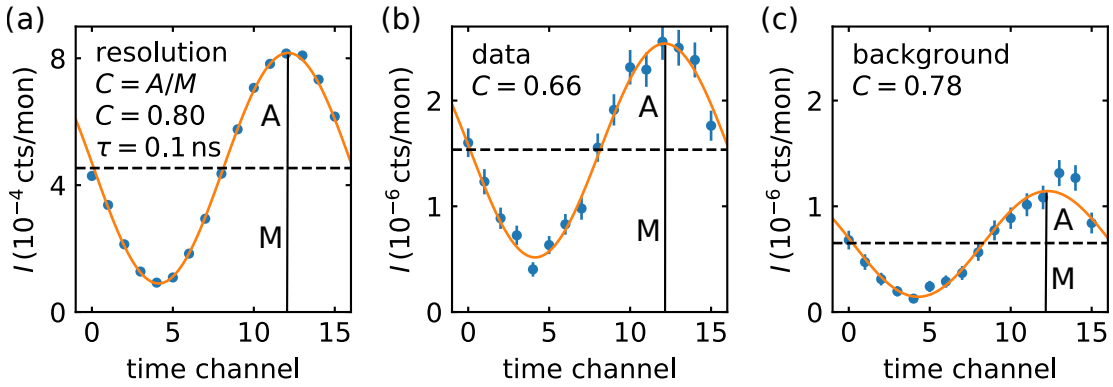

Figure 3.3.: Typical MIEZE signal. (a) Intensity as a function of time channel for (a) an elastic scatterer, (b) the sample and (c) the background at a spin echo time $\tau = 0.1\,\mathrm{ns}$ and a momentum transfer $q = 0.018\,\mathrm{Å}^{-1}$. The detector frequency is set to $2(\omega_\mathrm{B} - \omega_\mathrm{A})$ to observe one period of the sinusoidal signal. The signals are fitted with a cosine function. The extracted amplitude A and mean value M define the contrast $C = A/M$.

Depending on the investigated sample, different experimental strategies are available to define the background. For magnetic systems with a clear transition from a magnetic to a paramagnetic state such as in UGe_2 (see Ch. 4), a measurement significantly above the transition temperature T_C where magnetic fluctuations are negligible is used to determine the background. The background can be subtracted in two ways. If the phase of the MIEZE signal is known precisely for the data and the background, the raw counts of the background can be subtracted directly for each time channel. The second possibility is to first fit the data and the background independently and perform the subtraction afterwards. This is possible if the statistics of the background are sufficient for fitting. For the latter, the intermediate scattering function corrected for background is given by

$$\frac{S(\boldsymbol{q},\tau)}{S(\boldsymbol{q},0)} = \frac{(A_\mathrm{sample} - A_\mathrm{bg})/(M_\mathrm{sample} - M_\mathrm{bg})}{(A_\mathrm{reso} - A_\mathrm{bg})/(M_\mathrm{reso} - M_\mathrm{bg})} \tag{3.6}$$

where bg denotes the background parameters. Typical resolution, data, and background measurements are shown in Fig. 3.3 with the intensity I as a function of time channel. Through a cosine fit the amplitudes and mean values are extracted and the intermediate scattering function for one spin echo time τ calculated following Eq. 3.6. The end result of performing background subtraction and normalisation is shown in Fig. 3.4 (b).

Grouping pixels and multiple detector foils

At RESEDA a position-sensitive, solid state CASCADE detector [183, 184] with 128×128 pixels and a pixel size of $1.56\,\mathrm{mm} \times 1.56\,\mathrm{mm}$ allows to cover a wide range of reduced

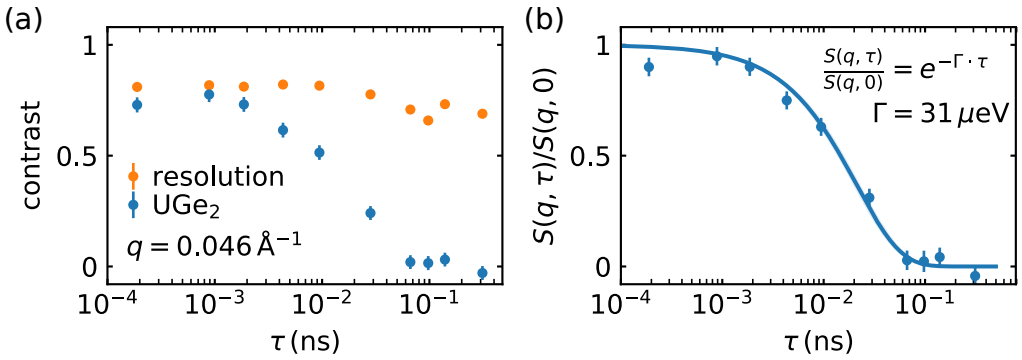

Figure 3.4.: Instrumental resolution correction of MIEZE data. (a) Contrast measured for active coal defining the instrumental resolution and for UGe_2 at the Curie temperature T_C as a function of spin echo time τ for a momentum transfer $q = 0.046\,\text{Å}^{-1}$. The background is already subtracted from the UGe_2 data set. (b) The result of the normalisation process is the normalised intermediate scattering function $S(q,\tau)/S(q,0)$. Fitting the curve with an exponential decay yields the inverse lifetime of the fluctuations Γ.

momentum transfer q. In the detector the isotope ^{10}B is used as solid neutron converter which splits up into two charged particles, an α-particle and ^{7}Li, after absorbing a neutron. Gas electron multiplier foils detect these charged particles and, hence, the neutron. To increase its efficiency, several conversion layers with subsequent read-outs are stacked. Since the count rate of a single pixel is in many cases too low, pixels and multiple detector foils must be combined to reach sufficient statistics. Hereby, two factors have to be taken into account. (1) Since the detector is flat, the time of arrival at the detector changes radially away from the direct beam and phase differences occur. (2) The spin echo point has a finite spatial width and especially for high spin echo times a non-zero contrast can only be observed on some or a single foil.

In Fig. 3.5 (a) the phase of the MIEZE signal over the whole detector is shown for the measurement of a static scatterer. If the region of interest where the signal is integrated over several pixels is chosen too large, the individual sinusoidal signals overlap destructively. With increasing spin echo time the width of regions with equal phase decreases. Because we are able to reproduce the absolute phase at the detector through the phase lock described in Sec. 3.1, we can compensate the phase differences originating from the flat detector geometry. Typically, a resolution measurement with an elastic scatterer such as active coal has sufficient statistics to fit the cosine within 4 pixels of 2×2. The extracted phase is subsequently used to shift the raw data.

As already referred to in Sec. 2.6, the spin echo point has a finite spatial width due to the finite wavelength bandwidth. Considering a wavelength distribution $f(\lambda)$ the modulated

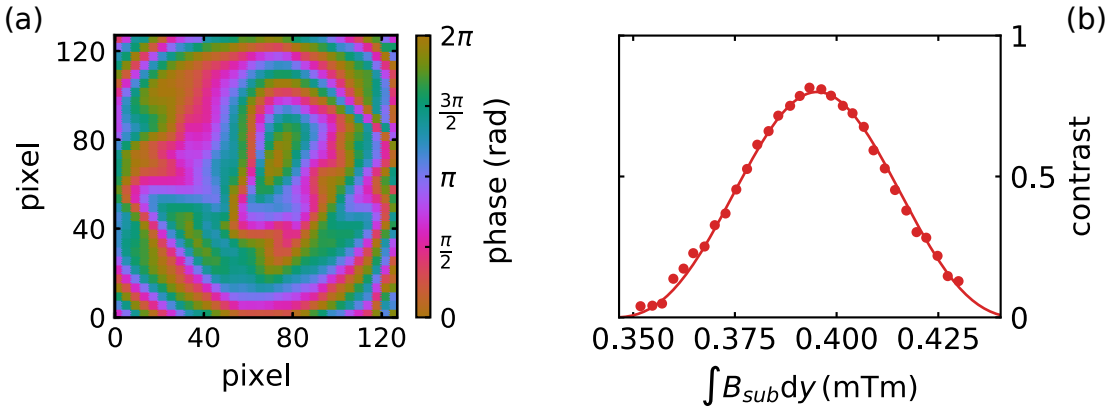

Figure 3.5.: Phase of the MIEZE signal and spin echo group width. (a) Phase of the MIEZE signal on one detector foil measured with an elastic scatterer. The phase changes radially away from the direct beam. Dents in the detector foil lead to the deviations. (b) Contrast as a function of field integral $\int B_{\mathrm{sub}}\mathrm{d}y$ in the field subtraction coil. The data is fitted by Eq. 3.8.

intensity reads

$$I = \frac{I_0}{2}\left(1 + \int \mathrm{d}\lambda f(\lambda)\cos 2(\omega_B - \omega_A)t_D \int \mathrm{d}\omega \cos(\omega\tau)S(\boldsymbol{q},\omega)\right). \tag{3.7}$$

Changing the position between the second rf-flipper and the detector, hence, the time of arrival at the detector t_{D}, the spin echo group can be recorded. Alternatively, the field integral can be altered through a frequency change of the second rf-flipper ω_{B} or a change of magnetic field in the field subtraction coil B_{sub}. At RESEDA, the last method is used since it is simple to accomplish and reliably reproducible. For a triangular wavelength distribution, as given at RESEDA, with a mean value $\bar{\lambda}$ and a FWHM of $\Delta\lambda$, the envelope function of the spin echo group reads

$$I = \frac{I_0}{2}\left(1 + \frac{4}{(\Delta\lambda)^2\alpha^2}\sin^2\left(\frac{\alpha\Delta\lambda}{2}\right)\right) \tag{3.8}$$

with $\alpha = 2(\omega_{\mathrm{B}} - \omega_{\mathrm{A}})(L_1 + L_2)/h \cdot m_{\mathrm{n}}$. The width of the spin echo group decreases with increasing detector frequency $2(\omega_{\mathrm{B}} - \omega_{\mathrm{A}})$ and wavelength bandwidth $\Delta\lambda$. A measurement of the envelope function for $\lambda = 5.918\,\text{Å}$, $\Delta\lambda = 0.117$ and $2(\omega_{\mathrm{B}} - \omega_{\mathrm{A}}) = 2\pi \cdot 20\,\mathrm{kHz}$ is shown in Fig. 3.5 (b). The data is well described by Eq. 3.8. Especially for spin echo times of some hundred picoseconds and above, the spin echo group is too narrow to be observed on all detector foils. Hence, to achieve the same statistics, longer count times are necessary.

3.1.4. Simulation

The MIEZE option at RESEDA covers a dynamic range of six orders of magnitude and is able to reach spin echo times in the picosecond regime and below. The derivation of the relation between contrast and intermediate scattering function uses the spin echo approximation, i.e. the energy change of the neutron through the scattering process should be much less than its initial energy $\Delta v \ll v$. For small spin echo times this is not valid anymore and two approaches have been developed to tackle the issue. (1) The Fourier transform is calculated explicitly by a numerical approach instead of using the simplification for the Fourier transformation in time enabled by the spin echo approximation [185]. (2) A ray-tracing simulation based on Python models the neutron path and phase through the instrument and allows to simulate the measured contrast for a given scattering function $S(q, \omega)$. The simulation code was written as part of this thesis.

In the simulation the classical description of MIEZE as given in Sec. 3.1 is used. The parameters assigned to every neutron are the initial wavelength λ_i, the time of entering the instrument t_i, and an energy transfer $\hbar\omega$ gained or lost in the scattering process. The probability distribution for the wavelength is triangular with mean value $\bar{\lambda}$ and a full-width-at-half-maximum $\Delta\lambda$. The probability distribution of the entering time is equal for all times and for the energy transfer the probability distribution is given by an arbitrary scattering function $S(q, \omega)$. The choice of parameters is not based on random numbers, but on a equally spaced grid [186]. This is in contrast to typical ray-tracing packages but avoids statistical noise that disturbs the minimisation algorithm of the fitting process and, hence, reduces computing time significantly. In addition, it became apparent that due to the simplicity of the approach and the versatility, the software is a great tool to better grasp the MIEZE option at RESEDA. In the future, more parameters as beam divergence, finite beam size, sample shape and detector efficiency will be implemented.

3.2. Small angle neutron scattering at SANS-1

SANS measurements were performed at the instrument SANS-1 at the MLZ in Garching, Germany, shown in Fig. 3.6[187]. With a collimation distance of 20 m, a sample-detector distance of 20 m and a wavelength band from 4.5 to 30 Å, length scales from 10 to 3000 Å are accessible. The instrument is ideally suited for the investigation of magnetic materials at high fields and low temperatures. A variety of different sample environments such as high magnetic fields and different cryostats are offered that are easily adjustable in position thanks to a flexible sample goniometer. The detailed adjustment of the instrument during each experiment is listed in the dedicated chapters.

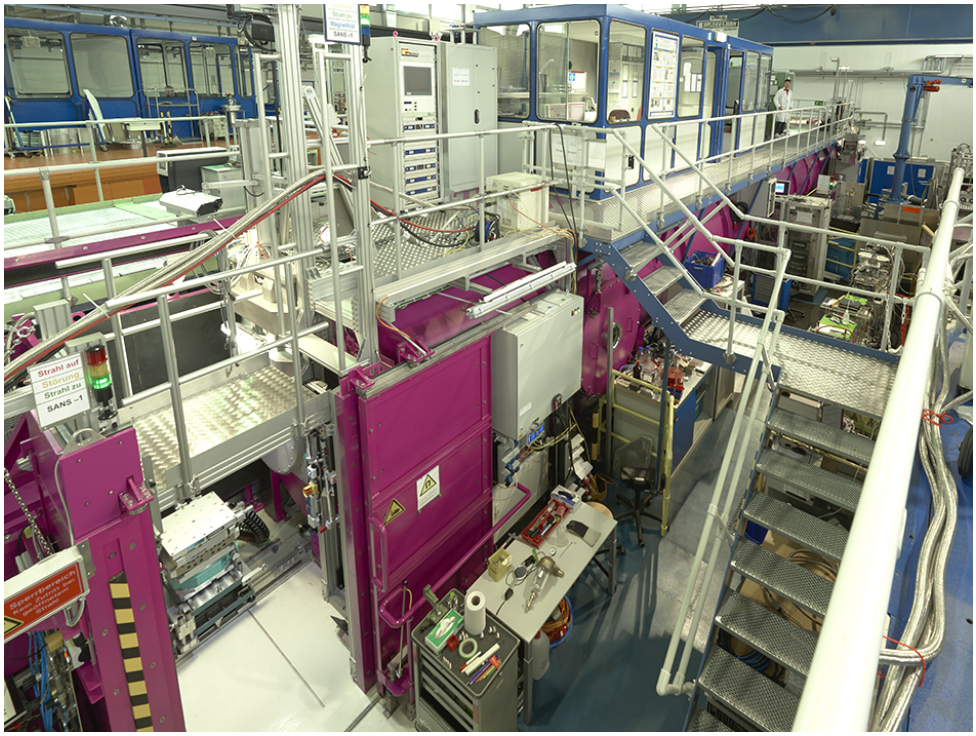

Figure 3.6.: The instrument SANS-1. On the left side is the sample table and the magenta detector tube stretches to the top right of the photograph. The collimation is not visible in the image. Photograph taken from Ref. [187]. Copyright by W. Schürmann, TUM.

3.3. Broadband ferromagnetic resonance spectroscopy

Broadband ferromagnetic resonance spectroscopy (bbFMR) is a widely used and well-established technique to probe magnetically ordered systems and their dynamics in an applied magnetic field at zero momentum transfer. In bbFMR, the linear dynamical response of the system to a small oscillating magnetic field perpendicular to a static field is measured. We performed measurements employing the vector network analyser ferromagnetic resonance (VNA-FMR) technique by means of a coplanar waveguide (CPW). The VNA allows to measure the amplitude and phase of the sample's response and the CPW allows to access a large frequency range, though, with the disadvantage of generating an inhomogeneous field. Subsequently, the FMR principles are briefly derived following Ref. [188], an overview over the VNA-FMR technique is given following Ref. [189, 190] and two procedures for data analysis are discussed.

3.3.1. Magnetic resonance spectroscopy

An externally applied magnetic field $\boldsymbol{H}$ exerts a torque on a magnetic moment $\boldsymbol{\mu}$

$$\frac{\mathrm{d}\boldsymbol{\mu}}{\mathrm{d}t} = -\gamma\mu_0\boldsymbol{\mu} \times \boldsymbol{H}. \tag{3.9}$$

leading to Larmor precession of angular frequency $\omega = \gamma\mu_0|\boldsymbol{H}|$ about the magnetic field where γ denotes the gyromagnetic ratio and μ_0 the vacuum permeability. The equation does not yet include any dissipation. In a continuum approach for a solid state material we can add up all single magnetic moments of electrons $\boldsymbol{\mu}_i$ to a macroscopic magnetisation

$$\boldsymbol{M} = \frac{1}{V}\sum_{\boldsymbol{\mu}_i \in V} \boldsymbol{\mu}_i, \tag{3.10}$$

where V is a finite volume of the sample. The precession of the magnetisation is then described by the Landau-Lifshitz-Gilbert equation

$$\frac{\mathrm{d}\boldsymbol{M}}{\mathrm{d}t} = -\gamma\boldsymbol{M} \times \mu_0\boldsymbol{H} + \frac{\alpha}{M_{\mathrm{sat}}}\boldsymbol{M} \times \frac{\mathrm{d}\boldsymbol{M}}{\mathrm{d}t} \tag{3.11}$$

with the saturation magnetisation M_{sat}. In addition, a phenomenological damping parameter α accounting for all types of losses in the system is added. The different vectors leading to the precession and damping are depicted in Fig. 3.7 (a). The relevant magnetic field is not the applied field but an effective field $\boldsymbol{H}_{\mathrm{eff}}$

$$\boldsymbol{H}_{\mathrm{eff}} = \boldsymbol{H}_0 + \boldsymbol{H}_{\mathrm{ani}} - \overleftrightarrow{N}\boldsymbol{M} \tag{3.12}$$

that takes into account magneto-crystalline anisotropy contributions $\boldsymbol{H}_{\mathrm{ani}}$ and demagnetisation effects $\overleftrightarrow{N}\boldsymbol{M}$ [191, 192]. In the Landau-Lifshitz-Gilbert equation, the magnetisation is conserved as can be seen by multiplying both sides with $\boldsymbol{M}$ which leads to $\frac{\mathrm{d}}{\mathrm{d}t}\boldsymbol{M}^2 = 0$.

In addition, a small oscillating magnetic field $\boldsymbol{h}_{\mathrm{rf}}$ ($|\boldsymbol{h}_{\mathrm{rf}}| \ll |\boldsymbol{H}|$) is applied perpendicular to the static field as depicted in Fig. 3.7 (a). The magnetisation and the magnetic field are split into a time-independent part ($\boldsymbol{M}_0$, $\boldsymbol{H}_0$) and a time-dependent part ($\boldsymbol{h}_{\mathrm{rf}}$, $\boldsymbol{m}$) where the latter is assumed to be harmonic. Solving the Landau-Lifshitz-Gilbert equation Eq. 3.11 yields

$$\begin{pmatrix} m_x \\ m_y \end{pmatrix} = \overleftrightarrow{\chi} \begin{pmatrix} h_{\mathrm{rf},x} \\ h_{\mathrm{rf},y} \end{pmatrix} \tag{3.13}$$

where $\overleftrightarrow{\chi}$ denotes the Polder susceptibility [193]

$$\overleftrightarrow{\chi} = \frac{\mu_0 M_{\mathrm{sat}}}{\mathrm{Det}(P)} \cdot \underbrace{\begin{pmatrix} H_0 + H_{\mathrm{ani}} + M_{\mathrm{sat}} \cdot (N_y - N_z) + \frac{i\omega\alpha}{\gamma\mu_0} & \frac{i\omega}{\gamma\mu_0} \\ -\frac{i\omega}{\gamma\mu_0} & H_0 + H_{\mathrm{ani}} + M_{\mathrm{sat}} \cdot (N_x - N_z) + \frac{i\omega\alpha}{\gamma\mu_0} \end{pmatrix}}_{\equiv P}. \tag{3.14}$$

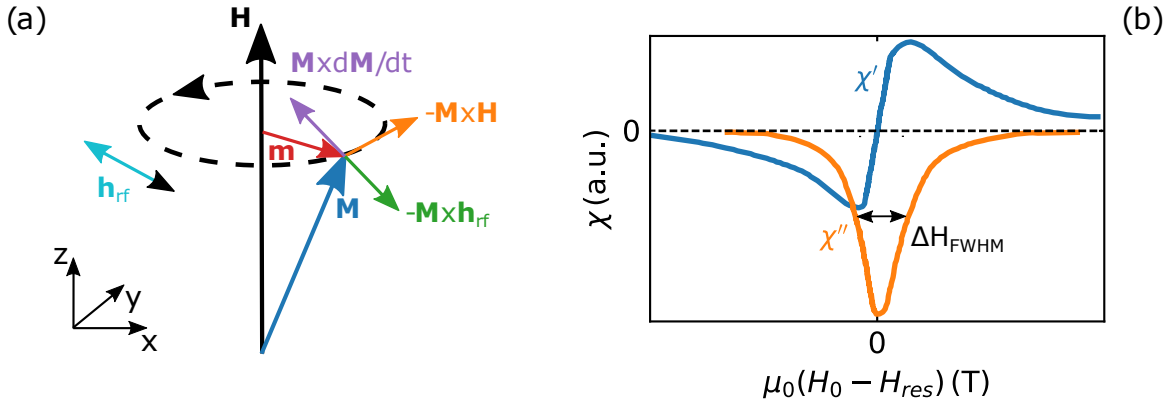

Figure 3.7.: Larmor precession and high-frequency magnetic susceptibility. (a) The torque originating from the external magnetic field $\boldsymbol{H}$ leads to a precessional motion of the magnetisation $\boldsymbol{M}$. An applied oscillating field $\boldsymbol{h}_{\mathrm{rf}}$ perpendicular to the static field $\boldsymbol{H}$ leads to a torque that opposes the damping torque $\boldsymbol{M} \times \mathrm{d}\boldsymbol{M}/\mathrm{d}t$ and drives the magnetisation out of its equilibrium. (b) The real and imaginary part of the high-frequency magnetic susceptibility as a function of magnetic field. The real part shows a zero-crossing at the resonance field H_{res} and the imaginary part a Lorentzian shape of width ΔH_{FWHM}.

The susceptibility is a tensor of second order and describes the response of the system to a small perturbation field. It can be split into a real and imaginary part $\overleftrightarrow{\chi} = \chi' + i\chi''$. Fig. 3.7 (b) displays typical field dependences of the real and imaginary part of the high frequency magnetic susceptibility χ about the resonance field H_{res}. By solving $\mathrm{Det}(\overleftrightarrow{\chi}) \stackrel{!}{=} 0$ for the real part, we can calculate the resonance condition that is given in the Kittel equation [194]

$$f = \frac{\gamma}{2\pi}\mu_0\sqrt{(H_0 + H_{\mathrm{ani}} + (N_x - N_z)\cdot M_{\mathrm{sat}})\cdot(H_0 + H_{\mathrm{ani}} + (N_y - N_z)\cdot M_{\mathrm{sat}})} \tag{3.15}$$

with the applied magnetic field H_0, the anisotropy field H_{ani}, the saturation magnetisation M_{sat} and the demagnetisation factors $N_{x,y,z}$. Solving the system of linear equations for the imaginary part, we obtain the linewidth

$$\Delta H_{\mathrm{FWHM}} = 2\frac{\alpha\omega}{\mu_0\gamma} \tag{3.16}$$

where ΔH_{FWHM} describes the FWHM linewidth as shown in Fig. 3.7 (b).

3.3.2. VNA-FMR setup by means of a coplanar waveguide

The VNA-FMR setup consists of three main components: a magnet producing a static, homogeneous magnetic field at the sample position, a CPW acting both as ac magnetic field generator and detector and a VNA [190]. In the following, the last two elements are described in more detail following Refs. [189, 190]. The setup is depicted in Fig. 3.8.

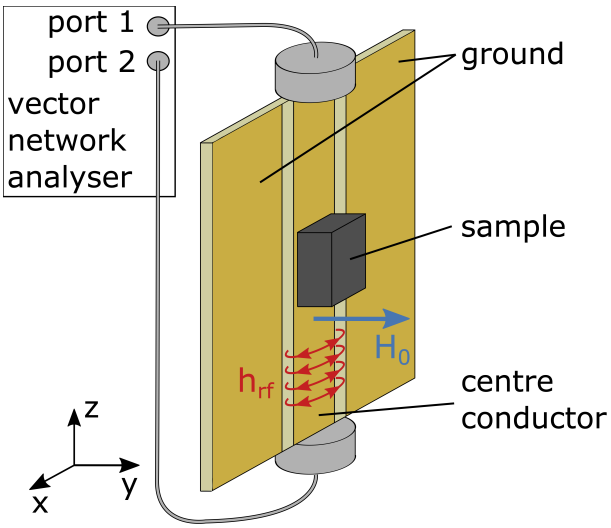

Figure 3.8.: Schematic setup of VNA-FMR. The sample is placed centred on the centre-conductor and is coupled solely inductively. The sinusoidal microwave through the centre-conductor generates an oscillating magnetic field $\boldsymbol{h}_{\mathrm{rf}}$.

The CPW consists of two electrodes on a common ground and a centre-conductor of width ω_{cc} transporting the induced microwave current that produces due to Ampere's law an elliptical, oscillating magnetic field $\boldsymbol{h}_{\mathrm{rf}}$ in the x, y-plane as shown in Fig. 3.8. The magnetic fields can be quantitatively calculated using the Karlqvist equations [195, 196]

$$h_x(x,y) = \frac{1}{\pi}\frac{I}{2\omega_{\mathrm{cc}}}\left(\arctan\left(\frac{y+\frac{\omega_{\mathrm{cc}}}{2}}{y}\right) - \arctan\left(\frac{y-\frac{\omega_{\mathrm{cc}}}{2}}{y}\right)\right) \tag{3.17}$$

$$h_y(x,y) = \frac{1}{2\pi}\frac{I}{2\omega_{\mathrm{cc}}}\ln\left(\frac{(y+\frac{\omega_{\mathrm{cc}}}{2})^2+z^2}{y-\frac{\omega_{\mathrm{cc}}}{2})^2+z^2}\right) \tag{3.18}$$

with the current I. It can be related to the applied power P by $I = \sqrt{P/Z_0}$ with the impedance Z_0. The sample is placed in the centre of the centre-conductor and is thereby inductively coupled to the CPW. Hence, the CPW detects ac magnetic flux generated by the sample. Although a cavity is advantageous as the generated ac magnetic field is homogeneous throughout the sample, it is fixed in frequency in contrast to the CPW that covers a large range of frequencies with the disadvantage of an inhomogeneous field.

A VNA fully characterises a radio frequency (rf) circuit. It generates a wave of frequency f at port 1 and measures the transmitted wave of the same frequency at port 2 that travelled through the circuit. Using the amplitude and phase of both signals, it calculates the complex $S_{i,j}$-parameters $(i, j = 1, 2)$. We measure the transmission parameter S_{21}

defined as the ratio of input voltage V_1 at port 1 and the measured voltage V_2 at port 2

$$S_{21} = \frac{V_2}{V_1} = \frac{|V_2|}{|V_1|} e^{i(\phi_2 - \phi_1)} \tag{3.19}$$

with the corresponding phases ϕ_i.

The complex transmission parameter S_{21} is composed of the transmission change ΔS_{21} originating from the sample and the frequency-dependent background $S_{21}^0(\omega)$ of the setup. Hence, the sample contribution can be written as

$$\Delta S_{21} = \frac{S_{21} - S_{21}^0(\omega)}{S_{21}^0(\omega)}. \tag{3.20}$$

The measurement system without the sample is impedance matched ($Z_0 = 50\,\Omega$). The sample placed onto the CPW introduces a complex inductance L in series. Hence, the system can be treated as a voltage divider where the change in microwave transmission yields [196]

$$\Delta S_{21} = -\frac{1}{2}\left(\frac{i\omega L}{Z_0 + i\omega L}\right) \approx \frac{-\omega L}{2Z_0} \tag{3.21}$$

with the microwave frequency ω and for $\omega L \ll Z_0$. As the voltage at port 2 is measured between the CPW signal and ground, the factor 1/2 is introduced.

The precessing magnetisation of the sample generates ac dipolar fields which leads to an inductance [190, 196]

$$\begin{aligned} L = \frac{\mu_0 l}{\omega_{\mathrm{cc}} d_{\mathrm{FM}} I^2} &\left(\int_{-\infty}^{+\infty} \mathrm{d}x \int_{\delta}^{\delta + d_{\mathrm{FM}}} \mathrm{d}y \left(\boldsymbol{q}(x,y) \overleftrightarrow{\chi}(\omega, H_0) \boldsymbol{h}_{\mathrm{rf}}(x,y,I)\right)\right) \\ &\cdot \left(\int_{-\infty}^{+\infty} \mathrm{d}x \int_{\delta}^{\delta + d_{\mathrm{FM}}} \mathrm{d}y \left(\boldsymbol{q}(x,y) \boldsymbol{h}_{\mathrm{rf}}(x,y,I)\right)\right) \end{aligned} \tag{3.22}$$

with the sample length l, the width of the centre conductor ω_{cc}, the sample thickness d_{FM} and the current I. δ denotes the finite spacing between sample and CPW and $\eta(\delta, \omega_{\mathrm{cc}}) = (2/\pi)\arctan(\omega_{\mathrm{cc}}/w\delta)$ acounts for the spacing losses which covers values from 0 to 1. $\boldsymbol{q}(x,y)$ is the normalised spatial amplitude of the FMR mode and equals 1 over the entire sample for the uniform mode. The first part of the equation describes the integrated amplitude of the mode which is excited by the driving ac magnetic field $\boldsymbol{h}_{\mathrm{rf}}$, whereas the second part comprises the CPW's inductive pickup sensitiviy. For a uniform ac magnetic field across the sample, i.e. for thin samples, and using the Karlqvist equations 3.17, Eq. 3.22 can be simplified to

$$L = \frac{\mu_0 l d_{\mathrm{FM}}}{4\omega_{\mathrm{cc}}} \chi_{xx}(\omega, H_0) \eta^2(z, \omega_{\mathrm{cc}}) \tag{3.23}$$

where the static magnetic field H_0 is applied out of plane.

Eventually, the measured VNA-FMR spectra S_{21} is related to the sample inductance and the Polder susceptibility combining Eqs. 3.20 and 3.21

$$\begin{aligned} S_{21}(\omega, H_0) &= S_{21}^0(\omega) + S_{21}^0(\omega) \cdot \Delta S_{21} = S_{21}^0(\omega) + S_{21}^0(\omega) \cdot \frac{-i\omega L_0}{2Z_0} \\ &= S_{21}^0(\omega) - S_{21}^0(\omega) \cdot \underbrace{i\,\omega \frac{1}{2Z_0} \frac{\mu_0 l d_{\mathrm{FM}}}{4\omega_{\mathrm{cc}}} \eta^2(\delta, \omega_{cc})}_{Ce^{i\phi}} \chi_{xx}(\omega, H_0) \\ &= S_{21}^0(\omega) - iCe^{i\phi}\chi_{xx}(\omega, H_0). \end{aligned} \tag{3.24}$$

The frequency-dependent parameter $S_{21}^0(\omega)$ comprises losses in the cables, connectors, endlaunches, or impedance mismatch of the CPW. Due to the finite length of the system an additional phase ϕ occurs.

3.3.3. Linear frequency sweep and FMR data reduction

The measurement protocol used throughout this study is the linear frequency sweep where the external magnetic field B is fixed, the frequency is swept and the complex transmission parameter S_{21} is thereby recorded as also described in the Master thesis by Liensberger [189]. The procedure is repeated for several magnetic fields and typical data measured on a Cu_2OSeO_3 sample as described in more detail in Sec. 6 is shown in Fig. 3.9 (a). The signal is dominated by the frequency-dependent background $S_{21}^0(\omega)$ and no resonance mode can be observed. Likewise, in a more detailed depiction in Fig. 3.9 (d) where the data is displayed as a function of frequency at a constant magnetic field B the resonance cannot be observed. Calibration of the VNA-FMR setup can remove the frequency-dependent background [197]. However, the background typically exhibits a temperature dependence and the reproducibility of the connection between endlaunches and CPW restricts this approach [198].

An alternative is the divide slice method. The signal is divided by a background measurement taken at a fixed magnetic field where no resonance modes are assumed and the signal only comprises the transmission of the VNA-FMR setup

$$S_{21}^{\mathrm{ds}}(\omega)|_{H_0} = 1 - i\frac{C}{S_{21}^0(\omega)}\chi_{xx}(\omega, H_0). \tag{3.25}$$

The real part of the resulting $S_{21}/S_{21}^{B=0\,\mathrm{mT}}$ is shown in Fig. 3.9 (b) where the Kittel mode is observed as minima for positive and negative magnetic fields. The signal is displayed for a constant magnetic field B in Fig.3.9 (e). It shows the same behaviour as the magnetic susceptibility in Fig. 3.7 (b) but the real and imaginary part are exchanged due to the multiplication with the complex number i in Eq. 3.25. The real part exhibits a Lorentzian

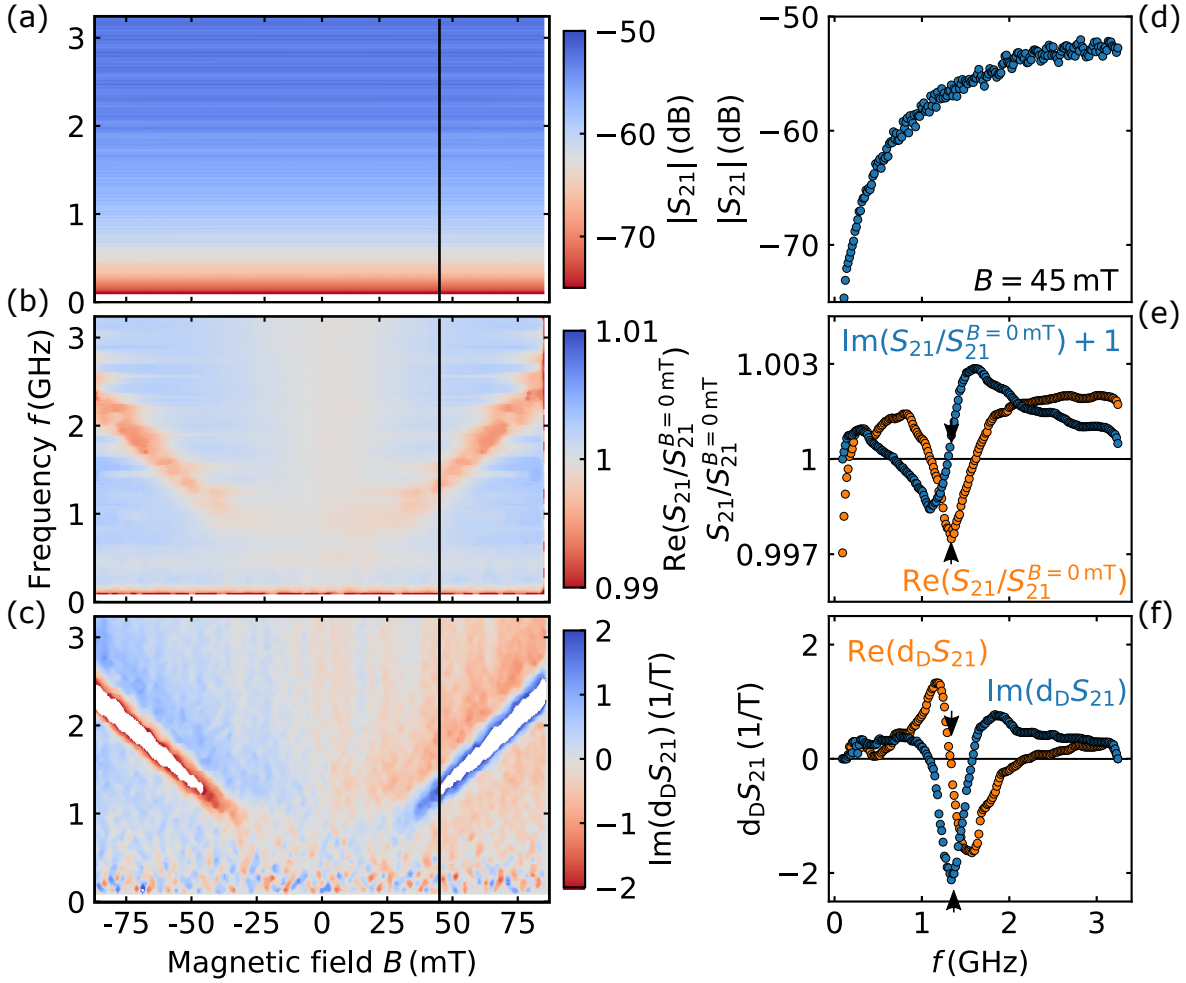

Figure 3.9.: Typical data of the complex transmission parameter S_{21} recorded with the VNA-FMR setup. (a) Frequency and field dependences of the complex transmission parameter S_{21}. The response of the sample is not observable as the signal is dominated by the transmission of the setup. (b) Divide slice of the real part of the transmission parameter S_{21} where the resonances appear as minima. The data is normalised to the measurement at $B = 0\,\mathrm{mT}$. (c) Imaginary part of the derivative divide of the transmission parameter S_{21}. The resonances appear as maxima or minima depending on their field dependence. (d) Cut at constant magnetic field through (a) where no sample signal is distinguishable. (e), (f) Real and imaginary part of the divide slice and derivative divide of S_{21}, respectively, at a constant magnetic field. Black markers denote the resonance.

shape with its minimum at the resonance frequency. The imaginary part shows a minimum, a subsequent zero-crossing and a maximum before decaying to zero again. The zero-crossing coincides with the resonance frequency.

Another possibility to eliminate the frequency-dependent background is the so-called derivative divide method which is denoted as $\mathrm{d_D}$ [198]. Here, the symmetric difference quotient of S_{21} with respect to H_0 is calculated

$$\begin{aligned} \mathrm{d_D}S_{21} &= \frac{S_{21}(\omega, H_0 + \Delta H_{\mathrm{mod}}) - S_{21}(\omega, H_0 - \Delta H_{\mathrm{mod}})}{S_{21}(\omega, H_0 \Delta H_{\mathrm{mod}})} \\ &\approx -i\omega A \frac{\chi(\omega, H_0 + \Delta H_{\mathrm{mod}}) - \chi(\omega, H_0 - \Delta H_{\mathrm{mod}})}{\Delta H_{\mathrm{mod}}} \\ &= -i\omega A \frac{\mathrm{d}\chi}{\mathrm{d}H_0} = -i\omega A \frac{\mathrm{d}\chi}{\mathrm{d}\omega}\frac{\partial\omega}{\partial H_0} = -i\omega A' \frac{\mathrm{d}\chi}{\mathrm{d}\omega} \end{aligned} \tag{3.26}$$

where ΔH_{mod} is a finite step width. The derivative divide $\mathrm{d_D}S_{21}$ is proportional to the derivative of the susceptibility with respect to the external field to second order in the amplitude A. χ varies smoothly as a function of magnetic field and frequency for small field steps and, hence, $\frac{\mathrm{d}\chi}{\mathrm{d}H} \propto \frac{\mathrm{d}\chi}{\mathrm{d}\omega}$ and $\frac{\partial\omega}{\partial H}$ adds only a real-valued factor that is comprised in $A \to A'$. Dividing by $S_{21}(\omega, H_0)$ eliminates the frequency-dependent background $S_{21}^0(\omega)$ and the associated phase shift ϕ.

Finally for a quantitative analysis, the distortion of the signal due to the finite modulation amplitude $\Delta\omega_{\mathrm{mod}}$ has to be considered. Hereby, the central difference quotient is numerically calculated and fitted instead of $\frac{\mathrm{d}\chi}{\mathrm{d}\omega}$

$$\mathrm{d_D}S_{21} = -i\omega A' \frac{\chi(\omega + \Delta\omega_{\mathrm{mod}}) - \chi(\omega - \Delta\omega_{\mathrm{mod}})}{2\Delta\omega_{\mathrm{mod}}}. \tag{3.27}$$

The modulation amplitude is known as $\Delta\omega_{\mathrm{mod}} = \Delta H_{\mathrm{mod}} \frac{\partial\omega}{\partial H_0} \approx \Delta H_{\mathrm{mod}} \gamma\mu_0$. Notably, the analysis takes place in the frequency space.

Typical data is displayed in Fig. 3.9 (c). The resonance modes are readily distinguishable as minima and maxima in the frequency- and field-dependent imaginary part of $\mathrm{d_D}S_{21}$. The signal as a function of frequency at a constant magnetic field is shown in Fig. 3.9 (f). Interestingly, the dispersion of the resonance determines the sign of the Lorentzian in the imaginary part as well as the direction of the zero-crossing in the real part. Vice versa, the sign of the two signals contain the information about the field dependence of the resonance.

4. Magnetic fluctuations in the ferromagnetic superconductor UGe_2

Several materials such as $ErRh_4B_4$ and $HoMo_6S_8$ are known where superconductivity and ferromagnetism coexist [40]. Though, in these compounds the coexistence is macroscopic. UGe_2 is among the few known systems where the coexistence of bulk superconductivity and ferromagnetism is microscopic [37, 52]. In UGe_2 superconductivity emerges in the vicinity of two quantum phase transitions under hydrostatic pressure and the superconducting dome lies entirely within the ferromagnetic phase. Superconductivity mediated by Cooper pairs that form spin singlets is incompatible with ferromagnetism because the associated large internal magnetic fields break the anti-parallel pairing of the electron spins and result in the destruction of superconductivity. Therefore, it is proposed that the spins pair in a parallel configuration rather than an anti-parallel alignment and the superconductivity is mediated by magnetic fluctuations instead of phonons. Interestingly, the transition temperature T_{SC} has its maximum at the transition between the low momentum ferromagnetic phase FM1 and the high momentum phase FM2 suggesting a close connection between the transition and superconductivity. Hence, the question arises, what role the corresponding magnetic fluctuations play in the emergence of superconductivity and if they are strong enough as the transition is of first-order.

Due to the required energy resolution of $\ll 1\,\mathrm{meV}$, neutron scattering remains the only technique to study the momentum dependence of critical magnetic fluctuations near phase transitions despite recent progress in resonant x-ray scattering techniques. Note that local probes such as NMR, NQR, and μSR are not able to reveal the momentum dependence. However, neutron triple axis spectroscopy (TAS) measurements performed on UGe_2 show ambiguous results even at ambient pressure [53]. Hence, we employed the newly developed longitudinal modulation of intensity with zero effort (MIEZE) technique exceeding previous studies in terms of energy resolution by at least one order of magnitude and by a factor of two in momentum transfer resolution. We determined the critical exponents at the paramagnetic to ferromagnetic phase transition that perfectly match a three-dimensional (3d) Ising ferromagnet. In addition, we observe a change from localised to itinerant character of the magnetic fluctuations on a length scale comparable to the

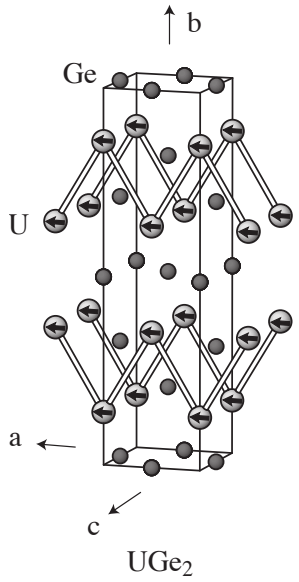

Figure 4.1.: Crystal structure of UGe_2. The uranium atoms form zig-zag chains along the a-axis and the magnetic moments are ordered along the easy a-axis. Figure taken from Ref. [205].

superconducting coherence length. This study, thus, paves the way for future high resolution measurements of magnetic fluctuations at quantum phase transitions of ferromagnets and antiferromagnets and, especially, future studies on UGe_2 under hydrostatic pressure.

Results of the presented work were published in Ref. [199], on which this chapter is based. The chapter is organised in the following way. At first, we give an introduction into the properties of UGe_2 and previous results on magnetic fluctuations in the system. The sample preparation and experimental setup are explained before we present results of our elastic and quasielastic measurements. The chapter concludes with a discussion and outlook.

4.1. The superconducting ferromagnet UGe_2

Following Ref. [37], we briefly summarise the main properties of UGe_2. The superconducting ferromagnet UGe_2 crystallises in the orthorhombic crystal structure *Cmmm* (space group 65) with lattice constants $a = 3.997(3)$ Å, $b = 15.039(7)$ Å, and $c = 4.087(2)$ Å [200, 201]. The crystal structure is shown in Fig. 4.1. It exhibits zigzag chains of U atoms along the a-axis with a spacing between U atoms of $d_{\mathrm{U-U}} = 3.85$ Å, which is above the Hill limit, in turn, suggesting that the f-electrons are predominantly localised [202]. The U chains form sheets stacked along the b-axis with alternating layers of Ge. This two-dimensional appearance manifests itself in the electronic structure with a large cylindrical Fermi surface sheet along the b-axis [203, 204].

At ambient pressure UGe_2 displays ferromagnetism below a Curie temperature of $T_C = 53\,K$ and an ordered moment of $\mu_{FM1} = 1.2\,\mu_B$ [37, 52]. The magnetically hard b- and c-axis exhibit large magnetic anisotropy fields compared to the easy a-axis ($\sim 100\,T$ for the c-axis) [206]. Due to the magnetic anisotropy, the magnetic properties have a strong Ising character, as indicated, for instance, by the temperature dependence of the ordered moment just below T_C, which varies as $M(T) \propto (T - T_C)^\beta$ with $\beta = 0.33$ close to the calculated value $\beta = 0.36$ of a 3d Ising ferromagnet [207, 208]. At $T_x \approx 25\,K$ a crossover into a second ferromagnetic phase (FM2) occurs, which is characterised by a larger ordered magnetic moment $\mu_{FM2} = 1.5\,\mu_B$. The crossover manifests itself in the resistivity via a broad maximum in $d\rho/dT$ [209], a pronounced minimum in the normal Hall effect [210], and in a minimum in the a-axis thermal expansion [211]. Furthermore, the T_x transition appears in the thermal conductivity [212] and in the specific heat [207].

Clear evidence for partially delocalised $5f$ electrons in UGe_2 is provided by the Curie-Weiss moment $\mu_{CW} = 2.7\,\mu_B$, which exceeds the zero-temperature ordered moment $\mu_{FM2} = 1.5\,\mu_B$ considerably. Moreover, in de Haas–van Alphen (dHvA) measurements carriers with cyclotron masses of 15 - $25\,m_0$ were observed [213]. For fully localised $5f$ electrons such large mass enhancements are not expected suggesting $5f$ electrons that hybridise with the conduction electrons [206]. However, UGe_2 is not as strongly correlated as conventional heavy-fermion U compounds as suggested by a specific heat coefficient $C(T)/T = \gamma \approx 35\,mJ\,K^{-2}\,mol^{-1}$ [206] that is about one order of magnitude smaller [204]. Band structure calculations based on more recent dHvA results show dominant f electron contributions at the Fermi level [203, 204, 214]. The magnetic form factor is equally well accounted for by a U^{3+} or U^{4+} configuration, respectively, as determined by polarised neutron scattering [208]. The ratio of orbital to spin magnetic moment R does not change substantially between the paramagnetic and ferromagnetic phase. The contribution of the conduction electrons to the total magnetic moment below T_C is less than 3 % again supporting that UGe_2 is not as strongly correlated. Altogether, the free-ion value is reduced for both configurations in the paramagnetic as well as the ferromagnetic phase suggesting a delocalisation of the $5f$ electrons. Finally, UGe_2 is a good electrical conductor with residual resistivities well below $1\,\mu\Omega m$, characteristic of itinerant ferromagnetism.

Unpolarised neutron diffraction determined the magnetic order to be strictly ferromagnetic with moments aligned along the a-axis and no evidence for a modulated component in the magnetic structure [208]. The strict alignment along the a-axis is also confirmed by neutron depolarisation measurements down to 4.2 K which additionally found a typical domain size in the b-c-plane of the order $4 - 5\,\mu m$ [215]. In contrast, earlier reports of macroscopic quantum tunneling of the magnetisation below 1 K suggest a domain size of only $\sim 40\,Å$ [216, 217].

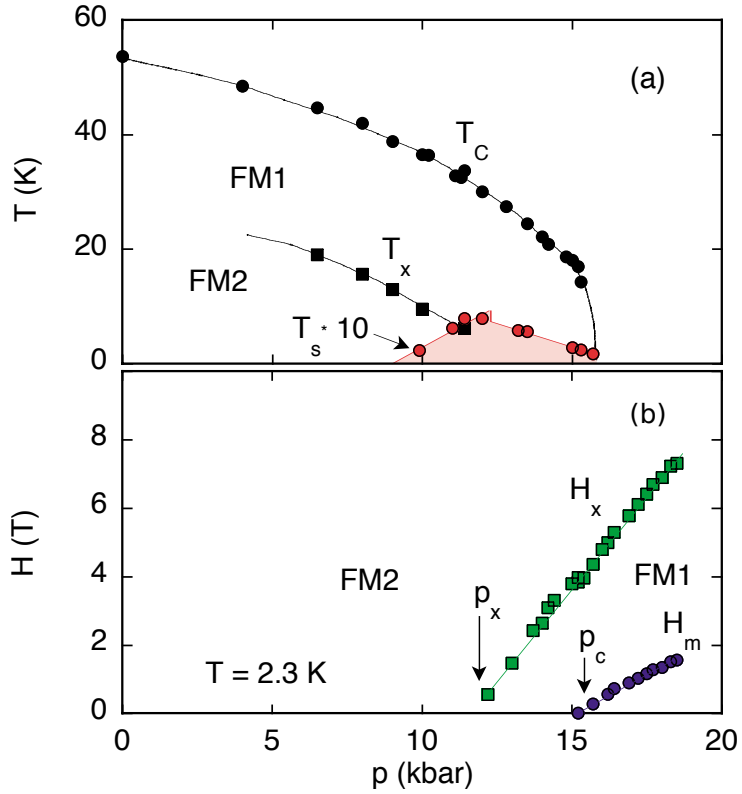

Figure 4.2.: Ferromagnetism and superconductivity in UGe_2. (a) The temperature vs. pressure phase diagram. T_C describes the transition from the paramagnetic to the ferromagnetic phase FM1 and T_x the transition between the ferromagnetic phases FM1 and FM2 (see text for details). T_S denotes the superconducting transition temperature. (b) Magnetic field vs. pressure phase diagram of UGe_2 at a temperature $T = 2.3\,\mathrm{K}$. H_x and H_m denote the metamagnetic transition where dM/dH exhibits a local maximum. Lines are guides to the eye. Figure taken from Ref. [218].

Under increasing pressure the Curie temperature T_C is suppressed monotonically and collapses at a critical pressure of $p_c \approx 15.8\,\mathrm{kbar}$ as shown in Fig. 4.2 (a). The transition changes from second- to first-order at a tricritical point $H = 0$, $T_{TCP} = 24\,\mathrm{K}$, $p_{TCP} = 14.2\,\mathrm{kbar}$ [219–221]. The shape of the phase diagram as well as the change from a second- to a first-order phase transition agree well with the mean-field Belitz-Kirkpatrick-Vojta (BKV) theory for clean itinerant ferromagnets which predicts a fluctuation-induced first-order transition at low temperatures as the magnetisation couples to electronic soft modes [34, 222]. Here, a discontinuous drop in the magnetisation confirms the first-order character at p_c [218]. A discontinuous change in the spin-lattice relaxation rate $1/T_1T$ [223] and dHvA studies [214] confirm the first-order transition at p_c. The broad anomaly at T_x is also suppressed under pressure and vanishes at $p_x \approx 12.2\,\mathrm{kbar}$ [207, 209, 224, 225]. In the magnetisation a broad hump emerges at T_x which with increasing pressure turns

into a sharp ferromagnetic phase transition near p_x as shown in Fig. 4.3 [207, 218, 226]. The crossover and the first-order phase transition are separated by a critical end-point at $H = 0$, $T^x_{CEP} \approx 7\,K$ and $p^x_{CEP} = 11.6\,kbar$ [221].

Detailed dHvA measurements with field along the crystallographic b-axis reveal a change of the Fermi surface when p_x and p_c, respectively, are crossed [214, 227]. In the high moment phase FM2 three fundamental frequencies (α, β, γ) are observed which are weakly pressure dependent. Crossing p_x into the low moment phase FM1, the α and γ branches vanish, the signal of the β branch decreases substantially and a new δ branch similar to the β branch emerges. Assuming that the Fermi surface volume remains unchanged through p_x, the δ branch can be understood as a result of the shrinking and breaking up of the γ hole surface. The spectra above p_c differs completely as it consists of four new branches which are not connected in any obvious manner with the spectra in the ferromagnetic phases suggesting a complete reconstruction of the Fermi surface. The abrupt change in the frequencies at p_c indicates a first-order character of the reconstruction.

For pressures above p_x and p_c, UGe_2 exhibits metamagnetic behaviour if a field is applied along the a-axis. Above p_x the full ordered moment is restored above a transition field H_x as shown in Fig. 4.2 (b) and for pressures exceeding p_c the system first reenters the FM1 phase at a field H_m followed by the recovery of the full magnetic moment at H_x [218]. The transition field H_m terminates at a quantum critical endpoint at $p_{QCEP} \approx 35\,kbar$ and $H_{QCEP} \approx 18\,T$ [219, 228]. The metamagnetic behaviour above p_x indicates additionally the first-order character of the transition between the ferromagnetic phases [218]. The behaviour under a small applied magnetic field again agrees well with the BKV theory that ascribes the field dependence of the phase diagram directly to the existence of the tricritical point and predicts the quantum critical behaviour in zero field [229]. Note, Sandeman *et al.* proposed a mean-field Stoner model where the majority spin Fermi level is driven through one of two peaks in the paramagnetic density of states to explain the phase diagram [230].

Finally, resistivity and ac susceptibility measurements reveal superconductivity emerging in a pressure range between $p \approx 9\,kbar$ and p_c as shown in Fig. 4.2 (a) [52, 207]. As a function of pressure the transition temperature T_{SC} increases below p_x and decreases towards p_c with a possible discontinuity at p_x. Neutron scattering experiments confirm the coexistence of FM and SC [231]. Bulk superconductivity can be inferred from the magnetic field dependence of the flux flow resistance [207] and a small yet distinct anomaly in the specific heat [226]. However, the specific heat suggests that bulk superconductivity exists only in a narrow range surrounding p_x [225].

The microscopic coexistence of FM and SC renders UGe_2 a candidate for unconventional spin-triplet superconductivity supported by several other properties: (i) The su-

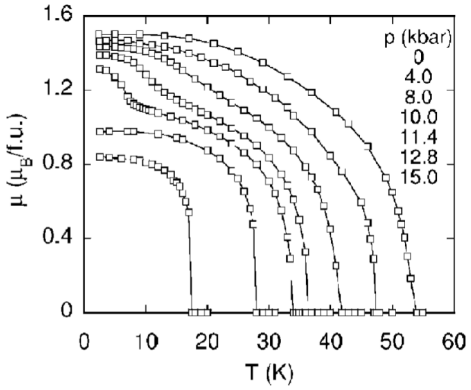

Figure 4.3.: The ordered ferromagnetic moment as a function of temperature for various pressures. The curves correspond from top to bottom to increasing pressures shown in the top right corner. The phase transition at T_{C} changes from second- to first-order at pressures close to p_{c}. Under pressure an additional transition at $T_{\mathrm{x}} < T_{\mathrm{C}}$ appears which becomes more pronounced under pressure and is suppressed at p_{x}. Figure taken from Ref. [218].

perconducting state is highly sensitive to impurities [232]. (ii) The superconductivity is extremely fragile with a critical current density $j_{\mathrm{c}} \approx 0.1\,\mathrm{A/cm^2}$, which is between one to two orders of magnitude smaller than for other heavy-fermion systems like UPt_3 and even three orders of magnitude lower than for conventional superconductors [207]. (iii) The combination of a superconducting transition temperature T_{SC} which is always at least two orders of magnitude smaller than T_{C} and the absence of superconductivity above p_{c} which is in contrast to the standard quantum critical point (QCP) scenario points to FM order being rather a precondition for SC than a competing order. (iv) The critical field H_{c2} exceeds conventional paramagnetic and orbital limits for weak s-wave SC pairing [233].

The confinement of the SC within the FM phase has attracted great scientific interest and a large number of mechanisms could be identified that promote superconductivity in a FM phase. These encompass special features of the density of states [230], the coupling of spin- and charge-density-wave order [234], magnon exchange [235], and the enhancement of longitudinal, pair-forming spin fluctuations in the ferromagnetic state [236]. As T_{SC} is largest close to p_{x}, the fluctuations associated with the critical endpoint of the T_{x} transition might indeed cause the emergence of superconductivity. In the following, we want to summarise the studies on the magnetic fluctuations in UGe_2 at ambient pressure and under pressure.

4.2. Magnetic fluctuations in UGe_2

Data on magnetic fluctuations in UGe_2 by means of TAS [53, 237] and μSR [238] have been reported.

Huxley *et al.* performed TAS measurements investigating the critical magnetic fluctuations at ambient pressure for a large temperature range from 25 to 70 K [53]. The measurements were performed near the (001) reciprocal lattice point with an energy resolution $\Delta E = 0.1\,\mathrm{meV}$ and a minimum momentum transfer of approximately $q = 0.03\,\mathrm{\AA}^{-1}$. They found critical exponents which are asymmetric about T_C corresponding to a 3d Ising ferromagnet below T_C and a mean-field transition above. Their main finding is that the magnetic fluctuation energy $\Gamma_\mathbf{q}$ shown in Fig. 4.4 (a) does not vanish for $q \to 0$ and even at T_C, which is characteristic of a first-order transition. This is in stark contrast with conventional thermally-driven FM phase transitions. Notably, the latter is a stereotypical example of a second-order phase transition. In addition, the product $\chi(\mathbf{q})\Gamma_\mathbf{q} = (2/\pi)v_\mathrm{F}\chi_\mathrm{p}q$ given by the Lindhard dependence where χ_p is the noninteracting Pauli susceptibility and v_F the Fermi velocity shows a weak q-dependence but remains finite for $q \to 0$ as shown in Fig. 4.4 (c). Due to the finite value of $\chi(\mathbf{q})\Gamma_\mathbf{q}$, they conclude that the average magnetisation density is not conserved which is not expected for a classical para- to ferromagnetic phase transition. They argue that strong spin-orbit interactions of the f electrons give rise to these non-spin-conserving terms.

Kepa *et al.* [237] performed TAS measurements on UGe_2 under hydrostatic pressure up to $p = 11.8\,\mathrm{kbar}$. Their main results are shown in Fig. 4.5. Following the temperature dependence of the integrated neutron intensity of the magnetic (001) Bragg peak, the PM-FM1 transition at T_C and the FM1-FM2 transition at T_x can be observed because the intensity is proportional to the squared magnetisation. They measured the magnetic fluctuations with an energy of $E = 0.15\,\mathrm{meV}$ and $E = 0.25\,\mathrm{meV}$, respectively, and see an increase of fluctuations at T_C corresponding to the second-order PM-FM1 phase transition, but no significant fluctuations can be observed at T_x. However, muon spin rotation measurements [239] suggest that the transition at T_x is caused by the conduction electrons which cannot be detected by a standard TAS setup since their signal is suppressed by the magnetic form factor.

As we discuss in Sec. 4.4, we overcome the limits of the TAS technique in terms of energy and momentum transfer resolution by employing MIEZE. We reveal purely longitudinal spin fluctuations in UGe_2 at ambient pressure with a dual nature arising from $5f$ electrons that are hybridised with the conduction electrons. Local spin fluctuations are perfectly described by the Ising universality class in three dimensions. In contrast to TAS, the SANS configuration of MIEZE allows us to observe itinerant spin fluctuations relevant for

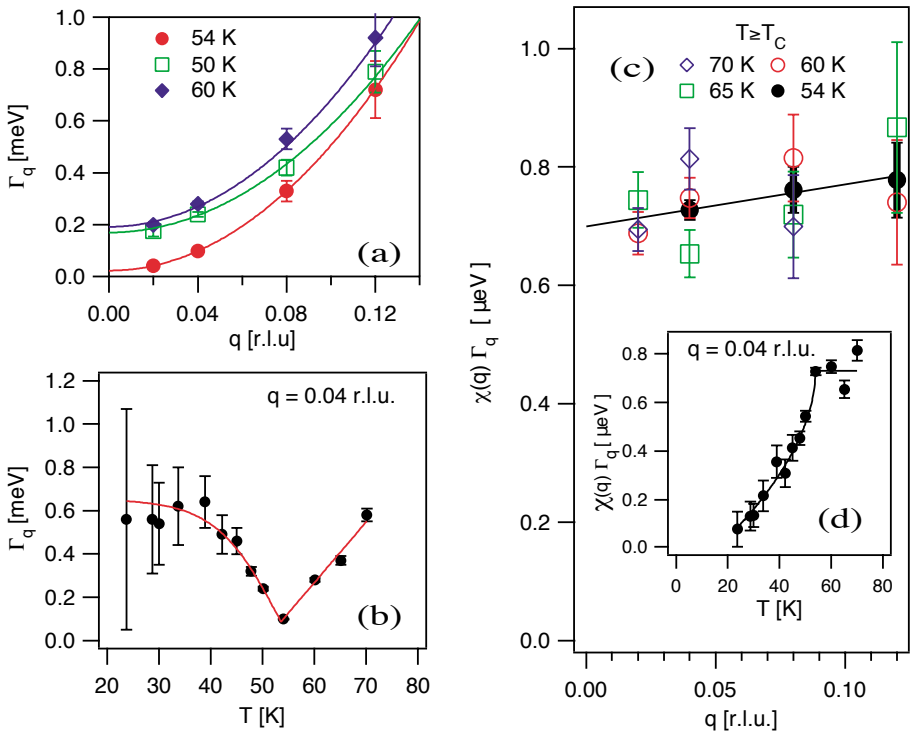

Figure 4.4.: Temperature and q-dependence of magnetic fluctuations measured by means of TAS in UGe_2. (a) The fluctuation energy Γ_q as a function of the momentum transfer q for temperatures above and below T_C. Γ_q does not vanish for $q \to 0$ away from T_C. (b) The temperature T-dependence of the magnetic fluctuation energy Γ_q at a finite momentum transfer q. (c) The product $\chi(q)\Gamma_q$ as a function of momentum transfer q for various temperatures exhibit only a slight q-dependence. The inset shows the temperature dependence of the product. All solid lines are guides to the eye. Figure taken from Ref. [53].

p-wave pairing occuring over length scales comparable to the superconducting coherence length.

4.3. Experimental methods

4.3.1. Sample preparation and characterisation

We employed a high-quality single crystal sample of UGe_2. It was grown in the desired crystal orientation by the Czochralski technique using an oriented seed crystal with subsequent annealing similar to Ref. [240]. A part of this thesis project was a stay at the Los Alamos National Lab, New Mexico, USA, assisting in growing the crystals. For the neutron scattering experiments a cylinder with an almost constant diameter of 7 mm and a length of 16 mm ($m = 6$ g) was cut with the crystallographic c-axis approximately along

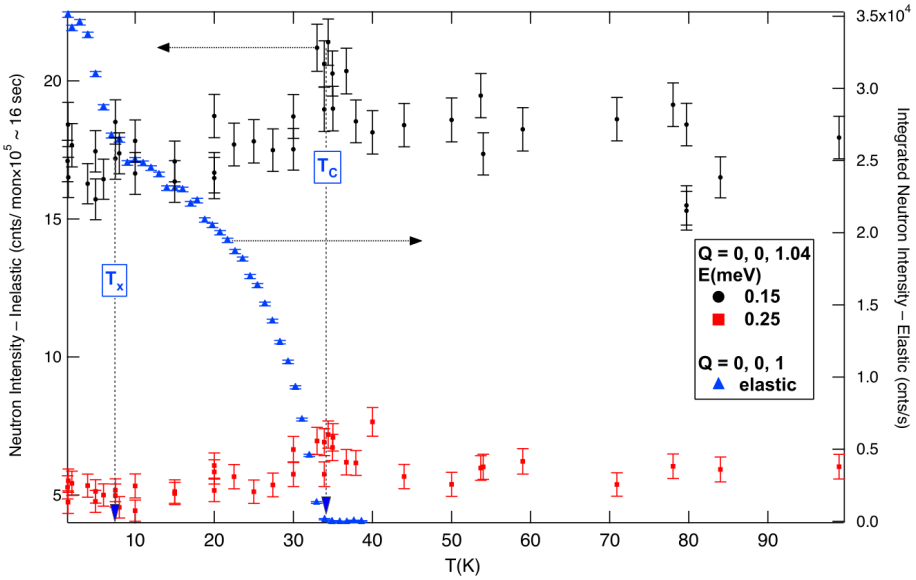

Figure 4.5.: Magnetic fluctuations in UGe_2 under pressure. The right axis shows the temperature dependence of the elastic neutron scattering intensity of the magnetic (001) Bragg reflection which is proportional to the square of the magnetisation. The sample is under a pressure of $p = 11.8\,\mathrm{kbar}$. The transitions at T_C and T_x are marked with dashed lines. The left axis shows the temperature dependence of the inelastic scattering signal for an energy transfer of $\Delta E = 0.15\,\mathrm{meV}$ and $\Delta E = 0.25\,\mathrm{meV}$, respectively. Figure taken from Ref. [237].

the cylinder axis (see Fig. 4.6 (a)). X-ray Laue diffraction was used to prealign the sample on the sample holder shown in Fig 4.6 (b) with the c-axis in vertical direction.

Using the neutron Laue diffraction technique at the nLaue instrument at the MLZ, the sample was oriented precisely. At the instrument a white beam is employed and a sapphire filter is positioned in the shielding to prevent background from fast neutrons and gamma radiation. This results in a neutron wavelength spectrum ranging from 0.8 to 4 Å. The experiments were carried out in a backscattering geometry. The Laue diffraction image in Fig. 4.6 (c) shows the orientation of the sample with the b-axis approximately parallel to the incident neutron beam. In addition, the measurements confirm that the sample consists of a single grain.

Neutron depolarisation imaging (NDI) was employed at the instrument ANTARES at the MLZ Garching to confirm the magnetic homogeneity, which is critical for the determination of critical exponents. The results in Fig. 4.7 confirm the homogeneity with a Curie temperature $T_\mathrm{C} = 52.68 \pm 0.03\,\mathrm{K}$. The NDI technique uses a neutron polarisation analysis setup on a neutron imaging beam line with a position sensitive detector. For a ferromagnet cooled below the Curie temperature components of the neutron beam polarisation perpendicular to the magnetisation start to precess leading to a partial depolarisation of

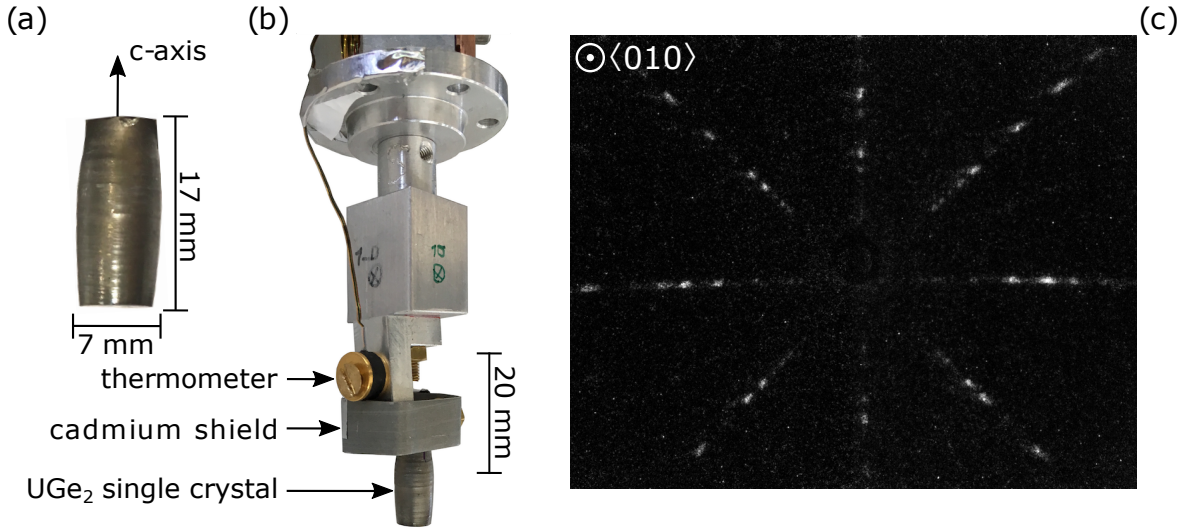

Figure 4.6.: UGe_2 single crystal and its neutron Laue diffraction image. (a) A UGe_2 single crystal was grown by the Czochralski method and a cylinder shaped piece cut out with a length of 17 mm and a diameter of 7 mm. (b) The UGe_2 sample attached to the sample holder is shown as used at RESEDA and SANS-1 with a Cernox thermometer and a cadmium aperture to minimise background scattering. (c) Neutron Laue diffraction imaging confirms that this sample is a high-quality single-grain crystal. The crystallographic b-axis is approximately parallel to the neutron beam.

the beam. In turn, the temperature dependence of the depolarisation, hence the Curie temperature T_C, can be resolved spatially. Details about the NDI setup are described in Ref. [241] and, in particular, for this experiment in the appendix of Ref. [199]. Fig. 4.7 (a) shows the spatial distribution of the Curie temperature T_C and Fig. 4.7 (b) the variation of the Curie temperature ΔT_C. The histogram in Fig. 4.7 (c) combines the data in Fig. 4.7 (a) and reveals the temperature dependence of the probability of the Curie temperature. The small standard deviation demonstrates that this sample is optimal for investigations of critical spin fluctuations.

4.3.2. Setup at RESEDA

Neutron spin-echo measurements using the MIEZE option (see Sec. 3.1) were performed at the instrument RESEDA in September 2017. The instrument parameters are shown in Tab. 4.1. We used neutrons with a wavelength of $\lambda = 5.918\,\text{Å}$ to cover a momentum transfer range from $0.015 \leq q \leq 0.083\,\text{Å}$ with sufficient neutron flux. The $\boldsymbol{q}$ resolution is mainly defined by the source aperture positioned between the two resonant flippers and the defining aperture installed directly in front of the sample. It can be calculated as described in Sec. 2.5. In vertical direction the resolution is $\Delta q_y = 0.003\,\text{Å}^{-1}$ and remains

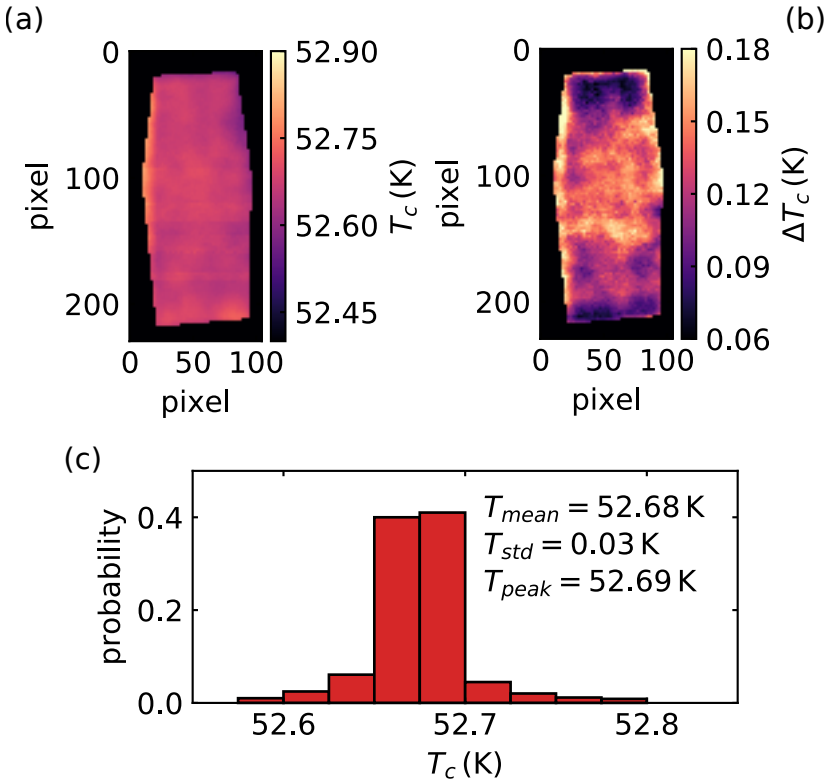

Figure 4.7.: Results of the neutron depolarisation imaging measurements performed at ANTARES. (a) The spatial distribution of the Curie temperature T_C and (b) the variation ΔT_C over the entire single crystal are shown. (c) Histogram of the probability of various T_C occurring across the sample is shown. Figure taken from Ref. [199].

constant over the entire momentum transfer range. The resolution within the scattering plane varies smoothly from $\Delta q_x = 0.003\,\text{Å}^{-1}$ to $\Delta q_x = 0.005\,\text{Å}^{-1}$ from the smallest to the highest momentum transfer. With frequency differences in the resonant coils between 20 Hz and 105.6 kHz a dynamic range from 0.2 ps to 310 ps was accessible.

We performed energy integrated measurements between 45 K and 65 K and time resolved measurements between 52.2 K and 54.7 K. The sample was cooled using a top-loading closed cycle cryostat (CCR) that reaches temperatures between $\sim 4\,\mathrm{K}$ and room temperature. The sample temperature was controlled using a Lakeshore 336 temperature controller with a calibrated Cernox sensor directly at the sample as shown in Fig. 4.6 (b). The temperature stability was better than $\Delta T \sim 0.01\,\mathrm{K}$ and no hysteresis was observed.

4.3.3. Setup at SANS-1

Complementary small angle neutron scattering (SANS) measurements were performed at the instrument SANS-1 at the MLZ to smaller momentum transfers to track the Porod

Table 4.1.: Instrument parameters for the energy-integrated and quasi-elastic measurements at RESEDA.

parameter	unit	variable	value
detector pixel size	(mm)	Δ	1.56
incoming wavelength	(Å)	λ	5.918
wavelength spread (FWHM)	(1)	$\Delta\lambda/\lambda$	0.117
scattering angles	(degrees)	2θ	0.98 - 4.54
source aperture horizontal (half width $\hat{=}$"radius")	(mm)	$r_{1,h}$	5
source aperture vertical	(mm)	$r_{1,v}$	10
defining aperture horizontal	(mm)	$r_{2,h}$	1.5
defining aperture vertical	(mm)	$r_{2,v}$	16
source aperture - defining aperture	(mm)	L	1450
distance defining aperture - detector	(mm)	l	≈ 2500
distance sample - detector	(mm)	L_{SD}	2230

scattering due to ferromagnetic domain walls. We used neutrons with a wavelength of $\lambda = 6.5\,\text{Å}$ with a wavelength spread (FWHM) of $\Delta\lambda/\lambda = 0.1$. The detector was positioned 20 m behind the sample and asymmetrically moved to one side of the direct beam to cover a momentum transfer range of $0.002 \leq q \leq 0.02\,\text{Å}^{-1}$. Together with the ^{3}He detector with a pixel size of 8×8 mm a momentum transfer resolution of $\Delta q \approx 8 \cdot 10^{-4}\,\text{Å}^{-1}$ was achieved following the calculations in Sec. 2.5.

4.4. Experimental results

In this section we present our neutron scattering results on the paramagnetic to ferromagnetic phase transition in UGe_2. We reveal purely longitudinal spin fluctuations with a dual character arising from $5f$ electrons which are hybridised with the conduction electrons. Local spin fluctuations are perfectly described by the Ising universality class in three dimensions whereas itinerant spin fluctuations occur over length scales comparable to the superconducting coherence length.

We performed SANS measurements around the paramagnetic to ferromagnetic phase transition at T_C in UGe_2. As derived in Sec. 2.3, the magnetic scattering cross-section is related to the imaginary part of the dynamical magnetic susceptibility $\chi''_{ij}(\boldsymbol{q}, \omega)$ via

$$\frac{\mathrm{d}^2\sigma}{\mathrm{d}\Omega \mathrm{d}\omega} \propto \frac{k_f}{k_i}(\delta_{ij} - \hat{q}_i\hat{q}_j)|F_{\boldsymbol{q}}|^2[n(\omega)+1]\chi''_{ij}(\boldsymbol{q}, \omega). \tag{4.1}$$

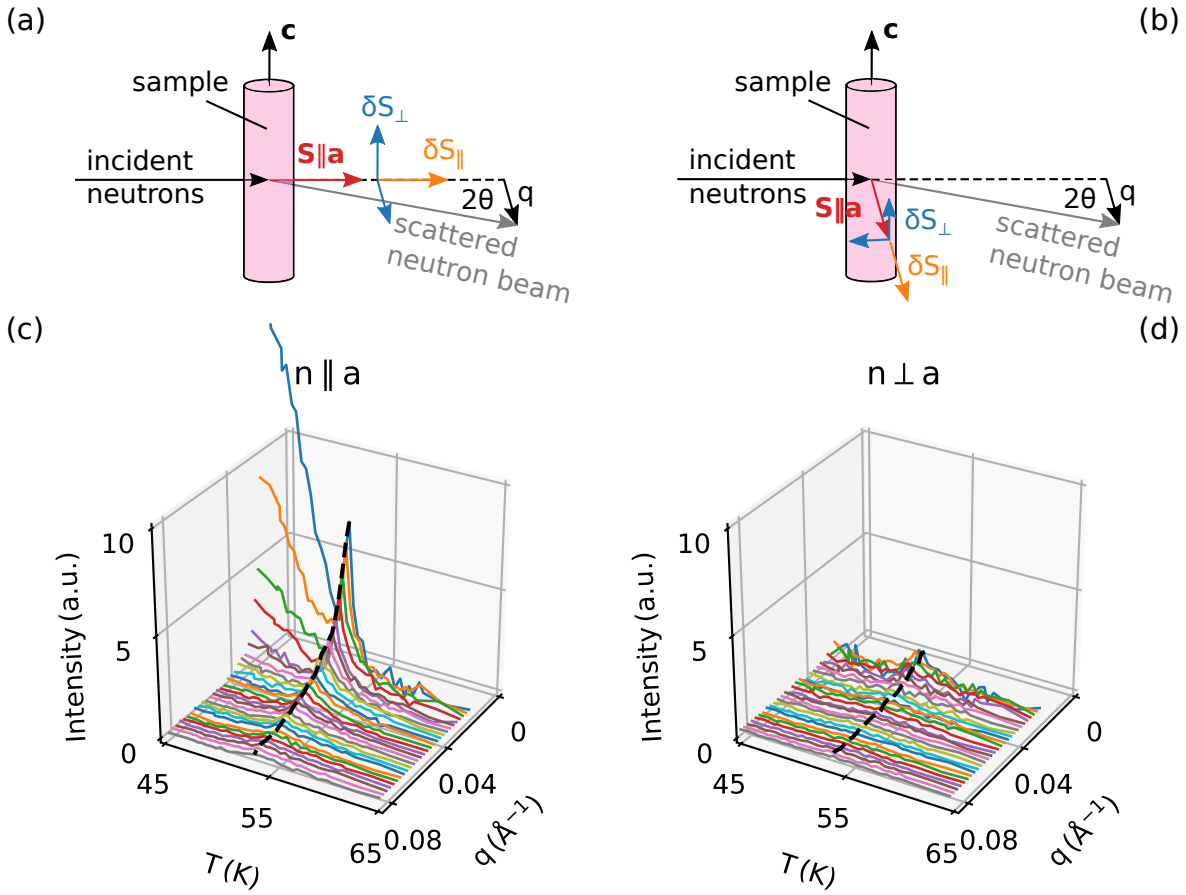

Figure 4.8.: Magnetic scattering intensity of UGe_2 near the Curie temperature $T_C = 52.7\,K$. (a) and (b) show two experimental configurations with the incident neutron beam $\boldsymbol{n}$ parallel or perpendicular to the magnetic easy axis a, respectively, which allows to differentiate between transverse and longitudinal fluctuations (see text). (c) and (d) show the energy-integrated scattering intensities for the two configurations $\boldsymbol{n} \parallel a$ and $\boldsymbol{n} \perp a$ as a function of temperature T and momentum transfer $\boldsymbol{q}$. The black dashed line marks T_C. In the parallel configuration we see critical scattering around T_C whereas in the perpendicular configuration it is absent. In addition, the onset of Porod scattering below T_C at lowest momentum transfer $\boldsymbol{q}$ is observable charactercteristic of the ferromagnetic ordering. Figure taken from Ref. [199].

k_f and k_i denote the wave vector of the scattered and incident neutrons, respectively, and $\hat{q}$ is a unit vector parallel to the scattering vector $\boldsymbol{q}$. $n(\omega)$ is the Bose function and $F_{\boldsymbol{q}}$ the uranium magnetic form factor.

In Fig. 4.8 we show the temperature T and momentum transfer $\boldsymbol{q}$ dependent energy-integrated scattering intensity of two different sample configurations that allow us to distinguish between transverse and longitudinal magnetic fluctuations. Background measured at $T = 65\,K$, well above T_C, was subtracted from all data sets shown. The temperature scans were carried out with the crystallographic a-axis, which is the magnetic easy

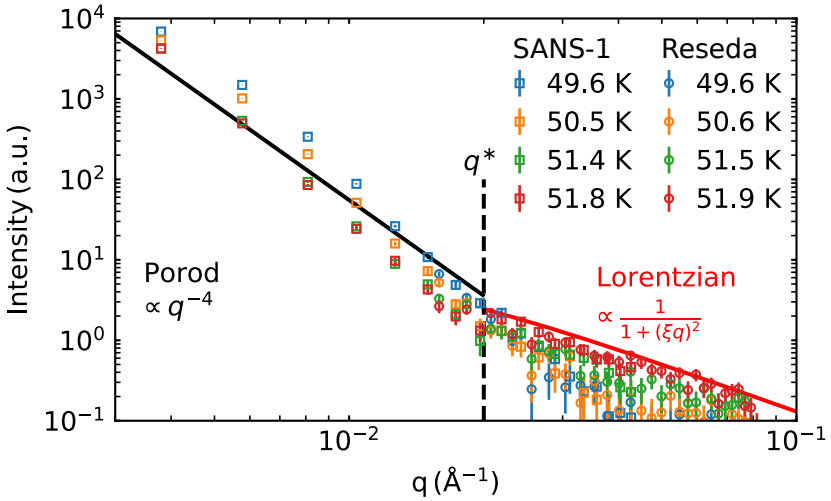

Figure 4.9.: Energy-integrated intensity as a function of momentum transfer $\boldsymbol{q}$ for selected temperatures T below T_C for the incident neutrons $\boldsymbol{n}$ parallel to the a-axis. Measurements at SANS-1 cover the whole q-range whereas RESEDA covers momentum transfers above $q = 0.016\,\text{Å}^{-1}$. The intensity below $q^* \approx 0.02\,\text{Å}^{-1}$ is well described by Porod scattering emerging from ferromagnetic domains (black solid line) whereas the Lorentzian shaped intensity above q^* originates from critical spin fluctuations. Figure taken from Ref. [199].

axis of UGe_2, parallel ($\boldsymbol{n} \parallel a$) and perpendicular ($\boldsymbol{n} \perp a$) to the incident neutron beam, respectively. As described in Sec. 2.3.1, neutrons are only sensitive to spin fluctuations perpendicular to the wavevector transfer $\boldsymbol{q}$ which is reflected in the term $\delta_{ij} - \hat{q}_i\hat{q}_j$ in Eq. 4.1. In SANS configuration the momentum transfer $\boldsymbol{q}$ is approximately perpendicular to the incident beam and we can separate longitudinal ($\delta S_\parallel$) from transverse spin fluctuations ($\delta S_\perp$) as illustrated in Fig. 4.8 (a) and (b). In the configuration $\boldsymbol{n} \parallel a$ both $\delta S_\parallel$ and $\delta S_\perp$ are perpendicular to $\boldsymbol{q}$ and we observe substantial magnetic intensity as shown in Fig. 4.8 (c). In contrast, for $\boldsymbol{n} \perp a$ only $\delta S_\perp$ is perpendicular to $\boldsymbol{q}$ and a vanishingly small signal is observed in this case (see Fig. 4.8 (d)) that can only come from transverse magnetic fluctuations. As we show in App. B, the small intensity arises from the finite $\boldsymbol{q}$ resolution, demonstrating that the critical spin fluctuations in UGe_2 are solely longitudinal. Differences in neutron transmission for the two orientations are negligible since the sample has a cylindrical shape. Inspecting the temperature dependence of the integrated intensity for $\boldsymbol{n} \parallel a$ shown in Fig. 4.8 (c), a pronounced peak is centred at $T_C = 52.7\,\text{K}$ due to the divergence of critical spin fluctuations. For low q and for $T < T_C$ additional intensity is observed that increases in a fashion proportional to the ferromagnetic order parameter, i.e. $I \propto M^2$.

Examining the signal of the configuration $\boldsymbol{n} \parallel a$ in Fig. 4.8 (c) in more detail, we show the q-dependence of the intensity for a few temperatures below T_C in Fig. 4.9. Below

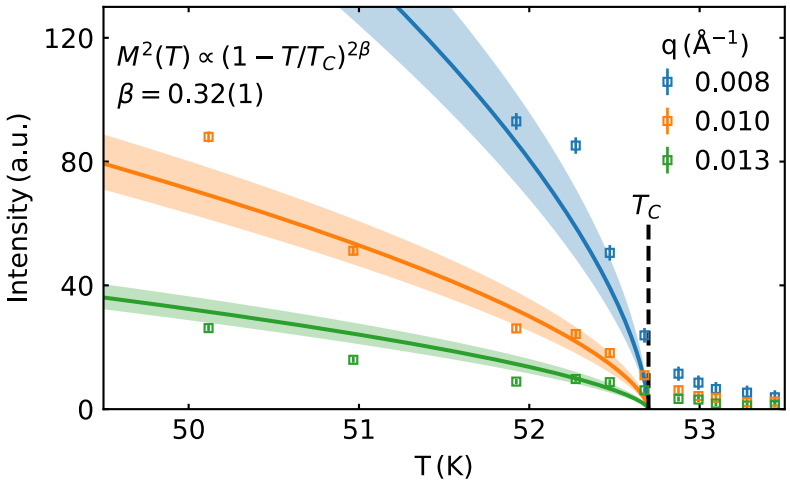

Figure 4.10.: T-dependence of the Porod scattering for $q < q^*$. The temperature dependence of the intensity is related to the ferromagnetic order parameter M via $M^2(T) \propto (1 - \frac{T}{T_C})^{2\beta}$ and well described for $\beta = 0.32(1)$ (solid lines). The shaded areas denote the uncertainty of the fit of β, i.e. 1σ standard deviation. Figure taken from Ref. [199].

$q^* \approx 0.02\,\text{Å}^{-1}$ the intensity is well-described by a q^{-4} dependence that is characteristic for scattering from FM domains that form below T_C [242, 243]. To follow this so-called Porod scattering towards lower q, we performed a supporting SANS experiment on the instrument SANS-1 at MLZ denoted with square symbols in Fig. 4.9 (e). The observation of Porod scattering down to $q_{\text{min}} = 0.004\,\text{Å}^{-1}$ implies the onset of long-range order over length scales $\gg 2\pi/q_{\text{min}} \approx 1600\,\text{Å}$. SANS is ideally suited to observe these length scales of long-range magnetic order in bulk samples as it allows to resolve the momentum dependence in contrast to local probes, such as NMR, NQR, and μSR, and offers the necessary momentum resolution down to $q = 0.001\,\text{Å}$. In Fig. 4.10, we show the temperature dependence of the intensity for selected q below q^*. Near T_C it evolves as

$$M^2(T) \propto \left(1 - \frac{T}{T_C}\right)^{2\beta}. \tag{4.2}$$

We find that $\beta = 0.32(1)$ describes our data perfectly in agreement with $\beta^{\text{theo}} = 0.32$ for a 3d Ising system [114]. This is also in good agreement with $\beta = 0.36(1)$ from neutron diffraction [208].

For $q \geq q^*$ and for $T \approx T_C$ the q-dependence is described by a Lorentzian line shape characteristic of critical spin fluctuations with a correlation length ξ as shown in Fig. 4.9. The corresponding dynamical magnetic susceptibility is

$$\frac{\chi''(\boldsymbol{q},\omega)}{\omega} = \chi(\boldsymbol{q})\frac{\Gamma_q}{\Gamma_q^2 + \omega^2} \tag{4.3}$$

$$\chi(\boldsymbol{q}) = \frac{\chi_0}{1 + (\xi q)^2}, \tag{4.4}$$

where Γ_q and χ_0 are the momentum dependent relaxation frequency and the static magnetic susceptibility, respectively. Because of the longitudinal character of the spin fluctuations only χ''_{aa} is non-zero and we have thus dropped the indices i, j. As we will show in the following, the quasi-static approximation [162, 244] is valid for our experimental conditions which allows to simplify Eq. 4.1 and obtain the static magnetic susceptibility χ_0 and the correlation length ξ from the energy integrated data.

The measured neutron cross-section for inelastic magnetic scattering provided in Eq. 4.1 can be simplified for $\hbar\omega \ll k_\mathrm{B}T$. Via a Taylor expansion in $x = \frac{\hbar\omega}{k_\mathrm{B}T}$, it follows that $\frac{1}{1-e^{-\frac{\hbar\omega}{k_\mathrm{B}T}}} \approx \frac{k_\mathrm{B}T}{\hbar\omega}$. In this case the scattering function simplifies to

$$S(\boldsymbol{q},\omega) = \frac{\chi''_{\alpha\beta}(\boldsymbol{q},\omega)}{1-e^{-\beta\hbar\omega}} \approx \chi''_{\alpha\beta}(\boldsymbol{q},\omega)\frac{k_\mathrm{B}T}{\hbar\omega}. \tag{4.5}$$

All data collection for our neutron scattering study in UGe_2 was carried out near $T_\mathrm{C} = 52.7\,\mathrm{K}$, which corresponds to $k_\mathrm{B}T_\mathrm{C} = 4.5\,\mathrm{meV}$. In addition, it is already known from previous TAS measurements that $\hbar\Gamma_q < \hbar\Gamma^{\max} = 0.3\,\mathrm{meV}$ for the q-range up to $0.08\,\mathrm{\AA}^{-1}$ that we have investigated here [53]. Our own measurements, as we will show later in this section, also confirm this (see Fig. 4.14). Hence, for the relevant energy range $\frac{\hbar\Gamma^{\max}}{k_\mathrm{B}T_\mathrm{C}} \approx 0.07 \ll 1$ and the Taylor expansion can be used.

Further, we can make use of the so-called quasi-static approximation [162, 244]. It states that in case the energy of the incident neutrons E_i is larger than the relaxation frequency $\hbar\Gamma$ of the spin fluctuations that are being investigated the energy-integrated neutron scattering cross-section is given by

$$\frac{d\sigma}{d\Omega} \propto (\delta_{\alpha\beta} - \hat{q}_\alpha\hat{q}_\beta)|F_{\boldsymbol{q}}|^2 S(\boldsymbol{q},0), \tag{4.6}$$

where

$$S(\boldsymbol{q},t) = \hbar\int S(\boldsymbol{q},\omega)e^{i\omega t}d\omega \tag{4.7}$$

is the intermediate scattering function, which is the Fourier transform of the scattering function $S(\boldsymbol{q},\omega) = 1/\pi[n(\omega)+1]\chi''_{ij}(\boldsymbol{q},\omega)$ (see Eq. 4.1) with respect to time. Eq. 4.6 is also called the instantaneous approximation. The experiments at RESEDA were carried out with an incident wavelength $\lambda = 6\,\mathrm{\AA}$ which corresponds to $E_i = 2.3\,\mathrm{meV}$ and, thus, we have $\frac{\hbar\Gamma^{\max}}{E_i} \approx 0.1 \ll 1$ and the quasi-static approximation is valid for our experiment.

Finally, we use Eq. 4.3 together with Eqs. 4.5 and 4.7 to obtain

$$S(\boldsymbol{q},t=0) = \int k_\mathrm{B}T\chi(\boldsymbol{q})\frac{\Gamma_q}{\Gamma_q^2+\omega^2}d\omega = \pi k_\mathrm{B}T\chi(\boldsymbol{q}). \tag{4.8}$$

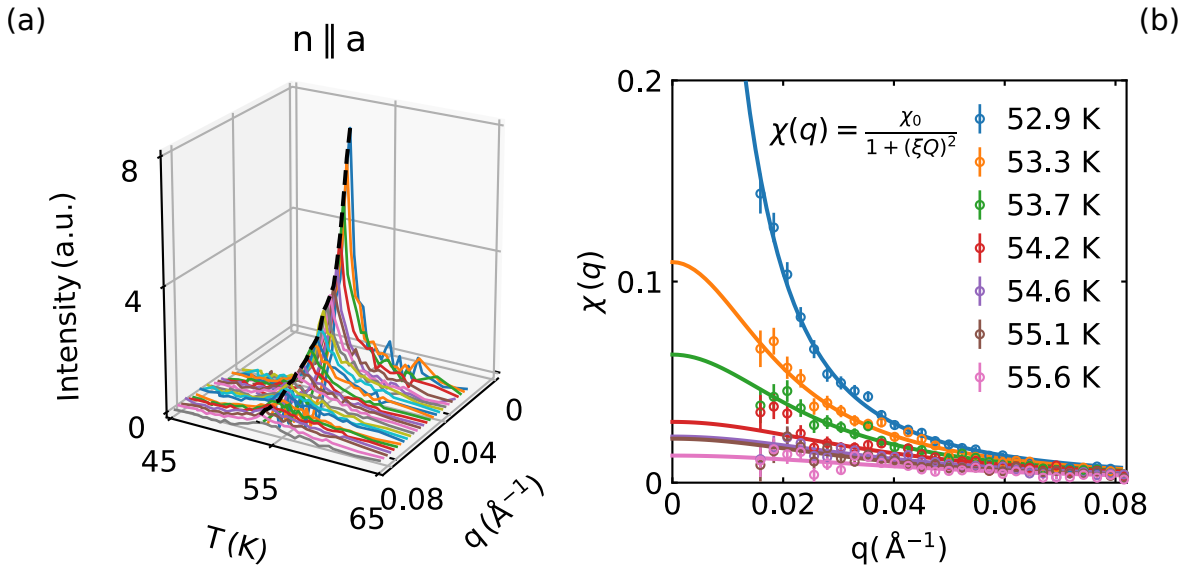

Figure 4.11.: T-dependence of the Lorentzian shaped critical scattering intensity. (a) Energy-integrated magnetic scattering intensity around T_c as a function of temperature T and momentum transfer q. (b) q-dependence of the magnetic susceptibility $\chi(q)$. Solid lines are fits to Eq. 4.3 where we use the quasi-static approximation (see text). Figure taken from Ref. [199].

Taking into account that in our SANS geometry $|F_{\boldsymbol{q}}|^2 \approx 1$, we find the energy-integrated neutron cross-section for the spin fluctuations in UGe_2 as

$$\frac{d\sigma}{d\Omega} \propto \pi k_B T \chi(\boldsymbol{q}) \tag{4.9}$$

$$= \pi \frac{k_B T \chi_0}{1 + (\xi q)^2}. \tag{4.10}$$

Hence, the static susceptibility χ_0 and the correlation length ξ can be directly obtained by fitting the observed energy-integrated intensities with Eq. 4.9.

To investigate the critical scattering quantitatively, we subtract the Porod scattering (see Figs. 4.9 and 4.10) from the observed intensities. The result is shown in Fig. 4.11 (a). As the quasi-static approximation is valid, we show $\chi(\boldsymbol{q})$ which we obtained by dividing the observed intensity by T for various temperatures in Fig. 4.11 (b). The solid lines are fits to Eq. 4.4 to extract the T-dependence of χ_0 and ξ shown in Figs. 4.12 (a) and (b). For comparison we show the static magnetic susceptibility H/M determined by bulk magnetisation measurements under an applied field of $H = 20\,\mathrm{mT}$ in Fig. 4.12 (a) (red circles) that scales perfectly with χ_0.

We find that $1/\chi_0 \propto (1 - T/T_C)^\gamma$ with $\gamma = 1.23(3)$ and $1/\xi = \kappa = \kappa_0(1 - T/T_C)^\nu$ with $\kappa_0 = 0.31(2)\,\text{Å}^{-1}$ and $\nu = 0.63(2)$ (solid lines in Figs. 4.12 (a) and (b)). The shaded area denotes the uncertainty of the fit with 1σ standard deviation. The critical exponents are in excellent agreement with a 3d Ising FM for which $\gamma^{\text{theo}} = 1.24$ and $\nu^{\text{theo}} = 0.63$ [114].

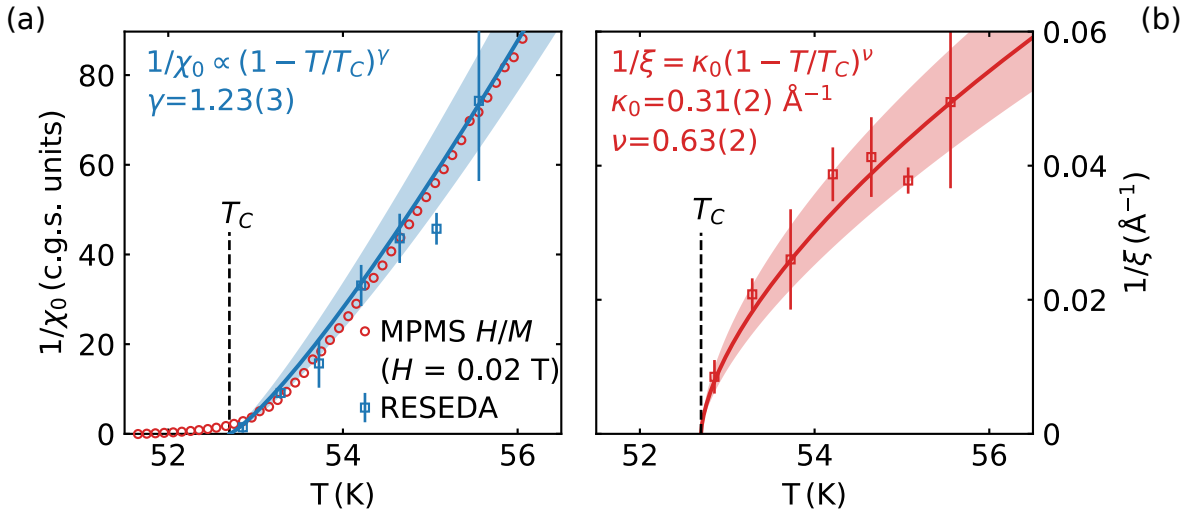

Figure 4.12.: Temperature dependence of the magnetic susceptibility χ and the correlation length ξ. (a) The inverse susceptibility extracted from fits in Fig. 4.11 (b) is shown as a function of temperature. The red circles denote the static easy-axis magnetic susceptibility H/M measured with a magnetic field $H = 0.1$ T. The solid blue line is a fit to the data to extract the critical exponent as $\gamma = 1.23(3)$. (b) The inverse correlation length $1/\xi$ as a function of temperature is well described by the fit (solid line) with a critical exponent $\nu = 0.63(2)$. The shaded areas denote the uncertainty of the fits as 1σ standard deviation. Figure taken from Ref. [199].

Huxley *et al.* found $\kappa_0 = 0.29\,\text{Å}^{-1}$ in good agreement with our result. In contrast, they determined $\nu = 1/2$ consistent with a mean-field transition [53]. However, their study was limited to $q > 0.03\,\text{Å}^{-1}$ and underestimates the divergence of the critical fluctuations.

We now discuss the results of our MIEZE measurements. As described in Sec. 2.6, MIEZE measures the intermediate scattering function $S(\boldsymbol{q}, \tau)$ that is the time Fourier transform of the scattering function $S(\boldsymbol{q}, \omega) = 1/\pi[n(\omega) + 1]\chi''_{ij}(\boldsymbol{q}, \omega)$ (see Eq. 2.39). In Fig. 4.13 we show the normalised intermediate scattering function $S(q, \tau)/S(q, 0)$ for various momentum transfers q at T_C. $S(q, \tau)/S(q, 0)$ for all other measured temperatures are shown in App. B. Because the spin fluctuations have Lorentzian lineshape (see Eq. 4.3) we fit an exponential decay (solid lines in Fig. 4.13)

$$S(q, \tau)/S(q, 0) = A \cdot \exp(-|\Gamma_q| \cdot \tau), \tag{4.11}$$

where the amplitude A is in general set to 1. Above T_C and for smallest momentum transfer q, the amplitude A is fitted as well since due to background scattering the measured polarisation was suppressed below 1. The fits are discussed in more detail in App. B. The resulting fluctuation frequency Γ_q is shown in Fig. 4.14.

The momentum dependence of Γ_q is described by the dynamical exponent z via $\Gamma_q \propto q^z$. For $T \leq T_C$, we find that Γ_q is fitted perfectly by $z = 2.0(1)$ (see Fig. 4.14 (b)). This is

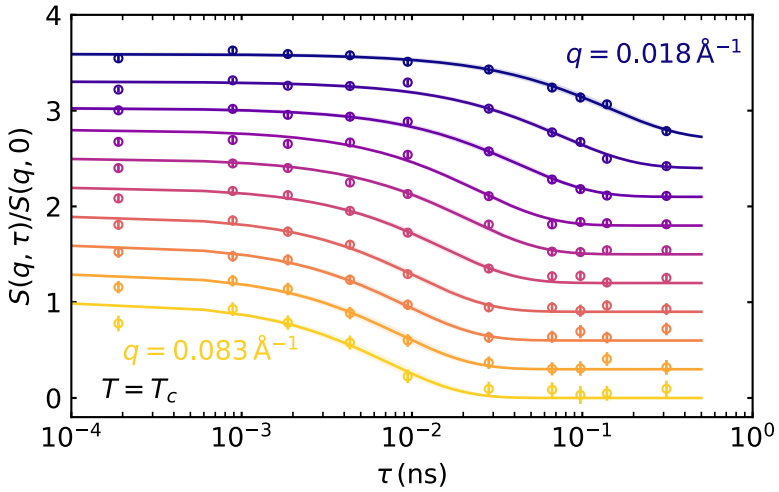

Figure 4.13.: Intermediate scattering function of UGe_2 at $T_C = 52.7\,K$ for various momentum transfers q. Solid lines are single exponential decay fits and the shaded areas denote the uncertainty of the fits as 1σ standard deviation. Figure taken from Ref. [199].

in excellent agreement with predictions for a 3d Ising FM for which $z^{\text{theo}} = 2$ [114]. For $T > T_C$, Γ_q is also well described by $z = 2$, however, only above a crossover value of $q^0 = 0.04\,\text{Å}^{-1}$. Below q^0, our data is best fit by $\Gamma_q = Aq^z$ with $z = 2.53(4)$ (see Fig. 4.14). This is consistent with $z = 5/2$ calculated for itinerant FMs within critical renormalisation group theory [245] and confirmed for various d-electron FMs such as Fe [246], Ni [247] and Co [248]. Notably, typical values reported for A are $3 - 350\,\text{meVÅ}^{5/2}$ consistent with $A = 200(2)\,\text{meVÅ}^{5/2}$ that we find for UGe_2 [246–249]. As demonstrated in Fig. 4.14 (a) for $T = 54\,K$, the fit for Γ_q with $z = 2.0(1)$ also describes the data of Huxley *et al.* [53] (black circles) perfectly. However, they conclude that Γ_q remains finite for $q \to 0$ in contrast to our findings. This discrepancy is easily explained by considering that their experiment was limited to $q \geq 0.03\,\text{Å}^{-1}$, which is only slightly below q^0 where we observe the crossover to $z = 5/2$.

Fig. 4.15 shows the T-dependence of Γ_q. For finite q, it follows the T-dependence of ξ via $\Gamma_q \propto (q/\xi)^z = (1 - T/T_C)^{z\nu}$ in agreement with the dynamical scaling prediction [250]. In Fig. 4.15 (a) we show that for $q = 0.06\,\text{Å}^{-1}$ both the results from Ref. [53] and our own are consistent with $z = 2$. Below q^0, $z = 5/2$ agrees well with our data (solid line) consistent with the fits of Γ_q shown in Fig. 4.14.

For clean itinerant FMs the fluctuation spectrum is characterised by Landau damping as has been demonstrated for $3d$ transition metal materials [251, 252]. Here, the product of the magnetic susceptibility with the fluctuation frequency, $\chi(q)\Gamma_q$, is given by the Lindhard dependence $(2/\pi)v_F\chi_P q$ for $T > T_C$, where v_F and χ_P are the Fermi velocity

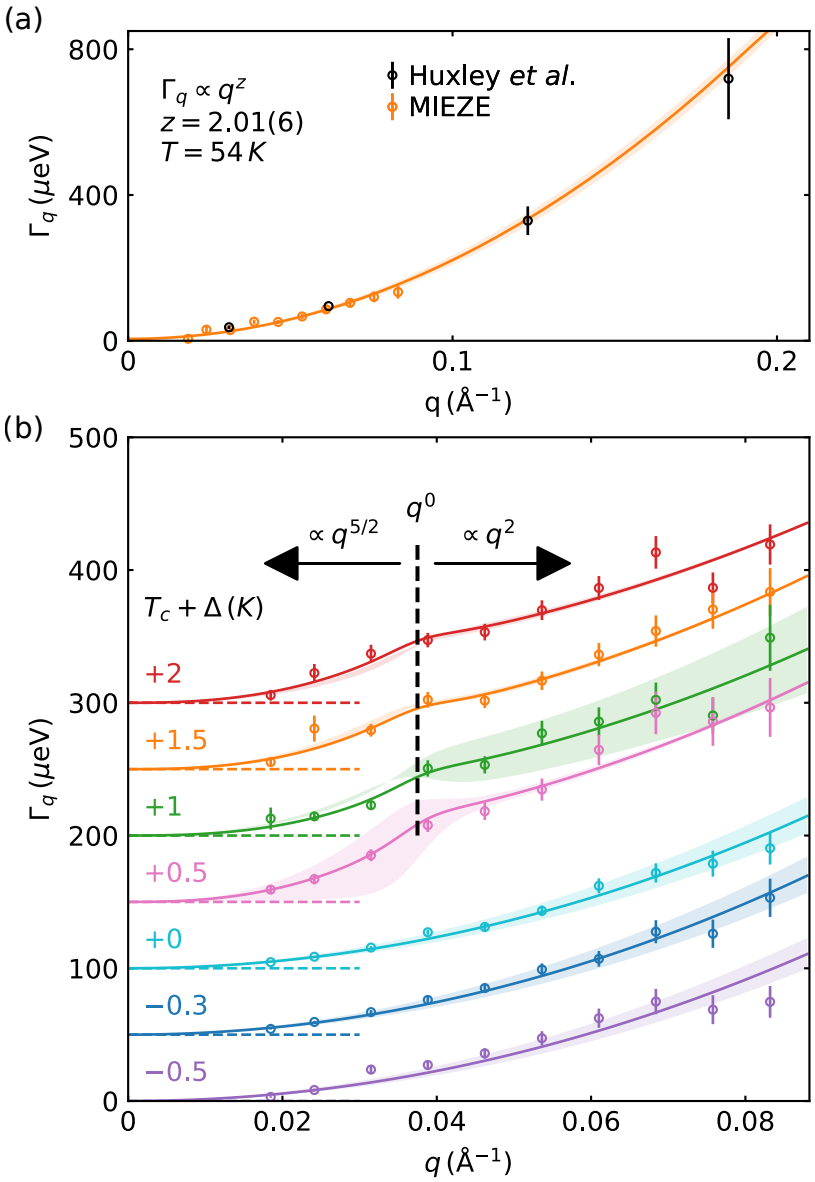

Figure 4.14.: Fluctuation energy Γ_q as a function of momentum transfer q for various temperatures T. (a) A comparison between former TAS measurements by Huxley *et al.* [53] covering higher momentum transfers q are in perfect agreement with our results. The solid line is a fit to the MIEZE data. (b) q-dependence of the fluctuation energy Γ_q in the low q-regime. Solid lines are fits to $\Gamma \propto q^z$ with the dynamical critical exponent z. We observe a crossover at $q^0 = 0.038\,\text{Å}^{-1}$ where the exponent changes from $z = 2.5$ below to $z = 2$ above. Data sets are shifted by 50 μeV for better readability as indicated by the horizontal dashed lines. The shaded areas denote the uncertainty of the fits as 1σ standard deviation. Figure taken from Ref. [199].

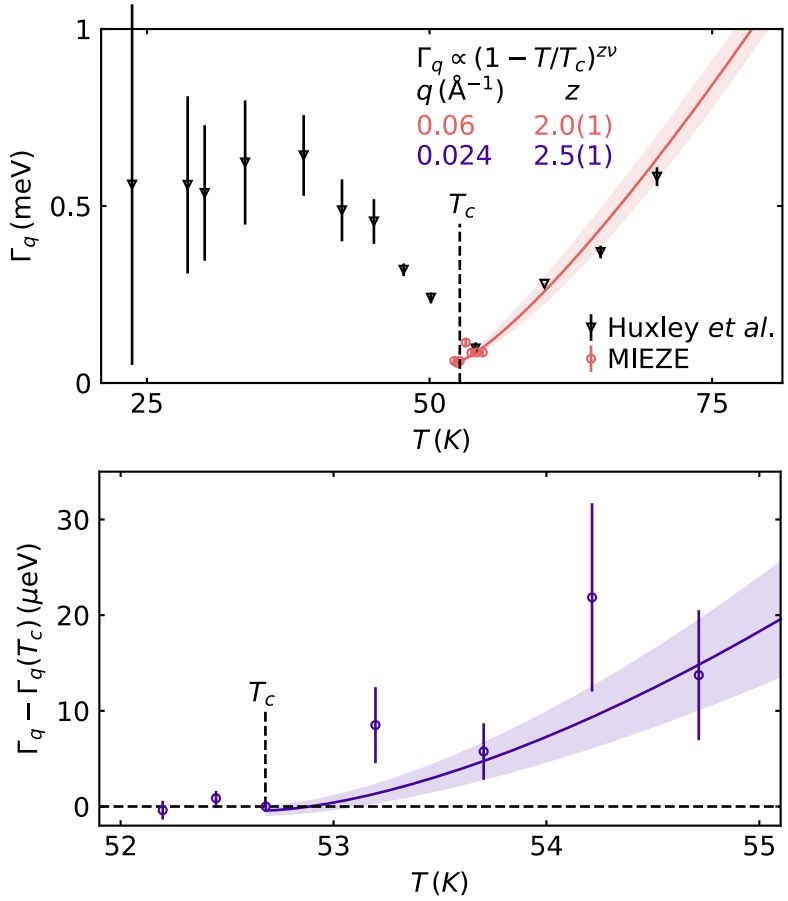

Figure 4.15.: Temperature dependence of the fluctuation energy Γ_q (a) for q above $q^0 = 0.038\,\text{Å}^{-1}$ and (b) below. (a) A comparison with data by Huxley *et al.* [53] which cover a larger temperature range. The solid line denotes a fit of $\Gamma_q \propto (1 - T/T_\text{C})^{z\nu}$ to our MIEZE data where z is given in the table for the two regimes. The critical exponent ν is given as $\nu = 0.63(2)$ by the elastic measurements shown in Fig. 4.12 (b). The data by Huxley *et al.* are consistent with our findings. (b) The T-dependence of the fluctuation energy which is shifted by $\Gamma_q(T_\text{C})$. The shaded areas denote the uncertainty of the fits as 1σ standard deviation. Figure taken from Ref. [199].

and the non-interacting Pauli susceptibility, respectively [253, 254]. We show $\chi(q)\Gamma_q$ for UGe_2 in Fig. 4.16. Huxley *et al.* [53] who carried out measurements for $q \geq 0.03\,\text{Å}^{-1}$ found that $\chi(q)\Gamma_q$ only weakly depends on q and concluded that it remains finite for $q \to 0$ (solid black line in Fig. 4.16). This difference with respect to prototypical $3d$ electron itinerant FMs is likely due to strong spin-orbit coupling that modifies the spin fluctuation spectrum. Our data agrees with the weak q dependence above q^0 but clearly shows that $\chi(q)\Gamma_q \to 0$ for $q \to 0$, implying that the uniform magnetisation is a conserved quantity in UGe_2. Our data is consistent with $\chi(q)\Gamma_q \propto q^{5/2}$ (solid blue line in Fig. 4.16). This more pronounced q-dependence is expected by theory near T_C [254] and agrees with $\Gamma_q \propto q^{5/2}$. Here, we

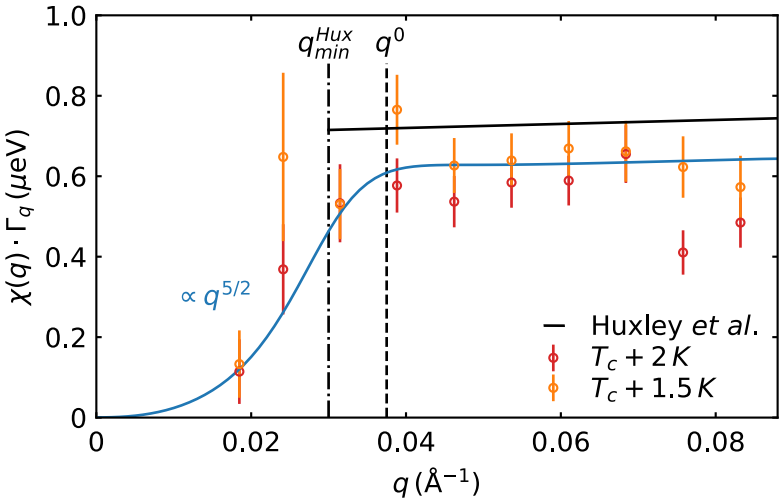

Figure 4.16.: Product of the magnetic susceptibility and the fluctuation energy $\chi(q) \cdot \Gamma_q$. The black solid line is $\chi(q)\Gamma_q$ as determined by Huxley *et al.* in Ref. [53] that reports measurements down to $q^{\mathrm{Hux}}_{\mathrm{min}}$ marked by the dashed-dotted line. We observe a weak q-dependence above q^0 but clearly see $\chi(q)\Gamma_q \to 0$ for $q \to 0$. The data is consistent with $\chi(q)\Gamma_q \propto q^{5/2}$ denoted as solid blue line. Figure taken from Ref. [199].

highlight that although the q-range over which q^z with $z = 5/2$ is observed is limited, this behaviour is corroborated via three independent methods that are illustrated in Figs. 4.14 to 4.16.

4.5. Summary and conclusions

Our results demonstrate that the spin fluctuations in UGe_2 exhibit a dual character associated with localised $5f$ electrons that are hybridised with itinerant d electrons. Notably, as expected for a local moment FM with substantial uniaxial magnetic anisotropy all critical exponents determined from our results are in perfect agreement with the 3d Ising universality class [114]. Further, $\chi(q)\Gamma_q$ is approximately constant as a function of q down to q^0 highlighting that the underlying spin fluctuations are localised in real space. In contrast, the dynamical exponent $z = 5/2$ and $\chi(q)\Gamma_q \to 0$ for $q \to 0$ observed below the crossover value q^0 are characteristic of itinerant spin fluctuations. Because the contribution of the conduction electrons to the total ordered moment is less than 3 % [208], below T_C fluctuations of localised f magnetic moments are dominant. Spin fluctuations with a dual character are consistent with the moderately enhanced Sommerfeld coefficient $\gamma = 34\,\mathrm{mJ/K^2mol}$ of UGe_2 [255, 256] and a next-nearest-neighbor uranium distance

$d_{\mathrm{U-U}} = 3.85\,\text{Å}$ [200] near to the Hill value of 3.5 Å [257] that both suggest that the $5f$ electrons in UGe_2 are hybridised with the conduction electrons.

The dual nature of spin fluctuations revealed by our MIEZE measurements strongly supports the scenario of p-wave superconductivity in UGe_2. First, to promote strong longitudinal fluctuations requires strong Ising anisotropy that typically is a result of localised f electrons with substantial spin-orbit coupling and is consistent with critical Ising exponents that we observed above q^0. Second, the theory for p-wave pairing assumes that it is the *same* itinerant electrons that are responsible for the coexisting FM and superconducting states [258] highlighting that the low-energy itinerant spin fluctuations below q^0 discovered here are crucial to mediate p-wave superconductivity. The maximum superconducting critical temperature T_{SC} occurs at the QPT at p_{x} [52, 218]. Here, a substantial increase of the Sommerfeld coefficient [225] and changes in the electronic structure observed near p_{x} [214, 227] suggest that the hybridisation of $5f$ electrons and conduction electrons increases at p_{x} and corroborates that spin fluctuations with a dual nature are relevant for p-wave superconductivity. This is supported by a theory based on competition of FM exchange and the Kondo interaction that results in a localised to itinerant transition at p_{x} [259, 260].

Further, we note that our findings of longitudinal critical fluctuations in UGe_2 are also consistent with the findings for UCoGe [261], which is another material that is a candidate for p-wave superconductivity. However, the results on UCoGe by Hattori *et al.* [261] were obtained by nuclear magnetic resonance measurements that are unable to probe spin fluctuations at finite q and, in turn, are unable to observe an itinerant-to-localised crossover as we report it here. Similarly, TAS measurements of UCoGe by Stock *et al.* [262] lack the required momentum and energy transfer resolution. In contrast to UGe_2, UCoGe exhibits superconductivity even at ambient pressure below a transition temperature of $T_{\mathrm{SC}} = 0.8\,\text{K}$ [263] and we intend to overcome these resolution limits to investigate the critical fluctuation spectrum using MIEZE. Though, the small ordered magnetic moment of $m_0 = 0.03\,\mu_{\mathrm{B}}$ [263] makes the measurements challenging.

Moreover, we note that the crossover value q^0 corresponds to a length scale of approximately 170 Å. The superconducting coherence length of UGe_2 was estimated as $\xi^{\mathrm{SC}} = 200\,\text{Å}$ [52], which shows that the spin fluctuations relevant to the p-wave pairing are present at $q < q^0$. This may explain why triple-axis measurements of the spin fluctuations near p_{x} with limited resolution were inconclusive [237]. Although the pressure dependence of the crossover length scale q^0 remains to be determined to unambiguously associate it with the unconventional superconducting state in UGe_2, our results highlight that recent developments in ultrahigh resolution neutron spectroscopy are critical for the study of low-energy spin fluctuations that are believed to drive the emergence of quantum

matter states. Here, the fluctuations that appear at zero q such as for ferromagnetic and electronic-nematic quantum states can immediately be investigated via the MIEZE SANS configuration used here. In addition, MIEZE can be extended in straightforward fashion to study quantum fluctuations arising at large q, allowing for insights in antiferromagnetic QPTs and topological forms of order [264].

Finally, unconventional superconductivity was recently discovered by Ran *et al.* in the material UTe_2 below a critical temperature $T_{SC} = 1.6\,K$ [265, 266]. The material exhibits two re-entrant superconducting phases with high anisotropic upper critical fields of more than 40 and 65 T, respectively, where the latter coexists with a field-polarised phase. Temperature-independent Knight shift data across T_{SC} measured in ^{125}Te NMR studies suggest p-wave superconductivity. Furthermore, scanning tunneling microscopy studies identified chiral in gap states suggesting UTe_2 as a candidate for chiral-triplet topological superconductivity [267]. Hence, the material sparks interest for topological quantum computing as it might host Majorana zero modes [268, 269].

The system shares similarities with the other Uranium-based ferromagnetic superconductors, but has a paramagnetic normal state with strong magnetic fluctuations where the scaling of the magnetisation indicates quantum critical ferromagnetism. It is believed that these fluctuations might mediate the superconducting pairing [265]. In contrast, inelastic neutron scattering has found incommensurate spin fluctuations close to an antiferromagnetic wave vector [270]. However, not all scattering planes have been probed. μSR measurements found no evidence for magnetic order down to 25 mK, but a slowing down of the magnetic fluctuations with decreasing temperature was observed indicating the existence of a magnetic instability [271]. Furthermore, NMR data suggest strong low-energy longitudinal magnetic fluctuations below $T = 20\,K$ [272]. But the latter two techniques are limited in their sensitivity to localised fluctuations. By contrast, MIEZE could probe the direction and character of the low-energy fluctuations at finite momentum down to $q \approx 0.005\,\mathring{A}^{-1}$ with highest energy and momentum resolution as well as the behaviour of the fluctuations under the application of magnetic field.

5. Weak crystallisation of fluctuating skyrmion textures in MnSi

In this chapter we report on our experimental study of the emergence of the topologically non-trivial skyrmion lattice phase when approaching it from the paramagnetic state in the transition metal helimagnet MnSi. As part of this work small angle neutron scattering (SANS) data were analysed and neutron resonance spin-echo measurements employing modulation of intensity with zero effort (MIEZE) conducted, which complete ac susceptibility and all-electrical microwave spectroscopy (FMR) results for a detailed picture of the paramagnetic-to-skyrmion lattice transition. As our key result, we find evidence of skyrmion textures in the paramagnetic state exceeding 10^3 Å with lifetimes above several nanoseconds. Our experimental findings establish that the paramagnetic-to-skyrmion lattice transition in MnSi is well described by the Landau soft-mode mechanism of weak crystallisation.

Results of the presented work have been published in Ref. [108] and this chapter is based on it. The chapter is organised as follows. At first, the key question is motivated and previous results concerning the paramagnetic-to-skyrmion lattice transition are given. Second, the employed samples and experimental setups are explained. Subsequently, experimental results of our neutron scattering studies from SANS and longitudinal MIEZE are presented. Finally, the results are combined with complementary ac susceptibility and all-electrical microwave spectroscopy data and discussed in the context of the weak crystallisation mechanism.

5.1. Motivation

In recent years skyrmions have been discovered in numerous systems such as bulk compounds, thin films, heterostructures, and nanoscaled systems [6, 12–25, 27, 28, 71–75]. A major question is the formation of skyrmions and the emergence of their non-trivial topology. The microscopic mechanisms underlying the transition of skyrmions into different types of conventional long-range magnetic order have been explored in various experimental and theoretical studies [15, 16, 70, 273–276]. In contrast, the formation

of skyrmions coming from an essentially paramagnetic state which is dominated by an abundance of fluctuations is not conclusively examined. This leads to the question if characteristics of non-trivial topology already exist in the paramagnetic state, if they are rather described as solitonic objects in real space or as smooth, wavelike textures [6, 13, 14, 18, 71, 109, 120, 277], and how the transition is described in the framework of the present-day classification of phase transitions [31, 278, 279].

In the helimagnetic compound FeGe it was argued that skyrmionic precursor phenomena exist in the paramagnetic state based on ac susceptibility and limited specific heat data at finite field [280, 281]. However, the interpretation lacked necessary microscopic information on the spatial, temporal, and topological character of the correlations. In addition, the interpretation assumed a spontaneous skyrmion liquid in zero magnetic field. Though, this scenario was eventually ruled out in the case of the archetypical helimagnet MnSi in comprehensive studies including SANS, neutron polarimetry, specific heat, and susceptibility measurements [112, 282]. In order to clarify the nature of the paramagnetic-to-skyrmion lattice transition, bulk information has to be combined with microscopic data and a critical assessment of the consistency with conventional Ginzburg-Landau theory is necessary.

An ideal candidate to approach the issue of the paramagnetic-to-skrmion lattice transition is the transition metal MnSi as one of the most extensively studied representative of the class of cubic chiral magnets [14, 69, 76, 77, 80, 86–88, 101–106, 110–112, 123, 135, 142–144, 158, 161, 282–285]. Its main characteristics concerning the phase diagram, phase transitions, the skyrmion lattice, and spin excitations are introduced in Sec. 1.2.

5.2. Experimental methods

For this study, high-quality single crystal samples of MnSi were grown by means of optical float zoning under ultrahigh-vacuum conditions [286–288]. For our SANS measurements, a spherical single crystal of MnSi was employed with a diameter of 5.75 mm. A crystallographic $\langle 110 \rangle$ direction was oriented perpendicular to the magnetic field and the neutron beam. MIEZE measurements were performed with a cylindrical MnSi single crystal sample with a diameter of 10 mm and a length of 30 mm (OFZ 119-3). The cylinder symmetry axis was a $\langle 110 \rangle$ direction and oriented vertically.

SANS measurements were conducted at the instrument SANS-1 at the Heinz Maier-Leibnitz Zentrum (MLZ) in Garching, Germany [187]. The instrument parameters of our study are listed in Tab. 5.1. A 5 T superconducting magnet (MAG-H-5.0T) was used to generate the magnetic fields and the sample was cooled using a closed cycle cryostat (CCR19). At the time of these measurements, SANS-1 was not equipped with goniometers.

Table 5.1.: Instrument parameters for the energy-integrated measurements at SANS-1.

parameter	unit	variable	value
detector pixel size	(mm)	Δ	8
incoming wavelength	(Å)	λ	5.5
wavelength spread (FWHM)	(1)	$\Delta\lambda/\lambda$	0.1
scattering angle	(degrees)	2θ	2.0
source aperture radius	(mm)	r_1	25
defining aperture	(mm)	r_2	2
source aperture - defining aperture	(mm)	L_1	12
distance defining aperture - detector	(mm)	L_2	10.35
distance sample - detector	(mm)	L_{SD}	10

Therefore, all data were recorded with rocking scans about the vertical axis. Numerous related studies performing two-axis rocking scans confirmed the full symmetry of the scattering pattern.

MIEZE measurements were performed at the instrument RESEDA at the MLZ in Garching, Germany [176–178]. A neutron wavelength of $\lambda = 6\,\text{Å}$ was used with a wavelength bandwidth of $\Delta\lambda/\lambda = 0.117$. The dynamic range was from 70 ps to 1.9 ns. The sample aperture was a pinhole with a diameter of 8 mm. Vertical and horizontal 40′ collimators reduced background from the analyser and reflections from the neutron guides. In addition, they defined the momentum transfer resolution. The sample-detector distance was 3430 mm. Magnetic fields were generated by a high temperature superconducting 2.2 T magnet (MAG 2.2 T-HTS) in two configurations, parallel and perpendicular to the neutron beam. The sample was cooled with a standard closed cycle cryostat. All measurements were performed field cooled.

5.3. Experimental results

In the following section, our results of neutron scattering experiments are presented. We observe SANS intensity on a surface of a sphere with a faint sixfold intensity pattern above the ordering temperature T_{c} reminiscent of skyrmion lattice order. The correlation length of the sixfold pattern is resolution limited and exceeds several thousand Å whereas contributions of conical character are subleading. MIEZE measurements reveal a fully dynamic paramagnetic regime where the sixfold pattern has lifetimes exceeding several 10^{-9} s.

5.3.1. Small angle neutron scattering

Comprehensive SANS measurements yield information on the nature and the correlation lengths of the magnetic correlations on a microscopic scale. The presented results were recorded in field heated measurements. A comparison with field cooled measurements showed the same behaviour without evidence of hysteresis in the scattering patterns. This result is consistent with bulk properties which did not exhibit any hysteresis effects between the skyrmion lattice phase and the fluctuation disordered regime. Both neutron scattering studies employing SANS and MIEZE were performed with the magnetic field along the crystallographic $\langle 110 \rangle$ direction. The isotropic behaviour of the FD regime observed in susceptibility measurements allows to link the results.

Typical 2d scattering patterns with magnetic field of $B = 0.15\,\mathrm{T}$ parallel to the neutron beam are shown in Figs. 5.1 (a1) to (a3). The typical sixfold scattering pattern of the skyrmion lattice phase of MnSi is observed for $T = 28.7\,\mathrm{K}$ in Fig. 5.1 (a1). The logarithmic intensity scale is chosen to minimise twofold appearance of the scattering pattern originating from the one-axis rocking scans as explained above. Increasing the temperature above T_c to $T = 29.3\,\mathrm{K}$ in Fig. 5.1 (a2), a ring of intensity is observed with a superimposed faint sixfold pattern reminiscent of the skyrmion lattice phase. The data suggests skyrmionic correlations in the FD regime as a precursor phenomenon prior to the onset of long-range skyrmion lattice order. However, it is important to note that SANS does not allow to distinguish between a multi-$\vec{Q}$ structure and a coincidental superposition of single-$\vec{Q}$ structures under 120°. We return to this point below. The faint sixfold pattern in the FD regime has the same azimuthal orientation as the skyrmion lattice phase. Increasing the temperature within the FD regime further to $T = 30.5\,\mathrm{K}$, only a broad ring of intensity remains and the sixfold pattern vanishes. Altogether, the sixfold scattering pattern is a key feature within the FD regime approaching the onset of long-range order in the skyrmion lattice phase.

Measurements with a magnetic field perpendicular to the neutron beam complement the SANS data set in Figs. 5.1 (b1) to (b3). Within the skyrmion lattice phase at $T = 28.7\,\mathrm{K}$ strong scattering intensity is observed vertically associated with the skyrmion lattice order and very weak intensity horizontally corresponding to conical correlations. Again, a ring of intensity is observed at $T = 29.3\,\mathrm{K}$ in the FD regime and additional Bragg peaks along the magnetic field associated with conical correlations. Furthermore, weak intensity occurs perpendicular to the field characteristic of the skyrmionic correlations already observed in Fig. 5.1 (a2). It is important to note that the phase space occupied by the intensity on a ring perpendicular to the applied magnetic field is much larger than the conical counterparts which are confined to regions close to wave vectors parallel to the field. Hence, the integrated intensity of the ring is larger than the intensity corresponding

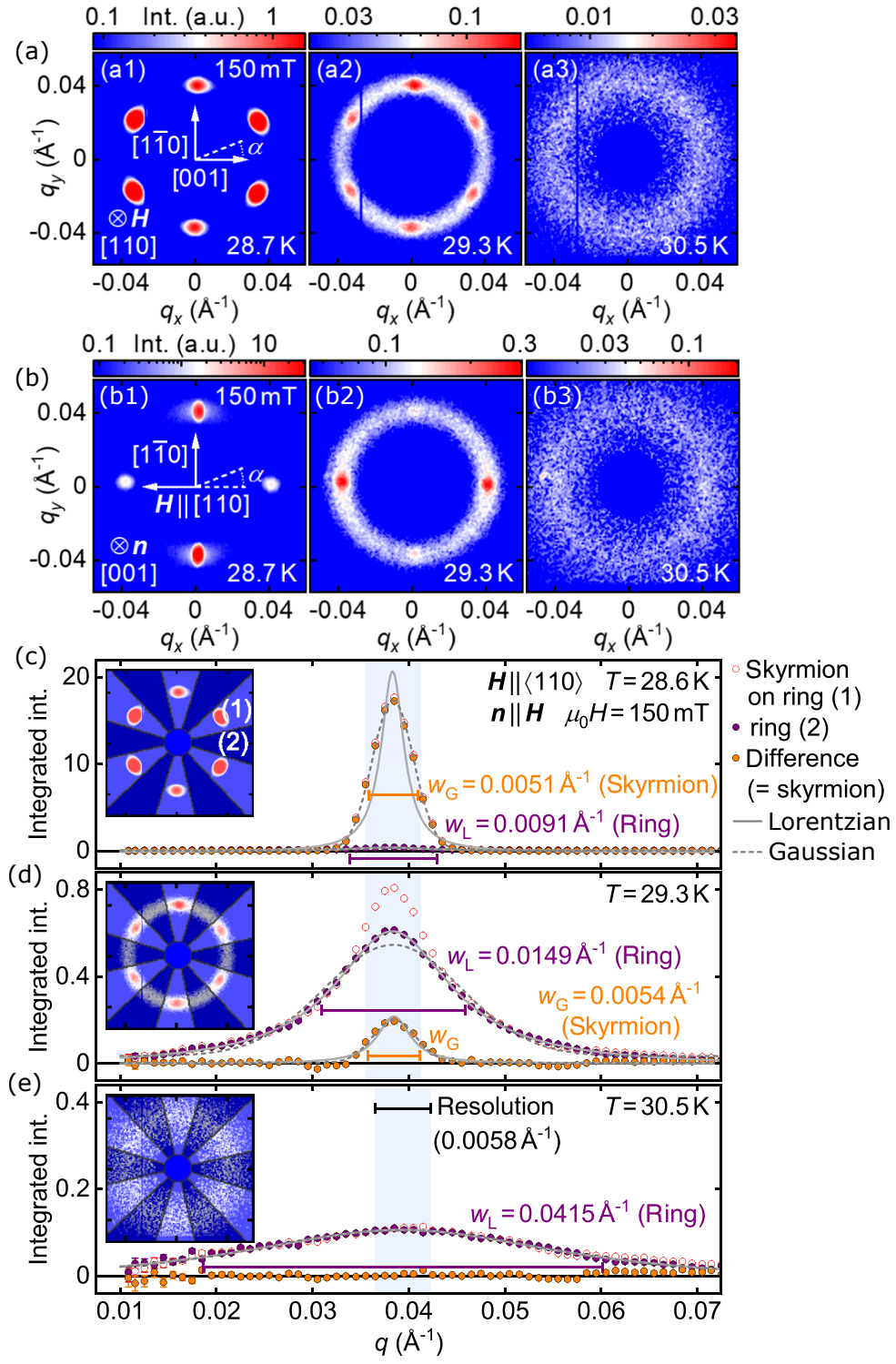

Figure 5.1.: SANS signal in an applied magnetic field parallel and perpendicular to the neutron beam. Typical 2d SANS patterns for temperatures within the skyrmion lattice phase, just above T_c and well above T_c for fields (a) parallel and (b) perpendicular to the neutron beam. (c) Intensity as a function of momentum transfer q in the skyrmion lattice phase with field parallel to the neutron beam, where data in 60° wide sectors marked (1) and (2) of the 2d intensity pattern shown in the inset were summed up. (c, d) Intensity as a function of q in the FD regime at $T = 29.3\,\mathrm{K}$ and the paramagnetic regime outside the FD regime at $T = 30.5\,\mathrm{K}$. Data in the sectors marked (1) and (2) are denoted "skyrmion on the ring" and "ring", respectively. The difference between sectors (1) and (2) is denoted "Skyrmion" in the panels. Further details are explained in the text. Figure taken from Ref. [108].

to the conical correlations. Increasing the temperature within the FD regime further to $T = 30.5\,\mathrm{K}$, a broad ring of intensity remains with a slight enhancement of intensity along the magnetic field direction.

Altogether, the data suggests neutron scattering intensity on the entire surface of a sphere with additional conical and skyrmionic correlations in the FD regime at an applied magnetic field of 0.15 T. Comparing intensities integrated in reciprocal space, the intensity of the ring perpendicular to the field is larger than the scattering intensity of the conical correlations. Increasing the temperature further to $T = 30.5\,\mathrm{K}$, the maxima of the skyrmionic correlations vanish and a gentle enhancement of intensity along the field remains. Evaluating the integrated intensities of the various correlations, they merge increasing the temperature from T_c towards $T = 30.5\,\mathrm{K}$, the highest investigated temperature.

Figs. 5.1 (c) to (e) show the intensity as a function of modulus of $\vec{q}$ in the skyrmion lattice phase and in the FD regime when the temperature is increased slightly above T_c as shown in Fig. 5.1 (a). The intensity represents the sum over sectors marked as (1) and (2) depicted in the insets corresponding to the sixfold pattern and the intensity in between, respectively. In the following, these two directions are denoted with subscripts s and r, respectively. For the subsequent considerations, it is important to note that a Lorentzian shape is expected for scattering intensity which is not restricted by the instrumental resolution. In contrast, resolution-limited scattering essentially gives rise to a Gaussian line shape. The instrumental resolution is given by $2\sigma_q = 0.0058\,\mathrm{Å}^{-1}$ taking into account the neutron wavelength spread, the scattering geometry, and the detector pixel size following Pedersen *et al.* [168]. It corresponds to twice the standard deviation of the Gaussian depicted as light-blue shading in Figs. 5.1 (b) to (d). The full width at half maximum is given by $\Delta_q = 2\sigma_q\sqrt{2\log 2} \approx 0.0068\,\mathrm{Å}^{-1}$.

In the skyrmion lattice phase shown in Fig. 5.1 (c) the intensity is Gaussian shaped in sector (1) corresponding to a resolution-limited scattering intensity. To emphasize this point an additional Lorentzian is shown for comparison. Quantitatively, the full width at half maximum of the measured Gaussian line shape is $w_G = 0.0051\,\mathrm{Å}^{-1}$ which is smaller than the calculated resolution $\Delta_q = 0.0068\,\mathrm{Å}^{-1}$. The measured resolution limit w_G permits to calculate a lower estimate of the correlation length of the sixfold scattering pattern. For our SANS setup we assume to be able to resolve a broadening of the magnetic Bragg peak by 20 % beyond the resolution limit. The correlation length of such a signal would be $\xi_s \gtrapprox 2/\sqrt{(1.2w_G)^2 - w_G^2} = 591\,\mathrm{Å}$. Hence, the correlation length ξ_s of the skyrmion lattice must be considerably larger than 591 Å which is consistent with very large correlation lengths inferred from the magnetic mosaicity [86]. Furthermore, we can analyse the intensity in sector (2). Although it is not distinguishable in the 2d scattering patterns,

the very weak intensity can be carefully assessed as a function of momentum transfer q revealing a Lorentzian line shape with FWHM $w_L = 0.0091\,\text{Å}^{-1}$. The result corresponds to a correlation length of $\xi_r = 2/\sqrt{w_L^2 - \Delta_q^2} \approx 330\,\text{Å}$. The value is consistent with the correlation length in zero magnetic field at the phase transition from paramagnetism to helimagnetic order in Ref. [112]. Importantly, it is significantly lower than ξ_s.

In the FD regime at $T = 29.3\,\text{K}$ displayed in Fig. 5.1 (d) the intensity within sector (1) and (2) are depicted as open and filled markers, respectively. The intensities essentially coincide except within a small range close to the maximum. The intensity in sector (2) is well described by a Lorentzian function with a FWHM of $w_L = 0.0149\,\text{Å}^{-1}$. A Gaussian line shape is shown for comparison as dashed line. The width of the Lorentzian line shape exceeds the resolution limit significantly and corresponds to a correlation length of $\xi_r \approx 150\,\text{Å}$. The difference between the intensity in sector (1) and (2) depicted as orange symbols represents the faint sixfold scattering intensity. Qualitatively, its line shape is best described by a Gaussian that is characteristic of resolution-limited scattering. For comparison a Lorentzian is shown as grey solid line. The Gaussian full width at half maximum is $w_G = 0.0054\,\text{Å}^{-1}$. Hence, the faint sixfold scattering intensity exhibits a correlation length substantially exceeding $\xi_s \gtrapprox 591\,\text{Å}$ as estimated beforehand in the skyrmion lattice phase and may be as large as several thousand Å [168].

Increasing the temperature even further to $T = 30.5\,\text{K}$, the sixfold intensity distribution vanishes. The intensity as a function of momentum transfer q coincides in sectors (1) and (2). The line shape is well described by a Lorentzian with a FWHM $w_L = 0.0415\,\text{Å}^{-1}$ corresponding to a correlation length of $\xi_r = 49\,\text{Å}$.

5.3.2. Neutron resonance spin-echo

The results of SANS measurements observing resolution-limited skyrmionic correlations in the FD regime raise the question of their lifetime. This information allows to demonstrate that the correlations are indeed skyrmionic as inferred from FMR results below. It is also essential to understand the nature of the condensation of the skyrmion lattice from the paramagnetic regime. Although there is no evidence for hysteresis effects in any of the investigated physical properties, we find it helpful to confirm that there are no remnants of the skyrmion lattice phase in the FD regime causing the faint sixfold intensity pattern.

An ideal probe to clarify this question is neutron spin-echo spectroscopy, which offers the necessary sub-μeV energy resolution. In our study, we focussed on the scattering intensity of the skyrmionic correlations. To confirm that our results are consistent with other studies, we performed longitudinal MIEZE measurements at RESEDA investigating the conical correlations for an applied magnetic field of 240 mT (not shown). These results

are in excellent agreement with previous measurements at IN15 at the ILL reported in Ref. [285], where ferromagnetic spin-echo spectroscopy was employed.

Shown in Fig. 5.2 are results of the MIEZE measurements. As in SANS measurements the field was applied along the crystallographic $\langle 110 \rangle$ direction. Data were recorded with magnetic field parallel and perpendicular to the neutron beam, respectively. In both cases the same Bragg peak was investigated associated with the sixfold scattering pattern of the SANS studies. Probing the same location in reciprocal space, the same dynamical properties are expected. It therefore proves that the data were not contaminated by spurious scattering.

Figs. 5.2 (a) and (b) display the intermediate scattering function $S(q,\tau)/S(q,0)$ as a function of spin-echo time τ for various temperatures above and below $T_{\rm c}$ for magnetic field parallel and perpendicular to the neutron beam, respectively. The data are shifted vertically for better visibility. In both cases data is fitted well by a single exponential decay $\exp(-(\Gamma/\hbar)\cdot\tau)$ shown as solid lines. Γ denotes the quasielastic linewidth and the associated lifetime is $t_0 = \hbar/\Gamma$. Summarised in Fig. 5.2 (c) is the temperature dependence of the energy-integrated scattering intensity characteristic of the long-range ordered skyrmion lattice below $T_{\rm c} \approx 28.8\,{\rm K}$ and the quasielastic linewidth Γ of the skyrmionic fluctuations observed above $T_{\rm c}$. The magnetic order in the skyrmion lattice phase is static within the tiny quasielastic energy resolution limit ($\ll 0.1\,\mu{\rm eV}$). The upper and lower limit of the skyrmion lattice phase is clearly determined by the elastic scattering intensity.

Above the transition temperature where the elastic scattering intensity vanishes, the quasielastic linewidth Γ is finite. As expected, the same quantitative temperature dependence for field parallel and perpendicular to the neutron beam is observed. The linewidth $\Gamma \approx 0.6\mu{\rm eV}$ determined at 29.3 K where the faint sixfold pattern is observed in SANS corresponds to a lifetime of $t_0 \approx 1\,{\rm ns}$. Towards the skyrmion lattice phase the linewidth decreases and lifetimes reach at least several ns. In summary, our measurements with ultrahigh energy resolution reveal that the magnetic correlations in the FD regime are fully dynamic.

5.4. Summary and conclusions

In summary, SANS measurements reveal scattering intensity on the surface of a sphere in reciprocal space in the fluctuation disordered regime. The intensity is more pronounced along the magnetic field and in a plane perpendicular to the applied field. The intensity in a plane perpendicular to the field exhibits a sixfold pattern reminiscent of skyrmion lattice order in three ways. First, the modulus of the wave vector $|\vec{Q}|$ has the same value as the long-range skyrmion lattice order below $T_{\rm c}$. Second, the orientation of the sixfold

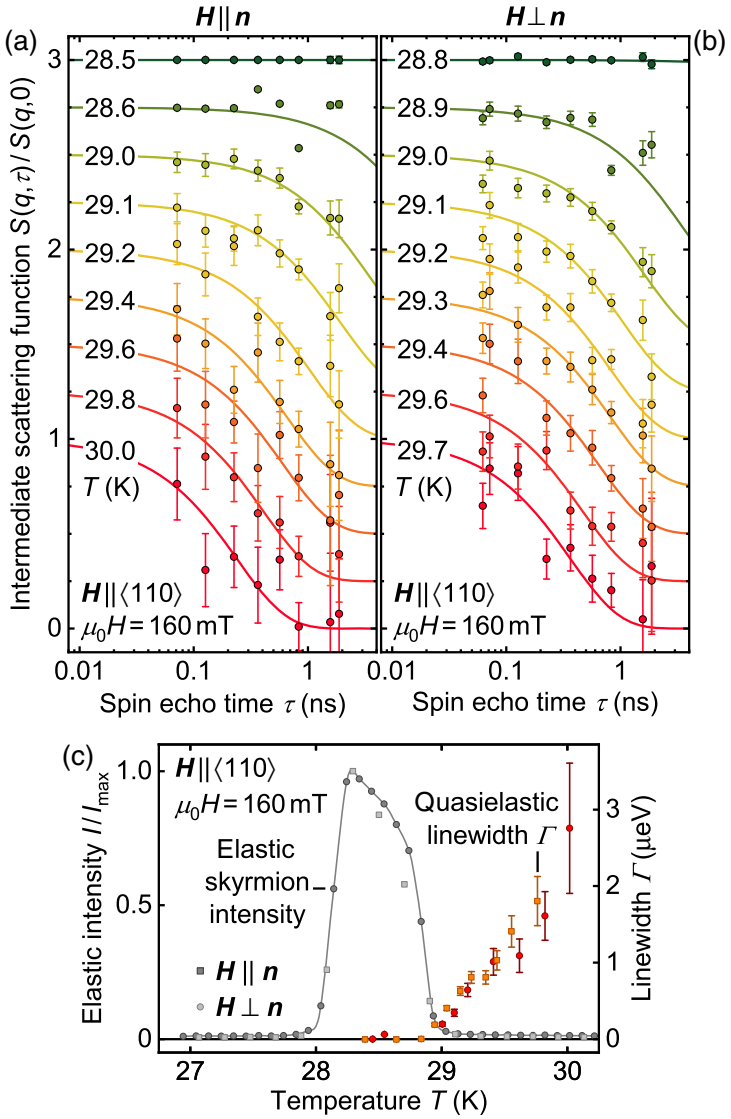

Figure 5.2.: Typical quasielastic behaviour of the skyrmion lattice-paramagnetic phase transition determined by the MIEZE technique. (a, b) Intermediate scattering function $S(q,\tau)/S(q,0)$ as a function of spin-echo time τ for various temperatures below and above T_c for magnetic fields parallel and perpendicular to the neutron beam. Solid lines correspond to fits of a single exponential decay. (c) Normalised elastic scattering intensity of the skyrmion lattice and quasielastic linewidth Γ, both as a function of temperature. Error bars of the elastic data are smaller than the marker size. The energy resolution of the quasielastic data is well below 0.1 μeV. Figure taken from [108].

pattern with respect to the crystallographic lattice is the same as below T_c. Third, the correlation lengths and line shapes are resolution limited and clearly reminiscent of long-range skyrmion lattice order.

Results from neutron resonance spin-echo spectroscopy measurements reveal that the sixfold pattern in the fluctuation disordered regime is fully dynamic down to the ordering temperature T_c and exclude the possibility of static remnants of long-range order of the skyrmion lattice phase. The fluctuations are characterised by a critical slowing down with lifetimes exceeding several nanoseconds.

Signal contributions in the fluctuation disordered regime that are reminiscent of the skyrmion lattice phase are also observed in complementary longitudinal and transverse ac susceptibility measurements as discussed in detail in Ref. [108]. Furthermore, all-electrical microwave spectroscopy allows to distinguish between fortuitous single-$\vec{Q}$ correlations under 120° and a multi-$\vec{Q}$ structure. Signatures are found in the fluctuation disordered regime reminiscent of the counter-clockwise gyration mode of the skyrmion lattice. Furthermore, the frequency of the excitations around 10 GHz is much faster than the lifetime of the fluctuations. Altogether, this result provides strong evidence of multi-$\vec{Q}$ correlations with an underlying rigid phase relationship that is reminiscent of long-range skyrmion lattice order and the associated non-trivial topological winding.

Finally, our findings can be interpreted in the framework of weak crystallisation. In the Landau soft-mode mechanism of the formation of crystals out of the liquid, the ordered state gains energy from cubic interactions of density waves $\rho_{\vec{q}}$ when three ordering vectors add up to zero, thus forming triangles which favour hexagonal lattices in two spatial dimensions. In the Ginzburg-Landau energy functional, that may describe the magnetisation field of helimagnets, the quartic term analogously yields a cubic term of the modulated moment amplitudes $\vec{m}_{\vec{q}}$ for a finite magnetisation that gains energy if three wave vectors add up to zero [14, 289, 290]. Due to symmetry the vectors lay in a plane perpendicular to the uniform magnetisation favouring the formation of a trigonal skyrmion lattice perpendicular to the field. Our observations are furthermore consistent with the hierarchy of energy scales and our classification is consistent with the Brazovskii scenario of a fluctuation-induced first-order transition at zero field. More details can be found in Ref. [108].

6. Search for microwave-induced instabilities in a chiral magnet

Numerical simulations by Mochizuki *et al.* show that under intense microwave radiation the counter-clockwise excitation of the skyrmion lattice is redshifted and the magnetic long-range order melts within nanoseconds [81]. In this chapter our experimental approach is discussed on applying strong microwave fields continuously to the magnetic skyrmion lattice in Cu_2OSeO_3. Simultaneously, the collective magnetic excitation spectra is recorded employing the newly developed 2-tone all-electrical microwave spectroscopy (FMR) technique. In addition, effects on the long-range order of the skyrmion lattice and conical phase are detected on a microscopic scale employing small angle neutron scattering (SANS) that is combined with a coplanar waveguide to apply intense microwave radiation to the sample.

Our study is limited by certain experimental boundary conditions. The penetration depth of the microwave due to the skin effect scales with $\propto \sqrt{1/\sigma\omega}$ with the electrical conductivity σ and the microwave frequency ω [30]. Therefore, the insulator Cu_2OSeO_3 was chosen among the helimagnets yielding skyrmion lattices. In numerical simulations excitation fields on the order of $\sim 2\,\mathrm{mT}$ were applied. Whereas cavities allow larger excitation values and a homogeneous excitation field, they are limited to a single frequency. Therefore, a coplanar waveguide allowing a wide range of frequencies was employed with the drawback of an inhomogeneous field and smaller field amplitudes of the order of $\sim 0.1\,\mathrm{mT}$.

The chapter is organised as follows. Specifics about the multiferroic Cu_2OSeO_3 are explained that are beyond the introduction of the properties of skyrmion lattices in chiral magnets in Sec. 1.2. Subsequently, the sample studied, the SANS setup, the 1-tone and 2-tone FMR technique, and the setup used to determine the temperature correction are presented in the experimental methods section. The results are presented in three parts. First, ohmic and resonant heating effects were recorded as a function of magnetic field, temperature, excitation frequency and field. This allowed to define a temperature correction procedure for the FMR and SANS data sets. Second, FMR spectra are presented probing the collective excitations under intense microwave radiation. Third, results of

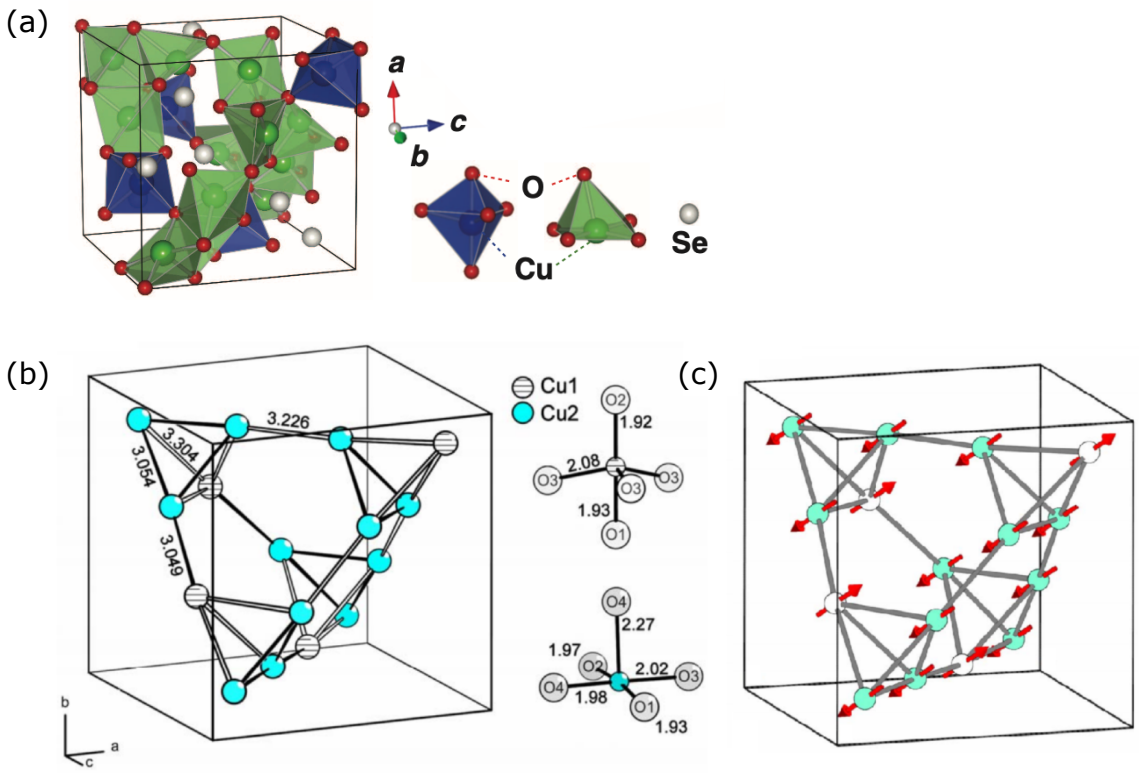

Figure 6.1.: Crystal and magnetic structure of Cu_2OSeO_3. (a) Crystal structure of Cu_2OSeO_3. (b) Simplified depiction showing only the two different types of Cu ions, their connectivity and distance in units of Angström. Edge sharing CuO_5 are indicated by solid lines and corner sharing CuO_5 by open lines. The local coordination environments of the Cu-ions are distorted to trigonal bipyramidal and square pyramidal units, respectively. (c) Ferrimagnetic spin arrangement at Cu^{2+}-sites. Figures taken and adapted from Refs. [20, 291].

SANS measurements are shown recording changes of the magnetic long-range order of the skyrmion lattice and conical phase under intense microwave fields. Finally, the results are summarised and discussed.

6.1. Topologically non-trivial spin textures in Cu_2OSeO_3

Cu_2OSeO_3 gained interest as an insulating multiferroic material with both dielectric and magnetic order before it was identified as a host of a skyrmion lattice order [20, 89, 291]. In magnetoelectric materials magnetisation can be induced by the application of an electric field and, vice versa, a magnetic field can lead to an induced electric polarisation. It allows an energy efficient manipulation of the magnetic order as dissipation effects of an electric

field in insulators is negligible as compared to a manipulation by means of electric currents in metals and semiconductors.

Cu_2OSeO_3 crystallises in the non-centrosymmetric space group $P2_13$ lacking inversion symmetry [292]. This is the same space group as the $B20$ compounds MnSi, $Fe_{1-x}Co_xSi$ and FeGe. But its unit cell with a lattice constant of $8.9235\,(2)$ Å ($T = 300$ K) is much more complex [291, 292]. The crystal structure consists of CuO_5 polyhedra and tetrahedral SeO_3 lone pairs as shown in Fig. 6.1 (a). The polyhedra form either trigonal bipyramidal (Cu1) or square pyramidal (Cu2) units in a ratio of 1:3 as displayed on the right hand side of Fig. 6.1 (b). The Cu-ions (Spin $S = 1/2$) with an oxidation number of 2+ form a network of distorted tetrahedra where neighbouring tetrahedra either share a corner or an edge indicated by solid and open lines, respectively.

The ferrimagnetic order below $T_c = 58.8$ K as shown in Fig. 6.1 (c) was determined by magnetisation measurements and neutron powder diffraction [291, 293]. Within each distorted tetrahedra the magnetic moments order according to the Kanamori-Goodenough rules with a ferromagnetic coupling between edge sharing and an antiferromagnetic coupling between corner sharing CuO_5 polyhedra. This combination leads to the collinear alignment with the three-up and one-down configuration. Due to the strong interactions within the tetrahedrons, each tetrahedron behaves as a spin-1 triplet with a large energy gap of $\Delta \sim 275$ K with respect to the lowest lying excitation, a 2 singlets state [294]. The coupling between the tetrahedra is weaker and the Kanamori-Goodenough rules are not fulfilled. The difference in intra- and intertetrahedral exchange interaction can be seen in the magnon spectrum which is split into high- and low-energy bands, respectively. The gap was observed at the Brillouin zone centre by means of thermodynamic data [294], Terahertz electron spin resonance [295], far-infrared [296] and Raman spectroscopy [297] before a complete picture of magnetic excitations was established by means of inelastic neutron scattering [145].

In addition, weak Dzyaloshinskii-Moriya interactions favouring a perpendicular spin alignment skew the ferrimagnetic order leading to the formation of an incommensurate helical spin structure [20, 89]. Its pitch length is $\lambda = 616(45)$ Å which corresponds to a propagation vector of $q = 0.0102(8)\,\text{Å}^{-1}$. Cubic magnetocrystalline anisotropies align the helical order along the $\langle 001 \rangle$ direction. Applying a small magnetic field the magnetic skyrmion lattice forms just below the ordering temperature T_c. Although Cu_2OSeO_3 has a different electronic structure than the metallic and semiconducting $B20$ compounds, the magnetic phase diagrams are very similar. Details about the magnetic phase diagram, the skyrmion lattice state, and the spin excitations are given in Sec. 1.2.

The structure of the skyrmion lattice in Cu_2OSeO_3 was first observed employing Lorentz transmission electron microscopy (LTEM) and SANS [20, 89]. Recently, the magnetic

structure of the skyrmion lattice phase in Cu_2OSeO_3 was studied employing REXS where a splitting of the Bragg peaks of the sixfold scattering pattern was observed. Langner *et al.* ascribe the splitting to two superposed skyrmion lattices forming a moiré pattern [298]. The authors observe an energy splitting between the peaks of 2 eV and suggest that the sublattices originate from the two inequivalent copper cites Cu^{I} and Cu^{II}. However, in a subsequent study Zhang *et al.* showed that the observation of multiple peaks can be simply explained by the presence of multiple domains of the skyrmion lattice [299]. Depending on the magnetic field history a multi-domain state can be created by the application of the magnetic field away from high symmetry directions by some degrees [299, 300]. In addition, the energy splitting of the Cu peaks could not be observed in x-ray-absorption measurements.

The standard technique to study collective spin excitations in helimagnets that host skyrmion lattices is all-electrical microwave spectroscopy as described in detail in Sec. 1.2.3. Pöllath *et al.* combined the technique with resonant elastic x-ray scattering (REXS), referred to as REXS FMR, in a study on Cu_2OSeO_3 [301]. A small excitation field of $3 - 10\,\mu$T using a coplanar waveguide is applied to the sample and the intensity of the magnetic Bragg peaks is recorded in reciprocal space for microwave fields turned on and off. If the resonant mode matches the microwave frequency, the intensity of the Bragg peak decreases. They determined the collective excitations and at the same time distinguished the contributions to the resonant modes from different magnetic states. However, the technique is limited since REXS is only sensitive to the surface states with a penetration depth of $\sim 30\,$nm in the case of Cu_2OSeO_3.

Concerning the lifetime of the collective excitations, the linewidth Δf can be extracted from FMR spectra as performed by Schwarze *et al.* [83]. These measurements are described in detail in Sec. 1.2.3. Furthermore, the effective damping parameter $\alpha_{\text{eff}} = \Delta f/(2f)$ with the resonant frequency f can be calculated. It comprises intrinsic and extrinsic damping and varies between 0.05 and 0.13 for MnSi, $Fe_{0.8}Co_{0.2}Si$, and Cu_2OSeO_3. In the case of Cu_2OSeO_3, the extrinsic damping, which comprises effects such as varying anisotropies in the sample, the wavevector distribution of the CPW, and magnons scattering from defects, is estimated to be substantial and the intrinsic damping parameter, that enters the Landau-Lifshitz-Gilbert equation, is only $\alpha_{\text{int}} \approx 0.02$ at $T \approx 57\,$K. This corresponds to a typical decay constant of the excitation $\tau = 1/\Delta f \approx 25\,$ns. In contrast, Ogawa *et al.* determine a decay constant of the CCW mode on the order of 1 ns in all-optical spin wave spectroscopy employing the inverse-Faraday effect and time-resolved magneto-optics [302]. However, compared to the microwave excitation the optical excitation can be different as it may only couple to spin waves with a finite range of frequencies and wave

numbers because the pump light exerts a localised ($\sim 100\,\mu$m), intense magnetic-field with possible spatial gradients.

6.2. Experimental methods

In this section we present the main aspects of the experimental setup and procedures employed for this study. After a short description of the sample dimensions and orientation, the SANS-FMR setup is presented used for neutron scattering experiments under microwave radiation. Subsequently, the FMR setup for all-electrical microwave spectroscopy by means of a coplanar waveguide (CPW) is described where the 1-tone as well as 2-tone FMR technique are introduced. In addition, the ac magnetic field distribution of the microwaves is discussed and results from sample pre-characterisation measurements are presented. Finally, we introduce the setup used to establish the temperature correction due to ohmic and resonant heating.

6.2.1. Sample and SANS setup

We used a high-quality single crystal Cu_2OSeO_3 sample which was grown by chemical vapor transport by Helmut Berger at École Polytechnique Fédérale de Lausanne, Switzerland. Samples from the same laboratory were investigated in several other experimental studies where further information on the growth procedure and further sample properties can be found in Refs. [297, 303–306]. The sample, its dimensions and orientation are shown in Fig. 6.2. It was aligned using Laue X-ray diffraction and attached to the CPW with GE varnish. The crystallographic [100] direction was vertical and the other faces were along a [110] and a $[1\bar{1}0]$ direction, respectively.

SANS measurements were performed at the beam line SANS-1 at the Heinz Maier-Leibniz Zentrum (MLZ) in Garching, Germany [187]. The properties of the setup are

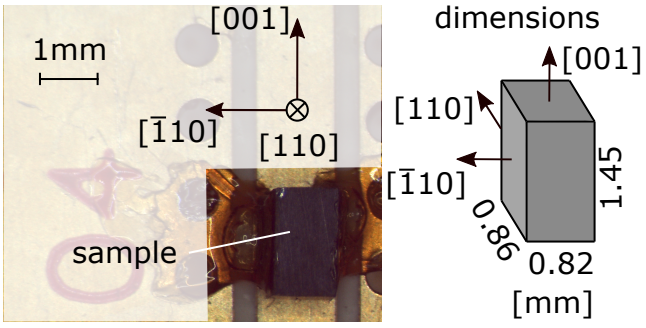

Figure 6.2.: Cu_2OSeO_3 sample orientation and dimensions as placed on the CPW.

Table 6.1.: Instrument parameters for the energy-integrated measurements at SANS-1.

parameter	unit	variable	value
momentum transfer	(Å^{-1})	q	0.01
detector pixel size	(mm)	Δ	8
incoming wavelength	(Å)	λ	6
wavelength spread (FWHM)	(1)	$\Delta\lambda/\lambda$	0.1
source aperture radius	(mm)	r_1	25
defining aperture	(mm)	r_2	0.5
source aperture - defining aperture	(mm)	L_1	20
distance defining aperture - detector	(mm)	L_2	20.35
distance sample - detector	(mm)	L_{SD}	20

listed in Tab. 6.1. We used neutrons with a wavelength $\lambda = 6\,\text{Å}$ and a bandwidth with full-width-at-half-maximum (FWHM) $\Delta\lambda/\lambda = 10\,\%$. The neutron beam was collimated over a length of 20 m where the source aperture had a diameter of 50 mm and the sample aperture a diameter of 1 mm. The sample-detector distance was 20 m. The position sensitive ^{3}He-detector with dimensions $1 \times 1\,\text{m}^2$ consisted of 128×128 pixels. The momentum transfer resolutions within the scattering plane and perpendicular can be calculated as described in Sec. 2.5. Within the scattering plane the FWHM $\Delta q = 2\sqrt{2\ln 2}\cdot\sigma = 2.83\cdot 10^{-3}\,\text{Å}^{-1}$ and the resolution expressed as FWHM for rocking scans about χ and ξ is $\Delta = 2\sqrt{2\ln 2}\cdot\sigma = 0.046°$ as depicted in Fig. 6.3. The azimuthal angular resolution expressed as FWHM is $\Delta\theta = 2\sqrt{2\ln 2}\cdot\sigma = 2.4°$.

A depiction of the SANS setup is shown in Fig. 6.3. The neutron beam enters from the left and is collimated by the sample aperture. Neutrons are detected behind the sample on the position-sensitive detector. We employed a horizontal superconducting 5 T magnet optimised for SANS measurements to apply a static magnetic field $\boldsymbol{H}_0$ along the crystallographic [110] direction and out-of-plane with respect to the CPW. The ac magnetic field $\boldsymbol{h}_{\text{rf}}$ was applied perpendicular to the static magnetic field $\boldsymbol{H}_0$ and generated by an ac current through the centre conductor as depicted in Fig. 6.3. The microwave signal with frequency f_{drive} from the frequency source (Rhode&Schwarz SMF100A) was amplified to a power P_{drive} and terminated with a diode. The linear amplifier (Mini-Circuits ZHL-5W-422+) with a maximum output power of 5 W had a bandwidth from 0.5 to 4.2 GHz. The voltage drop at the diode was measured by a lock-in amplifier.

The sample was mounted on a CPW with a width of the centre conductor of $\omega_{cc} = 1.3\,\text{mm}$ which is wider than the sample. Further details on the CPW configuration are reported below. The setup is shown in Fig. 6.4. Two cernox sensors were used to monitor the

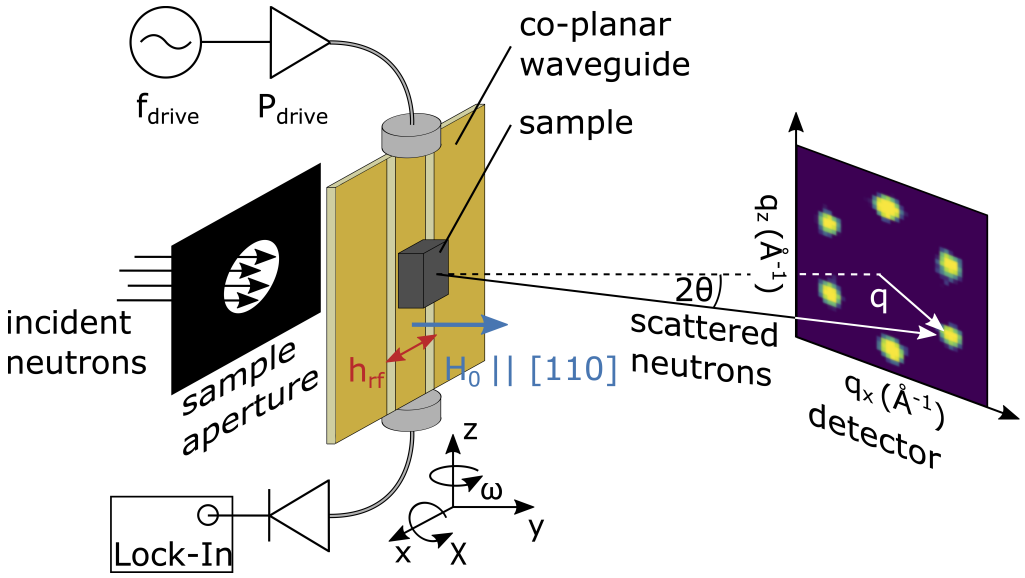

Figure 6.3.: SANS-FMR setup. Neutrons entering the instrument from the left are collimated by the sample aperture, scattered by the sample and detected. A static magnetic field $\boldsymbol{H}_0$ and an oscillating magnetic field $\boldsymbol{h}_{\mathrm{rf}}$ are applied parallel and perpendicular to the neutron beam, respectively. The latter is generated by the ac current in the coplanar waveguide. The ac frequency f_{drive} and the power P_{drive} are defined by a combination of frequency generator and broadband amplifier. The transmitted signal is analysed by a diode connected to a lock-in amplifier.

temperature as positioned close to the sample on the holder and the CPW, respectively. Temperatures in a range between 4 and 300 K were accessible using a standard closed cycle cryostat (CCR-19) from the sample environment group of the MLZ Garching. To optimise the thermal coupling, 120 mbar of Helium at a temperature of $T = 50$ K were used as exchange gas within the cryostat .

Every temperature sweep was performed following the same measurement procedure. First, the static magnetic field as well as the ac magnetic field were applied and, subsequently, the system was cooled from $T = 65$ K, a temperature far above the magnetic ordering temperature T_{c}. At each temperature the system equilibrated for several minutes before rocking scans in horizontal and vertical directions were performed.

6.2.2. Ferromagnetic resonance spectroscopy setup

To observe the local dynamic response of the system to the intense microwave excitation, complementary all-electrical microwave measurements were performed at the Walther-Meißner-Institute in Garching, Germany. The measurements were part of the Master thesis by Lukas Liensberger. The description of the setup follows Ref. [189].

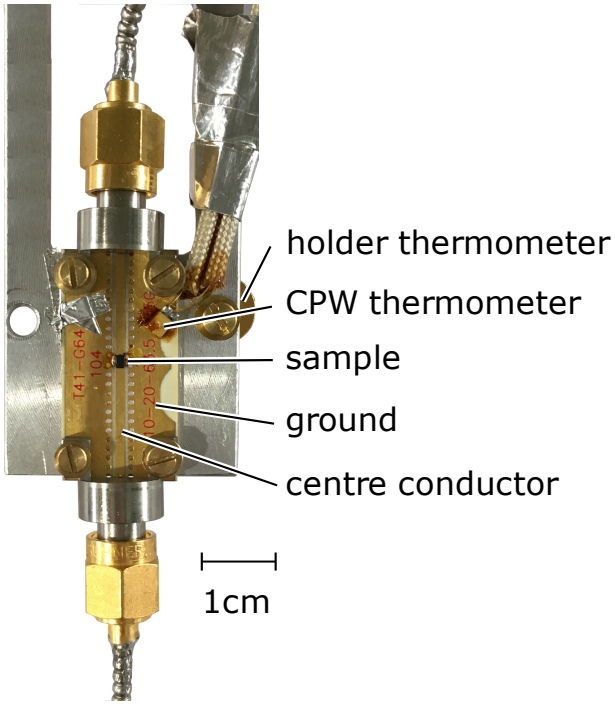

Figure 6.4.: Cu_2OSeO_3 sample on the coplanar waveguide during SANS measurements. The holder thermometer T_{holder} was positioned on the aluminium holder with a brass screw and the CPW thermometer was attached to the ground of the CPW with GE varnish. Both thermometers are cernox sensors.

The same sample and CPW as employed in the neutron scattering study were used for the investigation and the sample was not removed from the waveguide during the transfer between the experiments. The waveguide was mounted on a copper dipstick as shown in Fig. 6.5 and inserted on a variable temperature inset into a cryostat. A superconducting magnet was used to apply magnetic fields perpendicular to the ac magnetic field and along the crystallographic [110]-direction identical to the neutron scattering experiments. A holder thermometer was positioned on the sample holder. In addition, a cernox thermometer was positioned onto the CPW, but it could not be monitored during the FMR measurements described in this section.

We used two different experimental setups which we refer to as "1-tone" and "2-tone", both depicted in Fig. 6.6. In the 1-tone setup the signal from the VNA was amplified by two consecutive amplifiers (Kuhne LNA BB 202 A and Rhode&Schwarz SMF100A) to drive the system with a power P at frequency f and the complex transmission S_{21} was measured as described in Sec. 3.3.1. Here, the intense microwave radiation drives the system and acts simultaneously as probe, hence, $f_{\mathrm{drive}} = f_{\mathrm{probe}} = f$. A 30 dB-attenuator protected port 2 of the VNA.

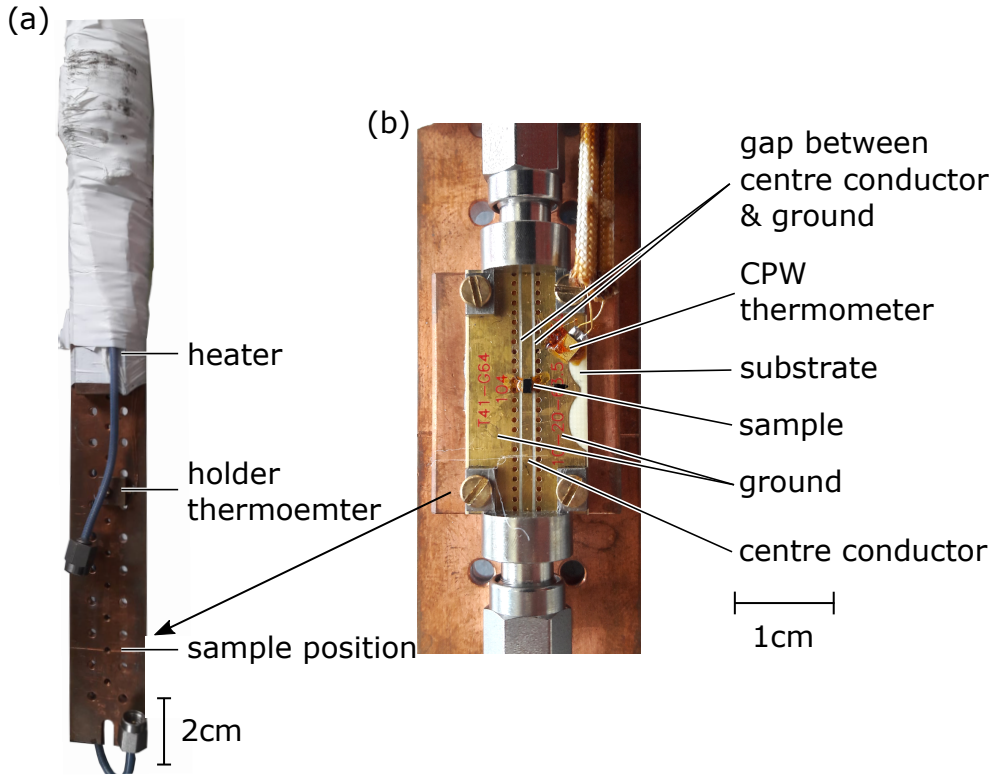

Figure 6.5.: Coplanar waveguide during FMR measurements. (a) A thermometer is positioned on the copper holder approximately 3 cm above the sample. (b) The sample is attached centrally on the CPW with GE varnish.

The 2-tone setup shown in Fig. 6.6 (b) aims to resemble the continuous pump-probe aspect of the neutron scattering measurements. The system is excited by an intense microwave with fixed frequency f_{drive} and a high power P_{drive} and simultaneously probed by a scanning signal with frequency f_{probe} and low power P_{probe}. A directional coupler (Mini-Circuis ZFBDC16-63HP+) was used to generate the necessary superposition of both signals at the OUT port which passes on to the CPW. The strong driving signal passed from the IN to the OUT port with a small attenuation, typically -0.5 dB, whereas the probe signal was attenuated by -20 dB from the REV to the OUT port.

The same frequency source (Rhode&Schwarz SMF100A) and amplifier (Mini-Circuis ZHL-5W-422+) were used as in the neutron scattering experiment. A vector network analyser (VNA) (Agilent N5242A PNA-X) measured 201 data points of the complex transmission parameter S_{21} with a port power $P = 10\,\text{dBm}$ in a frequency range $0.1 \leq f_{\text{probe}} \leq 3.25\,\text{GHz}$ with an intermediate frequency (IF) bandwidth of 200 Hz and averaged 10 times over the frequency trace. The directional coupler attenuated the probe signal by -20 dB leading to a signal power of $-10\,\text{dBm} \approx 0.1\,\text{mW}$ at the OUT port, between 4 to 5 orders of magnitude smaller than the driving signal $P_{\text{drive}} \approx 37\,\text{dBm}$. The driving

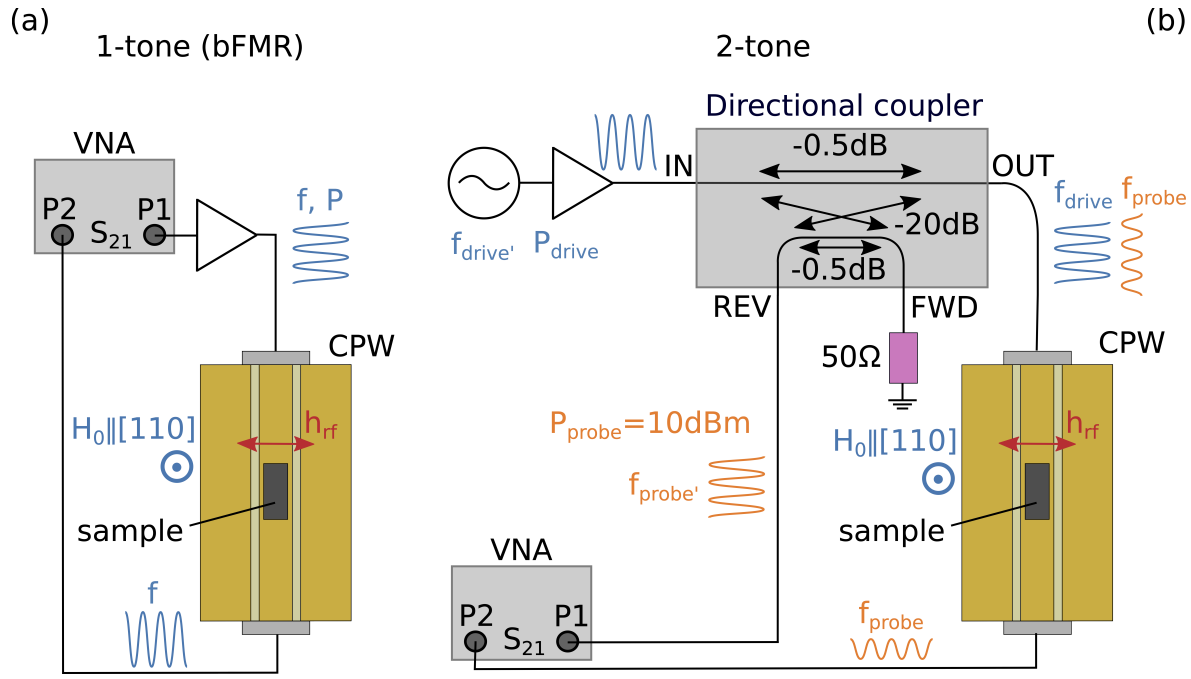

Figure 6.6.: 1- and 2-tone FMR setup. (a) In the 1-tone setup, the VNA signal with frequency f is amplified to a power P before it passes on to the CPW where the sample is positioned centrally. The static magnetic field is along a crystallographic [110]-direction and perpendicular to the ac magnetic field $\boldsymbol{h}_{\mathrm{rf}}$. The VNA measures the complex transmission parameter S_{21}. (b) In contrast, a directional coupler in the 2-tone experiment generates a superposition of a large driving power P_{drive} at frequency f_{drive} and a scanning signal with frequency f_{probe} and much smaller power P_{probe} at the OUT port which passes on to the CPW.

frequency source and the VNA were not phase-locked, i.e. they both used their own internal oscillator. Hence, the VNA did not measure the strong driving signal which would have dominated at the driving frequency f_{driving}.

We performed magnetic field sweeps at a constant driving frequency and a constant power as well as a constant holder temperature T_{holder}. Temperatures between 51 and 59 K were investigated with a step size of $\Delta T = 0.25\,\mathrm{K}$. For each driving frequency and power the measurement protocol started at the lowest temperature at zero magnetic field. The magnetic field was decreased down to $\mu_0 H_0 = -90\,\mathrm{mT}$ and, subsequently, ramped up to $\mu_0 H_0 = 90\,\mathrm{mT}$ with a ramp rate of $2\,\mathrm{mT/min}$. The VNA continuously measured the complex transmission parameter S_{21} as described above. After reaching 90 mT, the magnetic field was set to zero, the temperature was changed by 0.25 K and the protocol was repeated.

Employing a CPW instead of a cavity allows to access a large frequency range with the disadvantage of an inhomogeneous ac magnetic field. Using the finite element method, the ac magnetic field distribution around the CPW was simulated as shown in Fig. 6.7. The in-

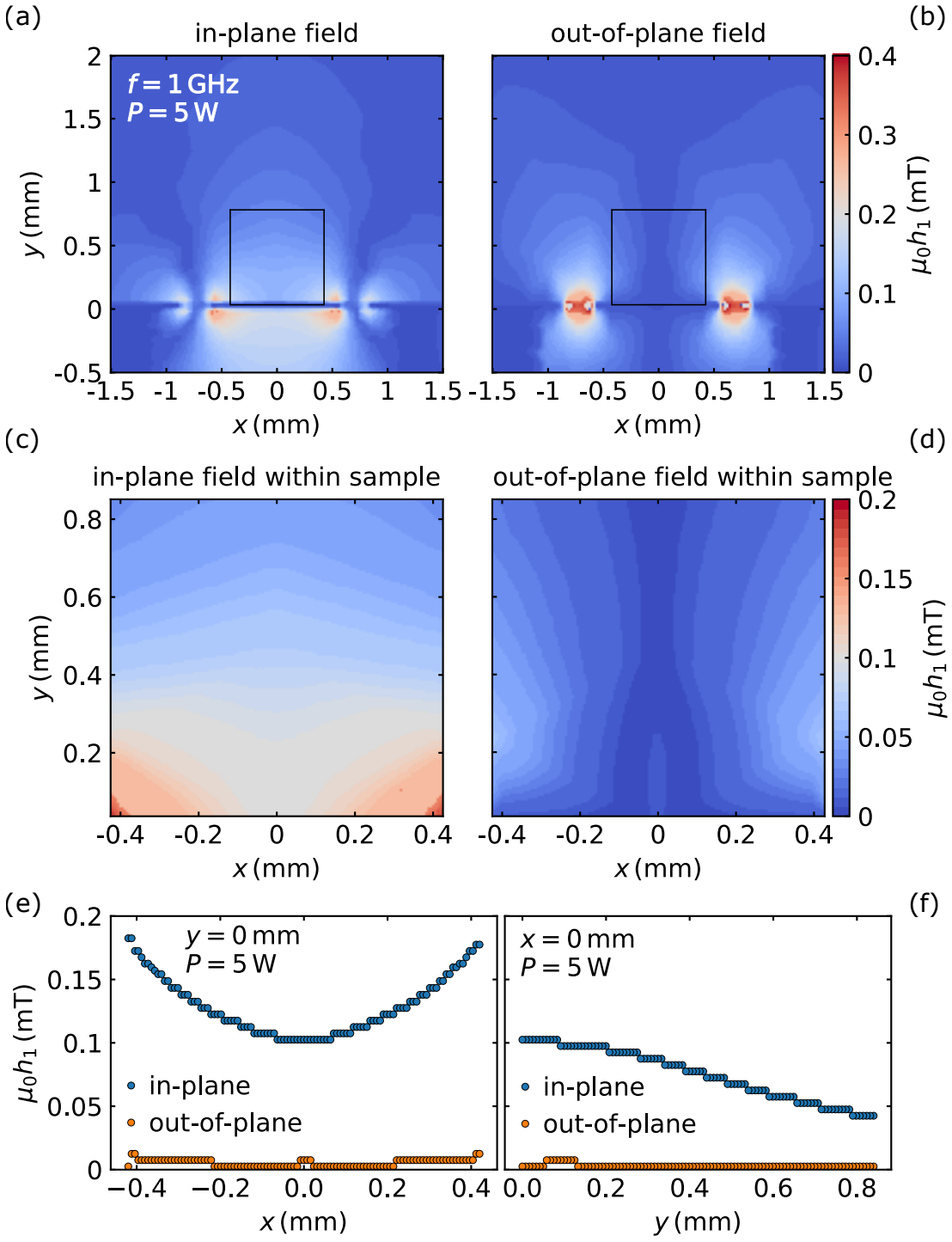

Figure 6.7.: AC magnetic field distribution. (a) The in-plane and (b) the out-of-plane ac magnetic field around the CPW simulated by the finite element method. Black lines depict the sample edges. (c) The in-plane and (d) the out-of-plane ac magnetic field within the sample. (e) A cut along the $x-$direction at the CPW surface showing the in- and out-of-plane ac magnetic field within the sample. (f) A cut along the $y-$direction showing the decrease of the ac magnetic field in the in-plane component with an increasing distance from the CPW.

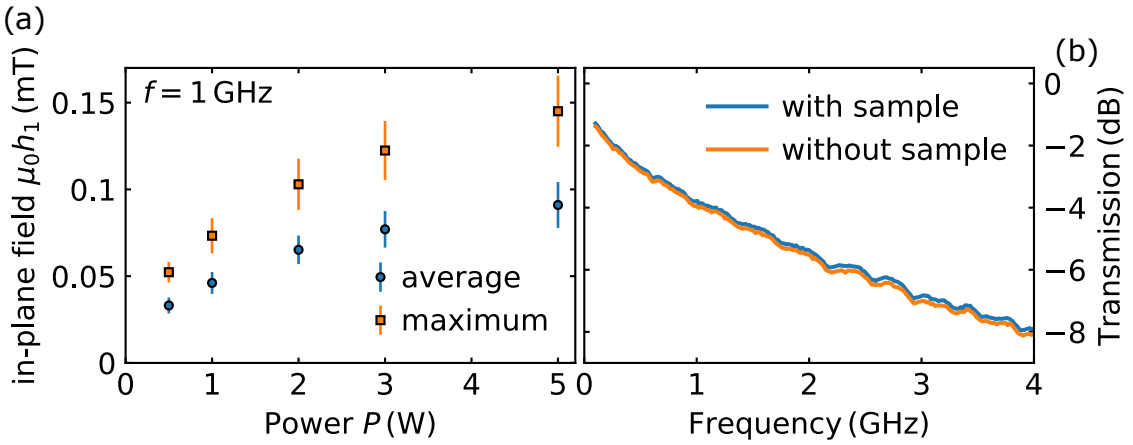

Figure 6.8.: Power and frequency dependence of the ac magnetic field. (a) The average and maximum value of the in-plane component of the ac magnetic field as a function of the frequency source output power. (b) The frequency dependence of the transmission of the dipstick as employed during the SANS measurements.

plane component dominates on the centre conductor but a strong out-of-plane component is observed at the edges around $\pm 0.65\,\mathrm{mm}$ as shown in Fig. 6.7 (b). The CPW width $\omega_{\mathrm{cc}} = 1.3\,\mathrm{mm}$ was chosen to minimise the out-of-plane component of the ac magnetic field within the sample although a larger centre conductor is disadvantageous for FMR as the sensitivity scales with $1/\omega_{\mathrm{cc}}$. The in-plane component dominates throughout the sample as shown in Fig. 6.7 (c) and (d). The cuts through the 2d ac magnetic field distribution in Fig. 6.7 (e) and (f) show that the field increases close to the CPW surface towards the centre conductor edges and decreases with increasing distance from the CPW.

Fig. 6.8 (a) shows the input power dependence of the maximum and average ac magnetic field for $f_{\mathrm{drive}} = 1.0\,\mathrm{GHz}$ where the input power corresponds to the output power of the amplifier and the ac magnetic field is averaged over the sample volume. Throughout this thesis power values correspond to the amplifier output for consistency and simplicity. The transmission of the dipstick, i.e. cables, connectors and CPW, as a function of frequency with and without sample is shown in Fig. 6.8 (b). The transmission with sample is slightly better than without over the entire frequency range. For ac magnetic field values in Fig. 6.7 and 6.8 the dipstick transmission is already considered.

To determine the different collective excitation modes of the system and the magnetic phase diagram, the sample was characterised using the 1-tone technique following the aforementioned procedure. Typical data is shown in Fig. 6.9 (a) to (c) where the imaginary part of the derivative divide of the transmission parameter $\mathrm{Im}(\mathrm{d_D} S_{21})$ is shown as a function of frequency and magnetic field for various sample temperatures. The signal is symmetric with respect to the magnetic field but changes its sign going from a negative

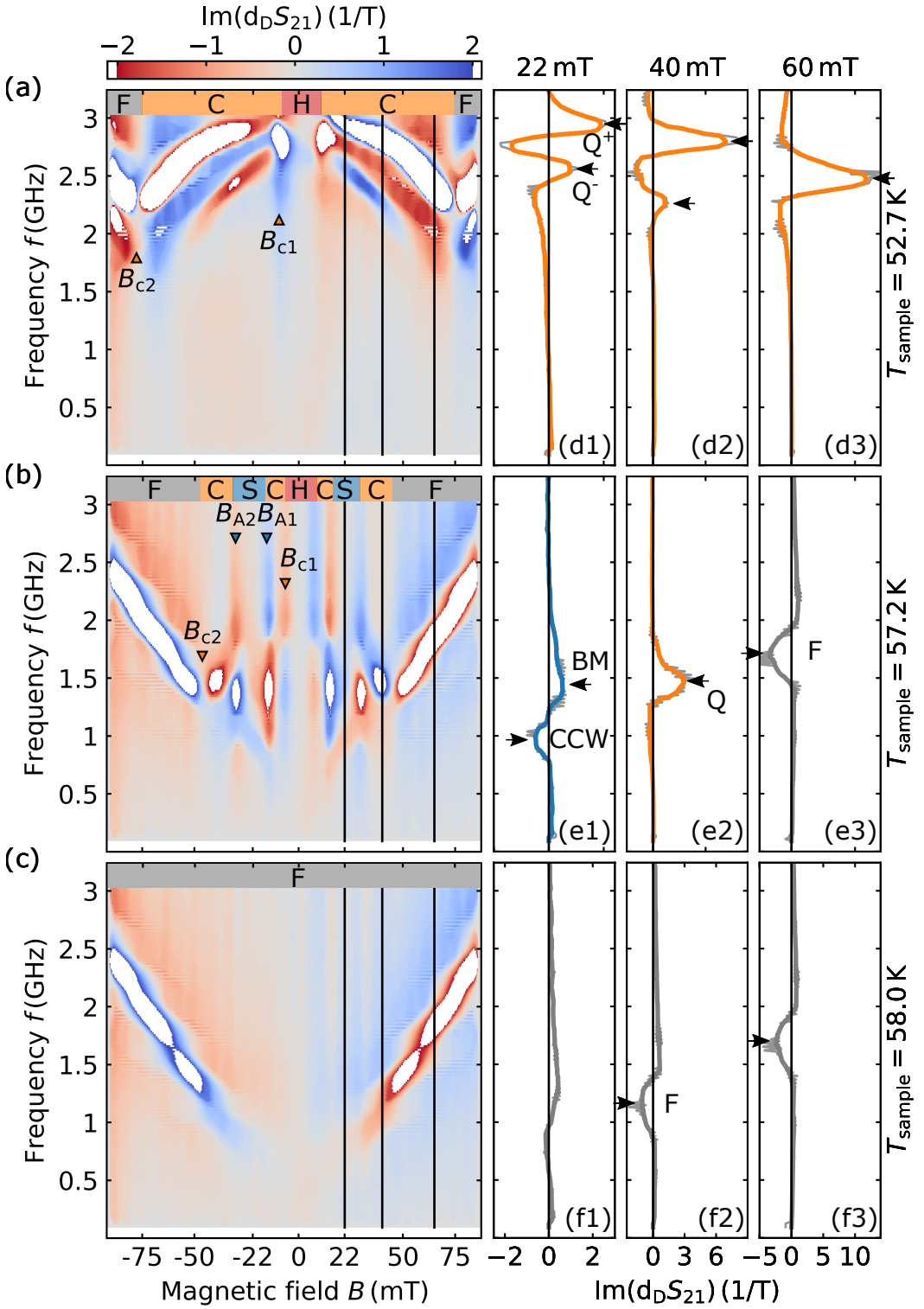

Figure 6.9.: All-electrical broadband spectroscopy in Cu_2OSeO_3. (a-c) Heat map depicting the imaginary part of the derivative divide of the complex transmission parameter S_{21} as a function of the frequency f and the magnetic field B for various sample temperatures. The spin excitations of the conical (C), the skyrmion lattice (S), and the field-polarised (F) phase can be observed. (d-f) Typical data for a constant field at selected field values. The signatures of the magnetic resonances are marked as conical (Q^+ and Q^-), counter-clockwise (CCW), breathing (BM) and field-polarised (F) mode.

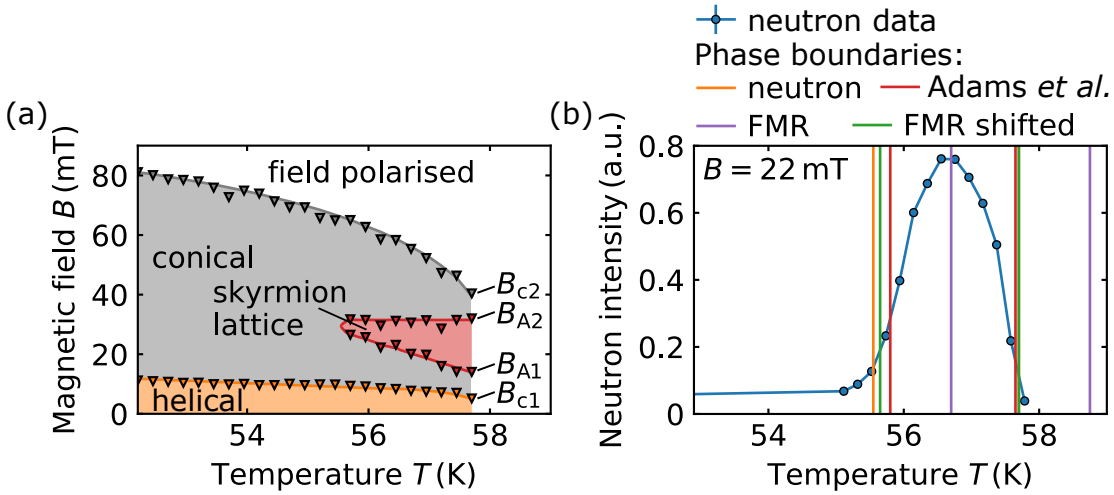

Figure 6.10.: Cu_2OSeO_3 phase diagram. (a) Magnetic phase diagram of Cu_2OSeO_3 inferred from FMR measurements. (b) Temperature correction of FMR measurements. Neutron intensity as a function of temperature to define the upper and lower phase boundaries of the skyrmion lattice phase (orange) and, in addition, phase boundaries derived from ac susceptibility by T. Adams et al. (red) [89]. Raw FMR data (purple) is off by $\Delta T = 1.05\,\mathrm{K}$ and overlaps with literature and neutron scattering data after a rigid shift (green).

to a positive magnetic field. Tracking the phase transition features (markers) for various temperatures, a phase diagram may be inferred. The features are either a change of the field dependence of the excitation as in the case when going from the field-polarised (F) to the conical (C) phase at B_{c2} or enhanced signal over several GHz as in the case when going from the conical to the skyrmion lattice (S) or the helical (H) phase at B_{A2}, B_{A1}, B_{c1}, respectively.

Cuts at constant magnetic fields in Fig. 6.9 (d1) to (f3) exhibit typical data where $\mathrm{Im}(\mathrm{d_D}S_{21})$ may be observed as maxima or minima at the resonance frequencies which are marked with arrows. These comprise the Q^+ and Q^- resonance modes in the conical phase, the counter-clockwise (CCW) and breathing (BM) mode in the skyrmion lattice phase, and the field-polarised (F) mode in the field-polarised phase. The clockwise (CW) mode may not be detected as its spectral weight is very low consistent with previous studies [83, 134] and our resolution is not sufficient. As observed in previous studies [83], the spectral weight of the conical Q^+ mode decreases towards higher fields where only signatures of the Q^- mode may be observed. Signatures of the helical excitation is not distinguishable in the heat maps but may be fitted. In addition, the transition from the conical to the helical phase may be tracked. The signal of the resonance modes observed in all phases is, in general, broad with a typical FWHM of $\Delta f \sim 0.25\,\mathrm{GHz}$.

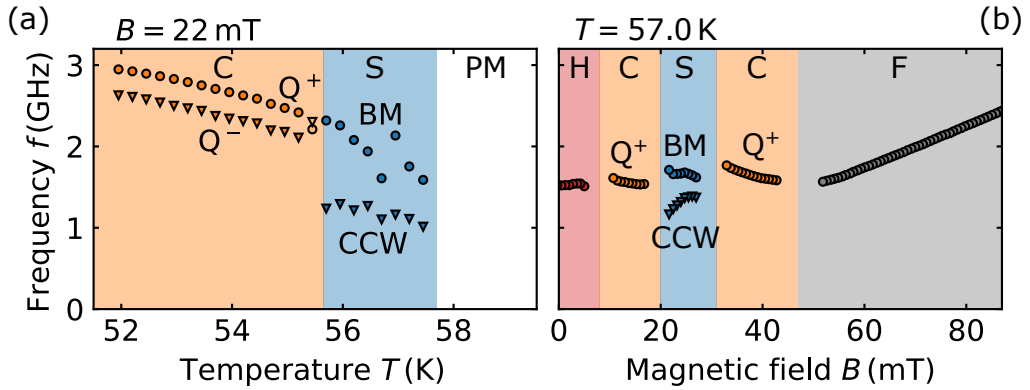

Figure 6.11.: Magnetic resonance frequencies in Cu_2OSeO_3 . (a) Temperature dependence of the conical (C) $Q^{+,-}$ resonance modes and the CCW as well as breathing mode (BM) of the skyrmion lattice for a constant magnetic field B. (b) Resonant frequencies of the helical (H), conical (C), skyrmion lattice (S) and field-polarised (F) mode as function magnetic field.

The magnetic phase diagram as inferred from the FMR spectra is shown in Fig. 6.10 (a). Fig. 6.10 (b) shows a comparison of the upper and the lower phase transition of the skyrmion lattice phase as inferred from the neutron scattering experiments and literature values with the FMR measurements [89]. The comparison shows that during the all-electrical microwave spectroscopy a constant temperature offset was present between the intrinsic sample temperature and the holder thermometer. The temperature of the FMR data can be corrected by a rigid temperature shift of $\Delta T = 1.05\,\mathrm{K}$ such that the phase transitions overlap. The data in Fig. 6.10 (a) is already corrected.

Fig. 6.11 shows the resonant frequencies as a function of (a) temperature for a constant magnetic field at $B = 22\,\mathrm{mT}$ and (b) a magnetic field for a constant temperature $T = 57\,\mathrm{K}$. In Fig. 6.11 (a) the breathing mode increases as a function of temperature from $f = 1.6$ to $2.3\,\mathrm{GHz}$ and featurelessly evolves into the conical Q^+ mode at $T = 55.7\,\mathrm{K}$. For $B = 22\,\mathrm{mT}$ the two fundamental conical excitations Q^+ and Q^- are observed. The CCW mode within the skyrmion lattice phase increases from $f = 1.0$ to $1.3\,\mathrm{GHz}$ for decreasing temperature.

The helical resonant mode at $f = 1.5\,\mathrm{GHz}$ does not exhibit a magnetic field dependence as shown in Fig. 6.11 (b). It transitions into the conical Q^+ mode at $B = 8\,\mathrm{mT}$ which exhibits a slightly negative slope as a function of field $\mathrm{d}f/\mathrm{d}H < 0$. Within the skyrmion lattice phase the breathing mode is observed at $f \approx 1.7\,\mathrm{GHz}$, changing little as a function of magnetic field, whereas the CCW mode increases from $f \approx 1.2$ to $1.4\,\mathrm{GHz}$ with increasing field. The resonant mode of the conical state at fields higher than the skyrmion lattice phase shows a negative slope and merges with the mode of the field-polarised state, which exhibits a positive slope, at $B = 47\,\mathrm{mT}$. Only the Q^+ mode is observed for fields above the skyrmion lattice phase as the spectral weight of the Q^- mode is low consistent with previous studies [83].

6.2.3. Temperature correction

The high ac currents through the CPW as well as the ac magnetic field driving the collective excitations resonantly generate strong local heating. To track these effects during the SANS measurements the thermometers were placed as closely as possible to the sample without being in the neutron beam to minimise background scattering. Nevertheless, a temperature offset between the sample and the thermometers was present. In turn, extensive measurements were performed in order to determine the precise sample temperature for the FMR and neutron scattering data sets. In the following, the two main heating effects are summarised and the temperature correction procedure is explained.

First, the ac current leads to ohmic heating of the centre conductor. The heat transfers directly to the sample which is attached to it with GE varnish as shown in Fig. 6.2. As there is apparently no direct contact between the centre conductor and the ground of the CPW, the heat transfers only indirectly through the substrate to the ground where the CPW thermometer is positioned. The gap between both as well as the underlying substrate are shown in Fig. 6.5 (b). Hence, a temperature offset between the CPW thermometer and the sample temperature must be present.

Second, the GHz magnetic microwave-field drives the uniform magnetisation and, thus, the intrinsic excitations of the sample resonantly, heating the sample. This effect depends on multiple parameters:

- the resonant frequencies of the conical, skyrmion, and field-polarised phase, which depend on the dc magnetic field and the sample temperature,
- the applied ac magnetic field amplitude and frequency,
- the temperature and magnetic field history, i.e., hysteretic effects of the magnetic state.

During the neutron scattering experiments the intensity of the conical phase was used to account for temperature differences between the sample and the thermometers since the resonant frequencies in the conical state are sufficiently larger than the resonant frequencies of the skyrmion lattice phase. However, this correction only accounts for ohmic heating by the CPW. Likewise during all-electrical microwave spectroscopy, the field-polarised phase was used as a reference to correct temperature differences between the sample and the thermometer, however, it also only accounted for the ohmic heating.

In order to track any thermal effects and the sample temperature accurately, a revised setup was used as depicted in Fig. 6.12. A small cernox thermometer (CS-1080-BR-HT) together with a small heater were attached to the top of the sample with GE varnish as pictured in the inset. The remaining parts were not changed and the same setup was

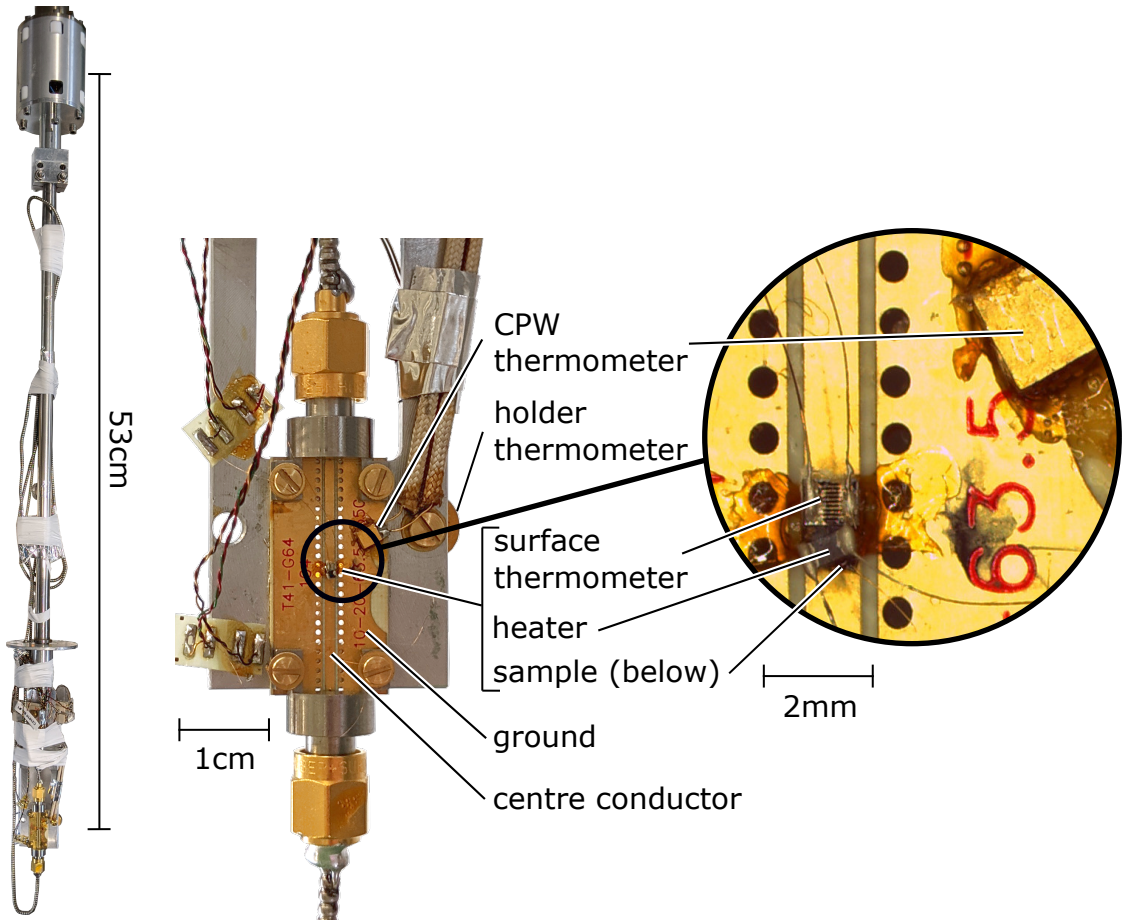

Figure 6.12.: Temperature correction setup. The previous setup was extended by a cernox sample thermometer and a heater glued directly on top of the sample.

used that was previously used during the neutron scattering experiments. In total, we monitored four temperatures which are shown in Fig. 6.12:

- T_{coupling}: Coupling temperature as recorded with a sensor at the thermal anchoring point of the sample stick. This temperature was controlled with a heater which was mounted in the vicinity of the coupling point. All other temperatures were not actively controlled during the experiments.
- T_{holder}: Holder temperature recorded with a cernox sensor at the aluminium holder.
- T_{CPW}: Temperature measured with a cernox sensor attached to the CPW ground several millimetres away from the sample as shown in Fig. 6.12 (b) and (c).
- T_{surface}: Surface temperature measured with a carbon glass thermometer (size $\approx 1\,\mathrm{mm} \times 1\,\mathrm{mm}$) attached directly to the surface of the sample with GE varnish.
- T_{sample}: Fully corrected sample temperature as determined according to the procedure described in Sec. 6.3.2. It represents the measured surface temperature, T_{surface}, as corrected by a small empirical offset listed in Tab. 6.2.

Temperature sweeps at constant dc magnetic field were performed following the same measurement protocol used in the neutron scattering experiments, but tracking the temperature progression only. Within and around the skyrmion phase the temperature was set in steps of 0.1 K and the system equilibrated for 5 min before recording data. Far above and below the skyrmion lattice phase larger temperature steps were chosen, using, however, the same equilibration time. To correct the FMR data, field sweeps were performed with a constant T_{coupling}. The system was cooled in zero dc magnetic field under an applied ac magnetic field to the lowest desired temperature. The dc magnetic field was decreased to $\mu_0 H = -120\,\text{mT}$ and increased to 120 mT with a sweep rate of 10 mT/min. Subsequently, the temperature was increased by 250 mK in zero dc magnetic field and the procedure was repeated.

6.3. Experimental results

In the following, the experimental results of the temperature correction measurements, the all-electrical microwave spectroscopy, and the SANS measurements on the effects of intense microwave radiation on the skyrmion lattice and conical phase in Cu_2OSeO_3 are presented. Excitation frequencies between 0.6 GHz and 3.6 GHz were chosen to focus on frequencies about the CCW as well as the BM resonance. At first, the ohmic and resonant heating effects of intense microwave radiation are presented. The onset of resonant heating above the ordering temperature T_c is reported which suggests coupling of the intense ac magnetic field to fluctuating skyrmion patches comparable to observations in MnSi [108]. In addition, coupling to various modes can be inferred from the temperature of the surface of the sample by means of resonant heating. Subsequently, all-electrical microwave spectroscopy as a local probe also shows a broad resonance above T_c in a limited magnetic field range reminiscent of results on MnSi [108].

In addition, two main observations were made. (1) Parts of the skyrmion lattice phase are not accessible under intense microwave radiation. In particular for excitation frequencies below the CCW mode, the sample temperature remains at or just above the ordering temperature T_c for sufficiently high excitation fields. For intermediate excitation fields the coupling to the CCW mode is observed in FMR spectra, but no long-range skyrmion lattice order emerges. (2) Azimuthal broadening of the hexagonal skyrmion lattice scattering pattern is observed for the highest excitation fields and all excitation frequencies near the skyrmion lattice resonant modes. As a function of the power of the microwave drive a threshold for the onset of azimuthal broadening is observed.

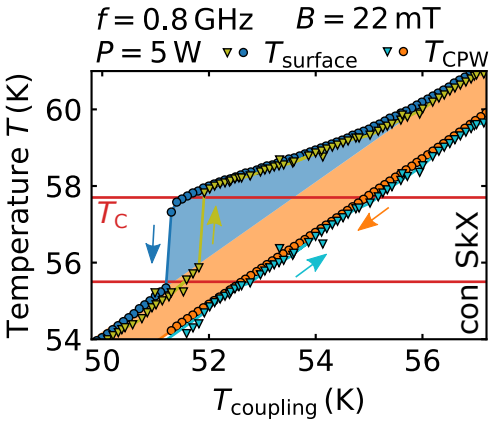

Figure 6.13.: Surface and CPW temperature in temperature sweeps. Sweeps are performed by actively changing the coupling temperature T_{coupling}. Red lines denote the paramagnetic to skyrmion lattice and the skyrmion lattice to conical phase transition, respectively. Arrows mark the sweep direction. Orange and blue shading denote ohmic and resonant heating, respectively. Solid lines are guides to the eye.

6.3.1. Temperature of the sample and setup in temperature and field scans

The temperatures at the surface of the sample, the CPW, the holder, and the coupling point were recorded as a function of magnetic field and temperature under an applied microwave field of various excitation frequencies and fields. The focus was to record the ohmic and resonant heating around the skyrmion lattice phase. In addition, measurements were carried out for several excitation frequencies and fields at temperatures down to $T = 20\,\mathrm{K}$ and dc magnetic fields up to 200 mT. Based on these measurements it became apparent that the sample temperature can be used as a probe to detect the resonance modes of the system as the coupling of the intense excitation field leads to resonant heating. In addition, the data was used to correct the FMR and SANS data for ohmic and resonant heating.

Typical temperature sweeps under increasing and decreasing temperature at a constant dc magnetic field are shown in Fig. 6.13. The surface temperature T_{surface} and the CPW temperature T_{CPW} are not actively controlled but follow the coupling temperature T_{coupling}. The dc magnetic field was chosen to be in the centre of the skyrmion lattice phase. Ohmic heating is observed as a constant offset over the whole temperature range (orange). Below $T_{\mathrm{surface}} = 59.5\,\mathrm{K}$ an increase of the temperature gradient is observed (blue) with decreasing temperature which increases when approaching T_{c} followed by a discontinuous change at the transition to the conical phase in which only ohmic heating persists. In the up-

sweep T_{surface} rises discontinuously when entering the skyrmion lattice phase tracking the temperature dependence with increasing temperature as observed for the down-sweep.

Considering the resonance frequencies shown in Fig. 6.11 and the associated widths, $f = 0.8\,\mathrm{GHz}$ is lower than the CCW mode at T_{c} of $f \approx 1.0\,\mathrm{GHz}$ and not within its FWHM. However, the data suggest that the excitation frequency overlaps with the tail of the broad CCW resonance. Notably, the resonance frequency of the CCW mode for low temperatures is $f \approx 1.3\,\mathrm{GHz}$ and far above the excitation frequency. However, resonant heating is observed as the sample transitions into the skyrmion lattice phase. The temperature progression suggests that the microwaves couple more effectively as the skyrmion lattice phase cannot be reached. The resonant heating in the up-sweep is consistent with a self-enforcing effect where an increase in temperature leads to the condensation of the skyrmion lattice and, hence, enhanced heating. Therefore, for all other measurements only down-sweeps were performed as an equilibrium between the thermal bath and the resonant heating is reached more easily. We return to a discussion of the onset of resonant heating $\sim 2\,\mathrm{K}$ above T_{c} below following the presentation of the frequency, power, and dc magnetic field dependencies observed in the temperature sweeps.

The typical dependence on the excitation frequency and field dependence of T_{surface} and T_{CPW} observed in down-sweeps is shown in Fig. 6.14. For all frequencies constant ohmic heating is observed over the whole temperature range (orange) which increases with increasing frequency as expected from the transmission of the sample stick (see Fig. 6.8 (b)). Resonant heating sets in about 2 K above T_{c} up to 1.8 GHz marked by arrows and ends in a discontinuous drop where the critical temperature is frequency-dependent. Whereas for $f = 0.6\,\mathrm{GHz}$ and 0.8 GHz the surface temperature declines discontinuously at T_{c}, temperatures extend far into the skyrmion lattice phase for higher frequencies, which has a temperature width of 2 K. At the highest frequency of $f = 3.6\,\mathrm{GHz}$ the onset of resonant heating may be attributed to the conical phase and no discontinuous drop is observed in the range of the skyrmion lattice phase and below down to lowest temperatures investigated.

The ohmic and resonant heating increases with increasing excitation field for a constant excitation frequency as shown in Fig. 6.14 (b). The temperature gradient again rises for all power values at about 59.5 K, $\sim 2\,\mathrm{K}$ above T_{c}. A discontinuous drop is only observed for 3 W and 5 W whereas there is a smooth transition for lower power values.

In Fig. 6.15, the dependence on different magnetic fields of the temperature gradient indicates that the resonant heating decreases with increasing field whereas ohmic heating is the same and essentially constant. At $B = 40\,\mathrm{mT}$ the resonant heating is still weakly visible and sets in about 2 K above T_{c} as marked by the arrow whereas it vanishes at 50 mT.

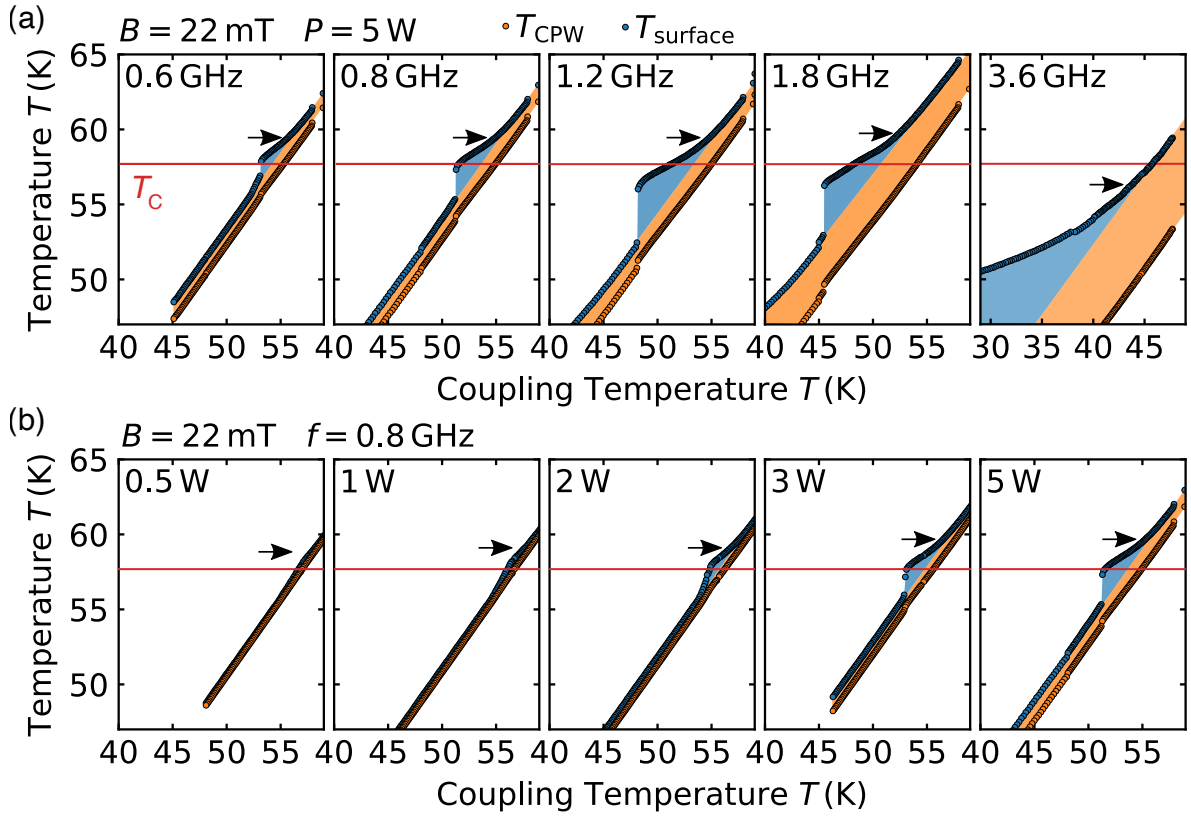

Figure 6.14.: Surface temperature and CPW temperature as a function of coupling temperature during temperature sweeps for (a) various frequencies and constant power and (b) various powers for constant frequency. Red lines denote the ordering temperature T_c and black arrows mark the inferred onset of resonant heating.

Tracking the surface temperature in magnetic field sweeps revealed a delicate dependence of the resonant heating on the excitation frequency and field, the temperature, and the magnetic field. The results allow the correction of the FMR data regarding resonant heating. Moreover, the amplifier was driven in saturation to improve the signal-to-noise ratio for the FMR measurements and generated weak higher harmonics. Additional heating was observed when these were in resonance with resonant modes. Hence, T_{surface} reflects if the system exhibits a resonant mode which is a harmonic of the driving frequency.

The surface temperatures recorded in field sweeps for various microwave frequencies and field values are shown in Fig. 6.16. Driving the system at a high microwave power leads to abrupt heating during the magnetic field sweeps when the resonance condition is fulfilled.

Field sweeps were performed from negative to positive field values at the maximum input power of $P = 5\,\mathrm{W}$. For $f = 0.6\,\mathrm{GHz}$ and $0.8\,\mathrm{GHz}$ resonant heating occurs in the skyrmion lattice phase where a discontinuous change in temperature above T_c is

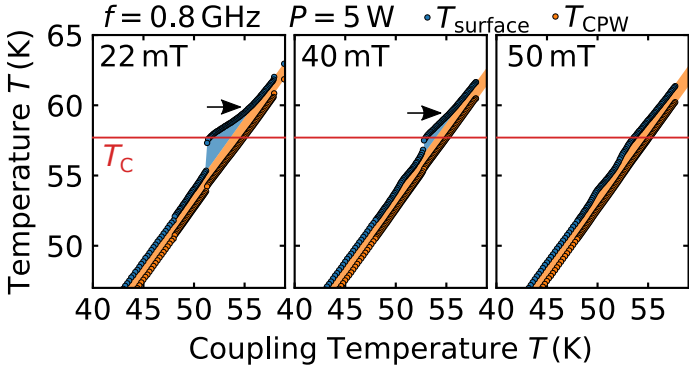

Figure 6.15.: Surface temperature, T_{surface}, and CPW temperature, T_{CPW}, as a function of coupling temperature, T_{coupling}, during temperature sweeps for various magnetic fields.

observed and a drop in the helical and conical phase, respectively (see Fig. 6.16 (a) and (b)). Interestingly, the former is far below the CCW resonant mode and outside its broad distribution which exhibits a FWHM of $\Delta f \approx 0.25\,\mathrm{GHz}$. For $f = 1.0\,\mathrm{GHz}$ and $1.2\,\mathrm{GHz}$, shown in Fig. 6.16 (c) and (d), the resonant heating is also observed in the skyrmion lattice phase, but at positive fields the surface temperature rises far enough such that the system matches the Kittel mode in the paramagnetic phase. This leads to additional heating (see small peak around $B = 40\,\mathrm{mT}$ and $50\,\mathrm{mT}$, respectively). Two small peaks of the sample

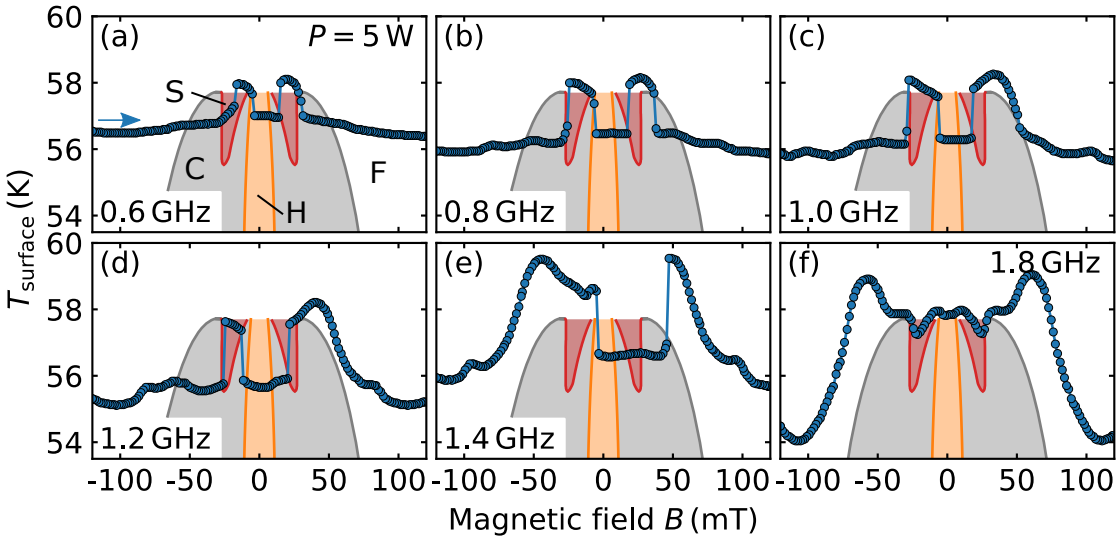

Figure 6.16.: Surface temperature T_{surface} as a function of magnetic field B for various drive frequencies f. The surface temperature T_{surface} as a function of magnetic field B under an applied microwave with a power $P = 5\,\mathrm{W}$, where the coupling temperature $T_{\mathrm{coupling}}$was regulated to be constant during the sweep. The sweep was performed from negative to positive field values. Colours mark the field-polarised (F), the conical (C), the helical (H) and the skyrmion lattice (S) phase.

temperature in the field-polarised state are identified which we assign to coupling of higher harmonics to the Kittel mode.

As shown in Fig. 6.16 (e), the microwaves couple to the Kittel mode already for negative fields leading to intense heating of the system with a maximum around $B = -45\,\mathrm{mT}$ before it discontinuously drops at low fields. Here, the temperature offset exceeds the resonant heating. The phase transition from conical to the field-polarised phase is again discontinuous as the sample couples to the Kittel mode of the field-polarised phase.

Eventually, for an excitation frequency of $f = 1.8\,\mathrm{GHz}$ we observe coupling to the Kittel mode around $B = \pm 70\,\mathrm{mT}$ in the field-polarised phase and, furthermore, discern coupling to the conical mode as the sample does not cool down into the conical phase but instead T_{surface} moves along T_{c} as the magnetic field is changed. We explain this behaviour by the increased resonant heating that is generated when the sample cools into the conical phase. However, the sample cools into the skyrmion lattice phase despite the coupling to the breathing mode. However, its spectral weight is smaller than the CCW mode and the conical modes, respectively, and the out-of-plane ac magnetic field component is much weaker than the in-plane component which couples to the CCW mode. Hence, the resonant heating effects are smaller in the skyrmion lattice phase.

Combining and linearly interpolating between the individual magnetic field sweeps results in a heat map which represents the difference between T_{surface} and T_{CPW} as a function of T_{CPW} and B as shown in Fig. 6.17. A constant temperature difference of $\Delta T \approx 1\,\mathrm{K}$ is present throughout the phase diagram due to ohmic heating as can be seen in the field-polarised phase (F). In addition, coupling to the various resonant modes in the magnetic phases lead in addition to resonant heating. The microwave frequency is set slightly below the CCW mode with $f \approx 1\,\mathrm{GHz}$ to $1.2\,\mathrm{GHz}$, depending on the sample temperature and the magnetic field.

At point (i) shown in Fig. 6.17 $T_{\mathrm{CPW}} \approx 55\,\mathrm{K}$ whereas $T_{\mathrm{surface}} \approx 56\,\mathrm{K}$. Increasing the magnetic field, the sample transitions to the skyrmion lattice phase and the temperature difference increases strongly to $\Delta T \approx 3\,\mathrm{K}$, i.e. T_{surface} increases above T_{c}. The phase boundaries without microwave radiation, i.e. $T_{\mathrm{surface}} = T_{\mathrm{CPW}}$ are indicated by white lines. The regime of the skyrmion lattice phase may be discerned as two yellow regions, marked as (ii), owing to resonant heating through the CCW mode. Above T_{c} heating is observed by coupling to the Kittel mode (iii) and, apparently, coupling to magnetic order at lower fields (iv). In addition, the higher harmonics of the amplifier couple to the field-polarised mode around $B \approx \pm 85\,\mathrm{mT}$ visible in terms of vertical lines (v) and the conical mode below the skyrmion lattice phase (vi) which, in contrast, exhibits a magnetic field and temperature dependence.

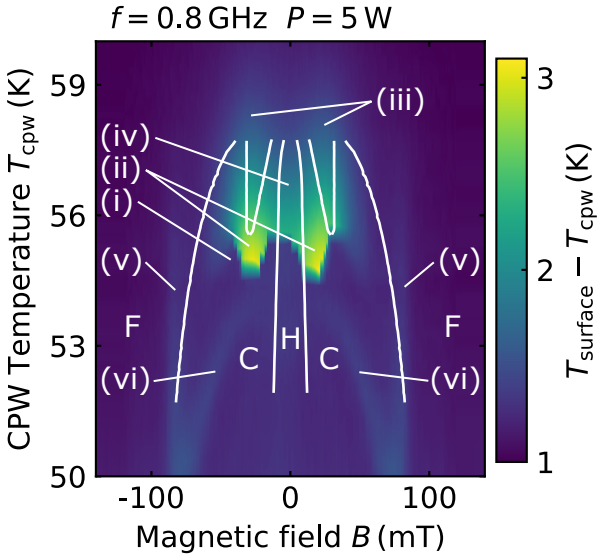

Figure 6.17.: Field-dependence of the surface temperature. The difference between the sample's surface temperature and the CPW temperature is shown as a function of T_{CPW} and B under an applied microwave field. The data was recorded performing B-sweeps. (i) T_{surface} is increased compared to T_{CPW} throughout the phase diagram due to ohmic heating. Regions with a strongly increased temperature difference may be discerned corresponding to resonant heating (ii) within and (iii) above the skyrmion lattice phase. (iv) An increased temperature difference is observed at low fields. Increased temperature corresponding to the coupling to (v) higher harmonics of the amplifier (see text for more details) and the (vi) conical modes. White lines mark the phase transition between the field-polarised (F), the conical (C), the helical (H), and the skyrmion lattice phase (S) without a temperature difference, i.e. $T_{\mathrm{surface}} = T_{\mathrm{CPW}}$.

In Fig. 6.18 heat maps of the temperature difference for various microwave frequencies at the highest microwave amplitude are shown. For $f = 0.6\,\mathrm{GHz}$, resonant heating is observed in the skyrmion lattice phase in terms of two yellow regions at $T_{\mathrm{CPW}} \approx 57.5\,\mathrm{K}$ and in the fluctuation disordered regime and paramagnetic phase, respectively. Furthermore, there is weak heating at low magnetic fields coinciding with the helimagnetic phase down to lowest temperatures. The resonant heating increases strongly in the skyrmion lattice phase for $f = 0.8\,\mathrm{GHz}$, $1.0\,\mathrm{GHz}$, and $1.2\,\mathrm{GHz}$ as the resonant frequency is approached. In addition, coupling of higher harmonics to the resonant modes of the conical and field-polarised phase at lower temperatures and up to higher fields may be observed. The vertical lines of increased temperature difference coincide with the field-polarised phase whereas the field and temperature dependent lines agree with the conical phase. It is important to note that the lines of enhanced heating are due to matching the resonant modes and not phase transitions. For comparison the phase diagram inferred from 1-tone FMR and SANS measurements is shown in Fig. 6.18 (f). In case of $f = 1.8\,\mathrm{GHz}$, only CPW temperatures

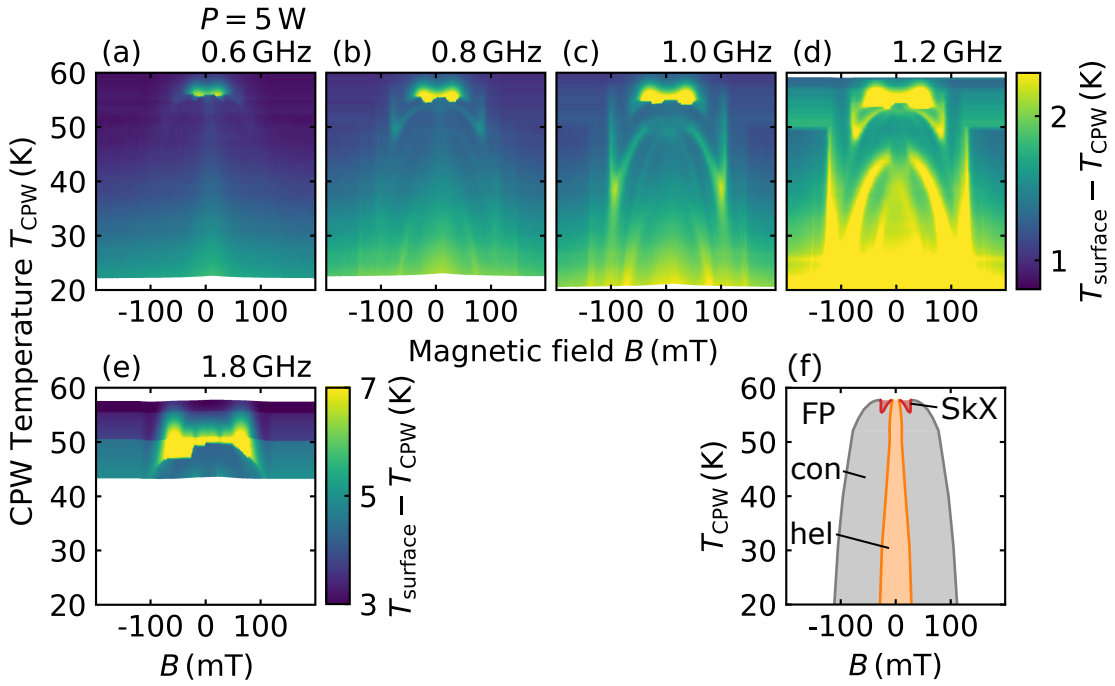

Figure 6.18.: Temperature gradient as a function of CPW temperature and dc magnetic field. (a-e) Temperature gradient between sample surface temperature and CPW temperature as a function of CPW temperature and dc magnetic field for various microwave frequencies as measured in magnetic field sweeps. (f) Phase diagram as determined by FMR and neutron scattering measurements with the field-polarised (F), skyrmion lattice (SkX), conical (con) and helical (hel) phase for comparison.

above $T_{\mathrm{CPW}} \approx 43\,\mathrm{K}$ were investigated. Around $B \approx \pm 70\,\mathrm{mT}$, the Kittel mode is observed at high temperatures. Between $T_{\mathrm{CPW}} \approx 43 - 50\,\mathrm{K}$ strong hysteresis effects as discussed beforehand for $f = 1.4\,\mathrm{GHz}$ in Fig. 6.16 (e) are observed. Finally, the phase boundary from the field-polarised to the conical phase is accentuated as at high temperatures the excitation frequency matches the conical resonance.

Finally, the dependence of the temperature difference between sample and CPW temperature on the excitation field amplitude is displayed in Fig. 6.19 for an excitation frequency $f = 0.8\,\mathrm{GHz}$. Down to lowest input power, the difference is elevated throughout the skyrmion lattice phase and the phase transition to the conical phase is observable as discontinuous change. Above T_{c}, resonant heating occurs due to the Kittel mode as well as at lower magnetic fields. Only at highest input power the amplifier is run in saturation and the higher orders of the microwave radiation couple to the field-polarised and conical mode observed as weak lines of an increased temperature offset.

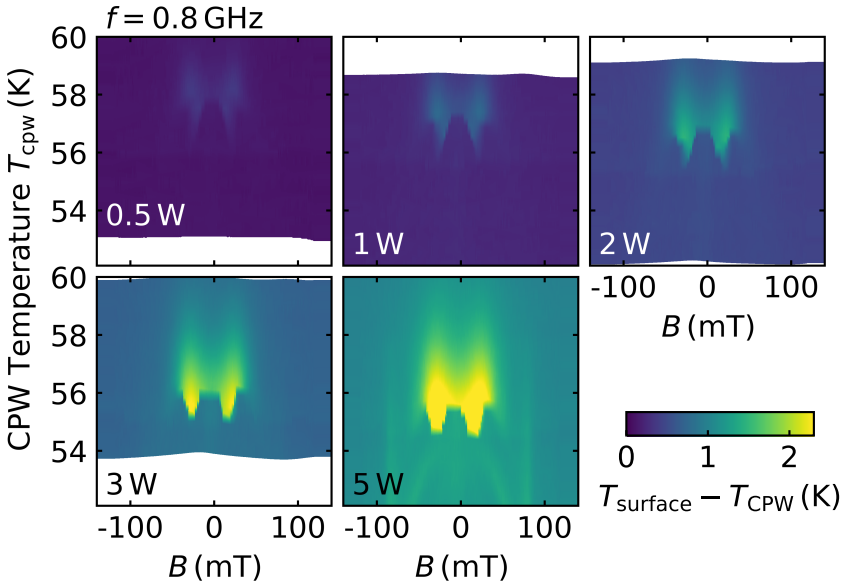

Figure 6.19.: Temperature gradient as a function of CPW temperature and dc magnetic field. Temperature gradient between sample surface temperature and CPW temperature as a function of CPW temperature and dc magnetic field for various power values as measured in magnetic field sweeps.

6.3.2. Temperature correction of the SANS and the FMR data

Although the thermometers were positioned as closely as possible to the sample without disturbing the measurements, a significant temperature difference between the sample temperature and the thermometers was present due to the intense ohmic and resonant heating as described above. Hence, a temperature correction of the SANS and FMR data sets was applied. The setup for the determination of the temperature correction is described in Sec. 6.2.3 and the definitions of the temperatures are given in Fig. 6.12. Two individual approaches are realised. For the SANS data the exact same setup was used with an additional thermometer attached on top of the sample, where the temperature sweeps were repeated as in the neutron scattering experiment. Furthermore, for the 2-tone FMR data, a more complex correction was required as the data acquisition was much faster in order to investigate a larger portion of the phase diagram. Resonant heating was therefore sensitive to temperature, magnetic field, excitation frequency and power. First, the FMR data is corrected for ohmic heating based on the magnetisation as inferred from the field-polarised resonance mode. Second, the temperature correction was used to compensate for resonant heating effects.

Neutron scattering data was corrected with respect to ohmic and resonant heating effects as depicted in Fig. 6.20. Fig. 6.20 (a) shows the dependence of the integrated neutron

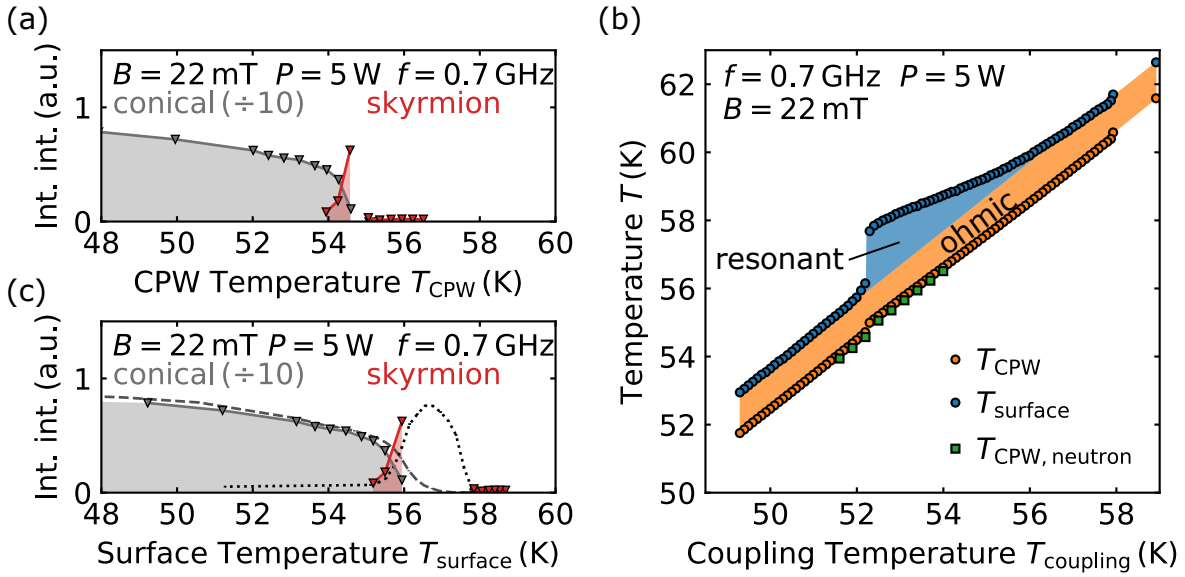

Figure 6.20.: Temperature correction procedure for neutron scattering data. (a) Integrated scattering intensity of the conical and skyrmion lattice phase as a function of CPW temperature under applied AC magnetic field. (b) Progression of the sample and CPW temperature during a temperature scan from high to low temperatures. Comparing the CPW temperatures, a sample temperature is assigned to every neutron scattering data point. (c) Integrated scattering intensity from (a) as a function of sample temperature. The dotted line corresponds to the skyrmion intensity if no AC magnetic field is applied and the dashed line to the conical phase, respectively.

scattering intensities of the conical and skyrmion lattice phase as a function of T_{CPW} under field-cooling with an excitation frequency of $f = 0.7\,\mathrm{GHz}$ and an input power $P = 5\,\mathrm{W}$. The integration of the scattered signal is described in Sec. 6.3.4. At high temperatures no scattering intensity is observed. Around $\sim 55\,\mathrm{K}$ the CPW temperature decreases discontinuously and the neutron scattering intensity of the skyrmion lattice phase is observed. Decreasing the temperature further, the system displays a transition into the conical phase. For the temperature correction T_{CPW} as recorded during the SANS and the temperature correction measurements were compared as shown in Fig. 6.20 (b). Wherever they matched, the corresponding surface temperature was assigned to the SANS data point. The integrated intensities are shown as a function of surface temperature in Fig. 6.20 (c). The intensities of the skyrmion lattice and conical state exhibit the same low temperature behaviour but with a constant offset of $\Delta T = 0.2\,\mathrm{K}$ with respect to the measurement without microwave excitation.

The conical intensities for all excitation frequencies and fields exhibit the same relative temperature dependence, but with a small constant offset even with the temperature correction taken into account as shown in Fig. 6.21 (a) and (c). The same is the case for the skyrmion lattice intensities in Fig. 6.21 (b) and (d). The temperatures of the intensities

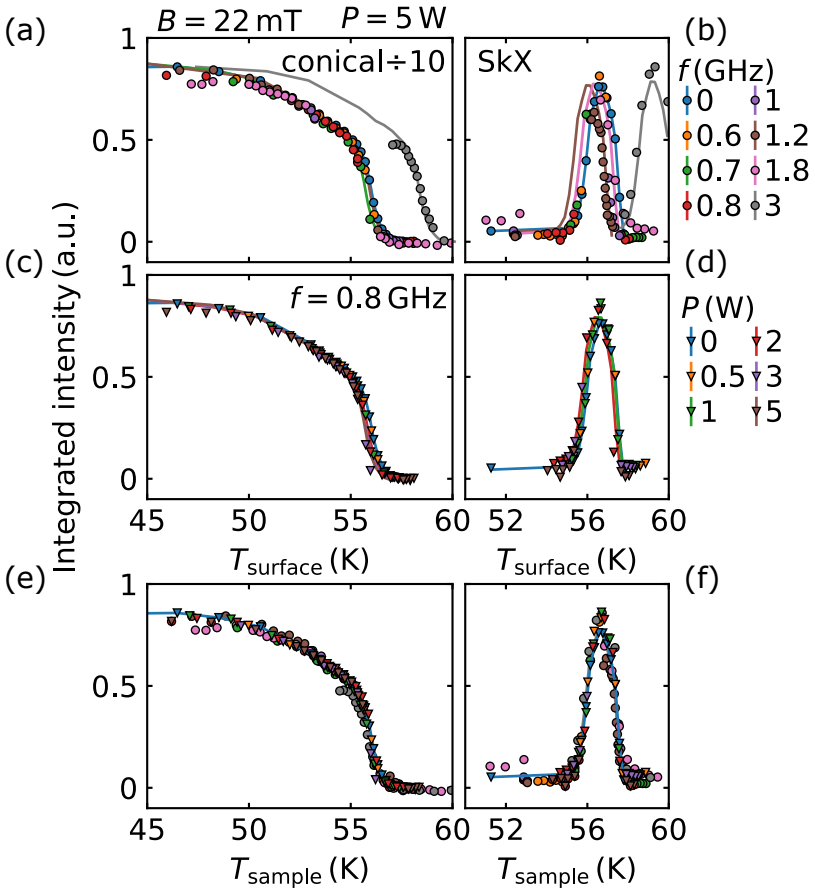

Figure 6.21.: Determination of sample temperature using neutron intensity. Integrated neutron scattering intensity of the (a) conical and (b) skyrmion lattice as a function of surface temperature T_{surface} for various frequencies and an applied power of $P = 5\,\mathrm{W}$. The surface temperature dependence for various applied ac magnetic field powers at fixed frequency is shown in (c) and (d). (e) After aligning the conical intensities which all exhibit the same relative temperature dependence and using the evaluated temperature shift ΔT to adjust the skyrmion intensities in (f), the intensities are plotted as a function of sample temperature.

of the conical state were therefore shifted by a constant value to match the temperature dependence without microwave drive as shown in Fig. 6.21 (e). Using these offset values, temperature values of the intensity of the skyrmion lattice were shifted as well and all intensity curves coincide. The values of the offsets are given in Tab. 6.2. The offset increases approximately linearly with increasing frequency except for the highest frequencies where the shift is lower and even opposite in sign. The offset also increases with increasing power for a constant frequency. In the following, all temperatures are sample temperatures, T_{sample}, except where stated otherwise. The comparison of temperatures during the neutron scattering experiments with temperature correction measurements is shown in more detail in App. C.1.

Table 6.2.: Constant temperature shift of the neutron intensity to correct for differences between T_{CPW} and T_{sample} (see text for details).

frequency f (GHz)	power P (W)	ΔT (K)
0.6	5	0
0.7	5	+0.2
0.8	5	+0.25
1.0	5	+0.5
1.2	5	+0.6
1.8	5	+0.2
3.0	5	−2.6
3.6	5	−1.0
0.8	0.5	0
0.8	1	+0.05
0.8	2	+0.3
0.8	3	+0.25
0.8	5	+0.25

In the case of the 2-tone FMR data, ohmic heating effects were corrected using the temperature dependent magnetisation which serves as an intrinsic thermometer as also described in the thesis by Lukas Liensberger [189]. The magnetisation was extracted at high fields in the field-polarised phase where the Kittel mode is at higher frequencies than the excitation frequency and only ohmic heating occurs. The procedure is described in Fig. 6.22. The real and imaginary part of the complex transmission parameter S_{21} are fitted simultaneously as shown in Fig. 6.22 (a) to extract the resonant frequency. To extract the magnetisation M, the resonance frequencies f_{res} of the 20 highest dc magnetic field points are fitted in the field-polarised phase with Eq. 3.15 shown in Fig. 6.22 (b). Here, the sample is approximated as ellipsoid with demagnetisation factors $N_z = 0.2$ and $N_x = N_y = 0.4$ and the Landé factor is set to $g = 2.0$. Plotting the magnetisation as a function of coupling temperature T_{coupling}, an offset between microwave excitations turned on or off is observed due to ohmic heating as shown in Fig. 6.22 (c). Rigidly shifting one curve onto the other, we can quantify the temperature difference ΔT. This temperature correction scheme is suitable for excitation frequencies up to $f = 1.8\,\mathrm{GHz}$ which is for all temperatures below the Kittel mode in the field-polarised phase.

Fig. 6.23 displays the dependence of the temperature differences between the sample and T_{holder} on the excitation frequency and input power due to ohmic heating for both setups. The FMR values are taken from the rigid shift described in Fig. 6.22 and the temperature

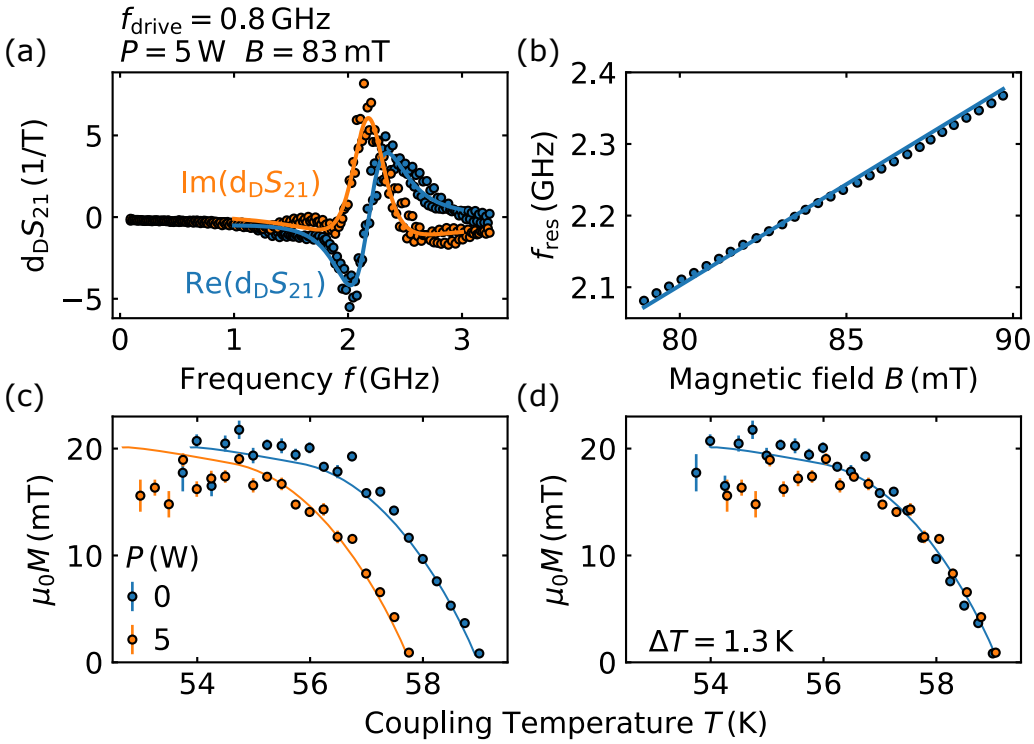

Figure 6.22.: Temperature correction of ohmic heating during FMR spectroscopy. (a) The derivative divide of the complex transmission signal S_{21} as a function of frequency is fitted to extract the resonance frequency under an applied intense microwave radiation. (b) The resonance frequencies extracted for the 20 highest magnetic field points are fitted to extract the magnetisation. (c) The magnetisation as a function of the coupling temperature with and without an applied microwave radiation, respectively. An offset due to ohmic heating is observed. (d) Both magnetisation curves overlap if the magnetisation data obtained under microwave radiation is rigidly shifted.

correction data are the average offset between surface and holder temperature above the onset of resonant heating as shown in Fig. 6.14. The positions of the corresponding thermometers are shown in Fig. 6.5 and Fig. 6.12, respectively. Notably, the position of the holder thermometer in the temperature correction measurements is $\sim 3\,cm$ closer to the centre conductor that is the ohmic heater. This might lead to a smaller offset.

An approximately linear dependence of ΔT as a function of excitation frequency is observed in Fig. 6.14 (a) for frequencies $f \leq 1.8\,GHz$. The ohmic heating increases with increasing frequency as the transmission of the FMR setup, i.e. the cables, the connectors, and the CPW, decreases as shown in Fig. 6.8 (b). For small frequencies $f < 1\,GHz$ the temperature offsets in both setups coincide whereas a small difference between $0.2 - 0.4\,K$ is observed for $1 \leq f \leq 1.8\,GHz$ that might be ascribed to the smaller distance between holder thermometer and centre conductor in the temperature correction measurements.

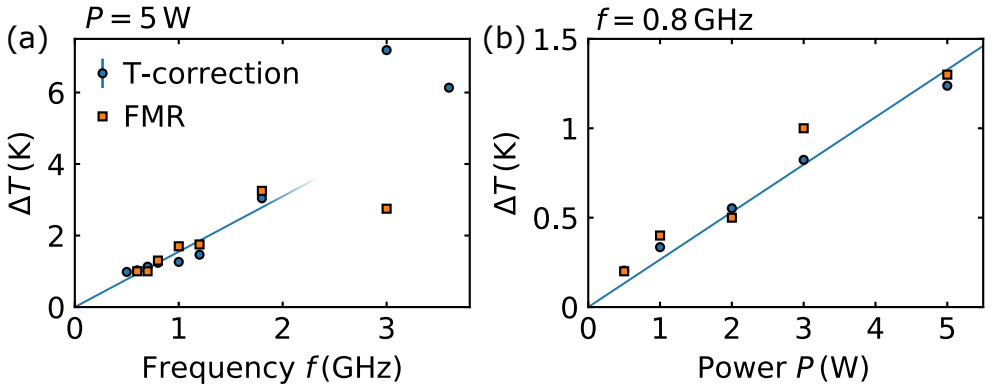

Figure 6.23.: Temperature difference ΔT due to ohmic heating. ΔT between T_{sample} and T_{holder} as a function of (a) frequency f and (b) power P. Blue markers correspond to the measured offset shown in Fig. 6.14 and orange markers correspond to the temperature correction using the magnetisation in the field-polarised state measured with FMR spectroscopy. Blue solid lines are guides to the eye.

For frequencies above 1.8 GHz electronics limited the temperature correction adding an additional shift of several Kelvin. This shift is constant as shown in Fig. 6.21 (a) where the relative temperature dependence of the scattering intensities coincide with the measurements without microwave excitation. In case of the FMR measurement, resonant heating occurs as the excitation frequency $f = 3\,\mathrm{GHz}$ matches the field-polarised resonance mode at the highest dc magnetic fields measured. The assumption that only ohmic heating occurs in the field-polarised phase is not correct in this case. The presence of resonant heating leads to a distortion in the determination of the magnetisation as well as an underestimation of ohmic heating effects. No all-electrical microwave spectroscopy were performed for $f = 3.6\,\mathrm{GHz}$.

Fig. 6.23 (b) shows ΔT as a function of input power P for a constant excitation frequency $f = 0.8\,\mathrm{GHz}$. The difference exhibits a linear dependence on P and coincides well. Overall, the coupling of sample and CPW to the thermal bath is approximately equal in both setups.

Eventually, temperatures in magnetic field sweeps of the all-electrical microwave spectroscopy are corrected for resonant heating to determine T_{sample}. As no thermometer was attached directly to the sample, results from the temperature correction are used to determine T_{sample}. The temperature corrected from ohmic heating represents T_{sample} in the field-polarised phase for frequencies $f \leq 1.8\,\mathrm{GHz}$ as the Kittel mode is higher in frequency and no resonant heating was present. This allows to link the FMR spectra and the temperature correction. Furthermore, in both measurements T_{coupling} is constant during field sweeps and the coupling of the CPW-sample system to the heat bath is approximately equal as discussed above. Hence, T_{sample} varying in a field sweep during the temperature

correction measurement represents T_{sample} during all-electrical microwave spectroscopy if T_{sample} from both measurements match at high fields in the field-polarised phase, here, at $B = 80\,\mathrm{mT}$.

The skyrmion lattice phase is narrow in temperature and field. In turn, small differences of several 100 mK or several mT may lead to considerable changes. Although the temperature correction captures the sample temperature quite accurately, a careful assessment of all available parameters, such as temperatures and fields of phase transitions, or resonant frequencies, is necessary to ensure its validity. It shows that the phase transition from the low-field conical to the skyrmion lattice phase which increases in field with decreasing temperature is in particular a meaningful indicator of the sample temperature.

6.3.3. Ferromagnetic resonance of the periodically driven SkX phase

In this section we report all-electrical microwave spectroscopy of the collective excitation spectra of Cu_2OSeO_3 around and within the skyrmion lattice phase under intense microwave radiation by means of a broadband coplanar waveguide. At first, typical data obtained by the 2-tone FMR technique are presented for an intermediate microwave field driving the system. This includes the excitation spectra as well as the temperature progression during magnetic field sweeps. Subsequently, data recorded for the highest microwave radiation for several microwave frequencies below, at, and above the CCW mode are presented.

For all excitation frequencies and fields a strong thermal response of the sample to the microwave field is observed. The sample temperature increases to or slightly above the ordering temperature T_{c} as the CCW mode moves into resonance with the microwave frequency. In addition, the signal of the CCW mode may vanish. However, a quasi-static state may be established in two cases where the sample temperature increases to or slightly above T_{c}, but the signal of the CCW mode may still be observed. Interestingly, under the same conditions the sample temperature also remains at T_{c} in neutron scattering measurements and no neutron scattering signal of the skyrmion lattice phase is observed. For an excitation frequency above the CCW mode, strong coupling to the conical mode is observed which results in intense resonant heating and significant changes of the excitation spectra. Finally, excitation spectra recorded just above T_{c} are presented that are reminiscent of features of the fluctuating skyrmion textures in MnSi [108].

The insufficient signal-to-noise ratio prohibits a quantitative analysis and a fit of the data as performed without the application of intense microwave radiation in Sec. 6.2.2. A centre conductor of the coplanar waveguide of reduced width would improve the signal quality. However, SANS measurements require a minimum sample size. Reducing the cen-

tre conductor width and at the same time keeping the sample size, the intense microwave only affects parts of the sample. Since in SANS measurements the signal is integrated over the whole sample, effects from the strong microwave field might be covered by the signal of the unaffected parts. This leads to the compromise of a 1.3 mm wide centre conductor.

Features of the collective excitations and the phase transitions may be tracked in heat maps of the complex transmission parameter S_{21} as a function of probe frequency f and magnetic field B. In these magnetic field sweeps T_{coupling} is kept constant whereas T_{sample} may vary by several Kelvin as discussed in Sec. 6.3.2. The heating effects depend sensitively on magnetic field, temperature, microwave frequency and field and may be hysteretic. Hence, a careful consideration of T_{sample} for every spectra is necessary. The microwave spectra were measured for eight microwave frequencies and at one frequency for five different microwave fields. For each setting 20 to 30 different T_{coupling} were recorded. Discussing all microwave spectra in heat maps with the corresponding T_{sample} exceeds the limits of this thesis. In the following, microwave spectra for selected microwave frequencies and fields comprising all main observations are presented.

It is helpful to present at first data recorded in all-electrical microwave spectroscopy at an intermediate input power of $P = 3\,\mathrm{W}$ and an excitation frequency $f_{\mathrm{drive}} = 0.8\,\mathrm{GHz}$ to illustrate essential features. Changes of T_{sample} were adjusted by means of the aforementioned temperature correction procedure in Sec. 6.3.2.

Fig. 6.24 displays typical frequency and field dependences of S_{21} as well as T_{sample} during field sweeps. T_{sample} is shown in Fig. 6.24 (a) during the field sweep from negative to positive fields. The shaded areas denote the different phases: field-polarised (F), conical (C), skyrmion lattice (S), helical (H), and paramagnetic (P). The fluctuation disordered regime just above T_{c} is not explicitly denoted. The phase diagram was inferred from 2-tone measurements without intense microwave radiation as shown in Fig. 6.10 (a). In the following, the conical phase at higher (lower) field values than the skyrmion lattice phase is referred to as high-field (low-field) conical phase.

T_{sample} is already elevated compared to T_{coupling} in the field-polarised and high-field conical phase due to ohmic heating but is constant as a function of field. Entering the skyrmion lattice phase the temperature rises sharply to $\sim 58\,\mathrm{K}$, marked as (i), just above the ordering temperature T_{c}. Subsequently, it drops to a plateau value in the low-field conical and helical phase at (ii). At the transition to the skyrmion lattice phase at positive field at (iii), the temperature rises discontinuously just above T_{c} and exhibits a dome shape with maximum at $B = 27\,\mathrm{mT}$ with a maximum temperature of $T = 58\,\mathrm{K}$. Subsequently, T_{sample} decreases sharply entering the high-field conical phase at (iv) and remains constant up to the field-polarised phase. To highlight any hysteresis, the full field sweeps are shown.

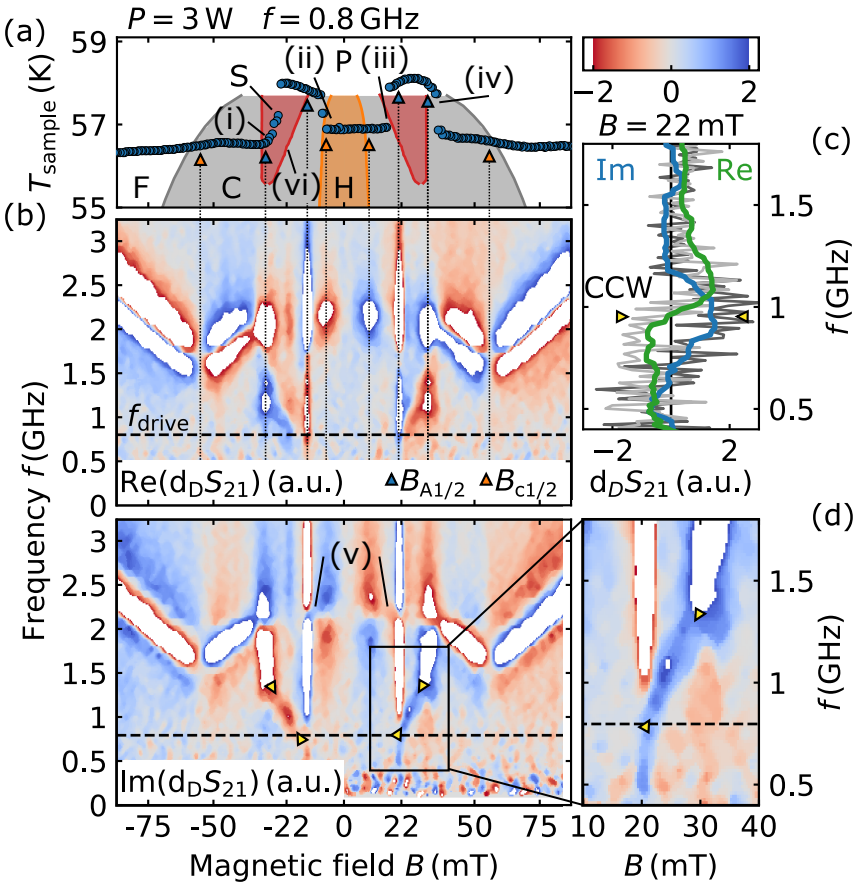

Figure 6.24.: All-electrical microwave spectroscopy at $f_{\mathrm{drive}} = 0.8\,\mathrm{GHz}$ below the CCW mode for intermediate microwave fields. (a) Sample temperature during field sweeps in FMR measurements. Shaded areas denote the phase diagram as inferred without intense microwave radiation. (b) Colormap depicting $\mathrm{Re}(\mathrm{d_D}S_{21})$ and $\mathrm{Im}(\mathrm{d_D}S_{21})$ as a function of f and B. The colour range is chosen to saturate for better distinction of the modes and better visibility of weaker modes such as the CCW. Dotted lines and triangles mark the phase transitions in the spectra. (c) $\mathrm{Im}(\mathrm{d_D}S_{21})$ as a function of f for a constant magnetic field. (d) Magnified signal of $\mathrm{Im}(\mathrm{d_D}S_{21})$ around the skyrmion lattice phase. Yellow arrows mark the signatures of the CCW mode.

The excitation spectra recorded by means of all-electrical microwave spectroscopy with the 2-tone FMR technique are shown in Fig. 6.24 (b). Here, heat maps of the real and imaginary part of the derivative divide of the complex transmission parameter $\mathrm{Re}(\mathrm{d_D}S_{21})$ and $\mathrm{Im}(\mathrm{d_D}S_{21})$, respectively, are displayed as a function of magnetic field B and frequency f. As discussed in Sec. 3.3.3, resonant modes appear as a zero-crossing in the real part and as a maxima in the imaginary part. The derivative is with respect to the magnetic field and, hence, the field dependence of the resonance defines the sign of the signal.

The transition between field-polarised and conical phase at B_{c2} is accompanied in a change of the slope of the resonance mode with respect to magnetic field. The resonances

merge seamlessly at the transition. The change between conical and skyrmion lattice phase at B_{A2} and B_{A1}, respectively, lead to a maximum in the spectra over a large frequency range. A narrow peak at B_{c1} marks the transition to the helical phase. The phase transitions are marked by dotted lines and triangles mark them in the phase diagram in Fig. 6.24 (a). The phase transitions obtained through the analysis of the excitation spectra in Fig. 6.24 (b) agree well with the transitions in Fig. 6.24 (a).

In particular, the transition from the skyrmion lattice to the low-field conical phase at B_{A1} at (vi), which increases under field with decreasing temperature, is well suited to confirm T_{sample} inferred from the temperature correction. Comparing the transition in the excitation spectra at $B_{\mathrm{A1}} = -14\,\mathrm{mT}$ with the phase diagram in Fig. 6.24 (a) shows indeed that T_{sample} corresponds to T_{c}.

However, comparing the temperature correction and the excitation spectra, the transitions from the low-field conical to the skyrmion lattice phase at B_{A1} for positive magnetic fields at (iii) do not coincide. The difference in magnetic field is 3 mT and corresponds to a difference in temperature of $\Delta T \approx 0.4\,\mathrm{K}$. Hence, the temperature of the excitation spectra in the low-field conical phase is most likely lower than suggested by the temperature correction. However, comparing the CCW resonant frequency of $f \approx 0.9\,\mathrm{GHz}$ at $B = 22\,\mathrm{mT}$ in the excitation spectra with the resonant modes without microwave radiation in Fig. 6.11 (a) clearly shows that T_{sample} rises to T_{c} within the skyrmion lattice phase.

The resonant mode in the field-polarised phase, which exhibits a positive slope, merges with the resonant mode of the conical phase, which exhibits a negative slope, at $B_{\mathrm{c2}} \approx -55\,\mathrm{mT}$. The signal of the two resonant modes is unaltered compared to the 2-tone experiment without intense microwave radiation in Fig. 6.9. The CCW mode corresponding to the skyrmion lattice phase is observed as maximum in the imaginary part between $f \approx 1.2$ and 0.9 GHz with positive field dependence and marked with yellow arrows. Signatures of the breathing mode are not distinguishable due to the weaker component $h_{\mathrm{ac},\parallel}$ of the microwave field which couples to it and its weak field dependence. The CW mode may be neither observed here under microwave radiation nor without microwave radiation. Its spectral weight is too low consistent with previous studies [83, 134].

As the CCW mode approaches the microwave frequency $f = 0.8\,\mathrm{GHz}$ with decreasing magnetic field, T_{sample} increases due to resonant heating and reaches its maximum around $B \approx -24\,\mathrm{mT}$. Lowering the magnetic field further, the system remains in a state slightly above T_{c} as shown in Fig. 6.24 (a). However, the CCW mode is still present throughout the phase down to the microwave frequency f_{drive} marked with yellow arrows in Fig. 6.24 (b). At $B_{\mathrm{c1}} \approx -14\,\mathrm{mT}$ the system transitions into the low-field conical phase where the signature of the CCW mode vanishes. At (v) signatures of the resonant modes of the low-field

conical phase are only very weakly observable. Within the helical phase no distinct features are visible in the excitation spectra.

In Fig. 6.9 (c), the real and imaginary part of S_{21} are shown as function of frequency within the skyrmion lattice phase where the signature of a broad CCW mode may be observed with a FWHM of $\Delta f \approx 0.25\,\mathrm{GHz}$. A similar behaviour may be observed for a microwave frequency of $f_{\mathrm{drive}} = 0.6\,\mathrm{GHz}$ and highest microwave fields with $P = 5\,\mathrm{W}$ shown in Fig. C.7 in App. C.2. Here, T_{sample} also increases just above T_{c} as the CCW mode approaches the microwave frequency. Nevertheless, signatures of the CCW mode may be discerned throughout the magnetic field range of the skyrmion lattice phase.

Spectra for lower microwave fields and a microwave frequency $f_{\mathrm{drive}} = 0.8\,\mathrm{GHz}$ are shown as well in App. C.2. Here, resonant heating is also present, but the sample is not heated above T_{c}. Instead, the entire skyrmion lattice phase is accessible and the signature of the CCW mode is present throughout the phase.

Performing the field sweep with $f_{\mathrm{drive}} = 0.8\,\mathrm{GHz}$, $P = 3\,\mathrm{W}$, and a slightly higher T_{coupling} of $\Delta T = +250\,\mathrm{mK}$ than shown in Fig. 6.24, the signatures of the CCW resonance mode vanish as it approaches the excitation frequency f_{drive} as shown in Fig. 6.25. T_{sample} again increases sharply within the skyrmion lattice phase as the CCW mode approaches the excitation frequency f_{drive} shown in Fig. 6.25 (a) at (i). T_{sample} subsequently remains elevated, decreases slightly before another maximum appears at (ii) in the skyrmion lattice phase at positive fields. The transition at negative fields from the skyrmion lattice to the low-field conical phase at (iii) at $B_{\mathrm{A1}} \approx 14\,\mathrm{mT}$ suggests that the temperature correction is accurate and that the sample temperature is just above T_{c}. However, there is again a discrepancy for positive fields at B_{A1}. T_{sample} is slightly lower entering the skyrmion lattice phase than captured in the temperature correction. Nevertheless, the elevated temperature within the skyrmion lattice phase to or above T_{c} is accurate considering the CCW resonance frequency at $B = 24\,\mathrm{mT}$ of $f \approx 0.9\,\mathrm{GHz}$ shown in Fig. 6.25 (b).

Fig. 6.25 (b) shows the real and imaginary part of S_{21}. As the CCW resonance frequency of the skyrmion lattice phase decreases with decreasing magnetic field for negative fields shown at (iv), T_{sample} increases just above T_{c} and the distinct mode vanishes as readily observed in the imaginary part. Although no distinct mode may be observed at (v), resonant heating is still present as T_{sample} remains above T_{c}. The excitation field may couple to magnetic correlations in the fluctuation disordered regime above T_{c} preventing the condensation of the skyrmion lattice. Alternatively, the ferromagnetic background the skyrmions are situated in is driven to such an extent that the probe excitation field does not pick up the signal of the skyrmion lattice phase. This issue is discussed in Sec. 6.4.

Both field sweeps show that the intense microwave field couples to the CCW resonance mode of the skyrmion lattice phase and heats the sample to or above T_{c}. Depending on

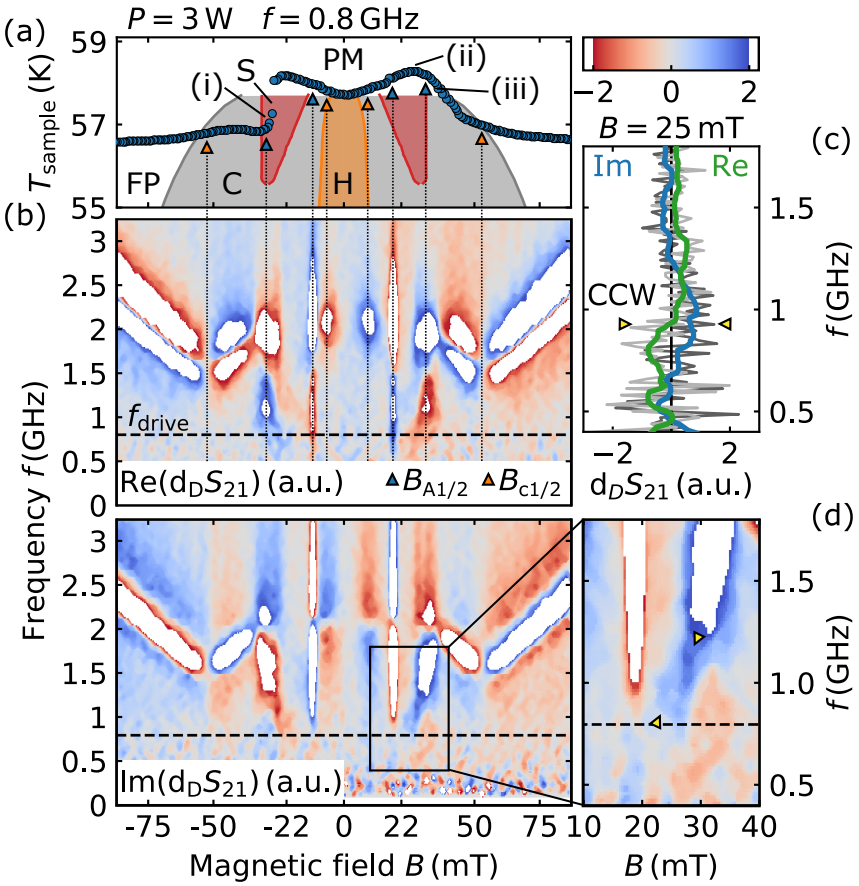

Figure 6.25.: All-electrical broadband spectroscopy at $f_{\mathrm{drive}} = 0.8\,\mathrm{GHz}$ below the resonant CCW mode for intermediate microwave fields. (a) Sample temperature behaviour during field sweeps in FMR measurements. (b) Colormap depicting $\mathrm{Re}(\mathrm{d_D}S_{21})$ and $\mathrm{Im}(\mathrm{d_D}S_{21})$ as a function of f and B. The colour range is chosen to saturate for better distinction of the modes and better visibility of weaker modes such as the CCW. Dotted lines and triangles mark the phase transitions in the spectra. (c) $\mathrm{Im}(\mathrm{d_D}S_{21})$ as a function of f for a constant magnetic field. (d) Magnified signal of $\mathrm{Im}(\mathrm{d_D}S_{21})$ around the skyrmion lattice phase. Yellow arrows mark the signatures of the CCW mode.

the temperature difference between sample and CPW, a quasi-static state is established at or slightly above T_c. If T_{coupling} is low enough and, therefore, the temperature difference between T_{sample} and T_{CPW} sufficient, a quasi-static state is established at T_c. Here, the observation of signatures of the CCW mode over the entire field range of the skyrmion lattice phase in Fig. 6.24 (b) reveals the presence of skyrmions.

Increasing the input power further to the maximum value of $P = 5\,\mathrm{W}$, the resonant heating increases as displayed in Fig. 6.26 (a). However, the general temperature progression is unaltered. For negative fields and within the skyrmion lattice phase the sample again heats up, marked as (i), just above $T_\mathrm{c} = 57.7\,\mathrm{K}$ as the CCW mode approaches the

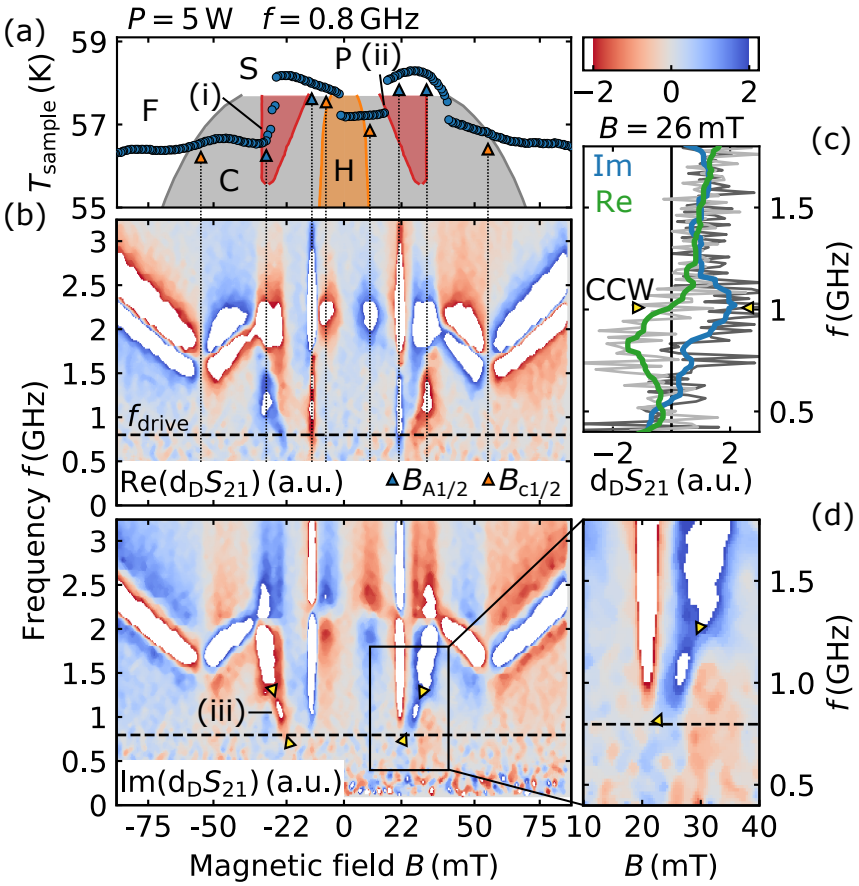

Figure 6.26.: All-electrical broadband spectroscopy at $f_{\mathrm{drive}} = 0.8\,\mathrm{GHz}$ below the resonant CCW mode for strongest microwave fields. (a) Sample temperature behaviour during field sweeps in FMR measurements. (b) Colormap depicting $\mathrm{Re}(\mathrm{d_D}S_{21})$ and $\mathrm{Im}(\mathrm{d_D}S_{21})$ as a function of f and B. The colour range is chosen to saturate for better distinction of the modes and better visibility of weaker modes such as the CCW. Dotted lines and triangles mark the phase transitions in the spectra. (c) $\mathrm{Re}(\mathrm{d_D}S_{21})$ and $\mathrm{Im}(\mathrm{d_D}S_{21})$ for a constant magnetic field. (d) Magnified signal of $\mathrm{Im}(\mathrm{d_D}S_{21})$ in the skyrmion lattice phase. Yellow arrows mark the signatures of the CCW mode.

excitation frequency. The phase transitions in Fig. 6.26 (a) and (b) coincide reasonably well, in particular, at B_{A1} at negative fields which indicates that T_{sample} is indeed at T_{c}. Again, the transitions from the low-field conical to the skyrmion lattice phase, marked as (ii), at B_{A1} and positive fields do not agree. As the transition may be discerned at higher fields in the excitation spectra, T_{sample} is presumably lower in the low-field conical phase than reflected by the temperature correction. The magnetic field offset of $\Delta B = 3\,\mathrm{mT}$ corresponds to a temperature difference of $\Delta T \approx 0.4\,\mathrm{K}$.

Fig. 6.26 (b) shows the real and imaginary part of the derivative divide of S_{21}. The signature of the CCW mode is only present in parts of the skyrmion lattice phase at (iii) towards the upper phase transition to the conical phase at B_{c2} between $f \approx 1.2$ and

0.95 GHz. As the CCW mode approaches the excitation frequency f_{drive} by decreasing the magnetic field for negative fields, the mode vanishes at $B \approx -22\,\mathrm{mT}$ as also observed for an intermediate excitation field in Fig. 6.25. The observed resonance frequency at $B = -24\,\mathrm{mT}$ is $f \approx 0.95\,\mathrm{GHz}$ consistent with the resonant frequency of the CCW mode at a temperature close to T_{c} as inferred from spectra without intense microwave fields in Fig. 6.11. In addition, T_{sample} reaches a maximum where the signature of the CCW mode vanishes in $\mathrm{Re}(\mathrm{d_D}S_{21})$ and $\mathrm{Im}(\mathrm{d_D}S_{21})$.

The real and imaginary part of S_{21} as a function of frequency is shown in Fig. 6.9 (c) for a constant magnetic field. The resonant mode may be discerned at $B = 26\,\mathrm{mT}$ with a FWHM of $\sim 0.3\,\mathrm{GHz}$.

In this case, with maximal input power $P = 5\,\mathrm{W}$ at $f_{\mathrm{drive}} = 0.8\,\mathrm{GHz}$, again, a quasi-static state seems to be reached at or just above T_{c} as the CCW mode is in the vicinity but still below the intense microwave frequency f_{drive}. The microwave field may couple to magnetic correlations within the fluctuation disordered regime leading to resonant heating above T_{c}. The temperature difference between T_{sample} and T_{CPW} may be insufficient to cool the sample low enough for the skyrmion lattice to condense. Alternatively, the ferromagnetic background is again driven to such an extent that the signal from the skyrmions in FMR is severely altered and the probe signal does not match the expectations inferred from the undisturbed system.

Driving the system with $f_{\mathrm{drive}} = 1.2\,\mathrm{GHz}$ matching the CCW resonance mode, the excitation spectra in the skyrmion lattice phase changes. T_{sample} shown in Fig. 6.27 (a) increases discontinuously in the skyrmion lattice phase to approximately T_{c} at (i) followed by a discontinuous cooling of the sample in the subsequent conical phase at (ii). T_{sample} within the low-field conical and helical phase is not elevated as in the case of $f_{\mathrm{drive}} = 0.8\,\mathrm{GHz}$. Passing into the skyrmion lattice phase at positive fields at (iii), resonant heating increases the temperature to above T_{c}. For higher fields the microwave couples to the Kittel mode and resonant heating increases even further with a maximal heating around $B \approx 40\,\mathrm{mT}$ at (iv). Similar to the previously discussed examples with lower f_{drive}, T_{sample} is increased to T_{c} in the field range of the skyrmion lattice phase.

S_{21} is unaltered in the field-polarised and high-field conical phase as shown in Fig. 6.27 (b) as f_{drive} is lower than the resonant modes. Within the skyrmion lattice phase the signal of the CCW mode vanishes completely and only a broad feature is observed in the imaginary part around $f \approx 1.5 - 1.6\,\mathrm{GHz}$ with weak magnetic field dependence marked with yellow arrows and magnified in Fig. 6.27 (d). The sign of the derivative divide in the imaginary part as well as the frequency range agree with the breathing mode. In addition, the breathing mode exhibits a relatively weak field dependence as shown in Fig. 6.11 (b). At (v) a small signal is consistent with the low-field conical mode.

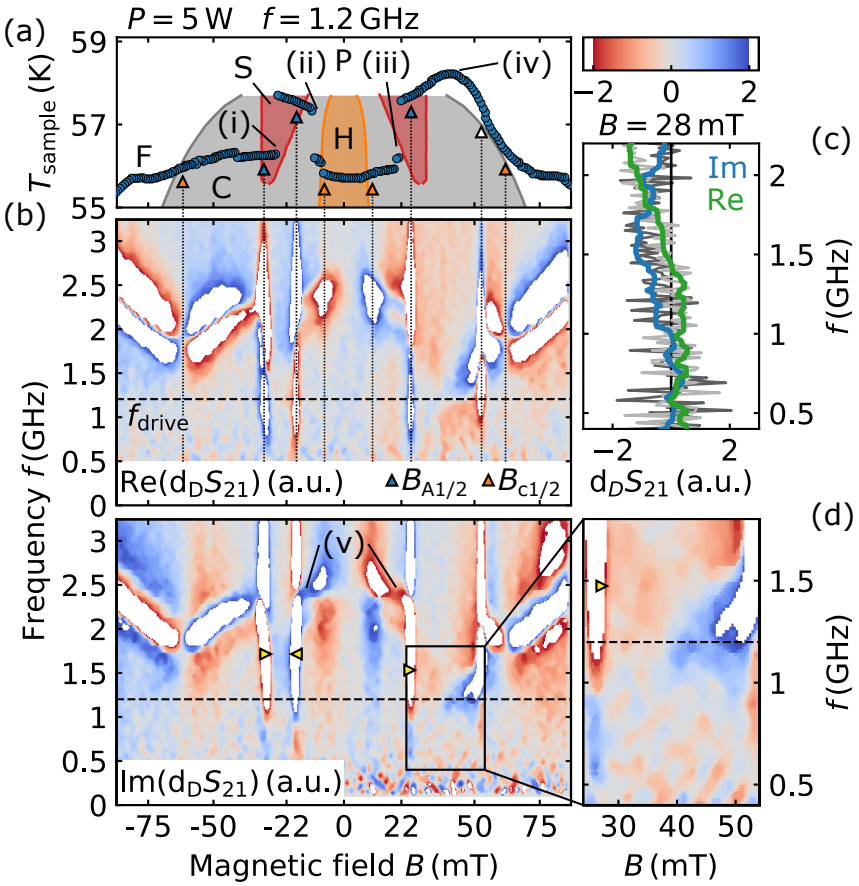

Figure 6.27.: All-electrical broadband spectroscopy at $f_{\mathrm{drive}} = 1.2\,\mathrm{GHz}$ matching the CCW mode for strongest microwave fields. (a) Sample temperature behaviour during field sweeps in FMR measurements. (b) Colormap depicting $\mathrm{Re}(\mathrm{d_D}S_{21})$ and $\mathrm{Im}(\mathrm{d_D}S_{21})$ as a function of f and B. The colour range is chosen to saturate for better distinction of the modes and better visibility of weaker modes such as the CCW. Dotted lines and triangles mark the phase transitions in the spectra. (c) $\mathrm{Re}(\mathrm{d_D}S_{21})$ and $\mathrm{Im}(\mathrm{d_D}S_{21})$ for a constant magnetic field. (d) Magnified signal of $\mathrm{Im}(\mathrm{d_D}S_{21})$ around the skyrmion lattice phase.

Fig. 6.28 shows an excitation spectra in a field-sweep for a microwave frequency of $f_{\mathrm{drive}} = 1.2\,\mathrm{GHz}$ at the largest microwave field with slightly lower T_{coupling} of $\Delta T = -250\,\mathrm{mK}$ than Fig. 6.27. T_{sample} shown in Fig. 6.28 (a) is constant as a function of field in the field-polarised and conical phase. It increases significantly at $B \approx -26\,\mathrm{mT}$ within the skyrmion lattice phase, marked as (i). The sample temperature increases slightly to below T_{c} before decreasing again at (ii) leaving the skyrmion lattice phase. For positive fields, the temperature increases sharply within the skyrmion lattice phase at (iii) at the border to the high-field conical phase and reaches T_{c}. Subsequently, the system couples to the Kittel mode with a maximum of resonant heating at $B \approx 40\,\mathrm{mT}$ at (iv) before cooling down to the conical phase again.

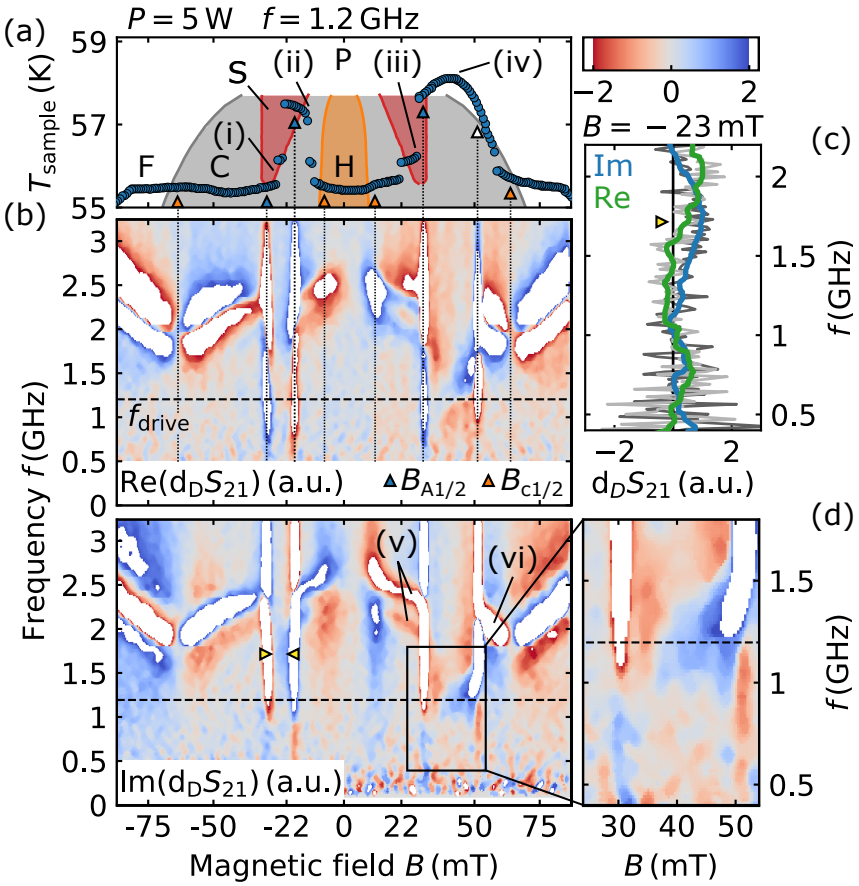

Figure 6.28.: All-electrical broadband spectroscopy at $f_{\mathrm{drive}} = 1.2\,\mathrm{GHz}$ matching the CCW mode for strongest microwave fields. (a) Sample temperature behaviour during field sweeps in FMR measurements. (b) Colormap depicting $\mathrm{Re}(\mathrm{d_D}S_{21})$ and $\mathrm{Im}(\mathrm{d_D}S_{21})$ as a function of f and B. The colour range is chosen to saturate for better distinction of the modes and better visibility of weaker modes such as the CCW. Dotted lines and triangles mark the phase transitions in the spectra. (c) $\mathrm{Re}(\mathrm{d_D}S_{21})$ and $\mathrm{Im}(\mathrm{d_D}S_{21})$ for a constant magnetic field. (d) Magnified signal of $\mathrm{Im}(\mathrm{d_D}S_{21})$ around the skyrmion lattice phase.

Fig. 6.28 (b) shows the real and imaginary part of S_{21}. The phase transitions from the field-polarised to the conical phase B_{c2} coincide well between the FMR spectra and the temperature correction shown in Fig. 6.28 (a). For negative fields the phase transition from the skyrmion lattice phase to the low-field conical phase in the FMR spectra at $B_{\mathrm{A2}} \approx -19\,\mathrm{mT}$ suggests that T_{sample} is lower by $\Delta T \approx 0.5\,\mathrm{K}$ than inferred from the temperature correction. Again, signatures of the CCW resonant mode may not be observed, but for negative fields a broad feature around $f = 1.7\,\mathrm{GHz}$ marked with yellow arrows in the imaginary part appears in the range of the breathing mode. The feature may also be seen in the frequency dependence of S_{21} recorded at constant magnetic field shown in Fig. 6.28 (c).

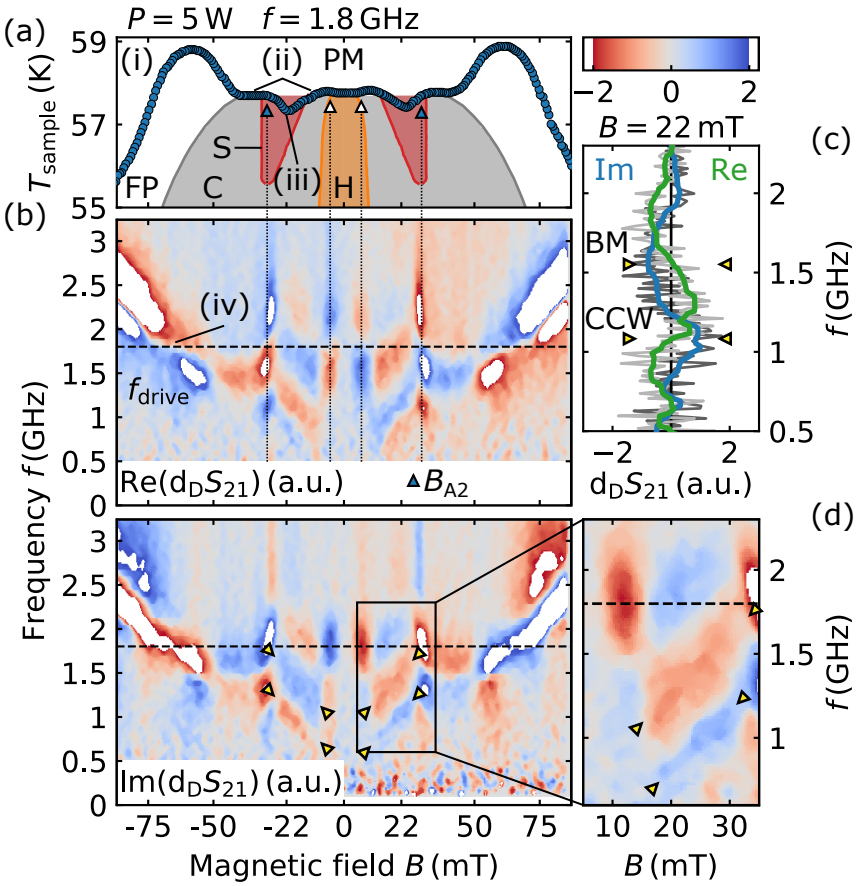

Figure 6.29.: All-electrical broadband spectroscopy at $f_{\mathrm{drive}} = 1.8\,\mathrm{GHz}$ for strongest microwave fields. (a) Sample temperature behaviour during field sweeps in FMR measurements. (b) Colormap depicting $\mathrm{Re}(\mathrm{d_D}S_{21})$ and $\mathrm{Im}(\mathrm{d_D}S_{21})$ as a function of f and B. The colour range is chosen to saturate for better distinction of the modes and better visibility of weaker modes such as the CCW. Dotted lines and triangles mark the phase transitions in the spectra. (c) $\mathrm{Re}(\mathrm{d_D}S_{21})$ and $\mathrm{Im}(\mathrm{d_D}S_{21})$ as function of frequency for a constant magnetic field. (d) Magnified signal of $\mathrm{Im}(\mathrm{d_D}S_{21})$ around the skyrmion lattice phase. Arrows mark the signatures of the CCW and breathing mode.

For positive fields the modes of the conical phase Q^+ and Q^- may be seen up to the transition at $B_{\mathrm{A2}} \approx 30\,\mathrm{mT}$, marked as (v), where T_{sample} increases above T_{c}. The sample may couple to magnetic correlations in the fluctuation disordered regime and, further, to the Kittel mode which may be discerned in the sample temperature dependence as well as in the real part of S_{21} marked with arrows in Fig. 6.28 (b). Subsequently, the sample cools down again to the conical phase as indicated by the conical mode at (vi) and further to the field-polarised phase.

Driving the system at an even higher frequency of $f_{\mathrm{drive}} = 1.8\,\mathrm{GHz}$, which corresponds to the breathing mode at low temperatures in the skyrmion lattice phase, S_{21} changes

significantly as shown in Fig. 6.29. The microwave field couples to the Kittel mode around $B \approx 60\,\mathrm{mT}$ leading to intense resonant heating as displayed in Fig. 6.29 (a) at (i). Matching approximately the conical resonance mode, the temperature remains above T_c at (ii) throughout the high- and low-field conical phase whereas it cools down to the skyrmion lattice phase at (iii). The cooling might be faster than reflected in Fig. 6.29 (a) due to the lower sweeping rate in FMR measurements (2 mT/min) compared to the sweep rate of 10 mT/min in the temperature correction, which corresponds to a longer equilibration time once the resonant mode of the conical phase is not matched anymore. As the coupling to the breathing mode is weaker, resonant heating is less pronounced within the skyrmion lattice phase.

S_{21} changes significantly in the field-polarised phase in Fig. 6.29 (b). As the excitation frequency crosses the resonant mode, the amplitude of the real part of the field-polarised mode is much smaller and a kink in the otherwise linear field dependence may be observed at (iv). The crossing coincides with the temperature maximum in Fig. 6.29 (a). Signatures consistent with the resonance mode of the conical phase appear just below the excitation frequency around $f = 1.6 - 1.7\,\mathrm{GHz}$ without a field dependence in contrast to measurements without intense microwave radiation.

The transition from the conical to the skyrmion lattice phase may be observed at $B_{A2} \approx 30\,\mathrm{mT}$ with an increased real and imaginary part of S_{21} over all frequencies. In contrast to measurements with lower microwave frequencies, two resonant modes may readily be observed in the skyrmion lattice phase, the CCW and the breathing mode, marked with yellow arrows. The linear field dependence with a positive slope of both modes may be the result of the temperature increase while decreasing the magnetic field. The CCW mode is rather flat as a function of temperature but has a positive dependence on field as shown in Fig. 6.11. The frequency of the breathing mode, on the contrary, decreases with increasing temperature but exhibits no magnetic field dependence. In the aforementioned cases, the breathing mode is presumably not observable as it is field independent for constant temperature and the derivative divide with respect to field may not capture it.

Notably, the signatures of the two excitations may be observed down to $|B| \approx 10\,\mathrm{mT}$ several mT lower than observed without intense microwave radiation. Furthermore, only a single transition is observed at even lower fields at $B \approx \pm 6\,\mathrm{mT}$ marked with white arrows. The field value agrees with the transition to the helical phase. The data suggests that the low-field conical phase may be significantly influenced by the microwave field that matches the Q^+-mode.

Finally as shown in the temperature dependent measurements shown in Sec. 6.3.1, resonant heating is observed above T_c between $\sim \pm 40\,\mathrm{mT}$ for frequencies from 0.6 GHz to

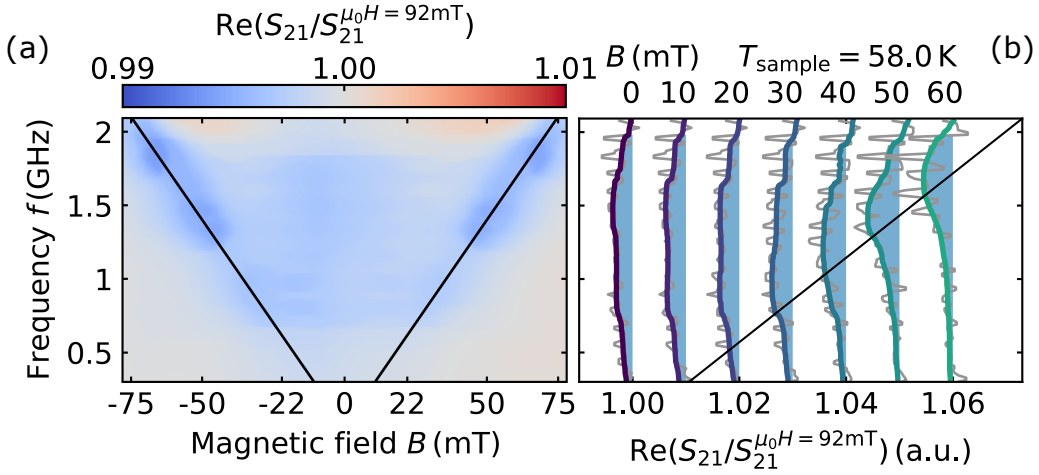

Figure 6.30.: Typical excitation spectra above T_c. (a) Divide slice microwave spectra as a function of f and B. (b) Cuts at constant magnetic fields of the divide slice microwave spectra. Curves are shifted by a constant value of 0.01 for better visibility. The Kittel mode is indicated as black lines.

1.8 GHz matching the range covering the CCW to breathing mode. Hence, this regime was chosen for the all-electrical microwave spectroscopy. Fig. 6.30 shows typical microwave spectra of the real part of the normalised complex transmission parameter $\mathrm{Re}(S_{21}/S_{21}^{\mu_0 H=92\,\mathrm{mT}})$ at $T_{\text{sample}} = 58.0\,\mathrm{K}$ above T_c. The data were recorded with the 2-tone FMR setup but without intense microwave radiation. The data is normalised to the highest available field of $B = 92\,\mathrm{mT}$ and the process is described in Sec. 3.3.3. For frequencies above 2 GHz, the signatures of the resonant mode of the field-polarised phase may be observed at 92 mT and this normalisation procedure is not possible. However, the divide slice depiction is used as the observed feature is too broad to be observed adequately in the derivative divide method.

In agreement with the temperature dependent measurements, a broad region of absorption appears, depicted in light blue, at low magnetic fields in a frequency range of at least $0.6\,\mathrm{GHz} \leq f \leq 2\,\mathrm{GHz}$ in Fig.6.30. Below $\approx -35\,\mathrm{mT}$ and above $\approx 35\,\mathrm{mT}$, respectively, the Kittel mode is present as a broad but distinct maxima. The black line denotes the Kittel mode for zero magnetisation to guide the eye and demonstrate that the absorption at low magnetic fields is of other origin.

Cuts at constant magnetic fields are shown in Fig. 6.30 (b) with $\mathrm{Re}(S_{21}/S_{21}^{\mu_0 H=92\,\mathrm{mT}})$ on the horizontal and the frequency on the vertical axis. A constant offset was added for better visibility and the black line again denotes the Kittel mode. At $B = 60\,\mathrm{mT}$ signatures of the the Kittel mode of the paramagnetic phase is observed as Lorentzian with a minimum at $\sim 1.7\,\mathrm{GHz}$ and a FWHM of $\sim 0.6\,\mathrm{GHz}$. Decreasing the magnetic field

towards $B = 40\,\mathrm{mT}$ the resonance frequency of the Kittel mode decreases linearly and the signal broadens symmetrically in frequency. Around 30 mT and below, the observed absorption is not centred about the extrapolated Kittel mode but around 1.2 GHz with a width over the entire frequency range from $\sim 0.4\,\mathrm{GHz}$ to $\sim 2\,\mathrm{GHz}$.

The broad feature is reminiscent of the signal attributed to fluctuating skyrmion textures in MnSi above T_c that also sharpens and merges under increasing fields with the Kittel mode [108]. The textures have sizes exceeding 10^3 Å and lifetimes above $10^{-9}\,\mathrm{s}$, i.e. at least ten times longer than a period of the excitations of typical frequencies $\sim 10\,\mathrm{GHz}$. Our observations may be empirically attributed to the presence of fluctuating skyrmion textures in Cu_2OSeO_3 above T_c. Further FMR spectroscopy is necessary with improved signal-to-noise ratio to compare the collective excitations above T_c with the excitations in the skyrmion lattice phase. Notably, the behaviour might deviate as skyrmions in Cu_2OSeO_3 are larger by a factor of ~ 4 [14, 89] and collective excitations an order of magnitude slower than in MnSi [83, 134].

In summary, we employed the 2-tone FMR technique to probe the collective excitation spectra of Cu_2OSeO_3 under intense microwave radiation. Strong ohmic and resonant heating occur in magnetic field sweeps that may be accounted for by a temperature correction. For an excitation frequency $f_\mathrm{drive} = 0.8\,\mathrm{GHz}$ just below the CCW mode, and up to an input power of $P = 2\,\mathrm{W}$, which corresponds to an average excitation field $B_\mathrm{ac,avg} \approx 70\,\mu\mathrm{T}$, the entire skyrmion lattice phase is accessible and the signatures of the CCW mode are observed throughout the phase.

Increasing the input power to $P = 3\,\mathrm{W}$, which corresponds to $B_\mathrm{ac,avg} \approx 80\,\mu\mathrm{T}$, resonant heating raises the sample temperature to or slightly above T_c. Nevertheless, the CCW mode may still clearly be observed over the entire field range of the skyrmion lattice phase. The same behaviour is observed for a lower excitation frequency $f_\mathrm{drive} = 0.6\,\mathrm{GHz}$ and highest excitation fields. As will be discussed in the subsequent sections, these results are in good agreement with observations in neutron scattering measurements.

Increasing the input power to the maximum of $P = 5\,\mathrm{W}$ for $f_\mathrm{drive} = 0.8\,\mathrm{GHz}$, T_sample increases just above T_c as the CCW mode approaches the driving frequency. Whereas the CCW mode may be observed within the skyrmion lattice phase for higher dc magnetic fields, it vanishes as it approaches the driving frequency coinciding with T_sample exceeding T_c. A similar behaviour may be observed for an intermediate input power of $P = 3\,\mathrm{W}$ if T_coupling is set higher than the aforementioned case. The data suggest that a sufficiently large temperature difference between T_sample and T_holder is necessary to establish a quasi-static state close to T_c as the sample may already couple to magnetic correlations above T_c in the fluctuation disordered regime. Alternatively, the ferromagnetic background is

driven to such an extent that the signal from the skyrmions is severely altered and the probe signal does not match the expectations inferred from the undisturbed system.

Noticeably for $f_{\mathrm{drive}} = 1.2\,\mathrm{GHz}$ matching approximately the CCW resonance mode, T_{sample} increases sharply just below or to T_{c} in the skyrmion lattice phase, but no signal of the CCW resonant mode is observed. However, signatures of a a field-independent, broad resonant mode appears in the range of the breathing mode. For an excitation frequency $f_{\mathrm{drive}} = 1.8\,\mathrm{GHz}$, which matches approximately the breathing mode and is above the CCW mode, the signal of the CCW mode recovers and, in addition, the breathing mode may be observed due to a change of temperature within the skyrmion lattice phase during field sweeps. Furthermore, the intense excitation field couples effectively to the resonant mode of the conical phase preventing the sample from cooling into the conical phase and altering the transition from the skyrmion lattice to the conical phase at B_{A1}. Finally, above T_{c} and at low magnetic fields absorption in the complex transmission parameter S_{21} is observed over a broad frequency range which is reminiscent of recent measurements of fluctuating skyrmion textures in the fluctuation disordered regime of MnSi [108].

6.3.4. Loss of long-range order in the SkX phase

Small angle neutron scattering yields microscopic information on the magnetic correlations. The position of magnetic Bragg peaks in reciprocal space originating from coherent neutron scattering provide direct evidence of the long-range order as the correlation lengths are inversely proportional to their widths. In this section, we report SANS measurements of the skyrmion lattice and conical magnetic correlations under intense microwave radiation. After a review of typical scattering patterns, the temperature dependence of the integrated intensities across the skyrmion lattice phase are discussed. Temperature sweeps were performed for various excitation frequencies at the strongest microwave fields and for several excitation amplitudes for a fixed frequency $f_{\mathrm{drive}} = 0.8\,\mathrm{GHz}$ just below the CCW mode. Subsequently, the evolution of the scattering pattern of the skyrmion lattice as a function of temperature, excitation frequency and field are discussed. Finally, the magnetic Bragg peaks are analysed and the evolution of the correlation lengths are presented.

Typical SANS patterns of the skyrmion lattice and the conical phase are shown in Fig. 6.31 (a) and (b). The skyrmion lattice scattering pattern in Fig. 6.31 (a) represents the sum of rocking scans through $\omega = \pm 3.6^{\circ}$ and $\chi = \pm 2.7^{\circ}$ at a temperture of $T = 56.8\,\mathrm{K}$ and under a magnetic field of $B = 22\,\mathrm{mT}$ parallel to the neutron beam. A single skyrmion lattice domain is observed which aligns along the crystallographic [110] direction. For the neutron scattering pattern of the conical phase in Fig. 6.31 (b) the magnetic field was

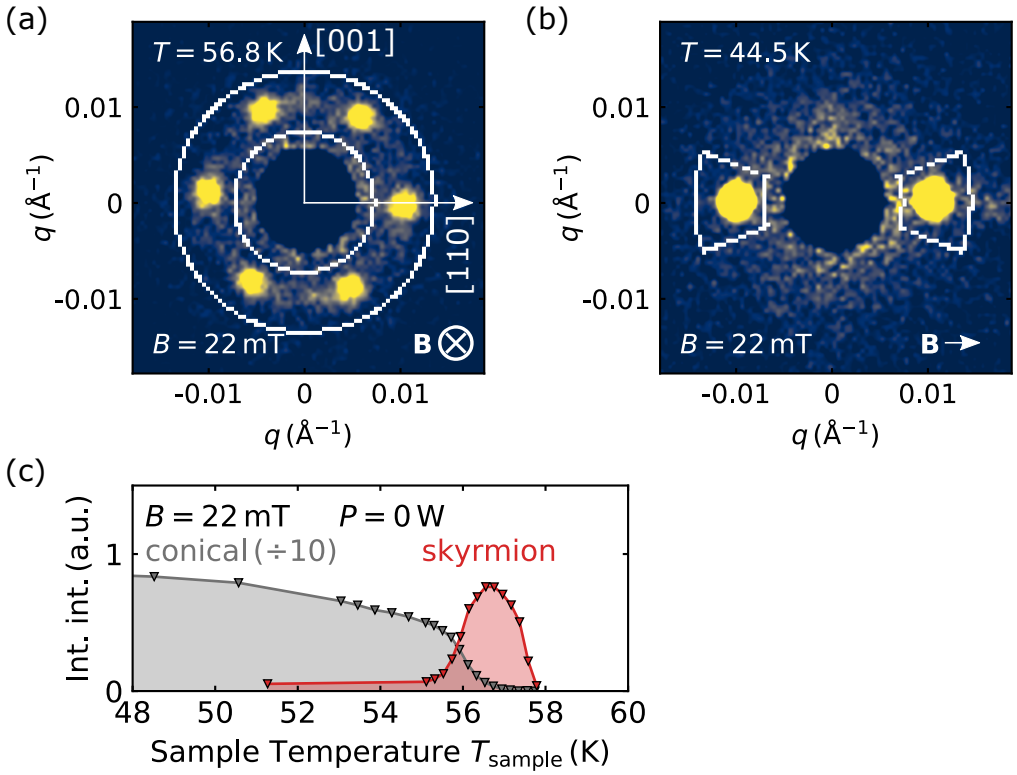

Figure 6.31.: Typical neutron scattering patterns and intensities. (a) Sum over two rocking scans about ω and χ of the SANS pattern of the hexagonal skyrmion lattice. (b) Sum over a rocking scan about ω of the SANS pattern of the conical phase. White lines mark the region of interest where intensity is summed up for comparison to various field values and temperatures. (c) Integrated scattering intensity of the signals from the skyrmion lattice and conical phase as a function of sample temperature T_{sample}. The conical intensity is divided by 10 for clarity.

aligned horizontal, perpendicular to the neutron beam. Rocking scans were performed through $\omega = \pm 3°$. The rocking axes are depicted in Fig. 6.3. All neutron scattering measurements were performed at a constant magnetic field of $B = 22\,\mathrm{mT}$.

The temperature dependence of the integrated intensities of the skyrmion lattice and conical phase is shown in Fig. 6.31 (c) under constant magnetic field without microwave excitation. Each data point corresponds to the integrated scattering intensity within the masks depicted in Fig. 6.31 (a) for the skyrmion lattice phase and in Fig. 6.31 (b) for the conical phase. Error bars are smaller than the symbols used. The data was recorded according to the protocol described in Sec. 6.2.1. The onset of skyrmion lattice order is at $T_{\mathrm{c}} = 57.7\,\mathrm{K}$ and the transition to the conical phase around $T \approx 56\,\mathrm{K}$. The intensity of the scattering pattern of the skyrmion lattice exhibits the same smooth decrease into the conical and the paramagnetic phase.

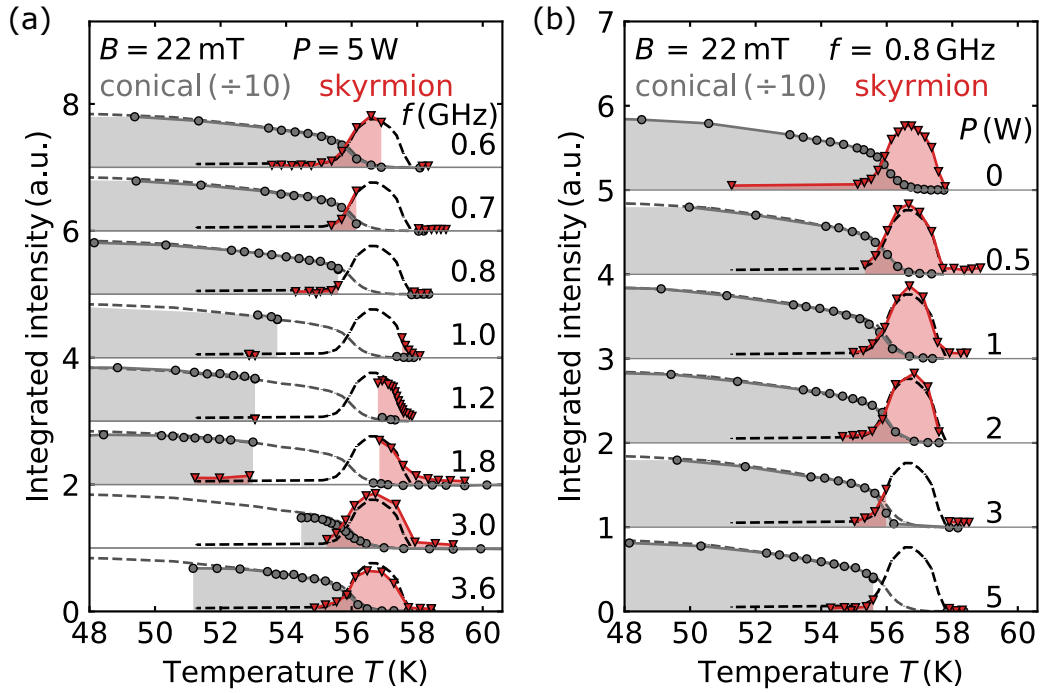

Figure 6.32.: Power and frequency dependence of conical and skyrmion scattering intensities. Temperature dependence of the integrated scattering intensity of the skyrmion and conical phase for (a) several AC magnetic field frequencies and a power $P = 5\,\mathrm{W}$ and (b) increasing power values for a frequency $f = 0.8\,\mathrm{GHz}$. Dashed lines denote the temperature dependence of the conical and skyrmion intensity without excitation through the AC magnetic field. Solid lines are guides to the eye.

The temperature dependence of the integrated intensities of the conical and the skyrmion lattice state are shown in Fig. 6.32 (a) for various microwave frequencies at an input power of $P = 5\,\mathrm{W}$, the largest power available. The intensities are shifted by a constant for better visibility. For frequencies between $f_{\mathrm{drive}} = 0.6\,\mathrm{GHz}$ and $1.8\,\mathrm{GHz}$ shown in Fig. 6.32 (a), temperature regions are not accessible due to resonant heating. The inaccessible temperature range increases with increasing frequency, but vanishes for $f_{\mathrm{drive}} \geq 3.0\,\mathrm{GHz}$. The skyrmion lattice signal may be observed at lower temperatures for frequencies below $f_{\mathrm{drive}} = 0.8\,\mathrm{GHz}$ and at higher temperatures for frequencies above.

As the resonance frequency of the CCW mode of the skyrmion lattice phase increases from $\sim 1.0\,\mathrm{GHz}$ to $\sim 1.2\,\mathrm{GHz}$ with decreasing temperature at $B = 22\,\mathrm{mT}$ as shown in Fig. 6.11, a microwave field at low frequency couples to the CCW mode at higher temperatures and moves out of resonance with decreasing temperature. For frequencies above $\sim 1.0\,\mathrm{GHz}$ heating increases with decreasing temperatures as the microwave field moves into resonance. The effect is evident for frequencies several 100 MHz above and below the resonance frequencies and may be attributed to the width of the CCW resonance

mode, which exhibits a FWHM of $\sim 0.3\,\mathrm{GHz}$ in FMR spectroscopy. However, the temperature dependence of the integrated scattering intensity of the skyrmion lattice as well as the conical phase are unaffected by the microwave radiation beyond the inaccessible temperature range.

For $f_{\mathrm{drive}} = 0.8\,\mathrm{GHz}$, just below the CCW resonant mode, the skyrmion lattice phase is not accessible except for vanishingly small scattering intensity at low temperature at the border of the conical state. Interestingly, at $f_{\mathrm{drive}} = 1.0\,\mathrm{GHz}$ the onset of a skyrmion lattice order can be discerned below T_{c}. At $f_{\mathrm{drive}} = 3.0\,\mathrm{GHz}$ and $3.6\,\mathrm{GHz}$ the temperature dependences of both the intensities of the conical and the skyrmion lattice phase are nearly unaffected since the driving frequency is far above any resonance mode. Though, towards lower temperatures, the conical state begins to deviate which is due to large temperature differences of $\sim 5 - 10\,\mathrm{K}$ between sample and sample holder and, consequently, the error in the temperature correction increases. Furthermore, the intensity of the skyrmion lattice at $f_{\mathrm{drive}} = 3.0\,\mathrm{GHz}$ is slightly larger throughout the skyrmion lattice phase, reaching up to $13\,\%$.

Since the intensity of the skyrmion lattice phase vanishes for $f_{\mathrm{drive}} = 0.8\,\mathrm{GHz}$, the dependence on microwave power was investigated in more detail as shown in Fig. 6.32 (b). For input powers up to $P = 2\,\mathrm{W}$, the temperature dependence of both the intensities of the conical and the skyrmion lattice phase are unchanged. Under field-cooling at $P = 3\,\mathrm{W}$ the sample temperature gets stuck just above T_{c} followed by a discontinuous change of the temperature of $\Delta T \approx 2\,\mathrm{K}$. Nevertheless, the temperature dependence at low temperatures is the same as for the system without microwave fields applied.

The overlap of the scattering intensities under intense microwave radiation for all microwave frequencies and input powers with the measurement of the undisturbed system suggests relatively small temperature gradients across the sample not larger than several hundred mK. As the temperature range of the skyrmion lattice phase is only $\sim 2\,\mathrm{K}$ and the intensity changes strongly with temperature, an inhomogeneous sample temperature distribution would affect the temperature dependence of the intensity, which is not observed.

Prior to a quantitative analysis of the correlation lengths extracted from fits of the magnetic Bragg peaks, it is instructive to discuss the scattering patterns in the skyrmion lattice phase. Typical patterns as observed for different microwave powers are shown in Fig. 6.33. Without microwave fields, as shown in Fig. 6.33 (a1) to (f1), two skyrmion lattice domains that are unequally populated and aligned along the [001] and [110] crystallographic direction, respectively, may be observed throughout the skyrmion lattice phase. Applying a microwave field with an input power $P = 0.5\,\mathrm{W}$ and $f_{\mathrm{drive}} = 0.8\,\mathrm{GHz}$, a single domain aligned along [001] is observed which evolves into two domains at lower temperatures.

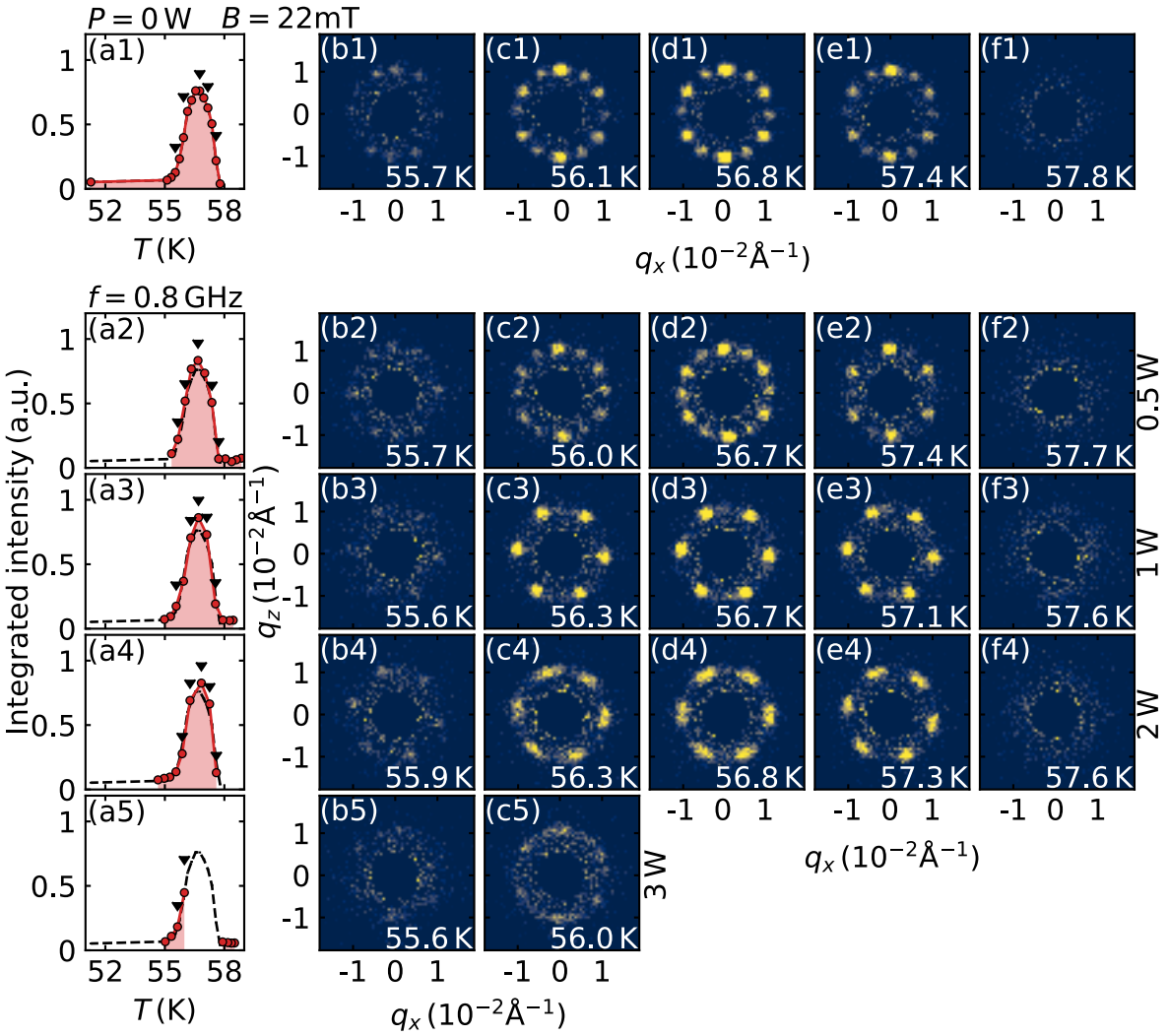

Figure 6.33.: Power dependence of the skyrmion lattice scattering pattern. (a1) Integrated scattering intensity of the skyrmion lattice as a function of temperature without ac magnetic field applied. Black arrows mark the temperatures of scattering patterns shown in (b1-f1). (a2-a6) Integrated scattering intensity of the skyrmion lattice as a function of temperature T for increasing power P between 0 W and 3 W. The dashed line represents the intensity without ac magnetic field applied. (b2-c5/f4) Temperature dependence of the two-dimensional neutron scattering patterns of the skyrmion lattice for several powers. For $P = 3$ W several temperatures cannot be reached, hence the vacant plots.

Increasing the input power further to 1 W, a single skyrmion lattice domain aligned along [110] is observed with sharp Bragg peaks. For $P = 2\,\mathrm{W}$, the temperature sweep accesses all temperatures as shown in Fig. 6.33 (a4) and the scattering intensity of the skyrmion lattice shows the same behaviour as observed without a microwave field. However, the Bragg peaks broaden azimuthally in Fig. 6.33 (c4) to (e4) and sharpen again for lowest temperatures in (b4). In comparison, the radial peak width is unchanged. Increasing the input power to $P = 3\,\mathrm{W}$, scattering intensity is only accessible at lower temperatures where it exhibits a ring with the same radial momentum transfer $q = 0.01\,\mathrm{Å}^{-1}$ as in the undisturbed skyrmion lattice, however, without a sixfold pattern.

The width of Bragg peaks may be extracted from the scattering patterns. We obtain the widths along the momentum transfer q, the rocking widths ω and χ, respectively, and the azimuthal width θ. In Fig. 6.34 (a) masks for the data integration are depicted. The radial width of the masks is chosen to cover $\pm 3\sigma$ of the Bragg peaks. The ω- and χ-masks correspond to an azimuthal width of 60°. For the intensity as a function of momentum transfer q in Fig. 6.34 (b) the entire detector was integrated. We expect Lorentzian shaped Bragg peaks for intensity which is not constraint by the instrumental resolution. In contrast, resolution-limited scattering yields Gaussian shaped peaks. Details of the instrumental resolution are discussed in Sec. 6.2.1. Hence, the Bragg peaks in Fig. 6.34 (b) to (e) were fitted by a Pseudo-Voigt function

$$V(q) = \eta \cdot L(q, f) + (1 - \eta) \cdot G(q, f) \quad \text{with } 0 \leq \eta \leq 1 \tag{6.1}$$

where $L(q, f)$ is a normalised Lorentzian function, $G(q, f)$ a normalised Gaussian function and η the weight factor between them. The azimuthal intensity distribution may be fitted by a superposition of Pseudo-Voigt functions. For cases where two individual skyrmion lattice domains were observed, as in Fig. 6.34 (e), each domain was fitted by a six-fold superposition of Pseudo-Voigt functions. In the superposition neighbouring peaks of the same domain were separated by a fixed angle of 60°.

Fig. 6.35 shows the results of fitting the magnetic Bragg peaks of the skyrmion lattice phase for different excitation powers at constant frequency $f_{\mathrm{drive}} = 0.8\,\mathrm{GHz}$ as a function of temperature. In addition, the integrated scattering intensity is shown as a function of temperature reflecting the signal strength and phase boundaries. The grey shaded area denotes the FWHM of the Gaussian-shaped instrumental resolution. The FWHM of the Bragg peaks along the momentum transfer q in Fig. 6.35 (a) is resolution limited and does not vary with temperature except when approaching the lower phase boundary where a slight increase is observed under increasing microwave power. Overall, the momentum transfer of the skyrmion lattice is $q = 0.010 \pm 0.001\,\mathrm{Å}^{-1}$ for all measurements and does not change even under intense microwave radiation within the 1σ standard deviation of the SANS resolution.

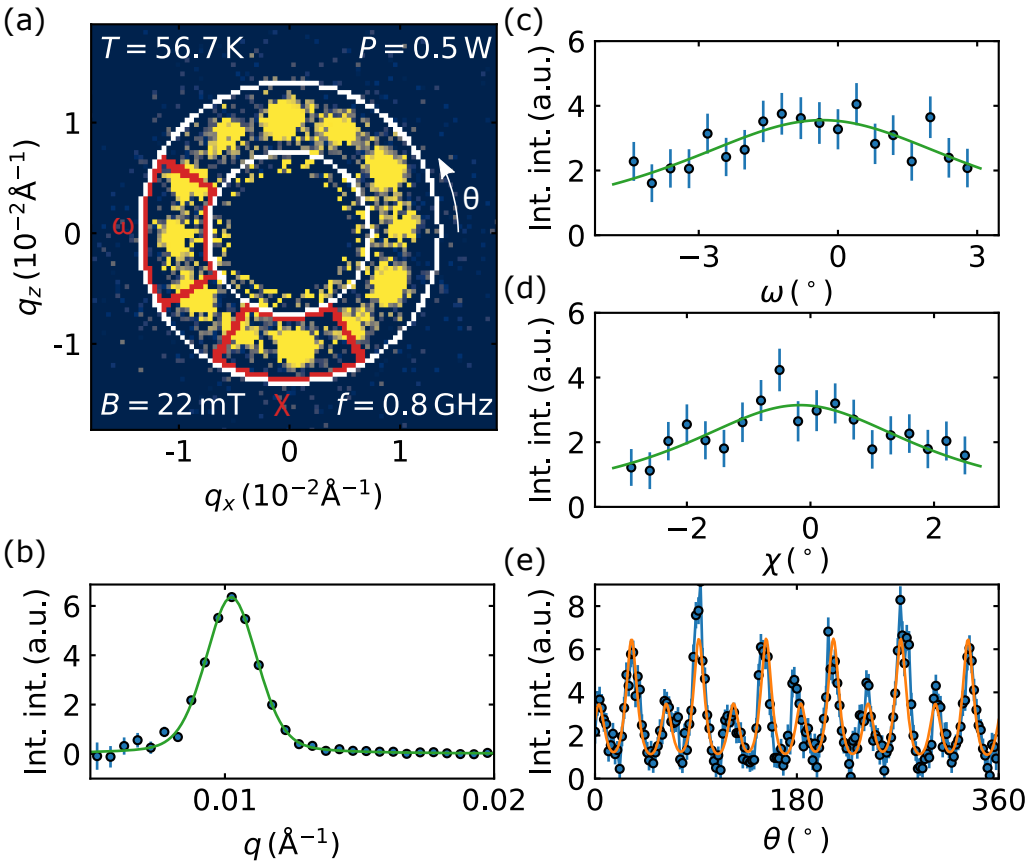

Figure 6.34.: Analysis of the skyrmion lattice Bragg peaks. (a) Typical skyrmion lattice scattering pattern and the evaluated masks. (b) Integrated scattering intensity over the entire detector as a function of momentum transfer q. (c) Integrated scattering intensity as a function of rocking angle ω and (d) χ. (e) Azimuthal neutron scattering intensity distribution of two domains, hence, the observed 12-fold symmetry, which are unequally populated.

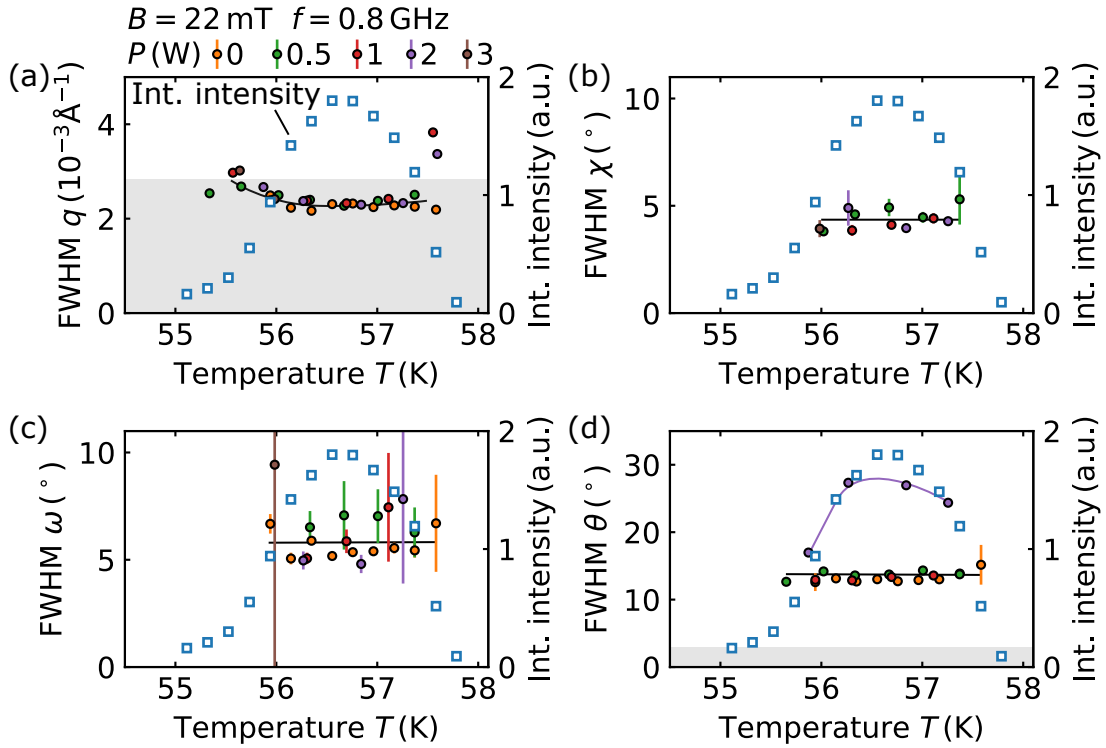

Figure 6.35.: Temperature and input power dependence of the Bragg peak widths of the skyrmion lattice. (a) FWHM along the momentum transfer q, (b) the rocking angle χ and (c) the rocking angle ω as a function of temperature T for input powers of the microwave field up to $P = 3\,\mathrm{W}$ and a constant frequency $f_{\mathrm{drive}} = 0.8\,\mathrm{GHz}$. Blue open squares mark the integrated scattering intensity. (d) FWHM along the azimuthal angle θ as a function of temperature T. Lines are guides to the eye. Black lines denote the behaviour of the undisturbed system and coloured lines correspond to individual input powers. The grey shaded area depicts the Gaussian shaped instrumental resolution expressed as FWHM.

The width of the rocking angle χ does not change with temperature and is approximately equal for all microwave powers. A rocking scan about χ without microwave excitation was not recorded. The widths of the rocking angle ω without microwave radiation is constant as a function of temperature. Applying microwave radiation, Bragg peaks do not broaden within the 1σ standard deviation compared to the undisturbed system. As expected, the widths in χ and ω are almost equal in value. The small difference may originate from the different rocking widths of ω and χ. The Bragg peaks are in general broad and their tails could not be fully recorded within the accessible rocking widths $\Delta\omega$ and $\Delta\chi$. The FWHM of the azimuthal width in Fig. 6.35 (d) is constant for input powers up to $P = 1\,\mathrm{W}$ and clearly exceeds the resolution limit. At $P = 2\,\mathrm{W}$ the peak width increases significantly throughout the skyrmion lattice phase. It increases with decreasing temperature before decreasing again close to the phase transition to the conical phase.

For $P = 3\,\mathrm{W}$ only a ring of intensity was observed where an azimuthal width could not be determined.

A detailed depiction of the azimuthal intensity distribution for increasing microwave power is shown in Fig. 6.36 for two temperature values. $T_1 = 55.95 \pm 0.1\,\mathrm{K}$ is close to the transition to the conical phase and $T_2 = 56.75 \pm 0.1\,\mathrm{K}$ is in the skyrmion lattice phase centre. Without microwaves applied and $P = 0.5\,\mathrm{W}$ two skyrmion lattice domains may be discerned oriented along the crystallographic [001] and [110] direction throughout the phase. The system changes to a single domain state for $P = 1\,\mathrm{W}$ aligned along the [110] direction without azimuthal broadening of the width of the peaks. Increasing the microwave power to $P = 2\,\mathrm{W}$, a six-fold scattering pattern may still be observed oriented along [110], but the azimuthal width of the peaks broadens significantly in the centre of the skyrmion lattice whereas the width remains unchanged towards the lower phase boundary. At $P = 3\,\mathrm{W}$ only the lower part of the skyrmion lattice phase is accessible due to resonant heating as shown in Fig. 6.32 (b). Here, the 6-fold scattering pattern vanishes and a ring of intensity may be observed. However, the integrated scattering intensity matches that recorded without microwave radiation as shown in Fig. 6.32 (b).

The scattering pattern of the skyrmion lattice for various microwave frequencies at a large power of $P = 5\,\mathrm{W}$ is shown in Fig. 6.37. For comparison, the scattering patterns without applied microwave field are shown in Fig. 6.37 (b1) to (f1). For $f_{\mathrm{drive}} = 0.6\,\mathrm{GHz}$ in Fig. 6.37 (b2) to (f2), only the lower temperature region of the skyrmion lattice is accessible. Fig. 6.37 (d2) shows the highest temperature where skyrmion lattice peaks could be observed, just below the discontinuous drop in temperature. The magnetic Bragg peaks are azimuthally broadened but sharp in radial direction. Cooling the system slightly by 0.3 K, two unequally populated domains may be observed aligned along [001] and [110]. $f_{\mathrm{drive}} = 0.8\,\mathrm{GHz}$ is omitted in this figure as the skyrmion lattice phase is not accessible at all.

For $f_{\mathrm{drive}} = 1\,\mathrm{GHz}$, corresponding approximately to the CCW mode, the sixfold pattern with azimuthally broadened peaks may be observed at higher temperatures. For a microwave frequency of $f_{\mathrm{drive}} = 1.2\,\mathrm{GHz}$, the system cools further into the skyrmion lattice phase. First, a ring of intensity emerges which evolves into a sixfold pattern (see Fig. 6.37 (f4-d4)). Nevertheless, the peaks remain broadened as compared to the data without microwave radiation. Likewise at a higher frequency of $f_{\mathrm{drive}} = 1.8\,\mathrm{GHz}$, the scattering pattern corresponds to a ring of intensity at higher temperatures, even at $T = 57.2\,\mathrm{K}$ close to the centre of the the skyrmion lattice phase. For $T = 56.8\,\mathrm{K}$, a weak sixfold scattering pattern emerges with broad peaks. Applying intense microwave radiation at $f_{\mathrm{drive}} = 3\,\mathrm{GHz}$, far above the modes of the skyrmion lattice or conical phase at

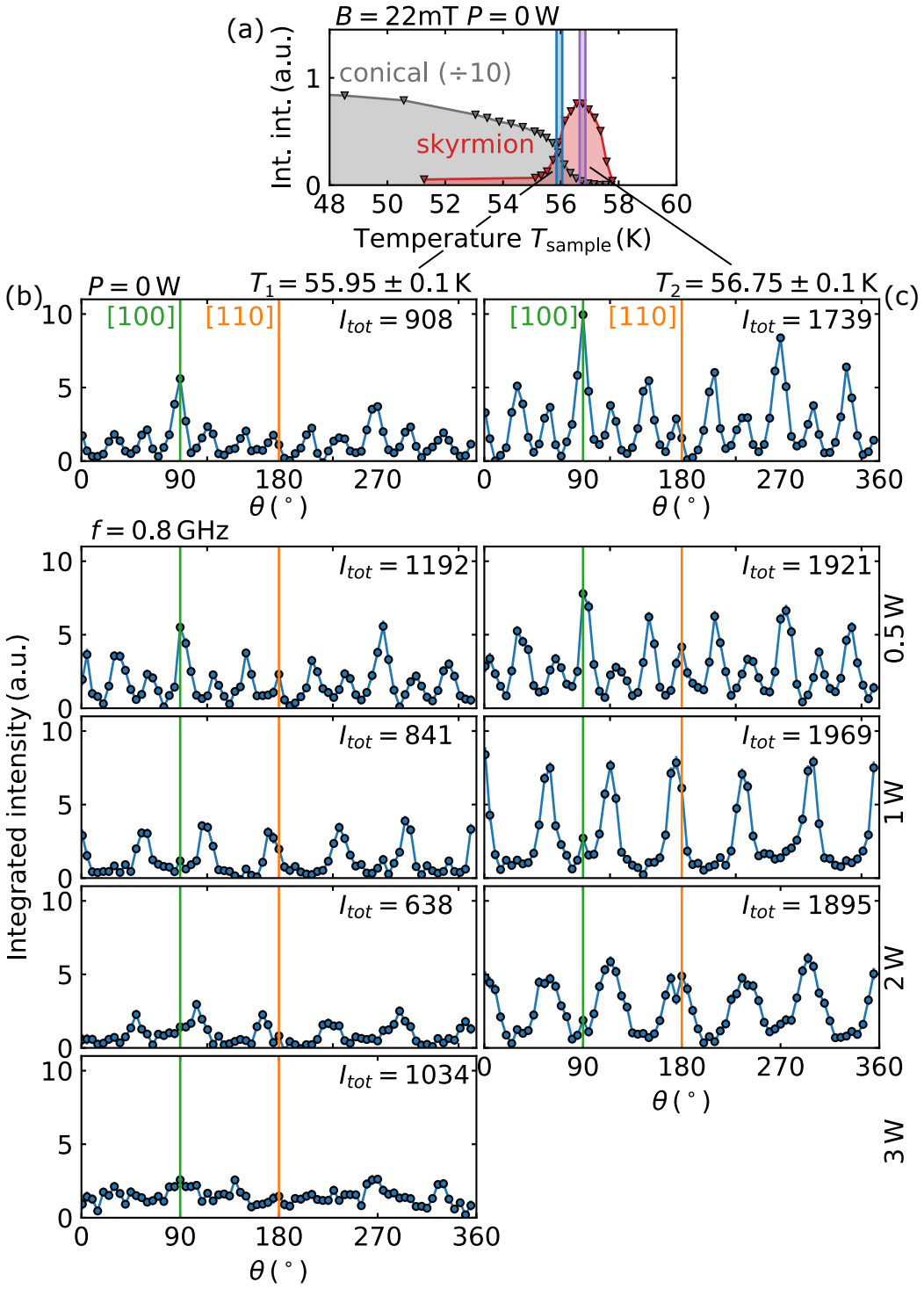

Figure 6.36.: Azimuthal distribution of the skyrmion lattice scattering intensity for increasing input power. (a) Skyrmion lattice and conical phase scattering intensities as a function of temperature. The blue and purple shaded areas mark the temperatures of plots in (b) and (c). Integrated scattering intensity as a function of azimuthal angle θ for increasing ac magnetic field power towards the phase boundary in (b) and in the phase centre in (c). Green and orange lines depict the crystallographic [001] and [110] direction, respectively.

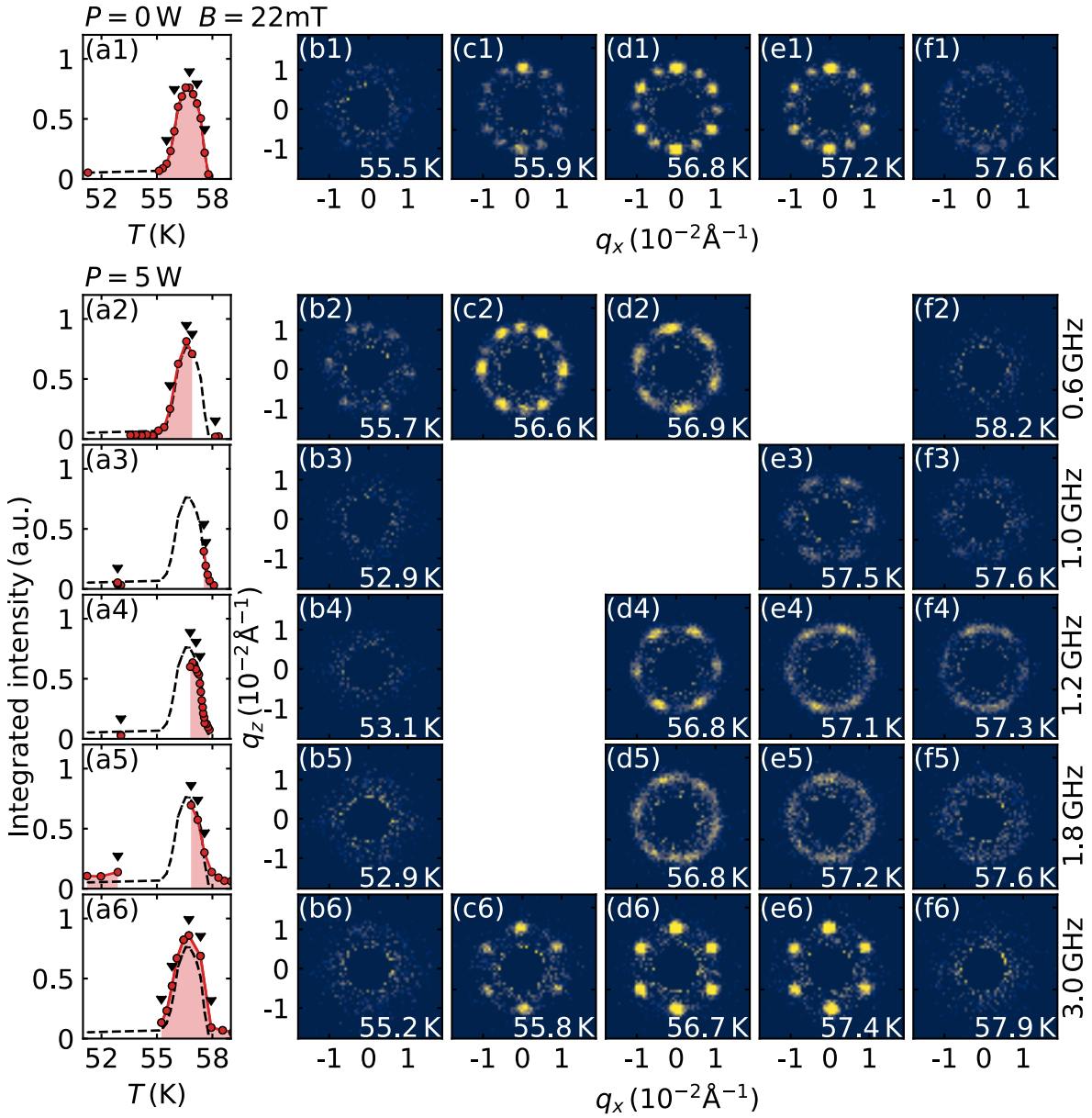

Figure 6.37.: Scattering patterns of the skyrmion lattice phase as a function of temperature and microwave frequency. (a1) Integrated scattering intensity of the skyrmion lattice as a function of temperature without microwave radiation. Black arrows mark the temperatures of scattering patterns shown in (b1-f1). (a2-a6) Integrated scattering intensity of the skyrmion lattice as a function of T for several f_{drive} between 0.6 GHz and 3.0 GHz. The dashed line represents the intensity without microwave radiation. (b2-f6) Temperature dependence of the two-dimensional neutron scattering patterns of the skyrmion lattice for several microwave frequencies. Several temperatures cannot be reached under certain frequencies, hence, the missing plots.

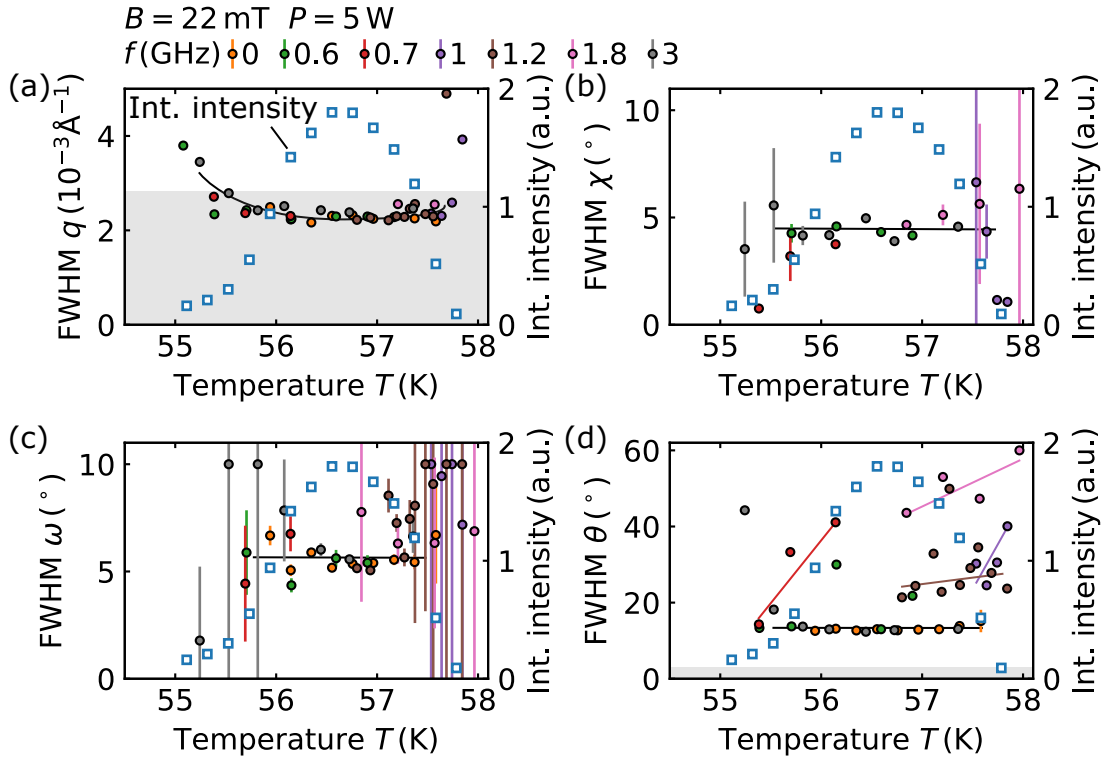

Figure 6.38.: Temperature and frequency dependence of the skyrmion lattice Bragg peak widths. (a) FWHM along the radial momentum transfer q, (b) the rocking angle χ and (c) the rocking angle ω as a function of temperature T for ac magnetic field frequencies up to $f = 3\,\mathrm{GHz}$ and a constant high input of $P = 5\,\mathrm{W}$. (d) FWHM along the azimuthal angle θ as a function of temperature T. The grey shaded area depicts the instrumental resolution. Lines are guides to the eye. Black lines denote the behaviour of the undisturbed system and coloured lines correspond to individual input frequencies. The grey shaded area depicts the instrumental resolution as FWHM of the Gaussian resolution.

$B = 22\,\mathrm{mT}$, a sixfold scattering pattern of a single domain is observed with sharp Bragg peaks.

Fig. 6.38 shows results of fitting the magnetic Bragg peaks of the frequency series at constant input power $P = 5\,\mathrm{W}$ and as a function of temperature using Eq. 6.1. The integrated scattering intensity yields the signal strength and reflects the phase boundaries. The measurement of the FWHM along the momentum transfer q in Fig. 6.38 (a) is resolution limited and does not change with temperature except for a slight increase close to the phase boundary at low temperatures. The width of the rocking angles χ and ω are both constant as a function of temperature and, as expected, similar in value. At the phase boundaries the scattering intensity is too low for a proper analysis, the error bars increase significantly or the fits become unreliable.

Finally, the FWHM of the azimuthal width in Fig. 6.38 (d) is temperature independent without microwave radiation and for excitation frequencies of $f_{\mathrm{drive}} = 3\,\mathrm{GHz}$. The data exceeds the resolution limit. For microwave frequencies in the range 0.7 GHz to 1.8 GHz the azimuthal width increases. At 0.7 GHz it is maximal within the skyrmion lattice phase and decreases when approaching the phase boundary. For 1 GHz and 1.2 GHz the width is broader by a factor of two as compared to no microwave radiation. Especially at 1.8 GHz, the width is enhanced by a factor of up to 3.

A detailed depiction of the azimuthal intensity distribution under increasing microwave frequency in the centre of the skyrmion lattice phase at $T_1 = 56.7 \pm 0.1\,\mathrm{K}$ and when approaching the phase transition to the paramagnetic phase at $T_2 = 57.5 \pm 0.1\,\mathrm{K}$, respectively, is shown in Fig. 6.39. Fig. 6.39 (a) indicates the temperature ranges shown in (b) and (c). Two plots for $f_{\mathrm{drive}} = 1\,\mathrm{GHz}$ and 0.6 GHz, respectively, are omitted as the temperature region is not accessible. Without microwave radiation, two skyrmion lattice domains may be observed that are aligned along the crystallographic [001] and [110] direction throughout the phase. Likewise for $f_{\mathrm{drive}} = 0.6\,\mathrm{GHz}$, two domains, both exhibiting similarly sharp Bragg peaks in azimuthal direction, may be observed. The domain population is, however, reversed. In the case of $f_{\mathrm{drive}} = 1\,\mathrm{GHz}$ and 1.2 GHz, a sixfold pattern may be observed with azimuthally broadened Bragg peaks. Increasing the frequency to 1.8 GHz, the peaks broaden even further. The data may be interpreted in terms of azimuthally broad peaks which overlap significantly which is the assumption for the fits in Fig. 6.38 where the constant offset is fixed at zero. In contrast, the scattering intensity can also be explained by a ring of intensity with a sixfold pattern on top, however, less broad. The origin of the broad Bragg peaks is discussed below. For the highest excitation frequency $f_{\mathrm{drive}} = 3\,\mathrm{GHz}$, a single domain with sharp Bragg peaks is observed aligned along [001].

In summary, we performed small angle neutron scattering measurements on Cu_2OSeO_3 under intense microwave radiation to search for changes of the long-range order of the skyrmion lattice state. Considering the temperature dependence of the integrated scattering intensity of the skyrmion lattice scattering pattern in field cooled scans, the microwave fields couple most effectively for frequencies just below the CCW mode. For an excitation frequency of $f_{\mathrm{drive}} = 0.8\,\mathrm{GHz}$, the sample temperature remains just above T_{c} and the skyrmion lattice phase cannot be accessed for the highest excitation fields of order $B_{\mathrm{ac,avg}} \sim 100\,\mu\mathrm{T}$ (see Fig. 6.8 (a)). For lower microwave powers $P \leq 2\,\mathrm{W}$ at $f = 0.8\,\mathrm{GHz}$, the intensity of the skyrmion lattice phase may be observed over the entire phase whereas for $P = 3\,\mathrm{W}$ only those parts of the phase pocket at low temperatures are accessible with a critical microwave amplitude around $B_{\mathrm{ac,avg}} \sim 75\,\mu\mathrm{T}$. Even for $f_{\mathrm{drive}} = 0.6\,\mathrm{GHz}$, which

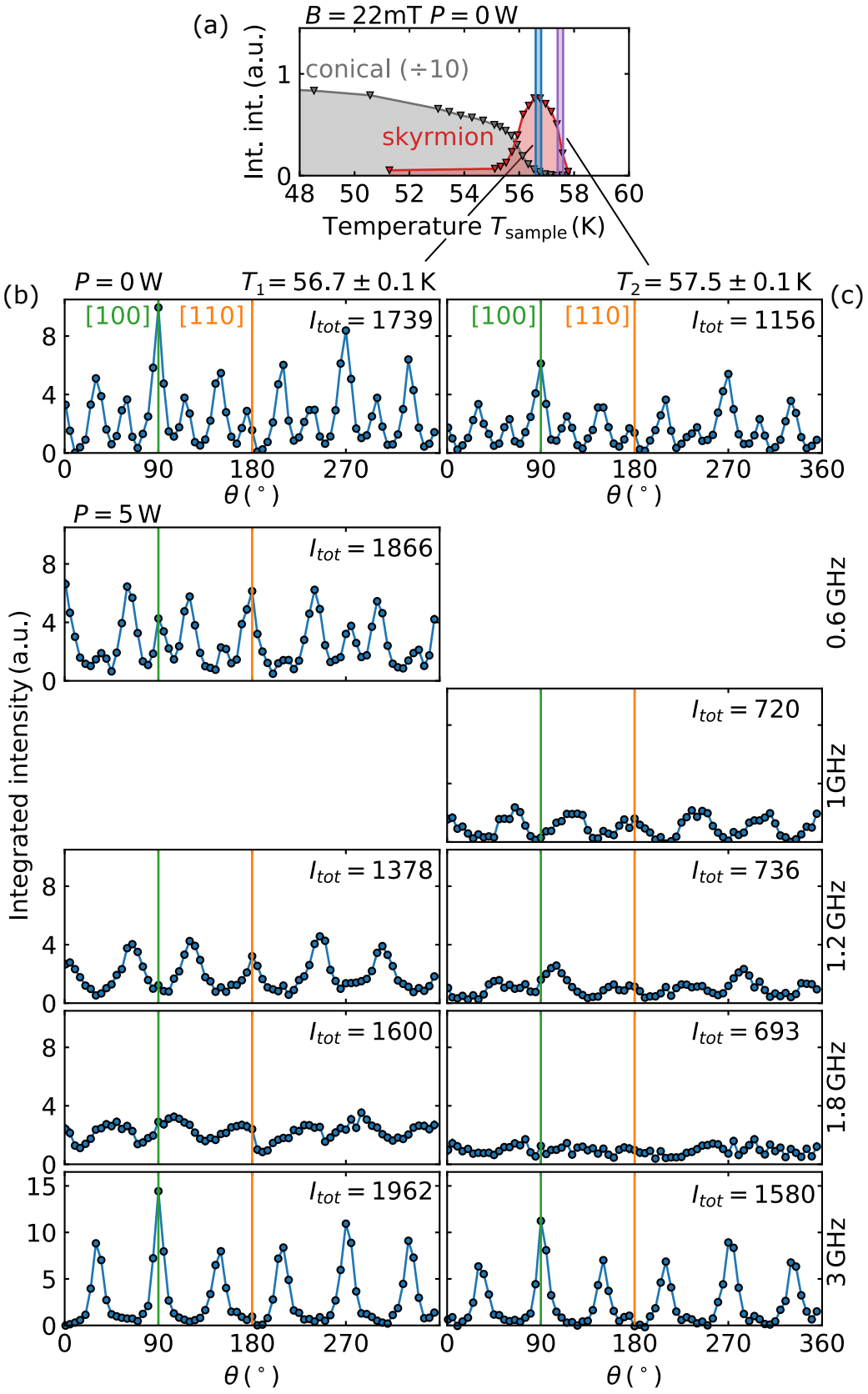

Figure 6.39.: Azimuthal distribution of the skyrmion lattice scattering intensity for increasing microwave frequency. (a) Scattering intensity of the skyrmion lattice and conical phase as a function of temperature. The blue and purple shaded areas mark the temperatures of plots in (b) and (c). Integrated scattering intensity as a function of azimuthal angle θ for increasing microwave input power towards the phase boundary in (b) and in the phase centre in (c). Green and orange lines depict the crystallographic [001] and [110] direction, respectively.

is $\sim 0.4\,\mathrm{GHz}$ below the CCW mode, T_{sample} is stuck at T_{c} where no scattering intensity may be observed before discontinuously cooling down into the skyrmion lattice phase.

Furthermore, increasing the microwave frequency for highest microwave fields, the scattering intensity of the skyrmion lattice phase may be observed in parts of the phase pocket at high temperatures close to T_{c} for $f_{\mathrm{drive}} = 1\,\mathrm{GHz}$ and $1.2\,\mathrm{GHz}$, both frequencies approximately matching the CCW mode. The intensity of the skyrmion lattice phase may also be observed partially for $f_{\mathrm{drive}} = 1.8\,\mathrm{GHz}$, which matches the breathing mode of the skyrmion lattice phase and, at lower temperatures, the resonant modes of the conical phase, respectively.

The width of the Bragg peaks and the corresponding correlation lengths along the momentum transfer q are resolution limited. The width of the Bragg peaks along the rocking angles ω and χ are constant as a function of temperature and do not change as microwave radiation is applied. However, a pronounced azimuthal broadening is observed for all frequencies $0.6\,\mathrm{GHz} \leq f_{\mathrm{drive}} \leq 1.8\,\mathrm{GHz}$ about the CCW and breathing mode at highest excitation fields. For $f_{\mathrm{drive}} \geq 3\,\mathrm{GHz}$, far above the resonant modes of the skyrmion lattice and conical phase, the scattering patterns are unaltered. Investigating the power dependence of the azimuthal broadening at an excitation frequency of $f_{\mathrm{drive}} = 0.8\,\mathrm{GHz}$ reveals a transition from sharp to broadened Bragg peaks between $P = 1\,\mathrm{W}$ and $2\,\mathrm{W}$.

The azimuthal broadening may have several origins and a careful discrimination of thermal effects is necessary. It is important to note that the SANS patterns represent an integration over the entire sample volume for several minutes. Furthermore, in SANS measurements the intensity is energy integrated and no information about the dynamics is obtained. For the temperature gradient across the sample we estimate an upper limit of some 100 mK. The integrated scattering intensity exhibits, on the one hand, the same temperature dependence for all excitation frequencies and fields and, on the other hand, is sensitive to small inhomogeneities because the intensity changes rapidly with temperature. The potential causes of the azimuthal broadening are discussed below.

6.4. Summary and conclusions

In this chapter, the collective excitations and the long-range magnetic order of the skyrmion lattice phase in Cu_2OSeO_3 were investigated under intense microwave fields. All-electrical microwave spectroscopy and small angle neutron scattering were employed as a function of dc magnetic field and temperature for various excitation frequencies and fields. The focus was on excitation frequencies near the resonant modes of the skyrmion lattice phase. To account for ohmic and resonant heating, temperature correction measurements were performed.

For these studies we developed an all-electrical spectroscopy setup, referred to as 2-tone FMR technique, that allows to drive magnetic excitations with a strong microwave field in the low GHz frequency regime by means of a coplanar waveguide. The response in the magnetisation dynamics is simultaneously and independently probed and recorded for a broad range of frequencies. Using a different setup, SANS was combined with the same CPW providing microscopic information on the long-range order of the magnetic correlations in reciprocal space under strong microwave fields up to $B_{\mathrm{ac,\ avg}} \sim 100\,\mu\mathrm{T}$.

The temperatures of the sample, the holder, and the CPW were recorded under intense microwave radiation as a function of dc magnetic field, temperature, microwave frequency and field. This allowed a determination of the true sample temperature in the FMR and SANS measurements. Resonant heating was observed already 2 K above the ordering temperature T_{c} for excitation frequencies $0.6 \leq f_{\mathrm{drive}} \leq 1.8\,\mathrm{GHz}$ and magnetic fields below $B \approx 50\,\mathrm{mT}$. The data suggests coupling of the microwave field to magnetic correlations well above T_{c} in the fluctuation disordered regime for excitation frequencies close to the resonant modes of the skyrmion lattice phase. Higher harmonics in the microwave field due to the amplifier operating in saturation were found to couple to further excitation modes of the sample. The resulting resonant heating could be tracked by the sample thermometer and the resonant modes might be determined.

The collective excitations under intense microwave radiation were recorded with the 2-tone FMR technique. For microwave fields below $B_{\mathrm{ac,avg}} \approx 75\,\mu\mathrm{T}$, i.e. for input powers $P \leq 2\,\mathrm{W}$, and a microwave frequency $f_{\mathrm{drive}} = 0.8\,\mathrm{GHz}$ below the CCW mode, the entire skyrmion lattice phase is accessible and the CCW mode observed throughout the phase. Just above this approximate threshold excitation field, a quasi-static state could be established at or slightly above the ordering temperature T_{c} where the CCW mode is still observed. For $f_{\mathrm{drive}} = 0.6\,\mathrm{GHz}$ this state could even be established for highest microwave fields. Increasing the microwave field for $f_{\mathrm{drive}} = 0.8\,\mathrm{GHz}$ further, the CCW mode vanishes.

For $f_{\mathrm{drive}} = 0.8\,\mathrm{GHz}$ and highest excitation fields, the data suggests that the temperature difference between sample and CPW was insufficient to stabilise the sample temperature at T_{c} in field scans. The CCW mode cannot be observed as the temperature is increased further due to, most likely, the coupling of the microwave field to the fluctuation disordered regime above T_{c}. For $f_{\mathrm{drive}} = 1.2\,\mathrm{GHz}$, matching approximately the CCW mode, and for highest microwave fields, the CCW mode cannot be observed within the field range of the skyrmion lattice phase, but a resonance mode that is broad in frequency can be discerned in the frequency range of the breathing mode. The sample temperature reveals that the sample is just below or at T_{c} which is supported by the phase transitions observed in the excitation spectra. For a microwave frequency above the

CCW mode $f_{\mathrm{drive}} = 1.8\,\mathrm{GHz}$, the signatures of the CCW mode reappear and, moreover, signatures reminiscent of the breathing mode are observed.

To obtain microscopic information, we performed small angle neutron scattering measurements on Cu_2OSeO_3 under intense microwave radiation. This allowed to record changes of the long-range order of skyrmion lattice correlations. Evaluating the scattering intensity of the skyrmion lattice phase, a similar behaviour compared to the all-electrical microwave spectroscopy is observed. For microwave fields below $B_{\mathrm{ac,avg}} \lesssim 75\,\mu\mathrm{T}$ and a microwave frequency $f_{\mathrm{drive}} = 0.8\,\mathrm{GHz}$ below the CCW mode, the entire skyrmion lattice phase is accessible and the sixfold scattering pattern of the skyrmion lattice phase may be observed. Increasing the microwave field, T_{sample} remains just above T_{c} under field-cooling and no scattering intensity may be observed. However, T_{sample} decreases discontinuously by $\Delta T > 2\,\mathrm{K}$ when the temperature difference between T_{sample} and T_{CPW} exceeds a certain value. Increasing the excitation frequency matching the CCW mode, parts of the skyrmion lattice phase are accessible and the sixfold scattering pattern is observed.

A pronounced azimuthal broadening of the magnetic Bragg peaks of the skyrmion lattice phase is observed for $0.6\,\mathrm{GHz} \leq f_{\mathrm{drive}} \leq 1.8\,\mathrm{GHz}$ about the CCW as well as the breathing mode at the highest microwave fields. In contrast, no azimuthal broadening may be observed for microwave frequencies far above, i.e $f_{\mathrm{drive}} \geq 3.0\,\mathrm{GHz}$. Investigating the power dependence of the azimuthal broadening at a microwave frequency of $f_{\mathrm{drive}} = 0.8\,\mathrm{GHz}$ reveals a transition from sharp to broadened Bragg peaks for input powers between $P = 1\,\mathrm{W}$ and $2\,\mathrm{W}$. This is just below the threshold excitation field $B_{\mathrm{ac,avg}} \approx 75\,\mu\mathrm{T}$ where parts of the skyrmion lattice phase are not accessible.

In the following, results from all measurements are combined and discussed. We made two main observations.

1. We observe coupling between the sample and the intense microwave radiation already some Kelvin above the ordering temperature T_{c} for frequencies about the resonant modes of the SkX. Furthermore, parts of the temperature range of the skyrmion lattice phase are not accessible under intense microwave radiation. In particular for microwave frequencies below the CCW mode, T_{sample} remains at or just above T_{c} for sufficiently high microwave fields in field-cooling scans.
2. Azimuthal broadening of the hexagonal scattering pattern of the skyrmion lattice phase may be observed for the highest microwave fields and microwave frequencies close to the resonant modes of the skyrmion lattice phase. As a function of microwave field a threshold for the onset of azimuthal broadening may be discerned.

For $f_{\mathrm{drive}} = 0.8\,\mathrm{GHz}$ and intermediate microwave fields with an input power of $P = 3\,\mathrm{W}$, T_{sample} increases to or slightly above T_{c} in field-sweeps, but signatures of the CCW mode may still be observed in FMR spectra (see Fig. 6.24). In contrast, under field-cooling at

$B = 22\,\mathrm{mT}$ no neutron scattering pattern of the skyrmion lattice phase emerges at T_c where the CCW resonant mode is $f = 1.0\,\mathrm{GHz}$. Instead T_sample remains at T_c. Notably, under field-cooling the temperature difference between T_sample and T_holder increases until a discontinuous change in temperature may be observed. Nevertheless, neutron scattering intensities from the skyrmion lattice phase are not observed at or below T_c(see Fig. 6.32).

Increasing the microwave frequency to $f_\mathrm{drive} = 1\,\mathrm{GHz}$ and $1.2\,\mathrm{GHz}$, respectively, matching the CCW mode, we are able to cool the sample into the skyrmion lattice phase and long-range order in terms of neutron scattering intensity of the skyrmion lattice phase may be observed.

In contrast, the signatures of the CCW mode may not be observed in FMR spectra, although the temperature correction shows that T_sample is below T_c for $f_\mathrm{drive} = 1.2\,\mathrm{GHz}$. Instead, signatures of a weak resonance in the frequency range of the breathing mode appear. It is important to note that the accuracy of the temperature correction for the FMR data is limited and T_sample may be higher. However, the transition from the skyrmion lattice to the low-field conical phase at B_A2, observed in the FMR spectra, suggests an even lower T_sample within the skyrmion lattice phase (see Figs. 6.27 and 6.28). This would be consistent with the neutron scattering data where T_sample reaches the centre of the skyrmion lattice phase for $f_\mathrm{drive} = 1.2\,\mathrm{GHz}$ in field-cooling scans. Hence, long-range order of the skyrmion lattice is observed but the signal of the CCW mode vanishes in the 2-tone FMR technique.

Our results are consistent with numerical studies by Mochizuki *et al.* [81] who predicts a redshift of the CCW resonant frequency under intense microwave radiation. At T_c and $B = 22\,\mathrm{mT}$ the CCW resonant frequency is $f = 1.0\,\mathrm{GHz}$ in the undisturbed system and through the strong microwave field at $f_\mathrm{drive} = 0.8\,\mathrm{GHz}$ the sample cannot be cooled below T_c. For $f_\mathrm{drive} = 1.0\,\mathrm{GHz}$ the resonant mode of the undisturbed skyrmion lattice phase is matched and long-range order of the skyrmion lattice may be observed in terms of neutron scattering intensity. As the system cools into the skyrmion lattice phase the resonant frequency of the CCW mode of the undisturbed system increases and, again, T_sample cannot be cooled below a critical temperature $T_\mathrm{critical} < T_\mathrm{c}$.

Our data also demonstrates that T_critical is associated with the skyrmion lattice phase and the CCW mode rather than the fluctuation disordered regime. For magnetic fields below $\sim 35\,\mathrm{mT}$ and just above T_c, which coincides well with the fluctuation disordered regime in Ref. [89], no signatures of a distinct Kittel mode may be observed in FMR spectra (see Fig. 6.30). Instead, excitations are detected for frequencies between $0.5 \leq f \leq 1.8$. Therefore, we would expect a similar T_critical for all microwave frequencies. However, T_critical for $f_\mathrm{drive} = 0.6\,\mathrm{GHz}$ and $0.8\,\mathrm{GHz}$ is at T_c and at lower temperatures for higher microwave

frequencies. Furthermore, T_{critical} for $f_{\mathrm{drive}} = 0.8\,\mathrm{GHz}$ and for lower microwave fields is also at T_{c}.

It is also instructive to consider the length and time scales of the skyrmion lattice required for its detection in all-electrical microwave spectroscopy and SANS measurements. All-electrical microwave spectroscopy is a local probe and the excitation of single skyrmions may be detected if their number is sufficiently large. Underlying the characteristic excitation spectra of skyrmions is thereby the phase relationship between Fourier components, i.e. three $\vec{Q}$-vectors under an angle of 120° in a plane perpendicular to the magnetic field and the magnetisation in the skyrmion core opposing the field. We expect furthermore that skyrmions need to be stable for at least one period of the rotational motion to be detected in FMR spectroscopy. This corresponds to a lifetime in excess of 1 ns or more for a resonant frequency of $\sim 1\,\mathrm{GHz}$. Schwarze *et al.* infer lifetimes of $\tau \approx 25\,\mathrm{ns}$ in an undisturbed system by means of all-electrical microwave spectroscopy whereas measurements employing the inverse-Faraday effect yield lifetimes on the order of 1 ns [83, 302].

In contrast, skyrmion textures composed of several correlated skyrmions are necessary in SANS for a coherent magnetic neutron scattering signal. In terms of time scales, neutron scattering may detect magnetic correlations which are only stable for picoseconds. Under field-cooling for $f_{\mathrm{drive}} = 0.6\,\mathrm{GHz}$ and $0.8\,\mathrm{GHz}$, T_{sample} remains at T_{c} between the skyrmion lattice phase and the fluctuation disordered regime. The latter is dominated by fluctuations of helical, conical, and skyrmionic correlations in the case of MnSi [108]. Our data would be consistent with a scenario where skyrmionic correlations are stable sufficiently long at T_{c} that the FMR spectroscopy and the intense microwave radiation may couple to it. However, the correlation length is not sufficient to be recorded in SANS measurements. Further cooling the sample is not feasible as it would lead to an increase of the skyrmion number and a larger spectral weight in the FMR spectroscopy, hence, increased resonant heating.

The data furthermore suggests that the intense microwave excitation drives the CCW mode of the skyrmion lattice phase for an excitation frequency $f_{\mathrm{drive}} = 1.2\,\mathrm{GHz}$, however, the signatures of the CCW resonant mode vanish in the FMR spectra. The CCW excitation might be driven to such an extent that the small probe microwave field no longer picks up a signal.

The azimuthal broadening of the Bragg peaks of the skyrmion lattice phase in SANS can be caused by different effects. The azimuthal width $\Delta\theta$ is sensitive to (1) distortions of the sixfold pattern within the skyrmion lattice domains. Within individual domains distortions, stationary or dynamical, of the hexagonal lattice may occur away from the high symmetry directions [001] and [110]. $\Delta\theta$ is also sensitive to (2) the orientation of the

domains within the plane perpendicular to the magnetic field. When domains fluctuate in a rotational mode about their equilibrium alignment or, alternatively, are statically distributed more broadly about the high symmetry directions, the Bragg peaks broaden azimuthally. It is important to note that with our SANS data a distinction between static and dynamic azimuthal broadening of the Bragg peaks cannot be made. (3) The azimuthal broadening of the Bragg peaks may be attributed empirically to the melting of the long-range SkX order and the emergence of a skyrmion liquid state.

One scenario for the observed azimuthal broadening of the Bragg peaks is the rotational motion of domains around the magnetic field. In LTEM a rotational motion of the skyrmion lattice was observed [126, 131]. The unidirectional rotation originates from magnon currents due to temperature gradients as the electron beam leads to local heating. In these experiments the rotational motion is continuous by 2π with a period of seconds. However, such a rotational motion would lead to a ring of intensity in SANS rather than azimuthally broadened Bragg peaks. The authors do not specify the magnitude of the thermal gradient but the skyrmion lattice phase in thin films as employed in LTEM measurements extends over several 10 K and temperature differences of several Kelvin are possible without leaving the phase [20]. In contrast, the temperature range of the skyrmion lattice phase in bulk samples is only $\sim 2\,\mathrm{K}$ and small temperature inhomogeneities on the order of several hundred 100 mK would lead to changes in the neutron scattering intensities.

The torque on the skyrmion lattice domains, that is caused by temperature gradients and the resulting magnon currents, is counteracted by restoring forces such as the magnetocrystalline anisotropy. In the case of azimuthally broadened Bragg peaks the torque might not be sufficient to entirely overcome these. For low microwave fields and $f_{\mathrm{drive}} = 0.8\,\mathrm{GHz}$ the magnetic Bragg peaks are sharp in azimuthal direction and broaden for a microwave field of $B_{\mathrm{ac,avg}} \approx 70\,\mu\mathrm{T}$ before the skyrmion lattice phase is not accessible anymore for $B_{\mathrm{ac,avg}} \gtrsim 80\,\mu\mathrm{T}$. Hence, the heat input through fully rotating domains might be too large with the result of non-accessible regions of the phase diagram. This is also in agreement with the observation of azimuthally broadened Bragg peaks instead of a ring of intensity.

The temperature gradients may occur within skyrmion lattice domains or on a larger scale. A reason for macroscopic temperature gradients on the order of the sample size may be the inhomogeneous excitation field and, thereby, inhomogeneous resonant heating. Fig. 6.40 (a) shows an approximation for the absorbed power in resonant heating. Here, we consider the resonant mode of the field-polarised phase as a limiting scenario because it has a larger spectral weight than the modes of the skyrmion lattice or conical phase. The amplitude of the resonant mode of the field-polarised phase in the divide slice

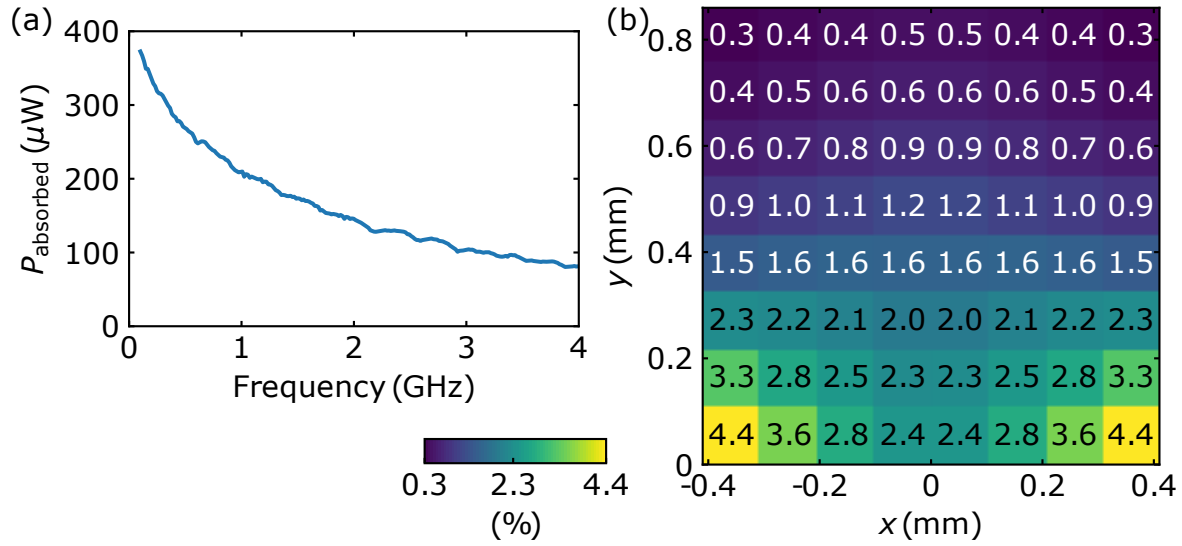

Figure 6.40.: Approximation of absorbed power in resonance. (a) Absorbed power in resonance as a function of applied excitation frequency with a constant input power of $P = 5\,\mathrm{W}$. (b) Percentage of absorbed power over the sample cross-section where the centre conductor is at $y = 0$.

depiction of S_{21} is approximately 1 %. Taking into account the transmission of the setup in Fig. 6.8 (b), we can estimate the absorbed power for a constant input power of $P = 5\,\mathrm{W}$. It ranges between $280\,\mu\mathrm{W}$ and $180\,\mu\mathrm{W}$ in the range of 0.6 to 1.8 GHz. Fig. 6.40 (b) shows the percentage of absorbed power over the cross-section of the sample where the coplanar waveguide is horizontal at $y = 0$. The heat input is higher at the bottom and the corners of the sample than at the top.

Considering the thermal conductivity of the sample and the GE varnish we use to glue the sample to the CPW, we expect the sample to be in good thermal equilibrium. The thermal conductivity for Cu_2OSeO_3 was determined in Ref. [307] at low temperatures up to 15 K. Extrapolating the data to 60 K, a thermal conductivity of $\kappa \approx 2 - 3\,\mathrm{W/(mK)}$ may be deduced. In comparison, GE varnish has a thermal conductivity of $0.22\,\mathrm{W/(mK)}$ at 77 K and $0.062\,\mathrm{W/(mK)}$ for 4.2 K. Hence, the heat transfer to the heat bath has a bottleneck in the GE varnish.

Similar to local heating in LTEM measurements [126], temperature gradients may occur on a much smaller scale comparable to the domain size through inhomogeneous heating. A possible scenario is that the sample cools down locally, the CCW mode moves into resonance with the microwave field inducing a short-pulsed resonant heating that decays into the surrounding through magnon currents creating a rotational motion.

Pöllath *et al.* recently established a combination of resonant elastic x-ray scattering (REXS) and FMR spectroscopy [301]. They show that the scattering intensity is reduced

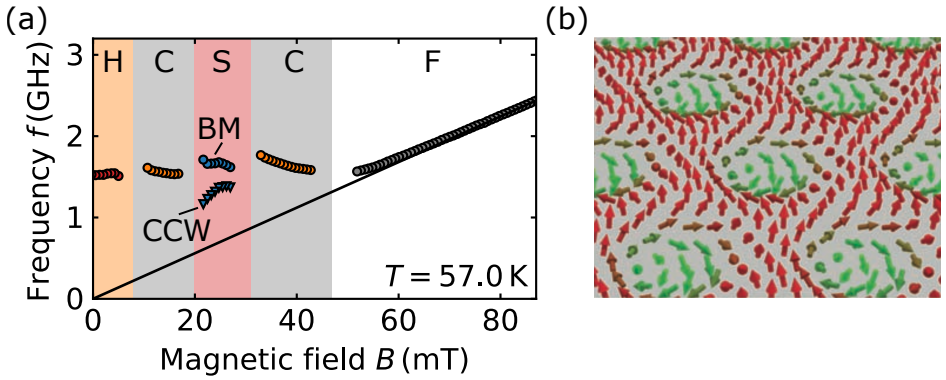

Figure 6.41.: Field dependence of the resonant modes. (a) Field dependence of the resonant modes of the helical (H), the conical (C), the skyrmion lattice (S) and the field-polarised (F) phase as inferred from FMR spectroscopy. The black line denotes the Kittel mode extrapolated to $B = 0\,\mathrm{T}$. (b) Real space spin alignment of the skyrmion lattice phase. Figure taken from Ref. [14].

if modes in Cu_2OSeO_3 are excited by the external magnetic field. Typical microwave fields range between 3 to 10 μT employing a coplanar waveguide. In contrast to SANS, REXS is surface sensitive with a photon penetration depth of about 30 nm. In this study a reduction of the x-ray scattering intensity up to 50 % is observed. This is contrary to our measurements where no reduction of the integrated scattering intensity is observed for the entire volume of the sample.

The resonant mode of the field-polarised phase is characterised by a collective precession of the uniform magnetisation $\vec{M}$ described by the Kittel mode. Fig. 6.41 (a) shows the field-dependence of the resonance frequencies of the different phases in Cu_2OSeO_3 and the extrapolation of the Kittel mode to zero field. At an intermediate magnetic field skyrmions emerge within the ferromagnetic background (red) as shown in Fig. 6.41 (b). The CCW mode of the skyrmion lattice phase is essentially characterised by the precession of the ferromagnetic background. In a simplified picture the skyrmions act as rigid tubes within the uniform magnetisation and, therefore, the resonant frequency increases compared to the extrapolated Kittel mode. Hence, the CCW resonant mode might exhibit an enhanced ferromagnetic character via the intense excitation of the ferromagnetic background leading to a redshift. In turn, the "melting" of the skyrmion lattice as observed in previous numerical studies might be a consequence of a dominant ferromagnetic fraction compared to the skyrmions [81]. The breathing mode on the contrary is connected to the non-trivial topology of the skyrmions. An intense excitation of the breathing mode may lead to a pronounced skyrmionic character of the excitations which might act as a promising basis for the search of non-linear behaviour in numerical simulations and experimentally.

In summary, our main observations are the coupling of the intense microwave radiation to the magnetic order already some Kelvin above T_c for frequencies about the resonant modes of the SkX. Furthermore, parts of the SkX phase are not accessible. Signatures of the emergence of long-range magnetic order are not observed at T_c for intense excitation fields and frequencies below the CCW mode suggesting a redshift of the modes. Furthermore, the neutron scattering pattern of the SkX phase broadens azimuthally under intense microwave radiation for frequencies about the resonant modes which indicates the loss of the long-range hexagonal order. We attributed empirically our observations to different scenarios, estimated limiting cases for thermal gradients and discussed the resonant behaviour of the SkX under intense microwave fields. Further theoretical investigations are necessary to understand the complex behaviour and explain our observations.

7. Conclusions

The focus of this thesis was the experimental investigation of thermally and periodically driven magnetic fluctuations by means of neutron scattering and all-electrical microwave spectroscopy. For this purpose, we advanced the longitudinal modulation of intensity with zero effort (MIEZE) option at the instrument RESEDA, developed an all-electrical microwave spectroscopy (FMR) technique referred to as 2-tone technique and combined microwave radiation with small angle neutron scattering (SANS). Using the MIEZE technique, critical spin excitations in the prototypical ferromagnetic superconductor UGe_2 were investigated. Moreover, the emergence of the skyrmion lattice from the paramagnetic phase in the transition metal helimagnet MnSi and fluctuation-induced instabilities in the skyrmion lattice phase of the helimagnetic insulator Cu_2OSeO_3 were studied.

After a brief introduction into neutron scattering and neutron scattering techniques, developments of the MIEZE technique at the instrument RESEDA were presented. As part of this work, the instrumental background was reduced, the momentum transfer range was extended towards the SANS regime, and the phase-locking of the MIEZE signal was implemented. In addition, new data analysis software was developed and instrumental control software was implemented.

The critical spin excitations in UGe_2 were studied at the paramagnetic-to-ferromagnetic phase transition by means of MIEZE overcoming limits of previous neutron triple-axis spectroscopy studies. The high quality of the sample was confirmed by neutron depolarisation imaging revealing a homogeneous Curie temperature across the sample which is indispensable for the determination of critical exponents. Employing MIEZE, we demonstrated that the spin fluctuations in UGe_2 exhibit a dual character associated with localised $5f$ electrons that are hybridised with itinerant d electrons. Analysing the momentum transfer dependence of the energy-integrated scattering intensity of the spin fluctuations, we found all critical exponents to perfectly agree with the 3d Ising universality class as expected for a local moment ferromagnet with strong uniaxial magnetic anisotropy. The product of magnetic susceptibility $\chi(q)$ and the fluctuation frequency Γ_q, the latter revealed by energy-resolved MIEZE measurements, is approximately constant as a function of momentum transfer q down to a crossover value q^0 further highlighting that the underlying spin fluctuations are localised. In contrast, the product $\chi(q)\Gamma_q \to 0$ for $q \to 0$ and the dy-

namical exponent $z = 5/2$ below the crossover value q^0 are characteristic of itinerant spin fluctuations. Taken together, the dual nature of spin fluctuations revealed in our study strongly support p-wave superconductivity in UGe_2. Interestingly, the crossover value q^0 corresponds to a length scale of approximately 160 Å and the superconducting coherence length in UGe_2 was estimated as $\xi^{SC} = 200$ Å [52]. Hence, spin fluctuations relevant to the p-wave pairing are present at $q < q^0$. Furthermore, we showed the potential of the newly developed longitudinal MIEZE with its ultrahigh energy resolution below 1 μeV and its momentum resolution from the SANS regime to large momentum transfers as a complementary technique to neutron triple-axis and time-of-flight spectroscopy for the study of quantum matter.

The emergence of topologically non-trivial winding and long-range order of the skyrmion lattice phase was studied starting in the paramagnetic state of MnSi. Our comprehensive study comprised high-resolution longitudinal and transverse ac susceptibility measurements, small angle neutron scattering, neutron resonance spin-echo spectroscopy, and all-electrical microwave spectroscopy. As part of this thesis SANS data were analysed and neutron resonance spin-echo measurements performed with the MIEZE option. Small angle neutron scattering revealed scattering intensity on a sphere in reciprocal space in the fluctuation-disordered regime above the ordering temperature T_c that is more pronounced in a plane perpendicular to the magnetic field. The pronounced intensity exhibits a sixfold pattern with the same orientation as the scattering pattern in the skyrmion lattice phase. In addition, it has the same modulus of the momentum transfer $|\vec{Q}|$ as the scattering pattern of the skyrmion lattice and its correlation length is resolution-limited revealing correlation lengths of several 10^3 Å.

The sixfold pattern in the fluctuation-disordered regime is fully dynamic down to T_c as determined by MIEZE and the fluctuations are characterised by a critical slowing down with lifetimes of several nanoseconds. Complementary all-electrical microwave spectroscopy revealed signatures reminiscent of the counter-clockwise skyrmion lattice excitation in the fluctuation-disordered regime and provided striking evidence for skyrmionic correlations. Finally, the paramagnetic-to-skyrmion lattice phase transition described in the framework of standard Ginzburg-Landau theory shares remarkable similarities with the Landau soft-mode mechanism of weak crystallisation of liquids. In both cases the ordered state gains energy if the magnetic Fourier components $\vec{m}_{\vec{q}}$ or the oscillatory components of the density $\vec{\rho}_{\vec{q}}$, respectively, form triangles which favours the formation of hexagonal lattices in two spatial dimensions.

Microwave-induced non-linearities in the skyrmion lattice phase of Cu_2OSeO_3 were investigated based on numerical simulations by Mochizuki *et al.* that predict a melting of the skyrmion lattice phase within nanoseconds under intense microwave radiation [154]. At

first, the SANS-FMR setup was introduced that allows to observe magnetic long-range order in reciprocal space on a microscopic scale and simultaneously apply microwave radiation by means of a coplanar waveguide with excitation frequencies in the low GHz regime and excitation fields on the order of 100 μT. Similarly, the 2-tone all-electrical microwave spectroscopy technique developed as part of this thesis allows to drive collective excitations with a strong excitation field in the low GHz regime and simultaneously and independently probe the collective excitation spectra of the sample.

We performed extensive measurements investigating the dependence of ohmic and resonant heating effects on temperature, dc magnetic field, excitation frequency and field as well as hysteresis effects. Here, coupling of the microwave radiation to magnetic correlations in the fluctuation-disordered regime was observed in the presence of resonant heating above the ordering temperature T_c. Furthermore, higher harmonics as a side effect of the linear microwave amplifier driven in saturation led to resonant heating at higher magnetic fields and might be employed for the detection of resonant modes. A broad absorption in FMR spectra observed above T_c in the fluctuation-disordered regime also suggested a coupling of the microwave excitation to magnetic correlations. For excitation frequencies below the CCW resonant mode of the skyrmion lattice phase an equilibrium could be established at T_c where the CCW resonant mode was observed but no signatures of magnetic long-range order were observed in SANS measurements. This agrees with the numerical simulations where the melting of the long-range skyrmion lattice order is accompanied by a redshift of the CCW resonant mode. In contrast, increasing the excitation frequency matching the CCW resonant mode, the sample temperature could be lowered into the skyrmion lattice phase, signatures of long-range order emerged in SANS, but the FMR signal of the CCW resonant mode vanished. Only a weak resonance remained reminiscent of the breathing mode.

Moreover, pronounced azimuthal broadening of the magnetic Bragg peaks of the skyrmion lattice phase was observed for all frequencies about the CCW and breathing mode for highest excitation fields. Measurements with intense microwave radiation below the CCW mode revealed a critical excitation field for the onset of azimuthal broadening, just below the threshold field where the skyrmion lattice phase was not accessible. We discussed several scenarios of temperature gradients generated by resonant heating as origin of the azimuthal broadening. We evaluated length and time scales necessary for the detection of skyrmions in our measurement techniques and concluded that skyrmionic correlations can occur at T_c on length scales sufficient for the detection in FMR but insufficient for SANS. Moreover, our observations may also be attributed empirically to the melting of the skyrmion lattice into a skyrmion liquid state. These results show that further theoretical investigations are necessary to understand the complex behaviour.

Finally, we argued that a redshift of the CCW resonant mode of the skyrmion lattice phase might originate from the intense excitation of the ferromagnetic background of the skyrmion lattice enhancing the ferromagnetic character of the mode. In turn, the melting of the skyrmion lattice observed in numerical studies might be a consequence of a dominant ferromagnetic fraction compared to the skyrmions. The intense excitation of the breathing mode, which is on the contrary connected to the non-trival topology of the skyrmions, might therefore be a good basis for the search of non-linear behaviour in future studies.

A. Experimental methods

A phase lock between the two resonant spin-flippers and the detector was implemented at RESEDA leading to a fixed phase of the spin-echo signal at the detector for each spin-echo time. This enables a phase correction of the spin-echo signal and, subsequently, allows to integrate the signal over arbitrarily sized regions-of-interest and over all detector foils. To show that the phase is fixed for each region-of-interest and detector frequency, Figs. A.1 and A.2 show the phase of the spin-echo signal as a function of temperature for each momentum transfer q and each detector frequency on one detector foil measured on UGe_2. The phase is constant within 1σ standard deviation of the mean value shown as blue solid line. A few exceptions occur at higher momentum transfers q. However, this is not due to a loss of the phase lock. Here, the count rate is low and some fits become unreliable. This has no detrimental effect on the data analysis in Sec. 4.

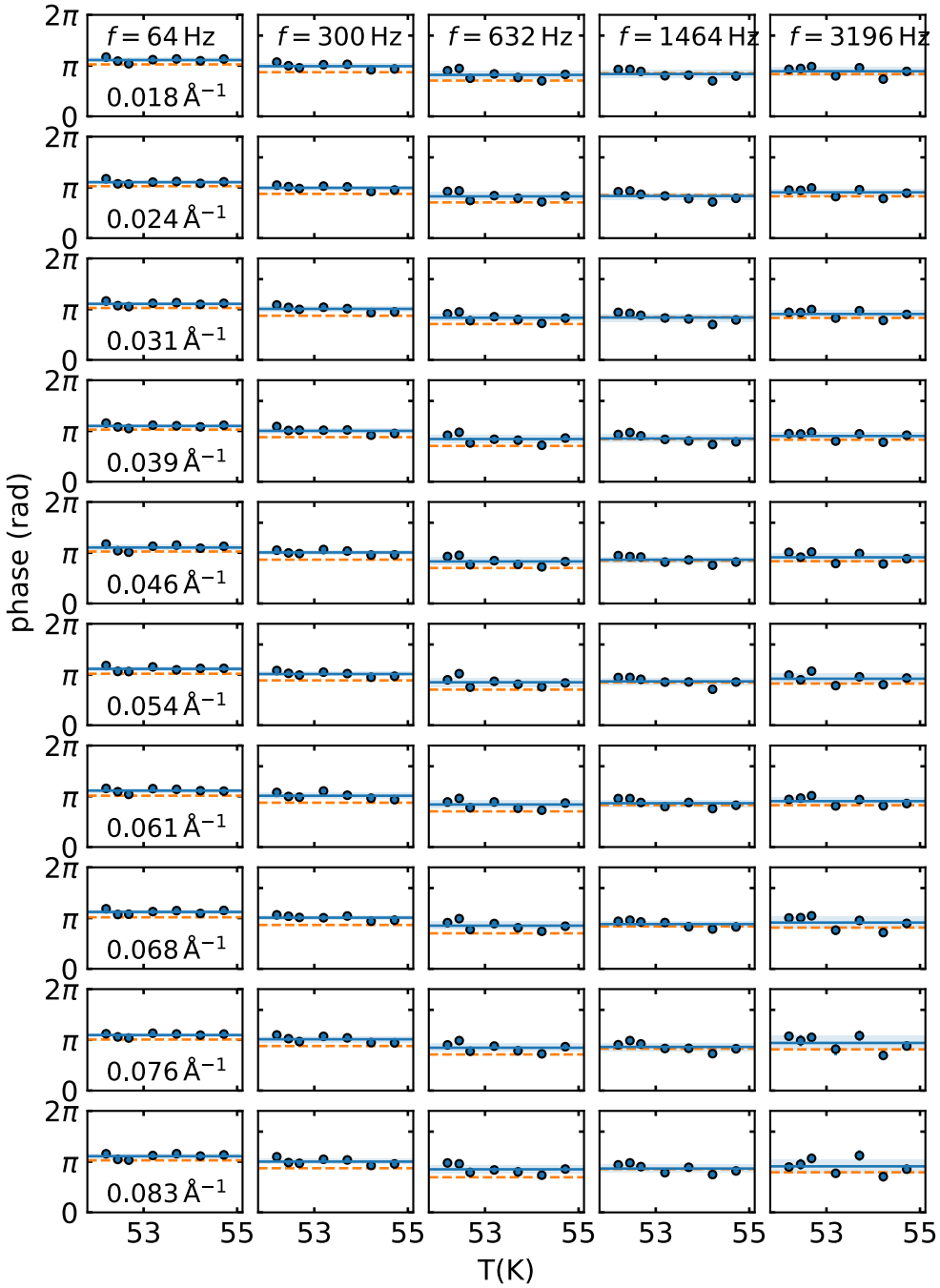

Figure A.1.: Phase of the spin-echo signal as a function of temperature measured in UGe_2 for various momentum transfers q and detector frequencies f. The solid blue line is the mean value and the shaded area denotes the uncertainty of the mean value as 1σ standard deviation. The orange dashed line is the phase of the resolution measurement.

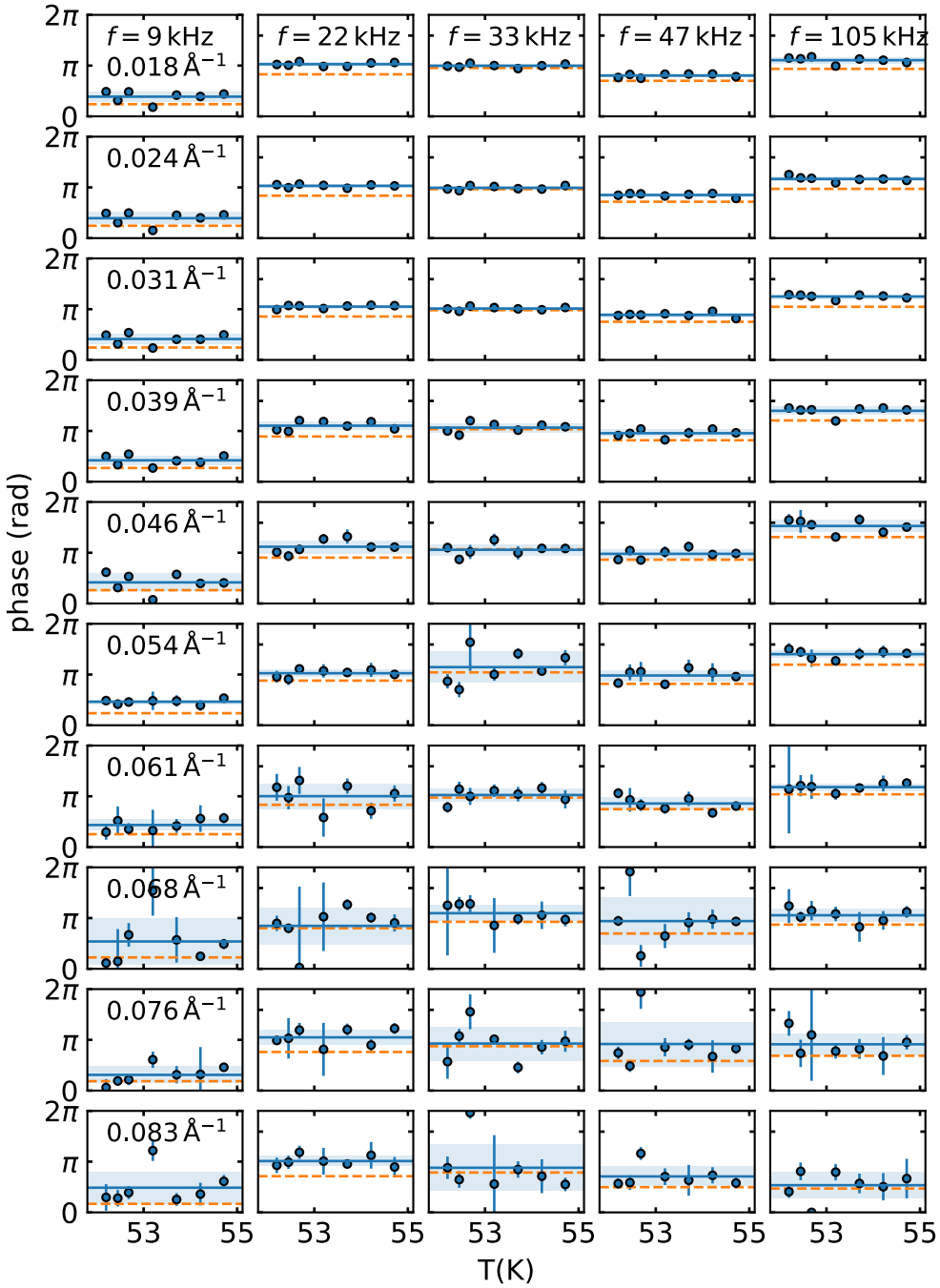

Figure A.2.: Phase of the spin-echo signal as a function of temperature measured in UGe_2 for various momentum transfers q and detector frequencies f. The solid blue line is the mean value and the shaded area denotes the uncertainty of the mean value as 1σ standard deviation. The orange dashed line is the phase of the resolution measurement.

B. Magnetic fluctuations in the ferromagnetic superconductor UGe_2

B.1. Resolution effects

In this section we show unambiguously that the critical spin fluctuations in UGe_2 are purely of longitudinal character $\delta S_{\parallel}$ and that the observed intensity for the configuration with the magnetic easy axis a perpendicular to the direction of the incident neutron beam $\boldsymbol{n}$ which solely probes transverse spin fluctuations $\delta S_{\perp}$ is due to resolution effects. This chapter follows the appendix of Ref. [199]. We consider the energy-integrated mode where the MIEZE option is turned off which corresponds to a SANS experiment.

Using the $\boldsymbol{q}$-resolution given in Sec. 4.3.2 of our experiment, we can simulate how the resolution impacts our experiment. We simulate the energy-integrated critical spin fluctuations at the temperature $T = 52.8\,\mathrm{K}$ as observed on the position sensitive detector at RESEDA using Eq. 4.9 and the parameters $\gamma = 1.23$, $\nu = 0.63$, $\kappa_0 = 0.31\,\mathrm{\AA}^{-1}$, and $T_c = 52.7\,\mathrm{K}$. In Fig. B.1, we show the results of our calculations for the two configuriations with the crystallographic a-axis, which is the magnetic easy axis in UGe_2, oriented parallel ($\boldsymbol{n} \parallel a$) and perpendicular ($\boldsymbol{n} \perp a$) to the direction of the neutron beam, respectively. As explained in the main text, transverse and longitudinal fluctuations can be observed for $\boldsymbol{n} \parallel a$, whereas only transverse fluctuations can be observed for $\perp a$. For this calculation we have assumed that the critical fluctuations are purely longitudinal and the instrumental resolution is perfect. In Fig. B.1 (c) and (d) we show the results for the same calculation and configurations, however, we convoluted the signal of the spin fluctuations with the instrumental resolution. The influence of the resolution on the result is obvious. In the main text we do not use the entire detector image, but only plot the intensity along a trajectory in reciprocal space denoted by the blue region of interest in Fig. B.1.

To compare the results from RESEDA with our calculations, we repeated the calculation above for various temperatures $45 \leq T \leq 65\,\mathrm{K}$. In Fig. B.2, we only show the intensity in the blue region of interest in Fig. B.1 for each configuration. Fig. B.2 (a) and (b) show the result for two configurations $\boldsymbol{n} \parallel a$ and $\boldsymbol{n} \perp a$, respectively, for the case of perfect instrumental resolution. Since in the calculation we have assumed that the critical

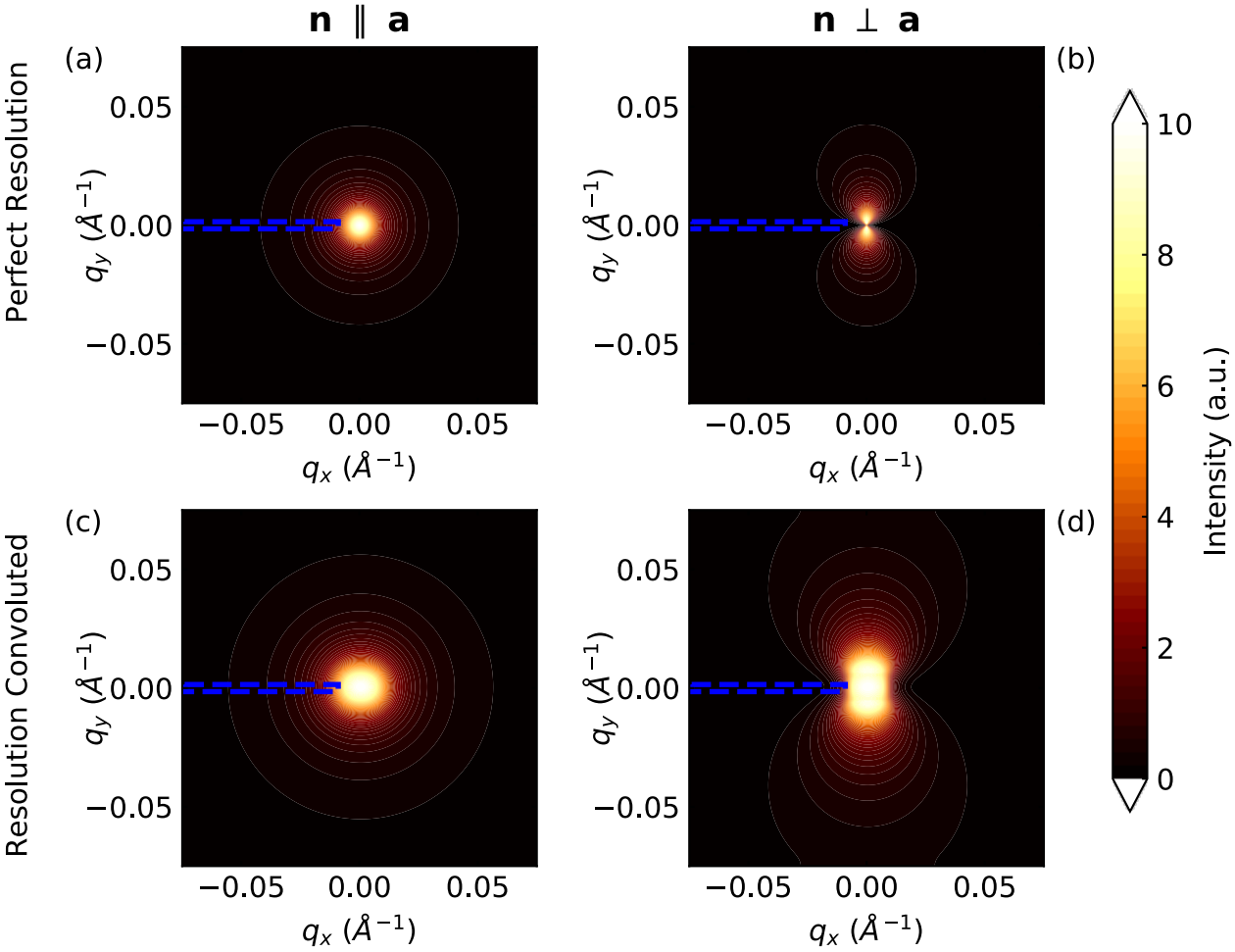

Figure B.1.: Simulation of the effects of instrumental resolution on the observation of intensity associated with longitudinal critical spin fluctuations in UGe_2 at $T = 52.8\,\mathrm{K}$ (see text for more details). (a) and (b) show simulated intensities for a perfect resolution for the two configurations with the crystallographic a-axis, which is the magnetic easy axis in UGe_2, oriented parallel ($\boldsymbol{n} \parallel a$) and perpendicular ($\boldsymbol{n} \perp a$) to the incident neutron beam. (c) and (d) show the same configurations as (a) and (b) but the simulated intensities were convoluted with the instrumental resolution. The blue region-of-interest denotes the q-cut which is plotted in Fig. B.2.

fluctuations are purely longitudinal, we don't see any intensity for $\boldsymbol{n} \perp a$ as shown in Fig. B.2 (b). In Fig. B.2 (c) and (d) we show the result for the same calculation and configurations, however, this time the signal associated with the longitudinal spin fluctuations is convoluted with the instrument resolution of our experiment. Now a small amount of intensity is visible for $\boldsymbol{n} \perp a$ shown in Fig. B.2 (d), illustrating that the instrumental resolution indeed introduces artefacts in the channel that is purely sensitive to transverse spin fluctuations. In conclusion, this shows unambiguously that the spin fluctuations in UGe_2 are purely longitudinal.

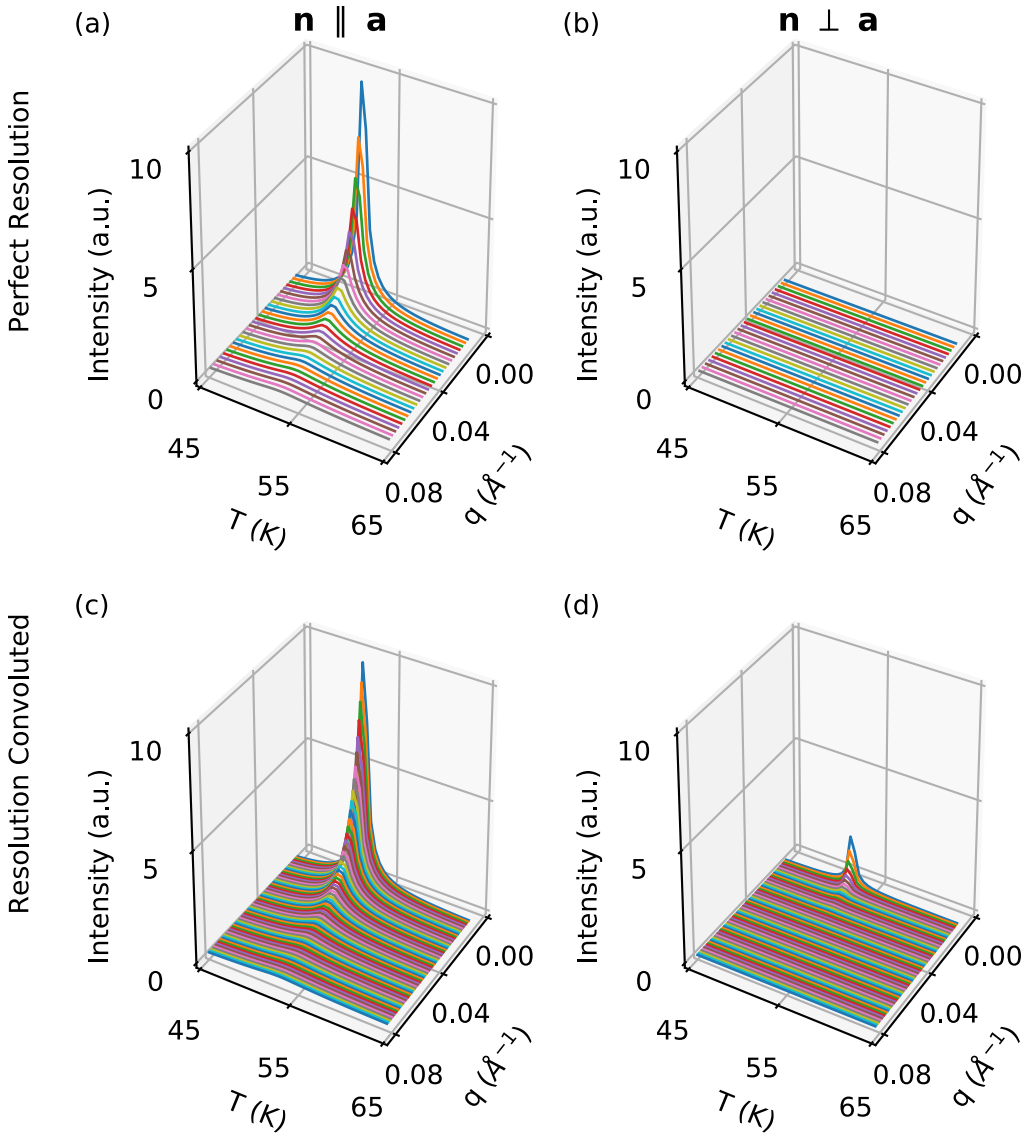

Figure B.2.: Simulation of the effects of instrumental resolution on the observation of intensity associated with critical spin fluctuations as a function of temperature T and momentum transfer q. The panels (a)-(d) show the q-cut denoted with the blue region-of-interest in Fig. B.1 (a)-(d). (a) and (b) show results assuming perfect resolution for the two configurations $\boldsymbol{n} \parallel a$ and $\boldsymbol{n} \perp a$, respectively (see text). (c) and (d) show results for the same configurations, but the simulated intensity is convoluted with the instrumental resolution corresponding to our experiments on UGe_2.

B.2. Quasielastic scattering in UGe_2

The normalised intermediate scattering function $S(q,\tau)/S(q,0)$ as measured in UGe_2 is shown for various temperatures T about the Curie temperature T_C and for various momentum transfers q in Fig. B.3. The data was treated as described in Sec. 3.1.3. A measurement significantly above T_C where magnetic fluctuations are absent was used to determine the background. Taking into account the background and normalising to an elastic signal, we expect the normalised intermediate scattering function to be normalised to 1 for $\tau \to 0$. For the smallest momentum transfer values $q \leq 0.031\,\text{Å}^{-1}$ the amplitude $A < 1$ and the fitting parameter A is fitted as opposed to being fixed for $q > 0.031\,\text{Å}^{-1}$. We are confident that the reduced contrast is an artefact from the beam stop positioned approximately 50 cm in front of the detector which was integrated into RESEDA shortly before the beam time. The beam stop is a cadmium sheet with a thickness of approximately 2 mm. The edges were not chamfered which can lead to reflections from the edges with small scattering angles. Close enough to T_C the signal to noise is sufficient that the influence is marginal whereas for temperatures further away from T_C the influence has to be considered. However, the background reduces the contrast over the whole dynamic range uniformly. Hence, the fluctuation energy Γ, i.e. the characteristic decay time of the exponential function, should not be affected. The beam stop has been adjusted with chamfered edges to eliminate these artefacts.

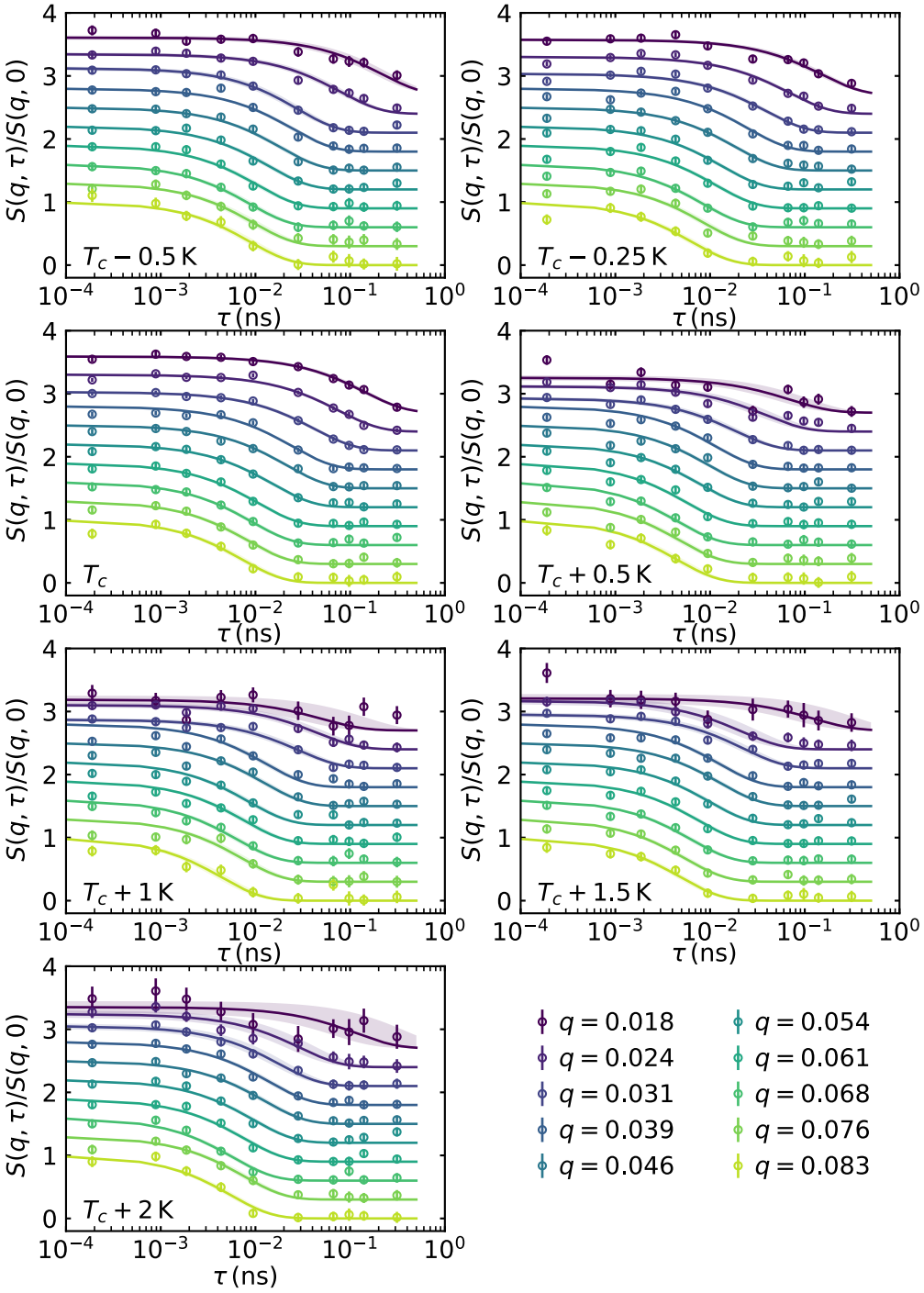

Figure B.3.: Normalised intermediate scattering function measured in UGe_2 for various temperatures and momentum transfer q. Solid lines are fits to Eq. 4.11. The shaded areas denote the uncertainty of the fits as 1σ standard deviation.

C. Search for microwave-induced instabilities in a chiral magnet

C.1. Temperature correction of neutron scattering data

During neutron scattering measurements, strong heating effects occurred and the precise sample temperature could not be monitored due to an offset between sample and CPW temperature. Hence, temperature correction measurements as described in Sec. 6.2.3 were performed with an additional thermometer on the sample. The measurements could not be repeated performing neutron scattering due to lack of neutron beamtime. In Figs. C.1 to C.4 temperature offsets between the sample and the coupling temperature as well as between the CPW and coupling temperature are shown as a function of CPW temperature. The data comprises all applied frequencies and powers measured during neutron scattering experiments.

A small deviation between the temperature offsets of CPW and coupling thermometers is observed for the neutron scattering measurements and the temperature correction measurements. It is between 0 and 0.3 K for frequencies up to $f_{\mathrm{drive}} = 1.8\,\mathrm{GHz}$. For $f_{\mathrm{drive}} = 3.0\,\mathrm{GHz}$ it is up to 1.5 K and for $f_{\mathrm{drive}} = 3.6\,\mathrm{GHz}$ it is up to 3 K, however, the absolute temperature offsets are significantly higher on the order of 10 to 20 K. The data with excitation frequencies $f_{\mathrm{drive}} = 1.0$ and $1.2\,\mathrm{GHz}$ in Fig. C.1 were recorded in several field-cooled measurements. The individual measurements are marked with different colours in Fig. C.1 (a4) and (a5) and are shown separately in Fig. C.1 (b1) to (c2).

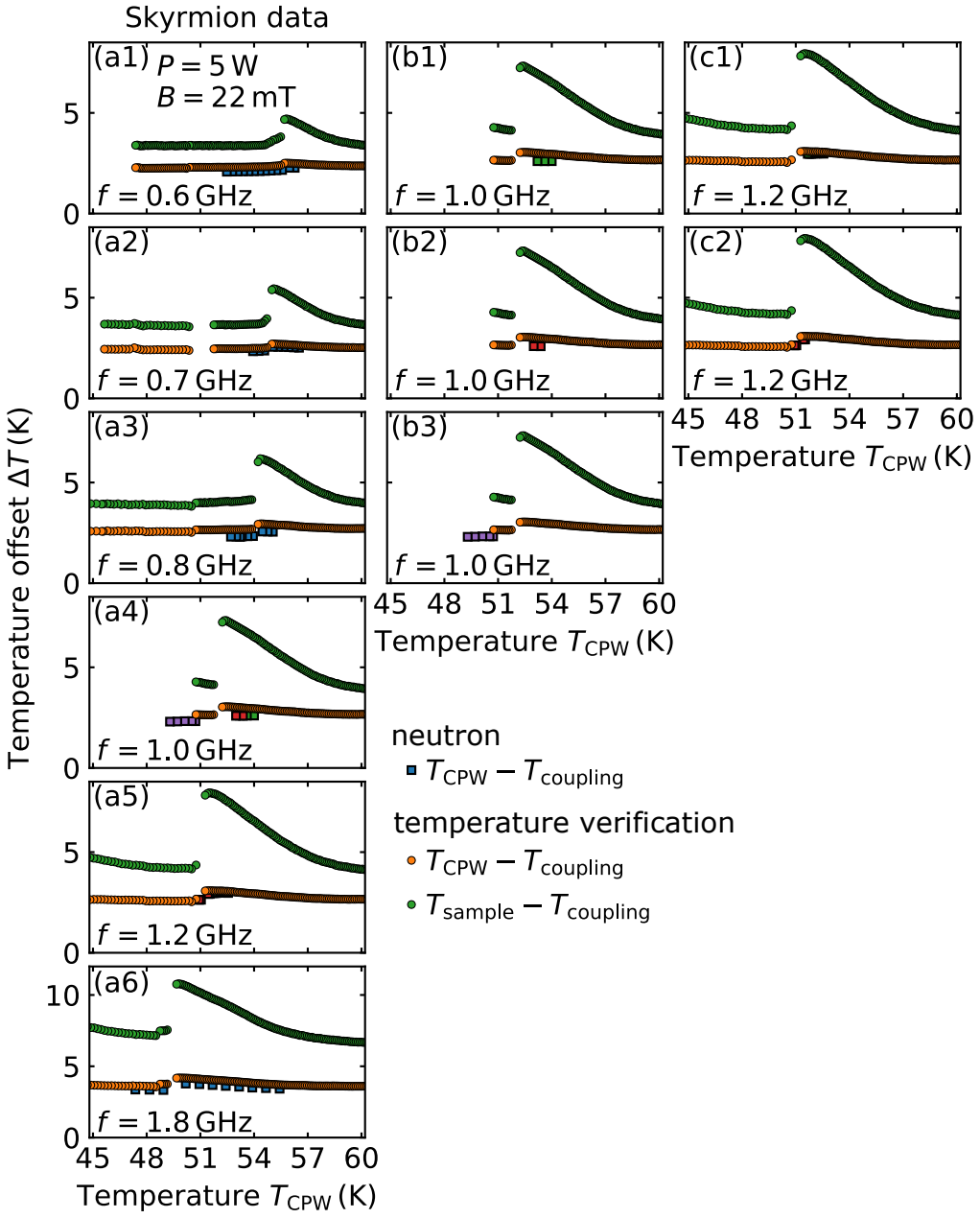

Figure C.1.: Comparison of temperature progressions. (a1)-(a6) Temperature offset between CPW and coupling position during field-cooled neutron scattering measurements of the skyrmion phase and temperature correction measurements, respectively, for various applied ac magnetic field frequencies. In the latter case, the offset between sample and coupling thermometer is in addition shown. Neutron scattering measurements with $f = 1.0\,\mathrm{GHz}$ and $f = 1.2\,\mathrm{GHz}$ are combined out of several temperature scans as shown in (b1)-(b4) and (c1)-(c2), respectively. (b1)-(b3) Temperature offset for individual field-cooled neutron scattering temperature scans at a frequency $f = 1.0\,\mathrm{GHz}$. (c1)-(c2) Temperature offset for individual field-cooled neutron scattering temperature scans at a frequency $f = 1.2\,\mathrm{GHz}$.

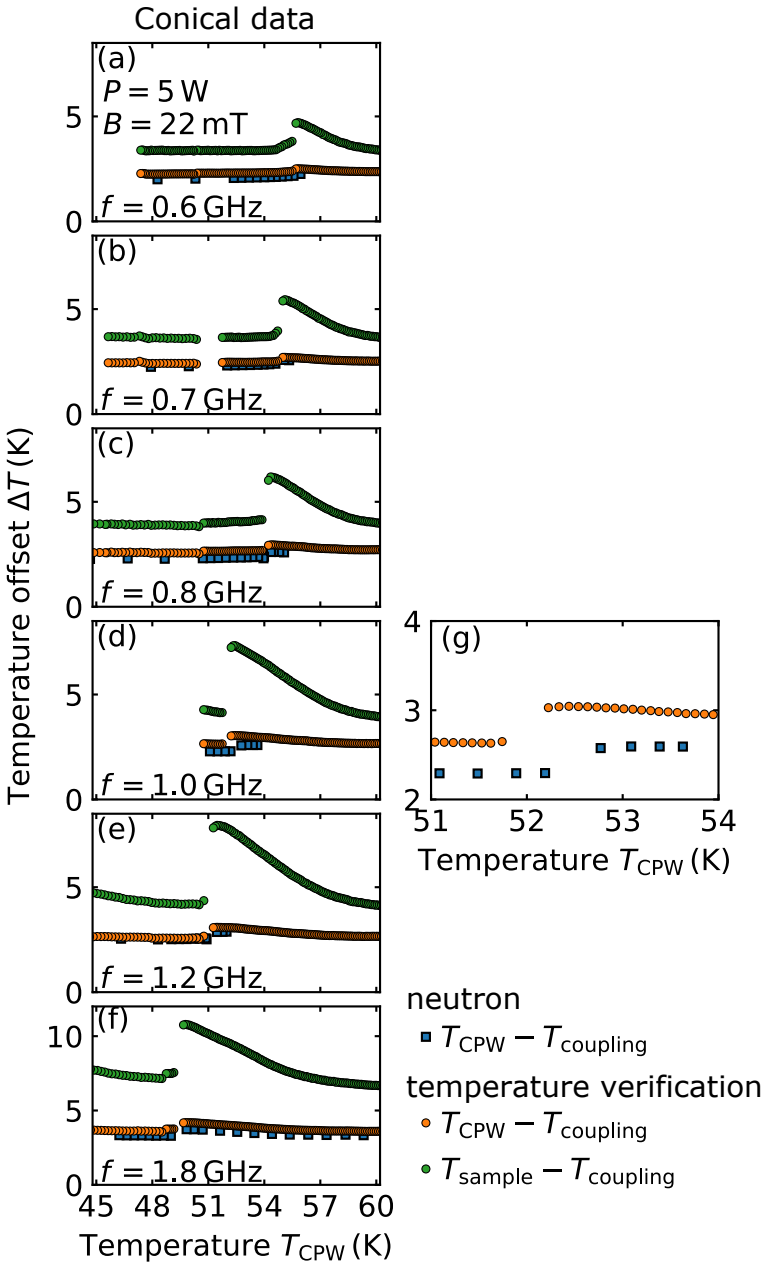

Figure C.2.: Comparison of temperature progressions. (a)-(f) Temperature offset between CPW and coupling position during field-cooled neutron scattering measurements of the conical phase and temperature correction measurements, respectively, for various applied ac magnetic field frequencies. In the latter case, the offset between sample and coupling thermometer is in addition shown. (g) Magnification of the measurement at $f = 1.0\,\mathrm{GHz}$ shown in (d).

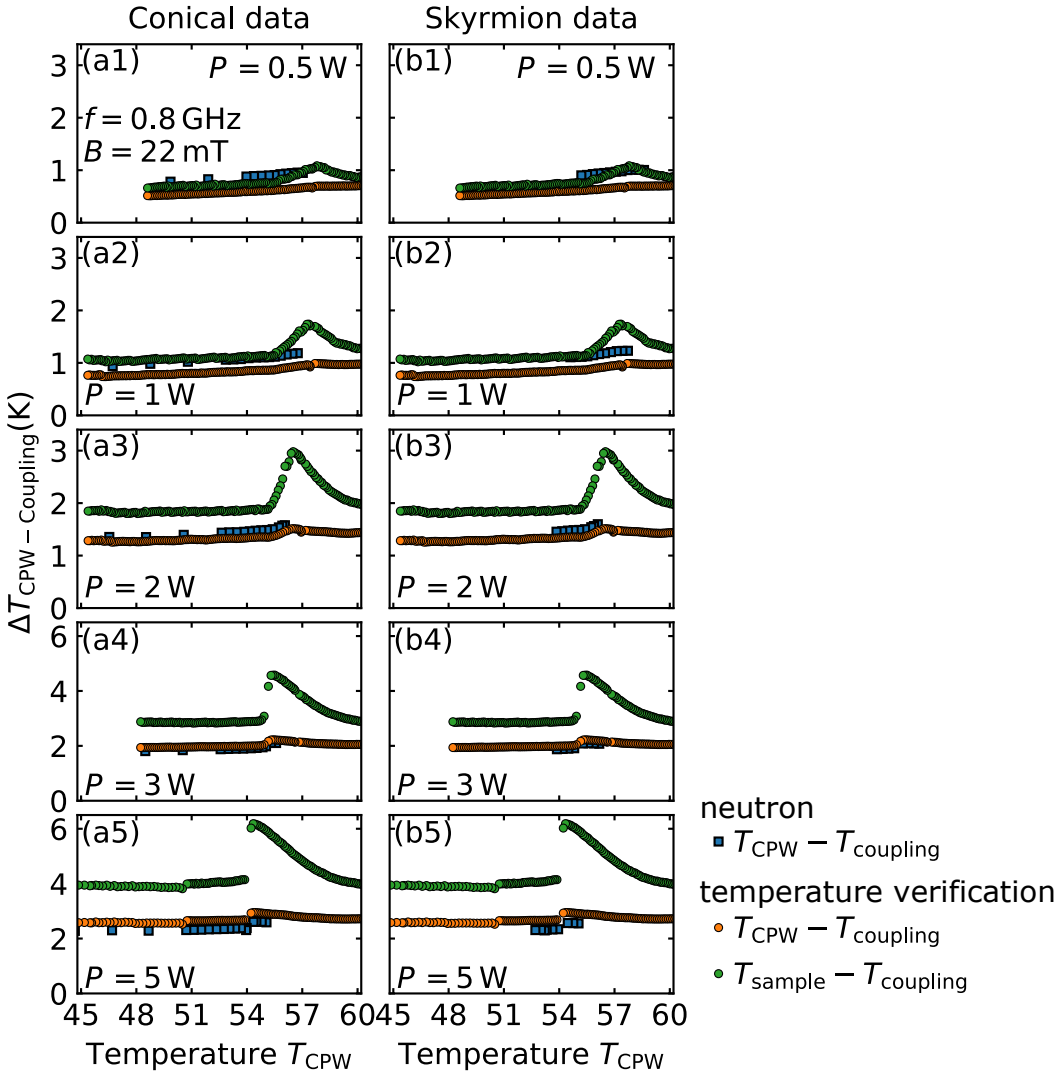

Figure C.3.: Comparison of temperature progressions. Temperature offset between CPW and coupling position during field-cooled neutron scattering measurements of (a) the conical phase and (b) the skyrmion lattice phase for an applied ac magnetic field frequency $f = 0.8\,\mathrm{GHz}$ and various input powers P. Furthermore, the offset between CPW and coupling position as well as sample and coupling position during temperature correction measurements are shown.

C.2. Excitation spectra of Cu_2OSeO_3 under intense microwave radiation

In Sec. 6.3.3 spectra of the spin excitations in Cu_2OSeO_3 under intense microwave radiation for various excitation frequencies and ac magnetic field amplitudes are discussed. For a frequency $f = 0.8\,\mathrm{GHz}$ spectra were recorded for input powers of $P = 0.5$, 1, 2, 3, and 5 W. Here, the overall field dependence of the sample temperature during field sweeps

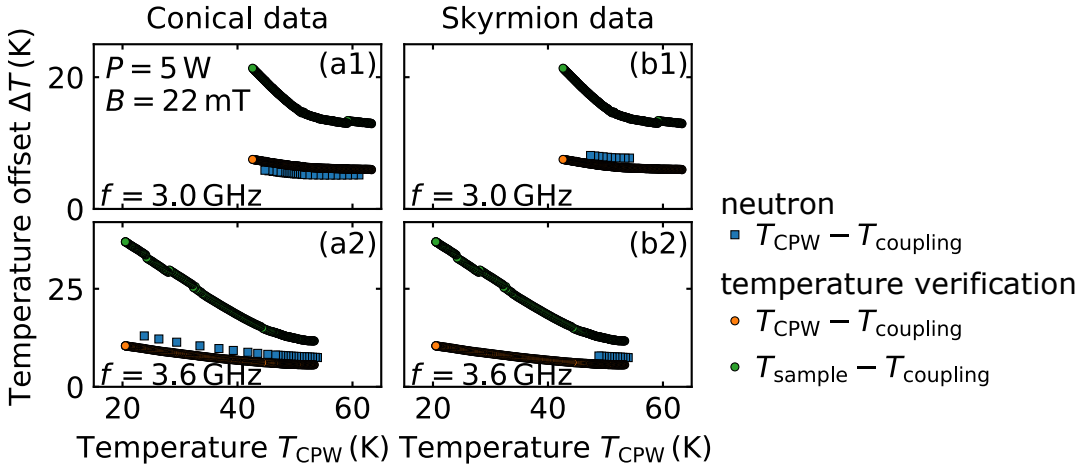

Figure C.4.: Comparison of temperature progressions. Temperature offset between CPW and coupling position during field-cooled neutron scattering measurements of (a) the conical phase and (b) the skyrmion lattice phase for applied ac magnetic field frequencies $f = 3.0$ and $3.6\,\mathrm{GHz}$, respectively and an input power $P = 5\,\mathrm{W}$. Furthermore, the offset between CPW and coupling position as well as sample and coupling position during temperature correction measurements are shown.

crossing the skyrmion lattice phase is similar, however, less pronounced for lower driving ac magnetic field amplitudes. For comparison typical data for $P = 2$ and $0.5\,\mathrm{W}$ are shown in Fig. C.5 and C.6, respectively. Furthermore, Fig. C.7 shows spectra obtained at a lower frequency of $f = 0.6\,\mathrm{GHz}$ for highest input power $P = 5\,\mathrm{W}$.

In the case of $P = 0.5\,\mathrm{W}$ shown in Fig. C.5, the sample temperature increases continuously within the skyrmion lattice phase by $\Delta T = 0.1\,\mathrm{K}$ and is constant as a function of field otherwise as shown in Fig. C.5 (a). The phase transitions extracted from the excitation spectra in Fig. C.5 (b) agree well with the phase transitions in Fig. C.5 (a) inferred from temperature and field compared with the undisturbed phase diagram. The CCW excitation mode is observed throughout the skyrmion lattice phase marked with arrows down to the driving frequency.

Fig. C.6 shows excitation spectra obtained with an input power $P = 2\,\mathrm{W}$ and an excitation frequency $f_{\mathrm{driving}} = 0.8\,\mathrm{GHz}$ for two different coupling temperatures. The field dependence of the sample temperature is displayed in Fig. C.6 (a1) and (a2). The temperature increases slightly entering the skyrmion lattice phase by $\Delta T = 0.3\,\mathrm{K}$ and, subsequently, it increases sharply by $0.5\,\mathrm{K}$ within the phase. In Fig. C.6 (a1) it increases just above the ordering temperature T_{c}, whereas in Fig. C.6 (a2) the temperature remains within the skyrmion lattice phase. Leaving the phase as a function of field, the temperature decreases

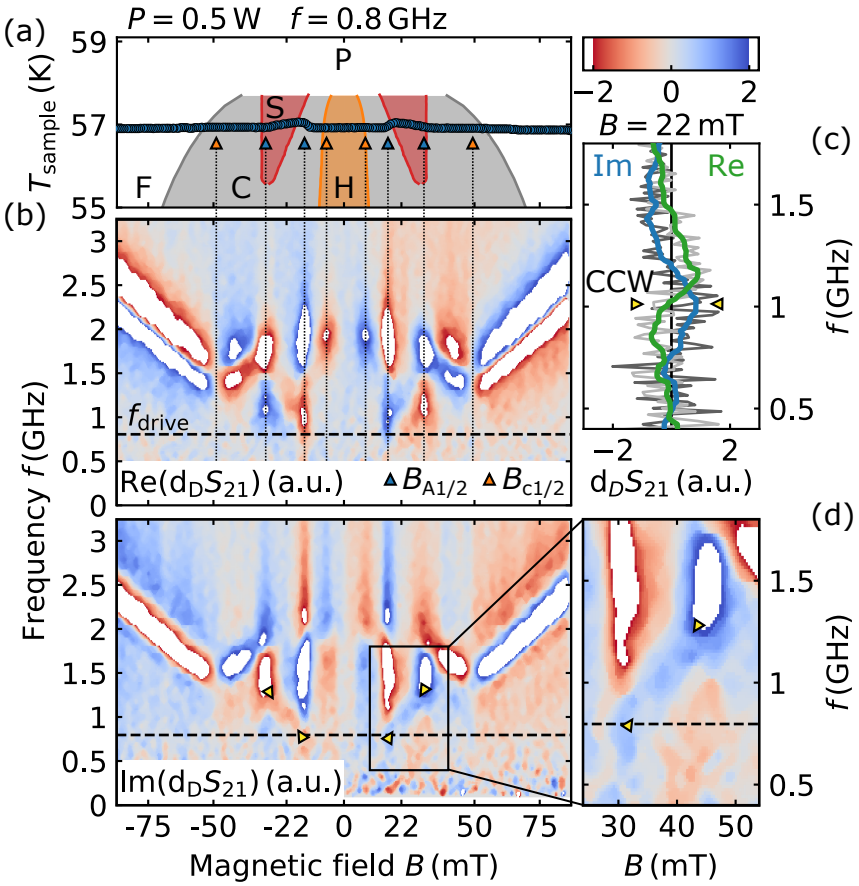

Figure C.5.: All-electrical broadband spectroscopy under intense microwave radiation at $f = 0.8\,\mathrm{GHz}$ and low power $P = 0.5\,\mathrm{W}$. (a) Sample temperature during field sweeps in FMR measurements with constant coupling temperature. Shaded areas denote the phase diagram as inferred without intense microwave radiation with the field-polarised (F), conical (C), helical (H), skyrmion lattice (S), and paramagnetic (P) phase. (b) Colormap depicting the real and the imaginary part of the derivative divide of the complex transmission parameter S_{21} as a function of frequency f and magnetic field B. Dotted lines and triangles mark the phase transitions. Yellow arrows mark the CCW mode. (c) Complex transmission parameter for a constant field. (d) Magnified signal around the skyrmion lattice phase.

again to the same temperature as observed in the high-field conical and field-polarised phase. The phase transitions marked in Fig. C.6 (b1) and (b2) agree with the phase transitions in (a1) and (a2). The CCW resonant mode is observed throughout the skyrmion lattice phase down to the driving frequency marked with arrows in $\mathrm{Im}(\mathrm{d_D}S_{21})$.

Fig. C.7 shows excitation spectra obtained with an input power $P = 5\,\mathrm{W}$ and an excitation frequency of $f_{\mathrm{drive}} = 0.6\,\mathrm{GHz}$. The field dependence of the sample temperature is displayed in Fig. C.7 (a). Within the skyrmion lattice phase, the temperature increases above the critical temperature T_{c} as the CCW mode approaches the excitation frequency.

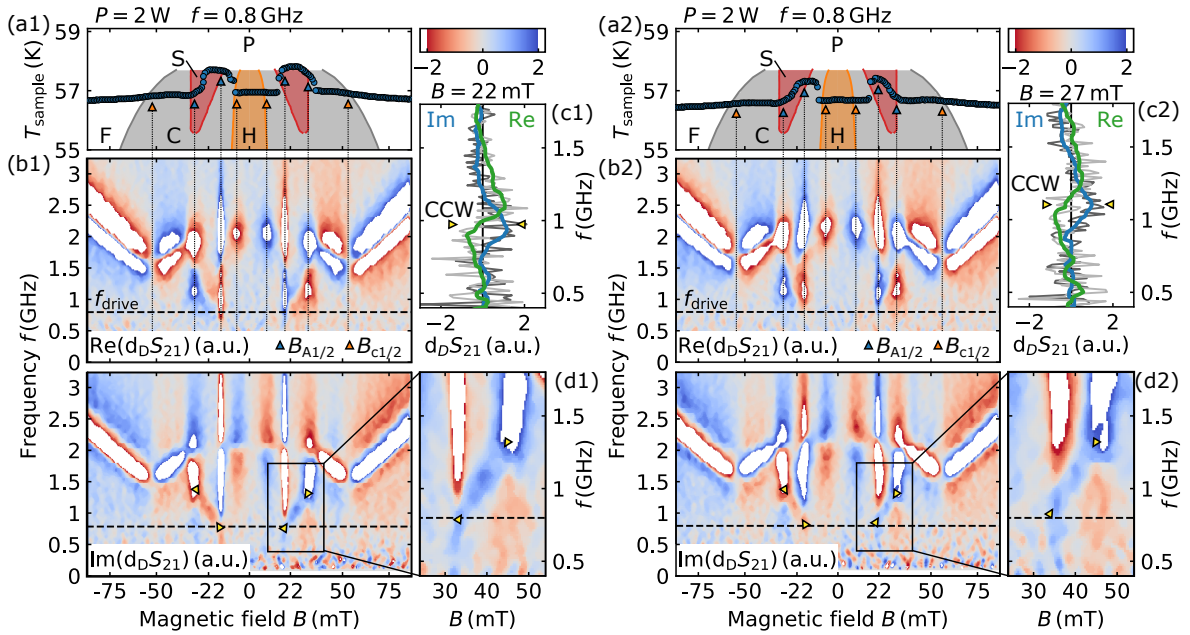

Figure C.6.: All-electrical broadband spectroscopy under intense microwave radiation at $f = 0.8\,\mathrm{GHz}$ and intermediate power $P = 2\,\mathrm{W}$ for two different coupling temperatures T_{coupling}. (a1, a2) Sample temperature during field sweeps in FMR measurements with constant coupling temperature. Shaded areas denote the phase diagram as inferred without intense microwave radiation with the field-polarised (F), conical (C), helical (H), skyrmion lattice (S), and paramagnetic (P) phase. (b1, b2) Colormap depicting the real and the imaginary part of the derivative divide of the complex transmission parameter S_{21} as a function of frequency f and magnetic field B. Dotted lines and triangles mark the phase transitions. Yellow arrows mark the CCW mode. (c1, c2) Complex transmission parameter for a constant field. (d1, d2) Magnified signal around the skyrmion lattice phase.

The temperature remains at an elevated temperature, decreases slightly in temperature in the helical phase and has another maximum in the skyrmion lattice phase at positive fields. Finally, the temperature decreases smoothly within the high-field conical phase. The phase transitions marked in Fig. C.7 (b) agree well with the phase transitions in (a). In particular, the transition from the skyrmion lattice phase to the low-field conical phase observed in the excitation spectra at $B \approx -14\,\mathrm{mT}$ shows that the sample is indeed at the critical temperature T_{c}. The CCW resonant mode is observed throughout the skyrmion lattice phase marked with arrows in $\mathrm{Im}(\mathrm{d_D}S_{21})$.

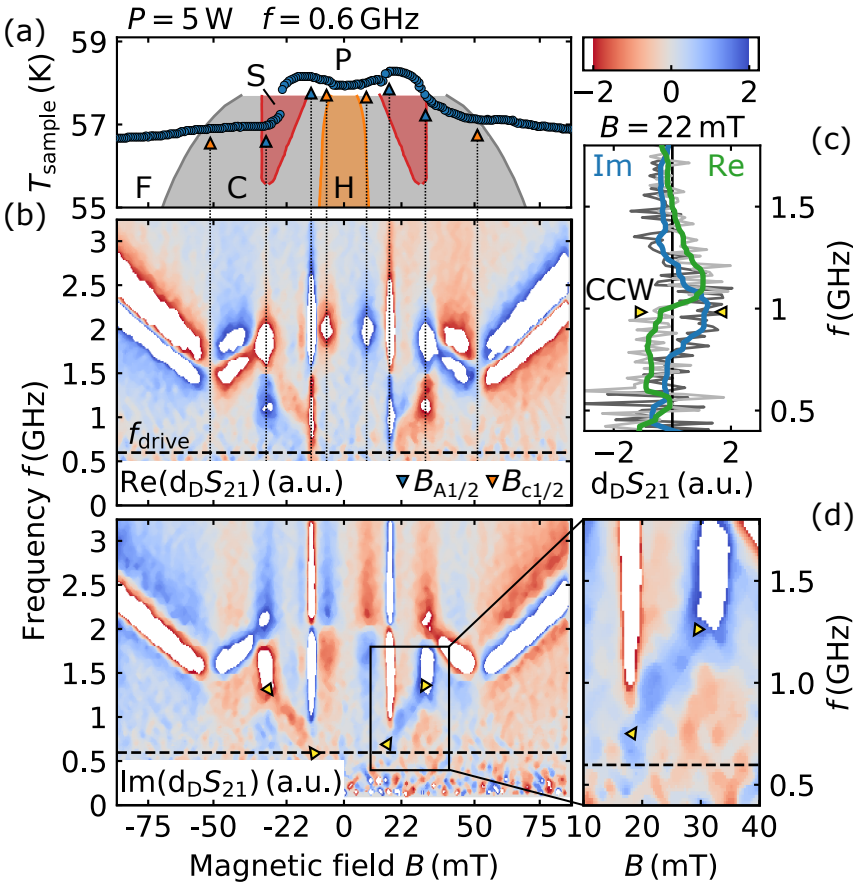

Figure C.7.: All-electrical broadband spectroscopy under intense microwave radiation at $f = 0.6\,\mathrm{GHz}$ and a maximum power $P = 5\,\mathrm{W}$. (a) Sample temperature during field sweeps in FMR measurements with constant coupling temperature. Shaded areas denote the phase diagram as inferred without intense microwave radiation with the field-polarised (F), conical (C), helical (H), skyrmion lattice (S), and paramagnetic (P) phase. (b) Colormap depicting the real and the imaginary part of the derivative divide of the complex transmission parameter S_{21} as a function of frequency f and magnetic field B. Dotted lines and triangles mark the phase transitions. Yellow arrows mark the CCW mode. (c) Complex transmission parameter for a constant field. (d) Magnified signal around the skyrmion lattice phase.

Bibliography

[1] V. L. Ginzburg and L. D. Landau, On the Theory of Superconductivity, Sov. Phys. JETP **20**, 1064 (1950).

[2] C. Kittel, Physical Theory of Ferromagnetic Domains, Rev. Mod. Phys. **21**, 541 (1949).

[3] A. Meshkovsky and A. Shalnikov, Sov. Phys. JETP **17**, 851 (1947).

[4] A. Hubert, Zur Theorie der zweiphasigen Domänenstrukturen in Supraleitern und Ferromagneten, Phys. Status Solidi B **24**, 669 (1967).

[5] V. G. Bar'yakhtar, A. N. Bogdanov, and D. A. Yablonskiĭ, The Physics of Magnetic Domains, Sov. Phys. Usp. **31**, 810 (1988).

[6] A. Bogdanov and A. Hubert, Thermodynamically Stable Magnetic Vortex States in Magnetic Crystals, J. Magn. Magn. Mater. **138**, 255 (1994).

[7] A. A. Abrikosov, On the Magnetic Properties of Superconductors of the Second Group, Sov. Phys. JETP **5**, 1174 (1957).

[8] P. Mangin and R. Kahn, The Intermediate State of Type I Superconductors, in *Superconductivity: An Introduction*, edited by P. Mangin and R. Kahn (Springer International Publishing, 2017) p. 87.

[9] A. Hubert and R. Schäfer, Introduction, in *Magnetic Domains: The Analysis of Magnetic Microstructures*, edited by A. Hubert and R. Schäfer (Springer, 1998).

[10] C. E. Sosolik, J. A. Stroscio, M. D. Stiles, E. W. Hudson, S. R. Blankenship, A. P. Fein, and R. J. Celotta, Real-Space Imaging of Structural Transitions in the Vortex Lattice of V_3Si, Phys. Rev. B **68**, 140503 (2003).

[11] A. Kovács, Z.-A. Li, K. Shibata, and R. E. Dunin-Borkowski, Lorentz Microscopy and Off-Axis Electron Holography of Magnetic Skyrmions in FeGe, Resolut. Discov. **1**, 2 (2016).

[12] I. Kézsmárki, S. Bordács, P. Milde, E. Neuber, L. M. Eng, J. S. White, H. M. Rønnow, C. D. Dewhurst, M. Mochizuki, K. Yanai, H. Nakamura, D. Ehlers, V. Tsurkan, and A. Loidl, Néel-Type Skyrmion Lattice with Confined Orientation in the Polar Magnetic Semiconductor GaV_4S_8, Nat. Mater. **14**, 1116 (2015).

[13] A. N. Bogdanov and D. A. Yablonskii, Thermodynamically Stable "Vortices" in Magnetically Ordered Crystals. The Mixed State of Magnets, Sov. Phys. JETP **68**, 101 (1989).

[14] S. Mühlbauer, B. Binz, F. Jonietz, C. Pfleiderer, A. Rosch, A. Neubauer, R. Georgii, and P. Böni, Skyrmion Lattice in a Chiral Magnet, Science **323**, 915 (2009).

[15] N. Romming, C. Hanneken, M. Menzel, J. E. Bickel, B. Wolter, K. von Bergmann, A. Kubetzka, and R. Wiesendanger, Writing and Deleting Single Magnetic Skyrmions, Science **341**, 636 (2013).

[16] W. Jiang, P. Upadhyaya, W. Zhang, G. Yu, M. B. Jungfleisch, F. Y. Fradin, J. E. Pearson, Y. Tserkovnyak, K. L. Wang, O. Heinonen, S. G. E. te Velthuis, and A. Hoffmann, Blowing Magnetic Skyrmion Bubbles, Science **349**, 283 (2015).

[17] M. Finazzi, M. Savoini, A. R. Khorsand, A. Tsukamoto, A. Itoh, L. Duò, A. Kirilyuk, T. Rasing, and M. Ezawa, Laser-Induced Magnetic Nanostructures with Tunable Topological Properties, Phys. Rev. Lett. **110**, 177205 (2013).

[18] X. Z. Yu, Y. Onose, N. Kanazawa, J. H. Park, J. H. Han, Y. Matsui, N. Nagaosa, and Y. Tokura, Real-Space Observation of a Two-Dimensional Skyrmion Crystal, Nature **465**, 901 (2010).

[19] X. Z. Yu, N. Kanazawa, Y. Onose, K. Kimoto, W. Z. Zhang, S. Ishiwata, Y. Matsui, and Y. Tokura, Near Room-Temperature Formation of a Skyrmion Crystal in Thin-Films of the Helimagnet FeGe, Nat. Mater. **10**, 106 (2011).

[20] S. Seki, X. Z. Yu, S. Ishiwata, and Y. Tokura, Observation of Skyrmions in a Multiferroic Material, Science **336**, 198 (2012).

[21] Y. Tokunaga, X. Z. Yu, J. S. White, H. M. Rønnow, D. Morikawa, Y. Taguchi, and Y. Tokura, A New Class of Chiral Materials Hosting Magnetic Skyrmions beyond Room Temperature, Nat. Commun. **6**, 7638 (2015).

[22] A. K. Nayak, V. Kumar, T. Ma, P. Werner, E. Pippel, R. Sahoo, F. Damay, U. K. Rößler, C. Felser, and S. S. P. Parkin, Magnetic Antiskyrmions above Room Temperature in Tetragonal Heusler Materials, Nature **548**, 561 (2017).

[23] S. Heinze, K. von Bergmann, M. Menzel, J. Brede, A. Kubetzka, R. Wiesendanger, G. Bihlmayer, and S. Blügel, Spontaneous Atomic-Scale Magnetic Skyrmion Lattice in Two Dimensions, Nat. Phys. **7**, 713 (2011).

[24] S. Woo, K. Litzius, B. Krüger, M.-Y. Im, L. Caretta, K. Richter, M. Mann, A. Krone, R. M. Reeve, M. Weigand, P. Agrawal, I. Lemesh, M.-A. Mawass, P. Fischer, M. Kläui, and G. S. D. Beach, Observation of Room-Temperature Magnetic Skyrmions and Their Current-Driven Dynamics in Ultrathin Metallic Ferromagnets, Nat. Mater. **15**, 501 (2016).

[25] R. Wiesendanger, Nanoscale Magnetic Skyrmions in Metallic Films and Multilayers: A New Twist for Spintronics, Nat. Rev. Mater. **1**, 16044 (2016).

[26] A. Fert, V. Cros, and J. Sampaio, Skyrmions on the Track, Nat. Nanotechnol. **8**, 152 (2013).

[27] A. Fert, N. Reyren, and V. Cros, Magnetic Skyrmions: Advances in Physics and Potential Applications, Nat. Rev. Mater. **2**, 17031 (2017).

[28] C. Moreau-Luchaire, C. Moutafis, N. Reyren, J. Sampaio, C. a. F. Vaz, N. V. Horne, K. Bouzehouane, K. Garcia, C. Deranlot, P. Warnicke, P. Wohlhüter, J.-M. George, M. Weigand, J. Raabe, V. Cros, and A. Fert, Additive Interfacial Chiral Interaction in Multilayers for Stabilization of Small Individual Skyrmions at Room Temperature, Nat. Nanotechnol. **11**, 444 (2016).

[29] C. Pfleiderer, Why First Order Quantum Phase Transitions Are Interesting, J. Phys.: Condens. Matter **17**, S987 (2005).

[30] R. Gross and A. Marx, *Festkörperphysik*, 2nd ed. (Oldenbourg Wissenschaftsverlag, 2012).

[31] K. G. Wilson, The Renormalization Group and Critical Phenomena, Rev. Mod. Phys. **55**, 583 (1983).

[32] H. v. Löhneysen, A. Rosch, M. Vojta, and P. Wölfle, Fermi-Liquid Instabilities at Magnetic Quantum Phase Transitions, Rev. Mod. Phys. **79**, 1015 (2007).

[33] S. Sachdev, Quantum Magnetism and Criticality, Nat. Phys. **4**, 173 (2008).

[34] M. Brando, D. Belitz, F. M. Grosche, and T. R. Kirkpatrick, Metallic Quantum Ferromagnets, Rev. Mod. Phys. **88**, 025006 (2016).

[35] M. Vojta, Quantum Phase Transitions, Rep. Prog. Phys. **66**, 2069 (2003).

[36] J. A. Hertz, Quantum Critical Phenomena, Phys. Rev. B **14**, 1165 (1976).

[37] C. Pfleiderer, Superconducting Phases of f-Electron Compounds, Rev. Mod. Phys. **81**, 1551 (2009).

[38] J. Paglione and R. L. Greene, High-Temperature Superconductivity in Iron-Based Materials, Nature Phys **6**, 645 (2010).

[39] N. D. Mathur, F. M. Grosche, S. R. Julian, I. R. Walker, D. M. Freye, R. K. W. Haselwimmer, and G. G. Lonzarich, Magnetically Mediated Superconductivity in Heavy Fermion Compounds, Nature **394**, 39 (1998).

[40] M. Brian Maple, R. E. Baumbach, N. P. Butch, J. J. Hamlin, and M. Janoschek, Non-Fermi Liquid Regimes and Superconductivity in the Low Temperature Phase Diagrams of Strongly Correlated d- and f-Electron Materials, J. Low Temp. Phys. **161**, 4 (2010).

[41] S. Sachdev, *Quantum Phase Transitions*, 2nd ed. (Cambridge University Press, 2011).

[42] S. Sachdev, Quantum Phase Transitions of Antiferromagnets and the Cuprate Superconductors, in *Modern Theories of Many-Particle Systems in Condensed Matter Physics*, edited by D. C. Cabra, A. Honecker, and P. Pujol (Springer, 2012).

[43] P. A. Lee, N. Nagaosa, and X.-G. Wen, Doping a Mott Insulator: Physics of High-Temperature Superconductivity, Rev. Mod. Phys. **78**, 17 (2006).

[44] R. Coldea, D. A. Tennant, E. M. Wheeler, E. Wawrzynska, D. Prabhakaran, M. Telling, K. Habicht, P. Smeibidl, and K. Kiefer, Quantum Criticality in an Ising Chain: Experimental Evidence for Emergent E8 Symmetry, Science **327**, 177 (2010).

[45] D. Bitko, T. F. Rosenbaum, and G. Aeppli, Quantum Critical Behavior for a Model Magnet, Phys. Rev. Lett. **77**, 940 (1996).

[46] F. Steglich, J. Aarts, C. D. Bredl, W. Lieke, D. Meschede, W. Franz, and H. Schäfer, Superconductivity in the Presence of Strong Pauli Paramagnetism: $CeCu_2Si_2$, Phys. Rev. Lett. **43**, 1892 (1979).

[47] G. R. Stewart, Heavy-Fermion Systems, Rev. Mod. Phys. **56**, 755 (1984).

[48] J. Flouquet, G. Knebel, D. Braithwaite, D. Aoki, J.-P. Brison, F. Hardy, A. Huxley, S. Raymond, B. Salce, and I. Sheikin, Magnetism and Superconductivity of Heavy Fermion Matter, C. R. Physique J **7**, 22 (2006).

[49] S. Peggs and European Spallation Source, *ESS Technical Design Report* (European Spallation Source (ESS), 2013).

[50] S. Seo, X. Lu, J.-X. Zhu, R. R. Urbano, N. Curro, E. D. Bauer, V. A. Sidorov, L. D. Pham, T. Park, Z. Fisk, and J. D. Thompson, Disorder in Quantum Critical Superconductors, Nature Phys **10**, 120 (2014).

[51] A. Rosch, Interplay of Disorder and Spin Fluctuations in the Resistivity near a Quantum Critical Point, Phys. Rev. Lett. **82**, 4280 (1999).

[52] S. S. Saxena, P. Agarwal, K. Ahilan, F. M. Grosche, R. K. W. Haselwimmer, M. J. Steiner, E. Pugh, I. R. Walker, S. R. Julian, P. Monthoux, G. G. Lonzarich, A. Huxley, I. Sheikin, D. Braithwaite, and J. Flouquet, Superconductivity on the Border of Itinerant-Electron Ferromagnetism in UGe_2, Nature **406**, 587 (2000).

[53] A. D. Huxley, S. Raymond, and E. Ressouche, Magnetic Excitations in the Ferromagentic Superconductor UGe_2, Phys. Rev. Lett. **91**, 207201 (2003).

[54] T. H. R. Skyrme, A Non-Linear Field Theory, Proc. Royal Soc. Lond. A **260**, 127 (1961).

[55] T. H. R. Skyrme, Particle States of a Quantized Meson Field, Proc. Royal Soc. Lond. A **262**, 237 (1961).

[56] T. H. R. Skyrme, A Unified Field Theory of Mesons and Baryons, Nucl. Phys. **31**, 556 (1962).

[57] G. S. Adkins, E. Witten, and C. R. Nappi, Static Properties of Nucleons in the Skyrme Model, Nucl. Phys. B **228**, 552 (1983).

[58] I. Zahed and G. E. Brown, The Skyrme Model, Phys. Rep. **142**, 1 (1986).

[59] E. Chabanat, P. Bonche, P. Haensel, J. Meyer, and R. Schaeffer, A Skyrme Parametrization from Subnuclear to Neutron Star Densities, Nucl. Phys. A **627**, 710 (1997).

[60] D. Diakonov, V. Petrov, and M. Polyakov, Exotic Anti-Decuplet of Baryons: Prediction from Chiral Solitons, Z. Phys. A **359**, 305 (1997).

[61] E. Chabanat, P. Bonche, P. Haensel, J. Meyer, and R. Schaeffer, A Skyrme Parametrization from Subnuclear to Neutron Star Densities Part II. Nuclei Far from Stabilities, Nucl. Phys. A **635**, 231 (1998).

[62] S. L. Sondhi, A. Karlhede, S. A. Kivelson, and E. H. Rezayi, Skyrmions and the Crossover from the Integer to Fractional Quantum Hall Effect at Small Zeeman Energies, Phys. Rev. B **47**, 16419 (1993).

[63] A. Schmeller, J. P. Eisenstein, L. N. Pfeiffer, and K. W. West, Evidence for Skyrmions and Single Spin Flips in the Integer Quantized Hall Effect, Phys. Rev. Lett. **75**, 4290 (1995).

[64] K. Yang, S. Das Sarma, and A. H. MacDonald, Collective Modes and Skyrmion Excitations in Graphene $SU(4)$ Quantum Hall Ferromagnets, Phys. Rev. B **74**, 075423 (2006).

[65] T.-L. Ho, Spinor Bose Condensates in Optical Traps, Phys. Rev. Lett. **81**, 742 (1998).

[66] U. A. Khawaja and H. Stoof, Skyrmions in a Ferromagnetic Bose–Einstein Condensate, Nature **411**, 918 (2001).

[67] L. S. Leslie, A. Hansen, K. C. Wright, B. M. Deutsch, and N. P. Bigelow, Creation and Detection of Skyrmions in a Bose–Einstein Condensate, Phys. Rev. Lett. **103**, 250401 (2009).

[68] J.-i. Fukuda and S. Žumer, Quasi-Two-Dimensional Skyrmion Lattices in a Chiral Nematic Liquid Crystal, Nat. Commun. **2**, 246 (2011).

[69] A. Bauer and C. Pfleiderer, Generic Aspects of Skyrmion Lattices in Chiral Magnets, in *Topological Structures in Ferroic Materials: Domain Walls, Vortices and Skyrmions*, edited by J. Seidel (Springer, 2016).

[70] P. Milde, D. Köhler, J. Seidel, L. M. Eng, A. Bauer, A. Chacon, J. Kindervater, S. Mühlbauer, C. Pfleiderer, S. Buhrandt, C. Schütte, and A. Rosch, Unwinding of a Skyrmion Lattice by Magnetic Monopoles, Science **340**, 1076 (2013).

[71] A. Bogdanov and A. Hubert, The Stability of Vortex-like Structures in Uniaxial Ferromagnets, J. Magn. Magn. Mater. **195**, 182 (1999).

[72] F. Büttner, C. Moutafis, M. Schneider, B. Krüger, C. M. Günther, J. Geilhufe, C. v. K. Schmising, J. Mohanty, B. Pfau, S. Schaffert, A. Bisig, M. Foerster, T. Schulz, C. a. F. Vaz, J. H. Franken, H. J. M. Swagten, M. Kläui, and S. Eisebitt, Dynamics and Inertia of Skyrmionic Spin Structures, Nat. Phys. **11**, 225 (2015).

[73] W. Jiang, X. Zhang, G. Yu, W. Zhang, X. Wang, M. Benjamin Jungfleisch, J. E. Pearson, X. Cheng, O. Heinonen, K. L. Wang, Y. Zhou, A. Hoffmann, and S. G. E. te Velthuis, Direct Observation of the Skyrmion Hall Effect, Nat. Phys. **13**, 162 (2017).

[74] J. Sampaio, V. Cros, S. Rohart, A. Thiaville, and A. Fert, Nucleation, Stability and Current-Induced Motion of Isolated Magnetic Skyrmions in Nanostructures, Nat. Nanotechnol. **8**, 839 (2013).

[75] D. Maccariello, W. Legrand, N. Reyren, K. Garcia, K. Bouzehouane, S. Collin, V. Cros, and A. Fert, Electrical Detection of Single Magnetic Skyrmions in Metallic Multilayers at Room Temperature, Nat. Nanotechnol. **13**, 233 (2018).

[76] C. Pfleiderer, S. R. Julian, and G. G. Lonzarich, Non-Fermi-Liquid Nature of the Normal State of Itinerant-Electron Ferromagnets, Nature **414**, 427 (2001).

[77] C. Pfleiderer, D. Reznik, L. Pintschovius, H. v. Löhneysen, M. Garst, and A. Rosch, Partial Order in the Non-Fermi-Liquid Phase of MnSi, Nature **427**, 227 (2004).

[78] R. Ritz, M. Halder, M. Wagner, C. Franz, A. Bauer, and C. Pfleiderer, Formation of a Topological Non-Fermi Liquid in MnSi, Nature **497**, 231 (2013).

[79] N. Nagaosa and Y. Tokura, Topological Properties and Dynamics of Magnetic Skyrmions, Nat. Nanotechnol. **8**, 899 (2013).

[80] F. Jonietz, S. Mühlbauer, C. Pfleiderer, A. Neubauer, W. Münzer, A. Bauer, T. Adams, R. Georgii, P. Böni, R. A. Duine, K. Everschor, M. Garst, and A. Rosch, Spin Transfer Torques in MnSi at Ultralow Current Densities, Science **330**, 1648 (2010).

[81] M. Mochizuki, Spin-Wave Modes and Their Intense Excitation Effects in Skyrmion Crystals, Phys. Rev. Lett. **108**, 017601 (2012).

[82] Y. Okamura, F. Kagawa, M. Mochizuki, M. Kubota, S. Seki, S. Ishiwata, M. Kawasaki, Y. Onose, and Y. Tokura, Microwave Magnetoelectric Effect via Skyrmion Resonance Modes in a Helimagnetic Multiferroic, Nat. Commun. **4**, 2391 (2013).

[83] T. Schwarze, J. Waizner, M. Garst, A. Bauer, I. Stasinopoulos, H. Berger, C. Pfleiderer, and D. Grundler, Universal Helimagnon and Skyrmion Excitations in Metallic, Semiconducting and Insulating Chiral Magnets, Nat. Mater. **14**, 478 (2015).

[84] B. Binz and A. Vishwanath, Chirality Induced Anomalous-Hall Effect in Helical Spin Crystals, Physica B **403**, 1336 (2008).

[85] M. Garst, Topological Skyrmion Dynamics in Chiral Magnets, in *Topological Structures in Ferroic Materials: Domain Walls, Vortices and Skyrmions*, edited by J. Seidel (Springer, 2016) p. 29.

[86] T. Adams, S. Mühlbauer, C. Pfleiderer, F. Jonietz, A. Bauer, A. Neubauer, R. Georgii, P. Böni, U. Keiderling, K. Everschor, M. Garst, and A. Rosch, Long-Range Crystalline Nature of the Skyrmion Lattice in MnSi, Phys. Rev. Lett. **107**, 217206 (2011).

[87] Y. Ishikawa, K. Tajima, D. Bloch, and M. Roth, Helical Spin Structure in Manganese Silicide MnSi, Solid State Commun. **19**, 525 (1976).

[88] P. Bak and M. H. Jensen, Theory of Helical Magnetic Structures and Phase Transitions in MnSi and FeGe, J. Phys. C **13**, L881 (1980).

[89] T. Adams, A. Chacon, M. Wagner, A. Bauer, G. Brandl, B. Pedersen, H. Berger, P. Lemmens, and C. Pfleiderer, Long-Wavelength Helimagnetic Order and Skyrmion Lattice Phase in Cu_2OSeO_3, Phys. Rev. Lett. **108**, 237204 (2012).

[90] T. Adams, M. Garst, A. Bauer, R. Georgii, and C. Pfleiderer, Response of the Skyrmion Lattice in MnSi to Cubic Magnetocrystalline Anisotropies, Phys. Rev. Lett. **121**, 187205 (2018).

[91] A. Chacon, L. Heinen, M. Halder, A. Bauer, W. Simeth, S. Mühlbauer, H. Berger, M. Garst, A. Rosch, and C. Pfleiderer, Observation of Two Independent Skyrmion Phases in a Chiral Magnetic Material, Nat. Phys. **14**, 936 (2018).

[92] S. Bordács, A. Butykai, B. G. Szigeti, J. S. White, R. Cubitt, A. O. Leonov, S. Widmann, D. Ehlers, H.-A. K. von Nidda, V. Tsurkan, A. Loidl, and I. Kézsmárki, Equilibrium Skyrmion Lattice Ground State in a Polar Easy-Plane Magnet, Sci. Rep. **7**, 7584 (2017).

[93] X. Yu, M. Mostovoy, Y. Tokunaga, W. Zhang, K. Kimoto, Y. Matsui, Y. Kaneko, N. Nagaosa, and Y. Tokura, Magnetic Stripes and Skyrmions with Helicity Reversals, PNAS **109**, 8856 (2012).

[94] M. N. Wilson, A. B. Butenko, A. N. Bogdanov, and T. L. Monchesky, Chiral Skyrmions in Cubic Helimagnet Films: The Role of Uniaxial Anisotropy, Phys. Rev. B **89**, 094411 (2014).

[95] A. Bauer, *Investigation of Itinerant Antiferromagnets and Cubic Chiral Helimagnets*, Ph.D. thesis, Technische Universität München (2014).

[96] L. D. Landau and E. M. Lifshitz, *Statistical Physics* (Pergamon Press, 1980).

[97] I. E. Dzyaloshinskii, Thermodynamic Theory of "Weak" Ferromagnetism in Antiferromagnetic Substances, Sov. Phys. JETP **5**, 1259 (1957).

[98] T. Moriya, Anisotropic Superexchange Interaction and Weak Ferromagnetism, Phys. Rev. **120**, 91 (1960).

[99] I. E. Dzyaloshinskii, Theory of Helicoidal Structures in Antiferromagnets, Sov. Phys. JETP **19**, 960 (1964).

[100] K. Motoya, H. Yasuoka, Y. Nakamura, and J. H. Wernick, Helical Spin Structure in MnSi–NMR Studies, Solid State Commun. **19**, 529 (1976).

[101] G. Shirane, R. Cowley, C. Majkrzak, J. B. Sokoloff, B. Pagonis, C. H. Perry, and Y. Ishikawa, Spiral Magnetic Correlation in Cubic MnSi, Phys. Rev. B **28**, 6251 (1983).

[102] M. Ishida, Y. Endoh, S. Mitsuda, Y. Ishikawa, and M. Tanaka, Crystal Chirality and Helicity of the Helical Spin Density Wave in MnSi. II. Polarized Neutron Diffraction, J. Phys. Soc. Jpn. **54**, 2975 (1985).

[103] Y. Ishikawa, Y. Noda, Y. J. Uemura, C. F. Majkrzak, and G. Shirane, Paramagnetic Spin Fluctuations in the Weak Itinerant-Electron Ferromagnet MnSi, Phys. Rev. B **31**, 5884 (1985).

[104] B. Lebech, Magnetic Ordering in Nearly Ferromagnetic Antiferromagnetic Helices, in *Recent Advances in Magnetism of Transition Metal Compounds*, edited by A. Kotani and N. Suzuki (World Scientific, 1993) p. 167.

[105] D. Bloch, J. Voiron, V. Jaccarino, and J. H. Wernick, The High Field-High Pressure Magnetic Properties of MnSi, Phys. Lett. A **51**, 259 (1975).

[106] A. Bauer and C. Pfleiderer, Magnetic Phase Diagram of MnSi Inferred from Magnetization and Ac Susceptibility, Phys. Rev. B **85**, 214418 (2012).

[107] A. Bauer, M. Garst, and C. Pfleiderer, History Dependence of the Magnetic Properties of Single-Crystal $Fe_{1-x}Co_xSi$, Phys. Rev. B **93**, 235144 (2016).

[108] J. Kindervater, I. Stasinopoulos, A. Bauer, F. X. Haslbeck, F. Rucker, A. Chacon, S. Mühlbauer, C. Franz, M. Garst, D. Grundler, and C. Pfleiderer, Weak Crystallization of Fluctuating Skyrmion Textures in MnSi, Phys. Rev. X **9**, 041059 (2019).

[109] U. K. Rößler, A. N. Bogdanov, and C. Pfleiderer, Spontaneous Skyrmion Ground States in Magnetic Metals, Nature **442**, 797 (2006).

[110] C. Pappas, E. Lelièvre-Berna, P. Falus, P. M. Bentley, E. Moskvin, S. Grigoriev, P. Fouquet, and B. Farago, Chiral Paramagnetic Skyrmion-like Phase in MnSi, Phys. Rev. Lett. **102**, 197202 (2009).

[111] C. Pappas, E. Lelièvre-Berna, P. Bentley, P. Falus, P. Fouquet, and B. Farago, Magnetic Fluctuations and Correlations in MnSi: Evidence for a Chiral Skyrmion Spin Liquid Phase, Phys. Rev. B **83**, 224405 (2011).

[112] M. Janoschek, M. Garst, A. Bauer, P. Krautscheid, R. Georgii, P. Böni, and C. Pfleiderer, Fluctuation-Induced First-Order Phase Transition in Dzyaloshinskii–Moriya Helimagnets, Phys. Rev. B **87**, 134407 (2013).

[113] S. A. Brazovskii, Phase Transition of an Isotropic System to a Nonuniform State, Sov. Phys. JETP **41**, 85 (1975).

[114] P. M. Chaikin and T. C. Lubensky, *Principles of Condensed Matter Physics*, Vol. 1 (Cambridge University Press, 1995).

[115] S. V. Grigoriev, S. V. Maleyev, E. V. Moskvin, V. A. Dyadkin, P. Fouquet, and H. Eckerlebe, Crossover Behavior of Critical Helix Fluctuations in MnSi, Phys. Rev. B **81**, 144413 (2010).

[116] S. V. Grigoriev, E. V. Moskvin, V. A. Dyadkin, D. Lamago, T. Wolf, H. Eckerlebe, and S. V. Maleyev, Chiral Criticality in the Doped Helimagnets $Mn_{1-y}Fe_ySi$, Phys. Rev. B **83**, 224411 (2011).

[117] I. Živković, J. S. White, H. M. Rønnow, K. Prša, and H. Berger, Critical Scaling in the Cubic Helimagnet Cu_2OSeO_3, Phys. Rev. B **89**, 060401 (2014).

[118] E. Fawcett, J. P. Maita, and J. H. Wernick, Magnetoelastic and Thermal Properties of MnSi, Int. J. Magn. **1**, 29 (1970).

[119] S. Kusaka, K. Yamamoto, T. Komatsubara, and Y. Ishikawa, Ultrasonic Study of Magnetic Phase Diagram of MnSi, Solid State Commun. **20**, 925 (1976).

[120] S. Buhrandt and L. Fritz, Skyrmion Lattice Phase in Three-Dimensional Chiral Magnets from Monte Carlo Simulations, Phys. Rev. B **88**, 195137 (2013).

[121] M. Halder, A. Chacon, A. Bauer, W. Simeth, S. Mühlbauer, H. Berger, L. Heinen, M. Garst, A. Rosch, and C. Pfleiderer, Thermodynamic Evidence of a Second Skyrmion Lattice Phase and Tilted Conical Phase in Cu_2OSeO_3, Phys. Rev. B **98**, 144429 (2018).

[122] C. Pfleiderer and A. Rosch, Condensed-Matter Physics: Single Skyrmions Spotted, Nature **465**, 880 (2010).

[123] A. Neubauer, C. Pfleiderer, B. Binz, A. Rosch, R. Ritz, P. G. Niklowitz, and P. Böni, Topological Hall Effect in the A Phase of MnSi, Phys. Rev. Lett. **102**, 186602 (2009).

[124] T. Schulz, R. Ritz, A. Bauer, M. Halder, M. Wagner, C. Franz, C. Pfleiderer, K. Everschor, M. Garst, and A. Rosch, Emergent Electrodynamics of Skyrmions in a Chiral Magnet, Nat. Phys. **8**, 301 (2012).

[125] K. Everschor, M. Garst, B. Binz, F. Jonietz, S. Mühlbauer, C. Pfleiderer, and A. Rosch, Rotating Skyrmion Lattices by Spin Torques and Field or Temperature Gradients, Phys. Rev. B **86**, 054432 (2012).

[126] M. Mochizuki, X. Z. Yu, S. Seki, N. Kanazawa, W. Koshibae, J. Zang, M. Mostovoy, Y. Tokura, and N. Nagaosa, Thermally Driven Ratchet Motion of a Skyrmion Microcrystal and Topological Magnon Hall Effect, Nat. Mater. **13**, 241 (2014).

[127] L. Kong and J. Zang, Dynamics of an Insulating Skyrmion under a Temperature Gradient, Phys. Rev. Lett. **111**, 067203 (2013).

[128] S.-Z. Lin, C. D. Batista, C. Reichhardt, and A. Saxena, Ac Current Generation in Chiral Magnetic Insulators and Skyrmion Motion Induced by the Spin Seebeck Effect, Phys. Rev. Lett. **112**, 187203 (2014).

[129] J. Iwasaki, A. J. Beekman, and N. Nagaosa, Theory of Magnon–Skyrmion Scattering in Chiral Magnets, Phys. Rev. B **89**, 064412 (2014).

[130] C. Schütte and M. Garst, Magnon–Skyrmion Scattering in Chiral Magnets, Phys. Rev. B **90**, 094423 (2014).

[131] S. Pöllath, J. Wild, L. Heinen, T. N. G. Meier, M. Kronseder, L. Tutsch, A. Bauer, H. Berger, C. Pfleiderer, J. Zweck, A. Rosch, and C. H. Back, Dynamical Defects in Rotating Magnetic Skyrmion Lattices, Phys. Rev. Lett. **118**, 207205 (2017).

[132] S. S. P. Parkin, M. Hayashi, and L. Thomas, Magnetic Domain-Wall Racetrack Memory, Science **320**, 190 (2008).

[133] S. Parkin and S.-H. Yang, Memory on the Racetrack, Nat. Nanotechnol. (2015), 10.1038/nnano.2015.41.

[134] Y. Onose, Y. Okamura, S. Seki, S. Ishiwata, and Y. Tokura, Observation of Magnetic Excitations of Skyrmion Crystal in a Helimagnetic Insulator Cu_2OSeO_3, Phys. Rev. Lett. **109**, 037603 (2012).

[135] Y. Ishikawa, G. Shirane, J. A. Tarvin, and M. Kohgi, Magnetic Excitations in the Weak Itinerant Ferromagnet MnSi, Phys. Rev. B **16**, 4956 (1977).

[136] B. Roessli, P. Böni, W. E. Fischer, and Y. Endoh, Chiral Fluctuations in MnSi above the Curie Temperature, Phys. Rev. Lett. **88**, 237204 (2002).

[137] F. Semadeni, P. Böni, Y. Endoh, B. Roessli, and G. Shirane, Direct Observation of Spin-Flip Excitations in MnSi, Physica B **267–268**, 248 (1999).

[138] B. Roessli, P. Böni, W. E. Fischer, and Y. Endoh, Magnetic Field Dependence of Chiral Fluctuations in MnSi, Physica B **345**, 124 (2004).

[139] M. Garst, J. Waizner, and D. Grundler, Collective Spin Excitations of Helices and Magnetic Skyrmions: Review and Perspectives of Magnonics in Non-Centrosymmetric Magnets, J. Phys. D **50**, 293002 (2017).

[140] M. Kataoka, Spin Waves in Systems with Long Period Helical Spin Density Waves Due to the Antisymmetric and Symmetric Exchange Interactions, J. Phys. Soc. Jpn. **56**, 3635 (1987).

[141] M. Date, K. Okuda, and K. Kadowaki, Electron Spin Resonance in the Itinerant-Electron Helical Magnet MnSi, J. Phys. Soc. Jpn. **42**, 1555 (1977).

[142] M. Janoschek, F. Bernlochner, S. Dunsiger, C. Pfleiderer, P. Böni, B. Roessli, P. Link, and A. Rosch, Helimagnon Bands as Universal Excitations of Chiral Magnets, Phys. Rev. B **81**, 214436 (2010).

[143] M. Kugler, G. Brandl, J. Waizner, M. Janoschek, R. Georgii, A. Bauer, K. Seemann, A. Rosch, C. Pfleiderer, P. Böni, and M. Garst, Band Structure of Helimagnons in MnSi Resolved by Inelastic Neutron Scattering, Phys. Rev. Lett. **115**, 097203 (2015).

[144] T. Weber, J. Waizner, G. S. Tucker, R. Georgii, M. Kugler, A. Bauer, C. Pfleiderer, M. Garst, and P. Böni, Field Dependence of Nonreciprocal Magnons in Chiral MnSi, Phys. Rev. B **97**, 224403 (2018).

[145] P. Y. Portnichenko, J. Romhányi, Y. A. Onykiienko, A. Henschel, M. Schmidt, A. S. Cameron, M. A. Surmach, J. A. Lim, J. T. Park, A. Schneidewind, D. L. Abernathy, H. Rosner, J. van den Brink, and D. S. Inosov, Magnon Spectrum of the Helimagnetic Insulator Cu_2OSeO_3, Nat. Commun. **7**, 10725 (2016).

[146] M. Krawczyk, S. Mamica, M. Mruczkiewicz, J. W. Klos, S. Tacchi, M. Madami, G. Gubbiotti, G. Duerr, and D. Grundler, Magnonic Band Structures in Two-Dimensional Bi-Component Magnonic Crystals with in-Plane Magnetization, J. Phys. D: Appl. Phys. **46**, 495003 (2013).

[147] R. L. Melcher, Linear Contribution to Spatial Dispersion in the Spin-Wave Spectrum of Ferromagnets, Phys. Rev. Lett. **30**, 125 (1973).

[148] Y. Iguchi, S. Uemura, K. Ueno, and Y. Onose, Nonreciprocal Magnon Propagation in a Noncentrosymmetric Ferromagnet $LiFe_5O_8$, Phys. Rev. B **92**, 184419 (2015).

[149] S. Seki, Y. Okamura, K. Kondou, K. Shibata, M. Kubota, R. Takagi, F. Kagawa, M. Kawasaki, G. Tatara, Y. Otani, and Y. Tokura, Magnetochiral Nonreciprocity of Volume Spin Wave Propagation in Chiral-Lattice Ferromagnets, Phys. Rev. B **93**, 235131 (2016).

[150] R. Takagi, D. Morikawa, K. Karube, N. Kanazawa, K. Shibata, G. Tatara, Y. Tokunaga, T. Arima, Y. Taguchi, Y. Tokura, and S. Seki, Spin-Wave Spectroscopy of the Dzyaloshinskii–Moriya Interaction in Room-Temperature Chiral Magnets Hosting Skyrmions, Phys. Rev. B **95**, 220406 (2017).

[151] T. J. Sato, D. Okuyama, T. Hong, A. Kikkawa, Y. Taguchi, T.-h. Arima, and Y. Tokura, Magnon Dispersion Shift in the Induced Ferromagnetic Phase of Noncentrosymmetric MnSi, Phys. Rev. B **94**, 144420 (2016).

[152] S. V. Grigoriev, A. S. Sukhanov, E. V. Altynbaev, S.-A. Siegfried, A. Heinemann, P. Kizhe, and S. V. Maleyev, Spin Waves in Full-Polarized State of Dzyaloshinskii-Moriya Helimagnets: Small-Angle Neutron Scattering Study, Phys. Rev. B **92**, 220415 (2015).

[153] G. Gitgeatpong, Y. Zhao, P. Piyawongwatthana, Y. Qiu, L. W. Harriger, N. P. Butch, T. J. Sato, and K. Matan, Nonreciprocal Magnons and Symmetry-Breaking in the Noncentrosymmetric Antiferromagnet, Phys. Rev. Lett. **119**, 047201 (2017).

[154] M. Mochizuki, Microwave Magnetochiral Effect in Cu_2OSeO_3, Phys. Rev. Lett. **114**, 197203 (2015).

[155] Y. Okamura, F. Kagawa, S. Seki, M. Kubota, M. Kawasaki, and Y. Tokura, Microwave Magnetochiral Dichroism in the Chiral-Lattice Magnet Cu_2OSeO_3, Phys. Rev. Lett. **114**, 197202 (2015).

[156] M. Mochizuki and S. Seki, Dynamical Magnetoelectric Phenomena of Multiferroic Skyrmions, J. Phys.: Condens. Matter **27**, 503001 (2015).

[157] I. Stasinopoulos, S. Weichselbaumer, A. Bauer, J. Waizner, H. Berger, M. Garst, C. Pfleiderer, and D. Grundler, Linearly Polarized GHz Magnetization Dynamics of Spin Helix Modes in the Ferrimagnetic Insulator Cu_2OSeO_3, Sci. Rep. **7**, 7037 (2017).

[158] T. Weber, J. Waizner, P. Steffens, A. Bauer, C. Pfleiderer, M. Garst, and P. Böni, Polarized Inelastic Neutron Scattering of Nonreciprocal Spin Waves in MnSi, Phys. Rev. B **100**, 060404 (2019).

[159] J. Zang, M. Mostovoy, J. H. Han, and N. Nagaosa, Dynamics of Skyrmion Crystals in Metallic Thin Films, Phys. Rev. Lett. **107**, 136804 (2011).

[160] O. Petrova and O. Tchernyshyov, Spin Waves in a Skyrmion Crystal, Phys. Rev. B **84**, 214433 (2011).

[161] T. Weber, J. Waizner, G. S. Tucker, L. Beddrich, M. Skoulatos, R. Georgii, A. Bauer, C. Pfleiderer, M. Garst, and P. Böni, Non-Reciprocal Magnons in Non-Centrosymmetric MnSi, AIP Adv. **8**, 101328 (2018).

[162] G. L. Squires, *Introduction to the Theory of Thermal Neutron Scattering* (Cambridge University Press, 1978).

[163] S. W. Lovesey, *Theory of Neutron Scattering from Condensed Matter: Volume I: Nuclear Scattering*, Vol. 1 (Oxford University Press, 1986).

[164] S. W. Lovesey, *Theory of Neutron Scattering from Condensed Matter: Volume II: Polarization Effects and Magnetic Scattering*, Vol. 2 (Oxford University Press, 1986).

[165] A. Furrer, J. Mesot, and T. Strässle, *Neutron Scattering in Condensed Matter Physics*, Vol. 0 (World Scientific, 2009).

[166] D. F. Johnston, On the Theory of the Electron Orbital Contribution to the Scattering of Neutrons by Magnetic Ions in Crystals, Proc. Phys. Soc. **88**, 37 (1966).

[167] S. Mühlbauer, *Vortex Lattices in Superconducting Niobium and Skyrmion Lattices in Chiral MnSi: An Investigation by Neutron Scattering*, Ph.D. thesis, Technische Universität München (2009).

[168] J. S. Pedersen, D. Posselt, and K. Mortensen, Analytical Treatment of the Resolution Function for Small-Angle Scattering, J. Appl. Crystallogr. **23**, 321 (1990).

[169] R. Gähler, R. Golub, and T. Keller, Neutron Resonance Spin Echo—a New Tool for High Resolution Spectroscopy, Physica B **180–181**, 899 (1992).

[170] P. Hank, W. Besenböck, R. Gähler, and M. Köppe, Zero-Field Neutron Spin Echo Techniques for Incoherent Scattering, Physica B **234–236**, 1130 (1997).

[171] W. Besenböck, R. Gähler, P. Hank, R. Kahn, M. Köppe, C.-H. de Novion, W. Petry, and J. Wuttke, First Scattering Experiment on MIEZE: A Fourier Transform Time-of-Flight Spectrometer Using Resonance Coils, J. Neutron Res. **7**, 65 (1998).

[172] J. Kindervater, N. Martin, W. Häußler, M. Krautloher, C. Fuchs, S. Mühlbauer, J. A. Lim, E. Blackburn, P. Böni, and C. Pfleiderer, Neutron Spin Echo Spectroscopy under 17 T Magnetic Field at RESEDA, EPJ Web Conf. **83**, 03008 (2015).

[173] F. Mezei, Neutron Spin Echo: A New Concept in Polarized Thermal Neutron Techniques, Z. Phys. **255**, 146 (1972).

[174] F. Mezei, The Principles of Neutron Spin Echo, in *Neutron Spin Echo*, edited by F. Mezei (Springer Berlin Heidelberg, 1980).

[175] R. Golub and R. Gähler, A Neutron Resonance Spin Echo Spectrometer for Quasi-Elastic and Inelastic Scattering, Phys. Lett. **123**, 43 (1987).

[176] C. Franz and T. Schröder, RESEDA: Resonance Spin Echo Spectrometer, J. Large-Scale Res. Facil. **1**, 14 (2015).

[177] C. Franz, O. Soltwedel, C. Fuchs, S. Säubert, F. Haslbeck, A. Wendl, J. K. Jochum, P. Böni, and C. Pfleiderer, The Longitudinal Neutron Resonant Spin Echo Spectrometer RESEDA, Nucl. Instrum. Methods Phys. Res. A **939**, 22 (2019).

[178] C. Franz, S. Säubert, A. Wendl, F. X. Haslbeck, O. Soltwedel, J. K. Jochum, L. Spitz, J. Kindervater, A. Bauer, P. Böni, and C. Pfleiderer, MIEZE Neutron Spin-Echo Spectroscopy of Strongly Correlated Electron Systems, J. Phys. Soc. Jpn. **88**, 081002 (2019).

[179] W. Häussler and U. Schmidt, Effective Field Integral Subtraction by the Combination of Spin Echo and Resonance Spin Echo. Phys. Chem. Chem. Phys. **7**, 1245 (2005).

[180] T. Unruh, Instrument Control at the FRM-II Using TACO and NICOS, arXiv: cond-mat/0210433 (2002), arxiv.org/abs/cond-mat/0210433.

[181] A. Schober, A. Wendl, F. X. Haslbeck, J. K. Jochum, L. Spitz, and C. Franz, The Software Package MIEZEPY for the Reduction of MIEZE Data, J. Phys. Commun. **3**, 103001 (2019).

[182] F. Bloch and A. Siegert, Magnetic Resonance for Nonrotating Fields, Phys. Rev. **57**, 522 (1940).

[183] W. Häussler, P. Böni, M. Klein, C. J. Schmidt, U. Schmidt, F. Groitl, and J. Kindervater, Detection of High Frequency Intensity Oscillations at RESEDA Using the CASCADE Detector, Rev. Sci. Instrum. **82**, 045101 (2011).

[184] M. Klein and C. J. Schmidt, CASCADE, Neutron Detectors for Highest Count Rates in Combination with ASIC/FPGA Based Readout Electronics, Nucl. Instrum. Methods Phys. Res. A **628**, 9 (2011).

[185] C. Franz, O. Soltwedel, S. Säubert, A. Wendl, W. Gottwald, F. Haslbeck, L. Spitz, and C. Pfleiderer, Longitudinal Neutron Resonance Spin Echo Spectroscopy under Large Energy Transfers, J. Phys.: Conf. Ser. **1316**, 012005 (2019).

[186] F. Groitl, T. Keller, K. Rolfs, D. A. Tennant, and K. Habicht, Anomalous Thermal Decoherence in a Quantum Magnet Measured with Neutron Spin Echo Spectroscopy, Phys. Rev. B **93**, 134404 (2016).

[187] A. Heinemann and S. Mühlbauer, SANS-1: Small Angle Neutron Scattering, J. Large-Scale Res. Facil. **1**, 10 (2015).

[188] A. G. Gurevich and G. A. Melkov, *Magnetization Oscillations and Waves* (CRC Press, 1996).

[189] L. Liensberger, *Spin-Orbit Torques and Magnetization Dynamics in Non-Collinear Magnets*, Master's thesis, Technische Universität München (2017).

[190] A. J. Berger, E. R. J. Edwards, H. T. Nembach, A. D. Karenowska, M. Weiler, and T. J. Silva, Inductive Detection of Fieldlike and Dampinglike AC Inverse Spin-Orbit Torques in Ferromagnet/Normal-Metal Bilayers, Phys. Rev. B **97**, 094407 (2018).

[191] J. A. Osborn, Demagnetizing Factors of the General Ellipsoid, Phys. Rev. **67**, 351 (1945).

[192] A. Aharoni, Demagnetizing Factors for Rectangular Ferromagnetic Prisms, J. Appl. Phys. **83**, 3432 (1998).

[193] D. Polder, VIII. On the Theory of Ferromagnetic Resonance, Philos. Mag. **40**, 99 (1949).

[194] C. Kittel, On the Theory of Ferromagnetic Resonance Absorption, Phys. Rev. **73**, 155 (1948).

[195] O. Karlqvist, *Calculation of the Magnetic Field in the Ferromagnetic Layer of a Magnetic Drum* (Elanders boktr., 1954).

[196] T. J. Silva, H. T. Nembach, J. M. Shaw, B. Doyle, K. Oguz, K. O'Brien, and M. Doczy, Characterization of Magnetic Nanostructures for Spin-Torque Memory Applications with Macro- and Micro-Scale Ferromagnetic Resonance, in *Metrology and Diagnostic Techniques for Nanoelectronics* (CRC Press, Taylor & Francis Group, 2016) p. 1454.

[197] C. Bilzer, T. Devolder, P. Crozat, C. Chappert, S. Cardoso, and P. P. Freitas, Vector Network Analyzer Ferromagnetic Resonance of Thin Films on Coplanar Waveguides: Comparison of Different Evaluation Methods, J. Appl. Phys. **101**, 074505 (2007).

[198] H. Maier-Flaig, S. T. B. Goennenwein, R. Ohshima, M. Shiraishi, R. Gross, H. Huebl, and M. Weiler, Note: Derivative Divide, a Method for the Analysis of Broadband Ferromagnetic Resonance in the Frequency Domain, Rev. Sci. Instrum. **89**, 076101 (2018).

[199] F. Haslbeck, S. Säubert, M. Seifert, C. Franz, M. Schulz, A. Heinemann, T. Keller, P. Das, J. D. Thompson, E. D. Bauer, C. Pfleiderer, and M. Janoschek, Ultrahigh-Resolution Neutron Spectroscopy of Low-Energy Spin Dynamics in UGe_2, Phys. Rev. B **99**, 014429 (2019).

[200] K. Oikawa, T. Kamiyama, H. Asano, Y. Ōnuki, and M. Kohgi, Crystal Structure of UGe_2, J. Phys. Soc. Jpn. **65**, 3229 (1996).

[201] P. Boulet, A. Daoudi, M. Potel, H. Noël, G. M. Gross, G. André, and F. Bourée, Crystal and Magnetic Structure of the Uranium Digermanide UGe_2, J. Alloy Compd. **247**, 104 (1997).

[202] K. T. Moore and G. van der Laan, Nature of the $5f$ States in Actinide Metals, Rev. Mod. Phys. **81**, 235 (2009).

[203] A. B. Shick, V. Janiš, V. Drchal, and W. E. Pickett, Spin and Orbital Magnetic State of UGe_2 under Pressure, Phys. Rev. B **70**, 134506 (2004).

[204] A. B. Shick and W. E. Pickett, Magnetism, Spin-Orbit Coupling, and Superconducting Pairing in UGe_2, Phys. Rev. Lett. **86**, 300 (2001).

[205] D. Aoki and J. Flouquet, Ferromagnetism and Superconductivity in Uranium Compounds, J. Phys. Soc. Jpn. **81**, 011003 (2011).

[206] Y. Ōnuki, I. Ukon, S. Won Yun, I. Umehara, K. Satoh, T. Fukuhara, H. Sato, S. Takayanagi, M. Shikama, and A. Ochiai, Magnetic and Electrical Properties of U–Ge Intermetallic Compounds, J. Phys. Soc. Jpn. **61**, 293 (1992).

[207] A. Huxley, I. Sheikin, E. Ressouche, N. Kernavanois, D. Braithwaite, R. Calemczuk, and J. Flouquet, UGe_2: A Ferromagnetic Spin-Triplet Superconductor, Phys. Rev. B **63**, 144519 (2001).

[208] N. Kernavanois, B. Grenier, A. Huxley, E. Ressouche, J. P. Sanchez, and J. Flouquet, Neutron Scattering Study of the Ferromagnetic Superconductor UGe_2, Phys. Rev. B **64**, 174509 (2001).

[209] G. Oomi, T. Kagayama, K. Nishimura, S. W. Yun, and Y. Ōnuki, Electrical Resistivity of Single Crystalline UGe_2 at High Pressure and High Magnetic Field, Physica B **206–207**, 515 (1995).

[210] V. H. Tran, S. Paschen, R. Troć, M. Baenitz, and F. Steglich, Hall Effect in the Ferromagnet UGe_2, Phys. Rev. B **69**, 195314 (2004).

[211] G. Oomi, K. Nishimura, Y. Ōnuki, and S. W. Yun, Anomalous Thermal Expansion of Single-Crystalline UGe_2, Physica B **186–188**, 758 (1993).

[212] H. Misiorek, J. Mucha, R. Troć, and B. Coqblin, Thermal Conductivity Anisotropy in a Ferromagnetic Superconductor, UGe_2, J. Phys.: Condens. Matter **17**, 679 (2005).

[213] Y. Ōnuki, S. Won Yun, I. Ukon, I. Umehara, K. Satoh, I. Sakamoto, M. Hunt, P. Meeson, P.-A. Probst, and M. Springford, High Field Magnetoresistance and de Haas–van Alphen Effect in UGe_2, J. Phys. Soc. Jpn. **60**, 2127 (1991).

[214] T. Terashima, T. Matsumoto, C. Terakura, S. Uji, N. Kimura, M. Endo, T. Komatsubara, and H. Aoki, Evolution of Quasiparticle Properties in UGe_2 with Hydrostatic Pressure Studied via the de Haas–van Alphen Effect, Phys. Rev. Lett. **87**, 166401 (2001).

[215] S. Sakarya, N. H. van Dijk, and E. Brück, Determination of the Magnetic Domain Size in the Ferromagnetic Superconductor UGe_2 by Three-Dimensional Neutron Depolarization, Phys. Rev. B **71**, 174417 (2005).

[216] T. Nishioka, G. Motoyama, S. Nakamura, H. Kadoya, and N. K. Sato, Unusual Nature of Ferromagnetism Coexisting with Superconductivity in UGe_2, Phys. Rev. Lett. **88**, 237203 (2002).

[217] E. Lhotel, C. Paulsen, and A. D. Huxley, Comment on "Unusual Nature of Ferromagnetism Coexisting with Superconductivity in UGe_2", Phys. Rev. Lett. **91**, 209701 (2003).

[218] C. Pfleiderer and A. D. Huxley, Pressure Dependence of the Magnetization in the Ferromagnetic Superconductor UGe_2, Phys. Rev. Lett. **89**, 147005 (2002).

[219] V. Taufour, D. Aoki, G. Knebel, and J. Flouquet, Tricritical Point and Wing Structure in the Itinerant Ferromagnet UGe_2, Phys. Rev. Lett. **105**, 217201 (2010).

[220] N. Kabeya, R. Iijima, E. Osaki, S. Ban, K. Imura, K. Deguchi, N. Aso, Y. Homma, Y. Shiokawa, and N. K. Sato, Tricritical Point of a Ferromagnetic Transition in UGe_2, J. Phys.: Conf. Ser. **200**, 032028 (2010).

[221] V. Taufour, A. Villaume, D. Aoki, G. Knebel, and J. Flouquet, Magnetic Field Evolution of Critical End Point in UGe_2, J. Phys.: Conf. Ser. **273**, 012017 (2011).

[222] D. Belitz, T. R. Kirkpatrick, and T. Vojta, First Order Transitions and Multicritical Points in Weak Itinerant Ferromagnets, Phys. Rev. Lett. **82**, 4707 (1999).

[223] H. Kotegawa, A. Harada, S. Kawasaki, Y. Kawasaki, Y. Kitaoka, Y. Haga, E. Yamamoto, Y. Ōnuki, K. M. Itoh, E. E. Haller, and H. Harima, Evidence for Uniform Coexistence of Ferromagnetism and Unconventional Superconductivity in UGe_2: A 73Ge-NQR Study under Pressure, J. Phys. Soc. Jpn. **74**, 705 (2005).

[224] Y. Ushida, H. Nakane, T. Nishioka, G. Motoyama, S. Nakamura, and N. K. Sato, Thermal Expansion Measurement under Pressure of UGe_2, Physica C **388–389**, 525 (2003).

[225] N. Tateiwa, T. C. Kobayashi, K. Amaya, Y. Haga, R. Settai, and Y. Ōnuki, Heat-Capacity Anomalies at T_{SC} and T^* in the Ferromagnetic Superconductor UGe_2, Phys. Rev. B **69**, 180513 (2004).

[226] N. Tateiwa, K. Hanazono, T. C. Kobayashi, K. Amaya, T. Inoue, K. Kindo, Y. Koike, N. Metoki, Y. Haga, R. Settai, and Y. Onuki, Magnetic Properties of a Pressure-Induced Superconductor UGe_2, J. Phys. Soc. Jpn. **70**, 2876 (2001).

[227] R. Settai, M. Nakashima, S. Araki, Y. Haga, T. C. Kobayashi, N. Tateiwa, H. Yamagami, and Y. Onuki, A Change of the Fermi Surface in UGe_2 across the Critical Pressure, J. Phys. Condens. Matter **14**, L29 (2002).

[228] H. Kotegawa, V. Taufour, D. Aoki, G. Knebel, and J. Flouquet, Evolution toward Quantum Critical End Point in UGe_2, J. Phys. Soc. Jpn. **80**, 083703 (2011).

[229] D. Belitz, T. R. Kirkpatrick, and J. Rollbühler, Tricritical Behavior in Itinerant Quantum Ferromagnets, Phys. Rev. Lett. **94**, 247205 (2005).

[230] K. G. Sandeman, G. G. Lonzarich, and A. J. Schofield, Ferromagnetic Superconductivity Driven by Changing Fermi Surface Topology, Phys. Rev. Lett. **90**, 167005 (2003).

[231] A. Huxley, E. Ressouche, B. Grenier, D. Aoki, J. Flouquet, and C. Pfleiderer, The Co-Existence of Superconductivity and Ferromagnetism in Actinide Compounds, J. Phys. Condens. Matter **15**, S1945 (2003).

[232] N. Tateiwa, T. C. Kobayashi, K. Hanazono, K. Amaya, Y. Haga, R. Settai, and Y. Onuki, Pressure-Induced Superconductivity in a Ferromagnet UGe_2, J. Phys. Condens. Matter **13**, L17 (2001).

[233] I. Sheikin, E. Steep, D. Braithwaite, J.-P. Brison, S. Raymond, D. Jaccard, and J. Flouquet, Superconductivity, Upper Critical Field and Anomalous Normal State in $CePd_2Si_2$ near the Quantum Critical Point, J. Low Temp. Phys. **122**, 591 (2001).

[234] S. Watanabe and K. Miyake, Coupled CDW and SDW Fluctuations as an Origin of Anomalous Properties of Ferromagnetic Superconductor UGe_2, J. Phys. Soc. Jpn. **71**, 2489 (2002).

[235] N. Karchev, Magnon Exchange Mechanism of Ferromagnetic Superconductivity, Phys. Rev. B **67**, 054416 (2003).

[236] T. R. Kirkpatrick, D. Belitz, T. Vojta, and R. Narayanan, Strong Enhancement of Superconducting T_C in Ferromagnetic Phases, Phys. Rev. Lett. **87**, 127003 (2001).

[237] M. W. Kepa, D. A. Sokolov, M. Böhm, and A. D. Huxley, Magnetic Excitations in the Ferromagnetic Superconductor UGe_2 under Pressure, J. Phys. Conf. Ser. **568**, 042016 (2014).

[238] A. Yaouanc, P. Dalmas de Réotier, P. C. M. Gubbens, C. T. Kaiser, A. A. Menovsky, M. Mihalik, and S. P. Cottrell, Evidence for Weak Itinerant Long-Range Magnetic Correlations in UGe_2, Phys. Rev. Lett. **89**, 147001 (2002).

[239] S. Sakarya, P. C. M. Gubbens, A. Yaouanc, P. Dalmas de Réotier, D. Andreica, A. Amato, U. Zimmermann, N. H. van Dijk, E. Brück, Y. Huang, and T. Gortenmulder, Positive Muon Spin Rotation and Relaxation Measurements on the Ferromagnetic Superconductor UGe_2 at Ambient and High Pressure, Phys. Rev. B **81**, 024429 (2010).

[240] N. T. Huy, Y. K. Huang, and A. de Visser, Effect of Annealing on the Magnetic and Superconducting Properties of Single-Crystalline UCoGe, J. Magn. Magn. Mater. **321**, 2691 (2009).

[241] M. Seifert, M. Schulz, G. Benka, C. Pfleiderer, and S. Gilder, Neutron Depolarization Measurements of Magnetite in Chiton Teeth, J. Phys. Conf. Ser. **862**, 012024 (2017).

[242] J. W. Lynn, L. Vasiliu-Doloc, and M. A. Subramanian, Spin Dynamics of the Magnetoresistive Pyrochlore $Tl_2Mn_2O_7$, Phys. Rev. Lett. **80**, 4582 (1998).

[243] C. Simon, S. Mercone, N. Guiblin, C. Martin, A. Brûlet, and G. André, Microphase Separation in $Pr_{0.67}Ca_{0.33}MnO_3$ by Small-Angle Neutron Scattering, Phys. Rev. Lett. **89**, 207202 (2002).

[244] W. Marshall and R. D. Lowde, Magnetic Correlations and Neutron Scattering, Rep. Prog. Phys. **31**, 705 (1968).

[245] P. C. Hohenberg and B. I. Halperin, Theory of Dynamic Critical Phenomena, Rev. Mod. Phys. **49**, 435 (1977).

[246] J. Kindervater, S. Säubert, and P. Böni, Dipolar Effects on the Critical Fluctuations in Fe: Investigation by the Neutron Spin-Echo Technique MIEZE, Phys. Rev. B **95**, 014429 (2017).

[247] V. J. Minkiewicz, M. F. Collins, R. Nathans, and G. Shirane, Critical and Spin-Wave Fluctuations in Nickel by Neutron Scattering, Phys. Rev. **182**, 624 (1969).

[248] C. J. Glinka, V. J. Minkiewicz, and L. Passell, Small-Angle Critical Neutron Scattering from Cobalt, Phys. Rev. B **16**, 4084 (1977).

[249] O. W. Dietrich, J. Als-Nielsen, and L. Passell, Neutron Scattering from the Heisenberg Ferromagnets EuO and EuS. III. Spin Dynamics of EuO, Phys. Rev. B **14**, 4923 (1976).

[250] B. I. Halperin and P. C. Hohenberg, Scaling Laws for Dynamic Critical Phenomena, Phys. Rev. **177**, 952 (1969).

[251] G. G. Lonzarich, The Magnetic Equation of State and Heat Capacity in Weak Itinerant Ferromagnets, J. Magn. Magn. Mater. **54–57**, 612 (1986).

[252] N. R. Bernhoeft, S. A. Law, G. G. Lonzarich, and D. M. Paul, Magnetic Excitations in $ZrZn_2$ at Low Energies and Long Wavelengths, Phys. Scr. **38**, 191 (1988).

[253] G. G. Lonzarich and L. Taillefer, Effect of Spin Fluctuations on the Magnetic Equation of State of Ferromagnetic or Nearly Ferromagnetic Metals, J. Phys. C **18**, 4339 (1985).

[254] G. G. Lonzarich, The Magnetic Electron, in *Electron: A Centenary Volume, Edited by M. Springford* (Cambridge University Press, 1997) p. 109.

[255] J. C. Lashley, R. A. Fisher, J. Flouquet, F. Hardy, A. Huxley, and N. E. Phillips, Ambient-Pressure Specific Heat of Single-Crystal UGe_2, Physica B **378–380**, 961 (2006).

[256] R. Troć, Z. Gajek, and A. Pikul, Dualism of the $5f$ Electrons of the Ferromagnetic Superconductor UGe_2 as Seen in Magnetic, Transport, and Specific-Heat Data, Phys. Rev. B **86**, 224403 (2012).

[257] H. H. Hill, *Plutonium and Other Actinides*, edited by W. N. Miner, Vol. 17 (The Metallurgical Society of AIME, 1970).

[258] D. Fay and J. Appel, Coexistence of p-State Superconductivity and Itinerant Ferromagnetism, Phys. Rev. B **22**, 3173 (1980).

[259] C. Thomas, A. S. da Rosa Simões, J. R. Iglesias, C. Lacroix, N. B. Perkins, and B. Coqblin, Application of the $S = 1$ Underscreened Anderson Lattice Model to Kondo Uranium and Neptunium Compounds, Phys. Rev. B **83**, 014415 (2011).

[260] S. Hoshino and Y. Kuramoto, Itinerant versus Localized Heavy-Electron Magnetism, Phys. Rev. Lett. **111**, 026401 (2013).

[261] T. Hattori, Y. Ihara, Y. Nakai, K. Ishida, Y. Tada, S. Fujimoto, N. Kawakami, E. Osaki, K. Deguchi, N. K. Sato, and I. Satoh, Superconductivity Induced by Longitudinal Ferromagnetic Fluctuations in UCoGe, Phys. Rev. Lett. **108**, 066403 (2012).

[262] C. Stock, D. A. Sokolov, P. Bourges, P. H. Tobash, K. Gofryk, F. Ronning, E. D. Bauer, K. C. Rule, and A. D. Huxley, Anisotropic Critical Magnetic Fluctuations in the Ferromagnetic Superconductor UCoGe, Phys. Rev. Lett. **107**, 187202 (2011).

[263] N. T. Huy, A. Gasparini, D. E. de Nijs, Y. Huang, J. C. P. Klaasse, T. Gortenmulder, A. de Visser, A. Hamann, T. Görlach, and H. v. Löhneysen, Superconductivity on the Border of Weak Itinerant Ferromagnetism in UCoGe, Phys. Rev. Lett. **99**, 067006 (2007).

[264] N. Martin, On the Resolution of a MIEZE Spectrometer, Nucl. Instrum. Methods Phys. Res. **882**, 11 (2018).

[265] S. Ran, C. Eckberg, Q.-P. Ding, Y. Furukawa, T. Metz, S. R. Saha, I.-L. Liu, M. Zic, H. Kim, J. Paglione, and N. P. Butch, Nearly Ferromagnetic Spin-Triplet Superconductivity, Science **365**, 685 (2019).

[266] D. Aoki, A. Nakamura, F. Honda, D. Li, Y. Homma, Y. Shimizu, Y. J. Sato, G. Knebel, J.-P. Brison, A. Pourret, D. Braithwaite, G. Lapertot, Q. Niu, M. Vališka, H. Harima, and J. Flouquet, Unconventional Superconductivity in Heavy Fermion UTe2, J. Phys. Soc. Jpn. **88**, 043702 (2019).

[267] L. Jiao, S. Howard, S. Ran, Z. Wang, J. O. Rodriguez, M. Sigrist, Z. Wang, N. P. Butch, and V. Madhavan, Chiral Superconductivity in Heavy-Fermion Metal UTe2, Nature **579**, 523 (2020).

[268] M. Janoschek, A Magnetic Field Boost for Superconductors, Nat. Phys. **15**, 1211 (2019).

[269] S. Ran, I.-L. Liu, Y. S. Eo, D. J. Campbell, P. M. Neves, W. T. Fuhrman, S. R. Saha, C. Eckberg, H. Kim, D. Graf, F. Balakirev, J. Singleton, J. Paglione, and N. P. Butch, Extreme Magnetic Field-Boosted Superconductivity, Nat. Phys. **15**, 1250 (2019).

[270] C. Duan, K. Sasmal, M. B. Maple, A. Podlesnyak, J.-X. Zhu, Q. Si, and P. Dai, Incommensurate Spin Fluctuations in the Spin-Triplet Superconductor Candidate UTe_2, Phys. Rev. Lett. **125**, 237003 (2020).

[271] S. Sundar, S. Gheidi, K. Akintola, A. M. Côté, S. R. Dunsiger, S. Ran, N. P. Butch, S. R. Saha, J. Paglione, and J. E. Sonier, Coexistence of Ferromagnetic Fluctuations and Superconductivity in the Actinide Superconductor UTe 2, Phys. Rev. B **100**, 140502 (2019).

[272] Y. Tokunaga, H. Sakai, S. Kambe, T. Hattori, N. Higa, G. Nakamine, S. Kitagawa, K. Ishida, A. Nakamura, Y. Shimizu, Y. Homma, D. Li, F. Honda, and D. Aoki, 125Te-NMR Study on a Single Crystal of Heavy Fermion Superconductor UTe2, J. Phys. Soc. Jpn. **88**, 073701 (2019).

[273] J. Wild, T. N. G. Meier, S. Pöllath, M. Kronseder, A. Bauer, A. Chacon, M. Halder, M. Schowalter, A. Rosenauer, J. Zweck, J. Müller, A. Rosch, C. Pfleiderer, and C. H. Back, Entropy-Limited Topological Protection of Skyrmions, Sci. Adv. **3**, e1701704 (2017).

[274] J. Rajeswari, P. Huang, G. F. Mancini, Y. Murooka, T. Latychevskaia, D. McGrouther, M. Cantoni, E. Baldini, J. S. White, A. Magrez, T. Giamarchi, H. M. Rønnow, and F. Carbone, Filming the Formation and Fluctuation of Skyrmion Domains by Cryo-Lorentz Transmission Electron Microscopy, PNAS **112**, 14212 (2015).

[275] G. Berruto, I. Madan, Y. Murooka, G. M. Vanacore, E. Pomarico, J. Rajeswari, R. Lamb, P. Huang, A. J. Kruchkov, Y. Togawa, T. LaGrange, D. McGrouther, H. M. Rønnow, and F. Carbone, Laser-Induced Skyrmion Writing and Erasing in an Ultrafast Cryo-Lorentz Transmission Electron Microscope, Phys. Rev. Lett. **120**, 117201 (2018).

[276] P.-J. Hsu, A. Kubetzka, A. Finco, N. Romming, K. von Bergmann, and R. Wiesendanger, Electric-Field-Driven Switching of Individual Magnetic Skyrmions, Nat. Nanotechnol. **12**, 123 (2017).

[277] N. Romming, A. Kubetzka, C. Hanneken, K. von Bergmann, and R. Wiesendanger, Field-Dependent Size and Shape of Single Magnetic Skyrmions, Phys. Rev. Lett. **114**, 177203 (2015).

[278] H. E. Stanley, *Introduction to Phase Transitions and Critical Phenomena* (Oxford University Press, 1987).

[279] J. J. Binney, N. J. Dowrick, A. J. Fisher, and M. Newman, *The Theory of Critical Phenomena: An Introduction to the Renormalization Group* (Oxford University Press, 1992).

[280] H. Wilhelm, M. Baenitz, M. Schmidt, U. K. Rößler, A. A. Leonov, and A. N. Bogdanov, Precursor Phenomena at the Magnetic Ordering of the Cubic Helimagnet FeGe, Phys. Rev. Lett. **107**, 127203 (2011).

[281] L. Cevey, H. Wilhelm, M. Schmidt, and R. Lortz, Thermodynamic Investigations in the Precursor Region of FeGe, Phys. Status Solidi B **250**, 650 (2013).

[282] J. Kindervater, W. Häußler, M. Janoschek, C. Pfleiderer, P. Böni, and M. Garst, Critical Spin-Flip Scattering at the Helimagnetic Transition of MnSi, Phys. Rev. B **89**, 180408 (2014).

[283] A. Neubauer, C. Pfleiderer, R. Ritz, P. G. Niklowitz, and P. Böni, Hall Effect and Magnetoresistance in MnSi, Physica B **404**, 3163 (2009).

[284] M. Janoschek, F. Jonietz, P. Link, C. Pfleiderer, and P. Böni, Helimagnons in the Skyrmion Lattice of MnSi, J. Phys. Conf. Ser. **200**, 032026 (2010).

[285] C. Pappas, L. J. Bannenberg, E. Lelièvre-Berna, F. Qian, C. D. Dewhurst, R. M. Dalgliesh, D. L. Schlagel, T. A. Lograsso, and P. Falus, Magnetic Fluctuations, Precursor Phenomena, and Phase Transition in MnSi under a Magnetic Field, Phys. Rev. Lett. **119**, 047203 (2017).

[286] A. Neubauer, J. Bœuf, A. Bauer, B. Russ, H. v. Löhneysen, and C. Pfleiderer, Ultra-High Vacuum Compatible Image Furnace, Rev. Sci. Instrum. **82**, 013902 (2011).

[287] A. Bauer, A. Neubauer, W. Münzer, A. Regnat, G. Benka, M. Meven, B. Pedersen, and C. Pfleiderer, Ultra-High Vacuum Compatible Induction-Heated Rod Casting Furnace, Rev. Sci. Instrum. **87**, 063909 (2016).

[288] M. Reiner, A. Bauer, M. Leitner, T. Gigl, W. Anwand, M. Butterling, A. Wagner, P. Kudejova, C. Pfleiderer, and C. Hugenschmidt, Positron Spectroscopy of Point Defects in the Skyrmion-Lattice Compound MnSi, Sci. Rep. **6**, 29109 (2016).

[289] B. Binz, A. Vishwanath, and V. Aji, Theory of the Helical Spin Crystal: A Candidate for the Partially Ordered State of MnSi, Phys. Rev. Lett. **96**, 207202 (2006).

[290] B. Binz and A. Vishwanath, Theory of Helical Spin Crystals: Phases, Textures, and Properties, Phys. Rev. B **74**, 214408 (2006).

[291] J.-W. G. Bos, C. V. Colin, and T. T. M. Palstra, Magnetoelectric Coupling in the Cubic Ferrimagnet Cu_2OSeO_3, Phys. Rev. B **78**, 094416 (2008).

[292] H. Effenberger and F. Pertlik, Die Kristallstrukturen der Kupfer(II)-oxo-selenite $Cu_2O(SeO_3)$ (kubisch und monoklin) und $Cu_4O(SeO_3)_3$ (monoklin und triklin), Monatsh. Chem. **117**, 887 (1986).

[293] K. Kohn, A New Ferrimagnet Cu_2SeO_4, J. Phys. Soc. Jpn. **42**, 2065 (1977).

[294] O. Janson, I. Rousochatzakis, A. A. Tsirlin, M. Belesi, A. A. Leonov, U. K. Rößler, J. van den Brink, and H. Rosner, The Quantum Nature of Skyrmions and Half-Skyrmions in Cu_2OSeO_3, Nat. Commun. **5**, 5376 (2014).

[295] M. Ozerov, J. Romhányi, M. Belesi, H. Berger, J.-P. Ansermet, J. van den Brink, J. Wosnitza, S. A. Zvyagin, and I. Rousochatzakis, Establishing the Fundamental Magnetic Interactions in the Chiral Skyrmionic Mott Insulator CuR_2OSeO_3 by Terahertz Electron Spin Resonance, Phys. Rev. Lett. **113**, 157205 (2014).

[296] K. H. Miller, X. S. Xu., H. Berger, E. S. Knowles, D. J. Arenas, M. W. Meisel, and D. B. Tanner, Magnetodielectric Coupling of Infrared Phonons in Single-Crystal Cu_2OSeO_3, Phys. Rev. B **82**, 144107 (2010).

[297] V. P. Gnezdilov, K. V. Lamonova, Y. G. Pashkevich, P. Lemmens, H. Berger, F. Bussy, and S. L. Gnatchenko, Magnetoelectricity in the Ferrimagnetic Cu_2OSeO_3: Symmetry Analysis and Raman Scattering Study, Low Temp. Phys. **36**, 550 (2010).

[298] M. C. Langner, S. Roy, S. K. Mishra, J. C. T. Lee, X. W. Shi, M. A. Hossain, Y.-D. Chuang, S. Seki, Y. Tokura, S. D. Kevan, and R. W. Schoenlein, Coupled Skyrmion Sublattices in Cu_2OSeO_3, Phys. Rev. Lett. **112**, 167202 (2014).

[299] S. L. Zhang, A. Bauer, H. Berger, C. Pfleiderer, G. van der Laan, and T. Hesjedal, Resonant Elastic X-Ray Scattering from the Skyrmion Lattice in Cu_2OSeO_3, Phys. Rev. B **93**, 214420 (2016).

[300] S. L. Zhang, A. Bauer, D. M. Burn, P. Milde, E. Neuber, L. M. Eng, H. Berger, C. Pfleiderer, G. van der Laan, and T. Hesjedal, Multidomain Skyrmion Lattice State in Cu_2OSeO_3, Nano Lett. **16**, 3285 (2016).

[301] S. Pöllath, A. Aqeel, A. Bauer, C. Luo, H. Ryll, F. Radu, C. Pfleiderer, G. Woltersdorf, and C. H. Back, Ferromagnetic Resonance with Magnetic Phase Selectivity by Means of Resonant Elastic X-Ray Scattering on a Chiral Magnet, Phys. Rev. Lett. **123**, 167201 (2019).

[302] N. Ogawa, S. Seki, and Y. Tokura, Ultrafast Optical Excitation of Magnetic Skyrmions, Sci. Rep. **5**, 9552 (2015).

[303] M. I. Kobets, K. G. Dergachev, E. N. Khatsko, A. I. Rykova, P. Lemmens, D. Wulferding, and H. Berger, Microwave Absorption in the Frustrated Ferrimagnet Cu_2OSeO_3, Low Temp. Phys. **36**, 176 (2010).

[304] M. Belesi, I. Rousochatzakis, H. C. Wu, H. Berger, I. V. Shvets, F. Mila, and J. P. Ansermet, Ferrimagnetism of the Magnetoelectric Compound Cu_2OSeO_3 Probed by ^{77}Se NMR, Phys. Rev. B **82**, 094422 (2010).

[305] C. L. Huang, K. F. Tseng, C. C. Chou, S. Mukherjee, J. L. Her, Y. H. Matsuda, K. Kindo, H. Berger, and H. D. Yang, Observation of a Second Metastable Spin-Ordered State in Ferrimagnet Cu_2OSeO_3, Phys. Rev. B **83**, 052402 (2011).

[306] A. Maisuradze, Z. Guguchia, B. Graneli, H. M. Rønnow, H. Berger, and H. Keller, μSR Investigation of Magnetism and Magnetoelectric Coupling in Cu_2OSeO_3, Phys. Rev. B **84**, 064433 (2011).

[307] N. Prasai, B. A. Trump, G. G. Marcus, A. Akopyan, S. X. Huang, T. M. McQueen, and J. L. Cohn, Ballistic Magnon Heat Conduction and Possible Poiseuille Flow in the Helimagnetic Insulator Cu_2OSeO_3, Phys. Rev. B **95**, 224407 (2017).

List of publications

1. **Tunable Cooperativity in Coupled Spin–Cavity Systems**
   L. Liensberger, F.X. Haslbeck, Andreas Bauer, Helmuth Berger, Rudolf Gross, Hans Huebl, Christian Pfleiderer, Mathias Weiler
   Physical Review B **104**, L100415 (2021)
2. **Evolution of magnetocrystalline anisotropies in $Mn_{1-x}Fe_xSi$ and $Mn_{1-x}Co_xSi$ as inferred from small-angle neutron scattering and bulk properties**
   J. Kindervater, T. Adams, A. Bauer, F.X. Haslbeck, A. Chacon, S. Mühlbauer, F. Jonietz, A. Neubauer, U. Gasser, G. Nagy, N. Martin, W. Häußler, R. Georgii, M. Garst, C. Pfleiderer
   Physical Review B **101**, 104406 (2020)
3. **Weak Crystallization of Fluctuating Skyrmion Textures in MnSi**
   J. Kindervater, I. Stasinopoulos, A. Bauer, F.X. Haslbeck, F. Rucker, A. Chacon, S. Mühlbauer, C. Franz, M. Garst, D. Grundler, C. Pfleiderer
   Physical Review X **9**, 041059 (2019)
4. **Ultrahigh-Resolution Neutron Spectroscopy of Low-Energy Spin Dynamics in UGe_2**
   F.X. Haslbeck, S. Säubert, M. Seifert, C. Franz, M. Schulz, A. Heinemann, T. Keller, P. Das, J. D. Thompson, E. D. Bauer, C. Pfleiderer, and M. Janoschek
   Physical Review B **99**, 014429 (2019)
5. **The software package MIEZEPY for the reduction of MIEZE data**
   A. Schober, A. Wendl, F.X. Haslbeck, J. Jochum, L. Spitz, C. Franz
   Journal of Physics Communications **3**, 103001 (2019)
6. **Longitudinal Neutron Resonance Spin Echo Spectroscopy under Large Energy Transfers**
   C. Franz, O. Soltwedel, S. Säubert, A. Wendl, W. Gottwald, F.X. Haslbeck, L. Spitz, and C. Pfleiderer
   Journal of Physics: Conference Series **1316**, 012005 (2019)
7. **The Longitudinal Neutron Resonant Spin Echo Spectrometer RESEDA**
   C. Franz, O. Soltwedel, C. Fuchs, S. Säubert, F.X. Haslbeck, A. Wendl, J. K.

Jochum, P. Böni, and C. Pfleiderer
Nuclear Inst. and Methods in Physics Research A **939**, 22-29 (2019)

8. **MIEZE Neutron Spin-Echo Spectroscopy of Strongly Correlated Electron Systems**
C. Franz, S. Säubert, A. Wendl, F.X. Haslbeck, O. Soltwedel, J. K. Jochum, L. Spitz, J. Kindervater, A. Bauer, P. Böni, and C. Pfleiderer
Journal of the Physical Society of Japan **88**, 081002 (2019)

9. **Dipolar Interactions in Fe: A Study with the Neutron Larmor Precession Technique MIEZE in a Longitudinal Field Configuration**
S. Säubert, J. Kindervater, F.X. Haslbeck, C. Franz, M. Skoulatos, and P. Böni
Physical Review B **99**, 184423 (2019)

Acknowledgements

An dieser Stelle möchte ich mich bei zahlreichen Menschen bedanken, die zum Gelingen dieser Doktorarbeit beigetragen und mich die letzten Jahre unterstützt haben. Mein besonderer Dank gilt

- Prof. Christian Pfleiderer für die Möglichkeit in einem abwechslungsreichen Thema zu promovieren, bei dem ich stets Neues lernen und entdecken konnte und mit vielen Wissenschaftlern weltweit arbeiten durfte. Du hast eine hervorragende, kollegiale Arbeitsgruppe etabliert, die mehr ist als nur ein Arbeitsplatz. Die Zusammenarbeit hat mir immer Freude bereitet. Vielen Dank für die unzähligen Gespräche, Ratschläge, Diskussionen und die Möglichkeiten Summer und Winter Schools, Konferenzen und Fortbildungen zu besuchen.
- Prof. Marc Janoschek, denn dein Fellowship in München und die Kooperation mit Christian machten meine Promotion noch vielseitiger und ich konnte in die diversen Geheimnisse der Neutronenstreuung vordringen. Vielen Dank für viele Gespräche über Festkörperphysik und Neutronenstreuung, Hilfe bei zahlreichen Messzeiten, die Karriere- und Lebensberatung und die unvergesslichen Aufenthalte in Los Alamos, Santa Fe und Daejeon.
- Prof. Peter Böni, dass du dem RESEDA Team und mir mit Rat und Tat geholfen hast Spin-Echo zu verstehen und die gute Zusammenarbeit mit deinem Lehrstuhl.
- der gesamten Bunga Bunga Truppe mit Andi Wendl, Alex Engelhardt, Alex Regnat, Alfonso Chacon, Andreas Bauer, Anh Tong, Christian Oberleitner, Christoph Schnarr, Denis Metus, Felix Rucker, Georg Benka, Grace Causer, Jan Spallek, Marc Seifert, Markus Halder, Markus Kleinhans, Nico Huber, Pau Jorba Cabre, Steffen Säubert, Vivek Kumar und Wolfgang Simeth für die vielen gemeinsamen Feierabendbiere, abstruse Diskussionen in der Kaffeerunde, schlaflose Konferenzen und TRR80 Meetings und famose Oktoberfestbesuche.
- dem RESEDA Team mit Christian Franz, Olaf Soltwedel, Thorsten Schröder, Johanna Jochum, Jonathan Leiner, Christian Fuchs, Philipp Bender, Steffen Säubert und Andreas Wendl für unvergessliche Stunden am Instrument mit Taco-Server-Restarts, Spin-Echo-Tunen, Probenmasken Basteln, spektakulären Probenwechseln,

Wasserschäden Aufwischen, Untergrund Suchen, Spin-Echo-Daten Entschlüsseln und last but not least erquickende Stunden mit Igor Pro.

- dem Herold Steffen Säubert und Generalsekretär Marc Seifert des Vergüngungstriumvirats, für herausragende Anstrengungen den Lehrstuhl im Bierdunst, ob am Oktoberfest oder in der Rennbahn, zusammenzubringen. Außerdem für die 24/7-Prokrastinationsmöglichkeiten und offene Ohren für gerechtfertigtes Gejammer.
- allen Kollegen am MLZ: Dem Team an SANS-1 Sebastian Mühlbauer, Andre Heinemann und Andreas Wilhelm für die Anstrengungen meine High-End Mikrowelle und ihren Einfluss auf Skyrmionen zu verstehen. Astrid Schneidewind, Michael Schulz, Anatoliy Senyshyn und Thomas Keller mit denen ich so einige Herausforderungen mit Druckzellen und Cer-Verbindungen lösen durfte. Dem Team der Probenumgebung Jürgen Peters, Heiner Kolb, Helga Ströhl, Peter Biber, Andreas Buchner und Milan Antic, dass ihr auch am Wochenende und bis spät abends geholfen habt Magnetfelder und Kryostaten zum Laufen zu bringen und halten. Dem Software Team Georg Brandl, Enno Faulhaber, Jens Krüger und Alex Lenz für schnelle Hilfe und das Verwerten meines Programmiercodes.
- Prof. Achim Rosch und Lukas Heinen von der Universität Köln für die Unterstützung und das Erklären theoretischer Physik rund um Skyrmionen.
- Prof. Christian Back für die Installation einer hervorragenden Siebträgermaschine am Nachbarlehrstuhl.
- Jonathan, Lukas, Teodora, Kathi, Sophia und Sina für die unvergessliche Zeit in der Kraepelin-WG, für gesellige Koch-, Trink- und Trash-TV-Abende. Ein Leben ohne die WG wäre nicht mal halb so unterhaltsam.
- allen Freunden aus München, der Studentenstadt und meiner Heimat Weigendorf, Jan, Michael, Dominik, Georg, Tobias, Julia, Lukas, Johanna, Christoph, Anna, Simon, Sarah, Felix, Ursa, Caro, Dani, Steffen, Suzan, Marc, Nessi, Felix, Alisa... durch die das Leben außerhalb der Promotion nie langweilig wurde und die die Wochenenden und Abende mit Leben und Gaudi füllten.
- meiner Familie, insbesondere meinen Eltern Gabriele und Wilhelm, dass ihr mich mein Leben lang und vor allem die letzten Jahre während des Studiums und der Promotion unterstützt habt und stets hinter mir steht. Meinen Geschwistern Max, Johannes und Anna für die heiteren Pendelfahrten in die niederbayrische Heimat und die großartigen Zeiten, die ich mit euch verbringen durfte.
- Dinah, denn deine Herzlichkeit, dein Humor und deine Liebe für die schönen Dinge im Leben bereichern mich Tag ein Tag aus. Danke, dass du immer an meiner Seite stehst und mich bei allen Vorhaben unterstützt. Ich freue mich schon auf die kommenden Abenteuer mit dir.